

ANALYSIS OF MYOCARDIAL CONTRACTILITY WITH MAGNETIC RESONANCE

Sharmeen Masood

**A dissertation submitted in partial fulfilment
of the requirements for the degree of
Doctor of Philosophy
of the
University of London**

**December 2003
Department of Computing
National Heart and Lung Institute
Imperial College of Science, Technology and Medicine**

بِسْمِ اللَّهِ الرَّحْمَنِ الرَّحِيمِ

In the Name of God, Most Gracious, Most Merciful

الَّذِينَ آمَنُوا وَتَطْمَئِنُّ قُلُوبُهُمْ بِذِكْرِ اللَّهِ أَلَا بِذِكْرِ اللَّهِ تَطْمَئِنُّ
الْقُلُوبُ ﴿٢٨﴾

*"Those who believe, and whose hearts find satisfaction in the remembrance
of God: for without doubt in the remembrance of God do hearts find
satisfaction. (13:28)*

Dedicated to my mother and father

ANALYSIS OF MYOCARDIAL CONTRACTILITY WITH MAGNETIC RESONANCE

ABSTRACT

Heart failure has considerable morbidity and poor prognosis. An understanding of the underlying mechanics governing myocardial contraction is a prerequisite for interpreting and predicting changes induced by heart disease. Gross changes in contractile behaviour of the myocardium are readily detected with existing techniques. For more subtle changes during early stages of cardiac dysfunction, however, it requires a sensitive method for measuring, as well as a precise criterion for quantifying, normal and impaired myocardial function. Cardiovascular Magnetic Resonance (CMR) imaging is emerging as an important clinical tool because of its safety, versatility, and the high quality images it produces that allow accurate and reproducible quantification of cardiac structure and function. Traditional CMR approaches for measuring contractility rely on tagging of the myocardium with fiducial markers and require a lengthy and often subjective dependant post-processing procedure. The aim of this research is to develop a new technique, which uses velocity as a marker for the visualisation and assessment of myocardial contractility. Two parallel approaches have been investigated for the assessment of myocardial velocity. The first of these is harmonic phase (HARP) imaging. HARP imaging allows direct derivation of myocardial velocity and strain without the need of further user interaction. We investigated the effect of respiration on the accuracy of the derived contractility, and assessed the clinical applicability and potential pitfalls of the technique by analysing results from a group of patients with hypertrophic cardiomyopathy. The second technique we have investigated is the direct measurement of myocardial velocity with phase contrast myocardial velocity mapping. The imaging sequence used employs effective blood saturation for reducing flow induced phase errors within the myocardium. View sharing was used to improve the temporal resolution, which permitted acquisition of 3D velocity information throughout the cardiac cycle in a single breath-hold, enabling a comprehensive assessment of strain rate of the left ventricle.

One key factor that affects the derivation of myocardial contractility based on myocardial velocity is the practical inconsistency of the velocity data. A novel iterative optimisation scheme by incorporating the incompressibility constraint was developed for the restoration of myocardial velocity data. The method allowed accurate assessment of both in-plane and through-plan strain rates, as demonstrated with both synthetic and *in vivo* data acquired from normal subjects and ischaemic patients. To further enhance the clinical potential of the technique and facilitate the visual assessment of contractile abnormality with myocardial velocity mapping, a complementary analysis framework, named Virtual Tagging, has been developed. The method used velocity data in all directions combined with a finite element mesh incorporating geometrical and physical constraints. The Virtual Tagging framework allowed velocity measurements to be used for calculating strain distribution within the 3D volume. It also permitted easy visualisation of the displacement of the tissue, akin to traditional CMR tagging. Detailed validation of the technique is provided, which involves both numerical simulation and *in vitro* phantom experiments.

The main contribution of this thesis is in the improvement of the effectiveness and quality of quantitative myocardial contractility analysis from both sequence design and medical image computing perspectives. It is aimed at providing a sensitive means of detecting subtle as well as gross changes in contractile behaviour of the myocardium. The study is expected to provide a clinically viable platform for functional correlation with other functional measures such as myocardial perfusion and diffusion, and to serve as an aid for further understanding of the links between intrinsic cardiac mechanics, localised genesis, and progression of cardiovascular disease.

Acknowledgments

First and foremost I would like to thank my supervisor Professor Guang-Zhong Yang. He provided me with constant encouragement, motivation, support and criticism, when necessary, throughout the course of this PhD. Professor Yang will always be a source of inspiration and admiration for me.

I am extremely grateful to my second supervisor Professor David Firmin and Dr Peter Gatehouse for teaching me everything I know about MR physics. This work would not have been possible without their guidance and help.

My thanks also go to Professor Sir Magdi Yacoub and Dr Hans Reiber for taking the time out to be my examiners.

Dr Jianxin Gao's efforts to perfect the Virtual Tagging framework are greatly appreciated. His lessons in solid mechanics and numerical methods helped me gain a deeper understanding of the field.

Dr Sanjay Prasad, Dr James Moon, Dr Andrew Elkington and Dr Raad Mohiaddin were kind enough to let me scan their patients. Sanjay's infectious enthusiasm for my work helped me retain mine at low times.

Miss Fani Deglianni's work on the HARP processing software has been invaluable to the content of this thesis and to future clinical work at the Royal Brompton Hospital. Her dedication to the work is greatly appreciated. I would also like to thank Dr Gavin Estcourt for his initial work on the virtual tagging framework.

The *in vivo* velocity mapping work would not have been possible without the breath-hold sequence and MatLab software developed by Mr Bernd Jung. I would like to thank Dr Nael Osman and Dr Joost Kuijer for their helpful discussions on HARP artefacts via email.

I would like to thank Dr R Wagner, Dr P-S Jouk, Dr JA Illingworth, Dr F Prinzen, Professor P Boesiger, Professor K Ugurbil, Dr N Tsekos and Professor Van Wende for permission to use their figures. Dr Torrent-Guasp's guidance in researching myocardial structure and gift of a rubber mould of the heart was a great help.

This work would not have been possible without all my volunteers over the years, too many to name; my friends, family, and colleagues from the MIC Lab and the Royal Brompton Hospital. The support provided to me over the last four years by my friends and colleagues will not be forgotten, especially Yusra Khreegi and Robert Merrifield.

I would like to thank my parents for instilling the confidence in me to do this. Their support, encouragement, guidance and, above all, love has enabled me to fully appreciate life and the opportunities it offers. My sisters, who remain my best friends, were a constant support. A big thank-you to Sherezad for putting up with my bad moods and mess, especially during the write-up period.

This project would not have been possible without the funding provided by the British Heart Foundation. Last but not least, I am grateful to God for granting me the opportunity and ability to do work which I enjoy.

Table of Contents

1 Introduction	23
2 Macroscopic Structure and Physiology of the Normal and Diseased Heart	28
2.1 Introduction	28
2.2 Histology and Cellular Structure	30
2.3 Macroscopic Muscle Structure.....	32
2.3.1 <i>Left Ventricle Apical Half</i>	33
2.3.2 <i>Left Ventricle Basal Half</i>	33
2.3.3 <i>Right Ventricle Apical Half</i>	34
2.3.4 <i>Right Ventricle Basal Half</i>	34
2.3.5 <i>One Muscle Band</i>	34
2.3.6 <i>Other Models</i>	35
2.4 The Cardiac Cycle and Ventricular Dynamics	37
2.4.1 <i>Narrowing of the ventricles</i>	41
2.4.2 <i>Shortening of the ventricles</i>	41
2.4.3 <i>Lengthening of the ventricles</i>	42
2.4.4 <i>Widening of the ventricles</i>	42
2.5 Coronary Circulation and Myocardial Mechanics	43
2.6 Perfusion	46
2.7 Atherosclerosis.....	47
2.8 Myocardial Ischaemia: Causes and Effects.....	48
2.9 Myocardial Remodelling	50
2.10 Myocardial Infarction.....	53
2.11 Myocardial Contractility: a Basic Representation	53
2.11.1 <i>The Need for Non-Invasive Imaging Techniques</i>	55
2.12 Conclusion.....	57
3 MR Techniques for Measuring Myocardial Motion and Fibre Architecture.....	59
3.1 Introduction	59

3.2 Mathematical Description of Myocardial Motion	61
3.3 MR Tagging.....	62
3.3.1 Sequence Design.....	62
3.3.2 Image Analysis.....	66
3.3.3 Clinical Applications.....	68
3.4 MR Velocity Encoding Using Phase Shifts.....	69
3.4.1 Pulse Sequences Design	70
3.4.2 Image Analysis.....	70
3.5 MR Diffusion Imaging.....	73
3.5.1 Pulse Sequence Design.....	74
3.5.2 Cardiac Diffusion Studies	76
3.6 Discussion and Conclusions	77
4 Measuring Myocardial Motion In Vivo Using HARP Imaging	79
4.1 Introduction	79
4.2 Extracting Myocardial Motion	80
4.2.1 MR Sequence Design	80
4.2.2 Respiratory Gating using Navigator Echoes.....	84
4.2.3 CSPAMM Sequence with Navigator Echoes.....	87
4.2.4 In Vivo Imaging Protocol.....	89
4.2.5 Calculating Strain and Velocity using HARP processing	91
4.2.6 Velocity Vector Field Restoration	93
4.3 In Vivo Strain and Velocity Measurements using HARP Imaging...	95
4.3.1 Effect of Variation in Respiration on Myocardial Strain	104
4.4 Changes in Contractility in Cardiomyopathy	107
4.4.1 Relevance of CMR in Cardiomyopathy.....	107
4.4.2 Hypertrophic Cardiomyopathy (HCM)	108
4.4.3 Measuring Contractility in HCM.....	109
4.4.4 Comparison of Hypertrophied to Normal Hearts.....	110
4.5 Discussion and Conclusion	118
4.5.1 HARP for Evaluating HCM	118
4.5.2 Conclusions	119
4.5.3 Limitations of HARP Imaging.....	120
5 MR Phase Contrast Myocardial Velocity Mapping	122

5.1 Introduction	122
5.2. Principle of Phase Contrast Velocity Mapping	124
5.3 CMR Phase Contrast Velocity Mapping Sequence	126
5.3.2 CMR Velocity Mapping with Respiratory Gating.....	130
5.3.3 Velocity to Noise Ratio	132
5.3.4 Errors due to Phase Shifts.....	132
5.4 Experimental Method	134
5.4.1 Artefact Reduction	134
5.4.2 Derivation of Strain Rate from MR Velocity Data	142
5.5 Discussion and Conclusion	151
6 Improving the Consistency of Velocity Data	153
6.1 Introduction	153
6.2 Principle and Methods.....	154
6.2.1 Iterative Velocity Field Restoration using the Incompressibility Constraint.....	155
6.2.2 3D Strain Rate Computation	156
6.3 Validation.....	157
6.3.1 Simulation Dataset.....	157
6.3.2 Image Acquisition for In Vivo Validation.....	159
6.3.3 Normalisation	160
6.4 Results	162
6.4.1 Choice of Weighting Factor.....	162
6.4.2 Simulation Data	164
6.4.3 In Vivo Validation	168
6.5 Discussion and Conclusion	177
7 The Virtual Tagging Framework.....	178
7.1 Introduction	178
7.2 Materials and Methods.....	179
7.2.1 Generation of Virtual Tags.....	179
7.2.2 Strain Calculation.....	181
7.2.3 Constraint of Mass Conservation.....	182
7.2.4 Optimisation	183
7.3 Experiments	184

7.3.1 Numerical Validation.....	184
7.3.2 Phantom Validation and Experimental Set-up	186
7.4 Results.....	187
7.5 Discussion and Conclusions	196
8 Conclusion.....	198
8.1 Importance of Measuring Myocardial Motion.....	198
8.2 Measuring Myocardial Motion	199
8.2.1 CMR Tagging	199
8.2.2 CMR Velocity Mapping.....	200
8.2.3 Virtual Tagging.....	201
8.3 Future Work.....	202
APPENDIX I: MR Tagging	205
Complementary SPAMM (CSPAMM).....	206
APPENDIX II: MR Velocity Mapping.....	209
APPENDIX III: Harmonic Phase (HARP) Imaging.....	214
MR Tagging: a Mathematical Description.....	214
Harmonic Images	216
Determining Strain from HARP Images	217
Velocity from HARP Images	221
Practical Implementation.....	222
References.....	226

List of Figures

Figure 2.1 The anatomy of the heart. The arteries carrying blood away from the heart, from the LV, are marked in red while the veins carrying blood to the heart, to the right atrium, are in blue..... 30

Figure 2.2 Cardiac muscle tissue is striated with the myocytes containing usually just one central nucleus and being connected to each other by intercalated discs. [Image courtesy of Dr R Wagner, Biological Sciences, University of Delaware] 31

Figure 2.3 A rubber mould of the heart reveals it to be a single muscle band which can be unwound to reveal the helical structure of the fibres making up the ventricles. There is a “double twist” in 3D if using a single muscle band as the basic structure of the model. 35

Figure 2.4 (A) One of the bundles, *i.e.*, the superficial bulbospiral muscle, described by Robb and Robb is shown. (B) Torrent-Guasp’s one muscle band model represents the myocardium as a ribbon wound in a double helix. (C) The left hand side shows Krehl’s (1891) model and the right hand side Streeter (1979) and Chadwick’s (1982). In Streeter’s model of the LV the myocardial fibres run like geodesics on toroidal surfaces. These surfaces or layers are nested within one another with the trajectories of fibres in each layer changing to more circumferential further into the myocardium. (D) Rushmer (1953) describes three layers, with the superficial layer, the middle layer or constrictor muscle and the deep layer. [Image courtesy of Dr PS Jouk, UF Biologie du developpement et Genetique clinique, Centre Hospitalier Universitaire de Grenoble, France] 37

Figure 2.5 Cardiac pressure variation throughout the cardiac cycle. The blue line shows the echocardiogram trace, in mV, whilst the purple line is the ventricular action potential, *i.e.*, the electrical stimulus to the ventricle. The red line, a trace of the ventricular pressure, rises rapidly after the mitral valve closes until the aortic valve opens to allow rapid ejection of the blood into the aorta. The green line is the aortic pressure, which rises in systole and then decreases slowly as flow slows due to ventricular pressure decreasing. [Image courtesy of Dr JA Illingworth, Dept of Biochemistry and Molecular Biology, University of Leeds, UK] 38

Figure 2.6 The electrical activation of the heart starts at the sino-atrial or sinus node, continues through the atria to the atrio-ventricular (AV) node. It then proceeds through the interventricular septum and out to the ventricles though the Purkinje fibres. Source: The Physiome Project (<http://physiome.org/>). [Image courtesy of Dr F Prinzen, Dept of Biomedical Engineering, Technische Universiteit Eindhoven, The Netherlands]..... 40

Figure 2.7 The muscle band can be divided up into four segments; ascendant, descendent, left and right depending on the orientation of the muscle fibre. Electrical stimulation has been shown to proceed from right to left to descendent and lastly to the ascendant segment, from right to left in this photograph, giving rise to the torsion seen during contraction. 41

Figure 2.8 Lengthening and shortening of the ventricles is produced by the torsion involved. Two counter rotations occur; a counter clockwise one at the base and a clockwise one at the apex (looking up from the apex towards the base), causing the muscle band to behave as a towel being wrung dry. 43

Figure 2.9 The major coronary arteries supplying blood to the myocardium and their anatomical locations..... 44

Figure 2.10 Schematic illustration of the perfusion of the heart. The main regions supplied by the three main coronary arteries are described. (a and c) Four chamber views of the heart. (b) A two chamber view of the LV and (d) a short axis view showing the LV ring. The bull’s eye plot in the centre can be used to quantify the perfusion to different regions..... 45

Figure 2.11 Collateral circulation arising from a normal artery to supply a neighbouring ischaemic zone. 46

Figure 2.12 Illustration of an atherosclerotic plaque. The transitional thrombus zone is where the lipid-filled plaque has ruptured and caused thrombus to develop in the artery..... 48

Figure 2.13 Starling’s Law: the end-diastolic pressure reflects the initial passive ‘stretch’ of the myocardium in response to systolic pressure. The relationship is not fixed and the shape of the curve depends on the outflow resistance. 55

Figure 3.1 The triangle defines a region of the heart, bounded by the markers a, b and c, assuming that the properties of the centroid (S) apply homogenously to all the material inside the triangle. The eigenvectors of the rotation and strain tensors associated with the centroid can be used to assess the contraction of the region..... 61

Figure 3.2 The effect of slice-following CSPAMM on the quality of myocardial tags. The top three figures are short-axis images obtained using slice-following CSPAMM, whereas the bottom three figures are the same slice obtained using conventional SPAMM. It can be seen that the contrast has been greatly improved using CSPAMM, and that the slice-following has helped overcome tag-fading⁶⁹. [Image courtesy of Prof P Boesiger, Institute of Biomedical Engineering, University and ETH Zurich, Switzerland] 64

Figure 3.3 Short apical-view tagged images at 4.7 Tesla of a canine heart, using the adiabatic DANTE inversion sequence, showing six phases of one cardiac cycle. The deformation of the 4?4mm grid clearly demonstrates translational and rotational motion of the myocardial wall⁷⁰. [Image courtesy of Prof K Ugurbil and Dr N Tsekos, Department of Radiology, University of Minnesota, USA] 65

Figure 3.4 Assessment of myocardial contractility with high sensitivity MR velocity imaging. (a) The anatomical structure of the image plane, (b) the MR velocity measurement, (c) the reconstructed longitudinal contractility mapping showing uniform contraction (sky blue) during systole and relaxation (red) during diastole for a normal subject. (d) The contractility mapping for a patient with ischaemic heart disease, showing delayed contraction during systole and abnormal contraction (broken and broadened red strip) during diastole. 73

Figure 3.5 Diffusion tensor MRI of the myocardial fibre orientation in the beating heart. 3D fibre orientation is represented at each pixel by a cylinder pointing along the first eigenvector of the diffusion tensor, and colour-coded according to the fibre helix angle¹²⁰. [Image courtesy of Prof Van J Wedeen, NMR Centre and Department of Radiology, Massachusetts General Hospital and Harvard Medical School, USA] 76

Figure 4.1 The basic sequence diagram. The sequence consisted of four such acquisitions. The first with +90,+90 tagging pulses, with the tagging gradient played in the x (phase encode) direction. The second acquisition with +90,-90 tagging pulses with the tagging gradient played again in the x (phase encode) direction. The whole process is then repeated with the phase encode direction switched and the tagging gradient played in the y (phase encode) direction. The tagging gradient has to be n the same direction as the phase encode to enable satisfactory resolution of the tags. 82

Figure 4.2 *k-space* representation of horizontal and vertical (a, e) SPAMM and (b, g) CSPAMM tagged images. As can be seen the central peak in *k-space* is significantly reduced in the CSPAMM images thus reducing possible artefacts in the HARP processing. 83

Figure 4.3 (a) The applied resolution constraint $r(y)$, and (b) the corresponding distribution of eigenvalues of the covariance matrix. (c) The selection of near optimal locations of *ky* phase encoding steps using the sequential back selection algorithm. In (c), the deleted encoding steps are represented as black strips. [Image courtesy of Prof. GZ Yang] 86

Figure 4.4 The normalised weighting function conforming to the spatial constraint prescribed by Figure 4.3. The horizontal axis denotes the *k_y* line to be acquired and the vertical axis the value of the weighting function. [Image courtesy of Prof GZ Yang.] 87

Figure 4.6 This diagram shows the timing of the navigators. The navigator echoes, NE, are played out right after the R-wave, followed by the tagging pulse, T. The imaging sequence then follows, typically 12 phases are acquired but this varies according to the subject's heart rate. 88

Figure 4.7 Piloting protocol for obtaining (c) the vertical long axis (two chamber view) and (d) the horizontal long axis (four chamber view) and subsequently (e) the short axis view. (a) A coronal image of the whole body is acquired followed by (b) a transverse cut through the heart, this is used to obtain the (c) vertical long axis and the subsequent views are piloted from there. 90

Figure 4.8 Imaging protocol used when acquiring images in a clinical setting. (a) Four chamber view, (b) 2 chamber view, (c) (d) and (e) basal, mid-ventricular and apical short axis images of the heart. For (a) and (b), only the horizontal tagged images are acquired while for (c-e) both horizontal and vertical tagged images are acquired. 91

Figure 4.9 The effectiveness of the vector restoration algorithm. (a) From left to right, original noisy dataset with 50% noise, restored vector map and original dataset without noise for comparison. (b) The convergence of the energy terms against number of iterations. The minimum energy is reached in around 10 iterations. 95

Figure 4.10 Velocity magnitude maps obtained using (a) and (e) CSPAMM and (c) and (g) SPAMM for frames 2 and 9 respectively, *i.e.*, near the beginning and end of the cardiac cycle. As can be seen from the *k-space* representation of the original images (b,d,f,h), the central peak is enhanced in the SPAMM images causing considerable artefact in the HARP velocity images especially in the later frames of the cardiac cycle. 96

Figure 4.11 Maximum principal strain maps in a mid-ventricular slice in a normal volunteer throughout the cardiac cycle. A positive value of strain indicates thickening which, as can be seen from Figure 4.12, occurs in the radial direction. 97

Figure 4.12 Eigenvector corresponding to the maximum principal strain maps shown in Figure 4.11. 97

Figure 4.12 Eigenvector corresponding to the maximum principal strain maps shown in Figure 4.11. 98

Figure 4.13 Minimum principal strain maps at a mid-ventricular slice in a normal volunteer. The negative values indicate circumferential shortening during systole. 99

Figure 4.14 Eigenvector corresponding to minimum principal strain maps shown in Figure 4.13. It can be seen that this acts primarily in a circumferential direction throughout the cardiac cycle. 99

Figure 4.14 Eigenvector corresponding to minimum principal strain maps shown in Figure 4.13. It can be seen that this acts primarily in a circumferential direction throughout the cardiac cycle.	100
Figure 4.15 Colour map showing v_x in normal subject at the same mid-ventricular slice. The pattern in diastole (i and j) can be seen to oppose that in systole (a and b).	101
Figure 4.16 Colour map showing v_y in normal subject at the same mid-ventricular slice. Some wrap-around in the velocity range can be seen in (h) and (i). This is confirmed by looking at the vector maps in Figure 4.17.	101
Figure 4.16 Colour map showing v_y in normal subject at the same mid-ventricular slice. Some wrap-around in the velocity range can be seen in (h) and (i). This is confirmed by looking at the vector maps in Figure 4.17.	102
Figure 4.17 Velocity vector map combining Figures 4.15 and 4.16. The pattern of torsion described by other researchers can be seen.	103
Figure 4.18 Longitudinal shortening in a normal volunteer. Top row shows the two-chamber, or vertical long axis, view showing the posterior and anterior walls at diastole and systole. Bottom row is the four-chamber, or horizontal long axis, view showing the lateral and septal walls at diastole and systole.....	104
Figure 4.19 SPAMM (a-c) and CSPAMM (d-f) subtraction images of the heart in diastole and systole.....	105
Figure 4.20 Percentage strain in the anterior, lateral, posterior and septal regions in a mid-ventricular short axis slice in five normal subjects at maximum contraction during free-breathing at (grey) end-expiration and (black) end-inspiration.	106
Figure 4.21 Maximum principal strain maps at a mid-ventricular short axis slice in a normal volunteer during free-breathing at (a) end-inspiration, (b) end-expiration and (c) during breath-hold.....	107
Figure 4.22 Anatomy of a hypertrophied heart using CMR SSFP imaging. Two chamber, four chamber and mid-ventricular short axis views at peak systole show the myocardium to be abnormally thickened.	108
Figure 4.23 Maximum and minimum principal strain in normals (black) and HCM patients (grey) in the basal slice. It can be seen that the difference was considerable, even though some of the patients did not display the phenotype using standard diagnosis techniques.	112

Figure 4.24 Maximum and minimum principal strain in normals (black) and HCM patients (grey) in the mid-ventricular slice.	113
Figure 4.25 Maximum and minimum principal strain in normals (black) and HCM patients (grey) in the apical slice.	114
Figure 4.26 (a,b,e,f) Maximum (left) and (c,d,g,h) minimum (right) principal strain and their corresponding directions in the basal slice in a normal (top row) and HCM patient (bottom row).	115
Figure 4.27 (a,b,e,f) Maximum (left) and (c,d,g,h) minimum (right) principal strain and their corresponding directions in the mid-ventricular slice in a normal (top row) and HCM patient (bottom row).	115
Figure 4.28 (a,b,e,f) Maximum (left) and (c,d,g,h) minimum (right) principal strain and their corresponding directions in the apical slice in a normal (top row) and HCM patient (bottom row). It can be seen that the maximum principal strain acts in a radial direction while the minimum acts in the circumferential direction.	116
Figure 4.29 Strain in the longitudinal direction in (a) lateral, (b) septal, (c) anterior and (d) posterior regions. The trend is for the strain to reduce as the ventricle shortens and then increase as it lengthens out again. The lateral and septal walls show that the standard deviation across the subjects increases in the later frames of the cardiac cycle. This could be due to the decreased SNR caused by tag fading.	117
Figure 5.2 This short axis image shows the blood flow artefact in a magnitude image. As the blood signal has a phase shift proportional to velocity and variable flow during each phase encode, it is encoded in a different part of <i>k-space</i> than where it should be, producing a streaking artefact in the phase encode direction, destroying signal in parts of the myocardium.	124
Figure 5.1 Bipolar gradient pulse. The timings and gradient amplitude can be used to calculate the velocity sensitivity of the sequence.	125
Figure 5.3 (a) The blue slices denote the saturation pulses and the yellow slice is the slice being imaged. This sort of scheme nulls the blood signal in (b) the short axis image. Giving an image with high signal intensity in the myocardium and “black blood”.....	127
Figure 5.4 The frequency domain shows a truncated sinc pulse which translates into a rectangular excitation profile once played out on the scanner. As can be seen the slice profile contains some ringing as it is physically impossible to use a non-truncated sinc RF pulse.	127

Figure 5.5 RF pulse design used to produce the black blood saturation. The time domain is the RF pulse transmitted producing the frequency domain profile in the image, *i.e.*, saturation bands next to the slice being images. The pulse was only 5.1ms long allowing repetition at every other phase. 128

Figure 5.6 This diagram illustrates the principle of view-sharing. Echoes are acquired for seven time frames, however by sharing the data between adjacent frames extra frames can be reconstructed resulting in 13 frames covering the cardiac cycle. 129

Figure 5.7 16 phase encode lines are acquired for the first frame, and 10 for each subsequent frame. 6 lines are acquired at the outer edges of k-space and shared with the next frame. This illustration shows how the image would be built up for the first four frames in the cardiac cycle. The dotted lines are the k-space lines shared from the last frame. 129

Figure 5.8 The sequence diagram showing the black blood pulse followed by slice selection and velocity encoding in the slice (through-plane) direction. The phase encode and readout gradients are then followed by spoilers to destroy any signal left in the transverse plane. The black blood pulse is repeated before every other frame, *i.e.*, 1, 3, 5, 7 and so on, at the beginning of each segment. 130

Figure 5.9 Timing diagram for the respiratory gated velocity mapping sequence. The navigator echo is applied at end-diastole and is 50ms long including the time needed to feedback to the pulse sequence. 131

Figure 5.10 Mid-ventricular short axis image. (a) True FISP image, segmented FLASH velocity mapping sequence (b) without and (c) with blood saturation. 134

Figure 5.11 Vector maps showing in-plane (*x,y*) velocities at (a) end-diastole and (c) start diastole. (b) and (d) show the corresponding through-plane (*z*) velocity. The colourbar represents velocities from +10cm/s to -10cm/s. 135

Figure 5.12 Segmentation of the mid-ventricular slice according to the standardised model as recommended by the American Heart Association Writing Group on Myocardial Segmentation and Registration for Cardiac Imaging¹⁴². 136

Figure 5.13 Mean velocity in the read (*x*) direction in the (a) anterior, (b) anterolateral, (c) inferolateral, (d) inferior, (e) inferoseptal and (f) anterosseptal regions of the same slice for one subject. The dashed line shows the scan without blood saturation and the solid line with the blood saturation. 137

Figure 5.14 Absolute difference in v_x between velocities in measured in different regions with and without the blood saturation pulse for five different subjects. 137

Figure 5.15 Mean velocity in phase encode (v_y) direction in the (a) anterior, (b) anterolateral, (c) inferolateral, (d) inferior, (e) inferoseptal and (f) anterosseptal regions for the same subject. Again the dashed line is the scan without blood saturation and the solid line is with blood saturation.....	138
Figure 5.18 Magnitude, phase and velocity images for the mid-ventricular slice corresponding to Figures 5.14-5.17. These images correspond to the scan with black blood saturation. (a, d, g) End-diastole which is the first frame, (b, e, h) systole which is the fifth frame, and (c, f, i) early diastole which is the last frame.	139
Figure 5.19 Magnitude, phase and velocity images for the mid-ventricular slice corresponding to Figures 5.14-5.17. These images correspond to the scan without black blood saturation. (a, d, g) End-diastole which is the first frame, (b, e, h) systole which is the fifth frame, and (c, f, i) early diastole which is the last frame. The blood flow artefact can be clearly seen on the diastolic images.	140
Figure 5.20 Absolute error in v_x averaged over all five subjects for all time frames in the different regions of the heart.	141
Figure 5.22 Circum-ferential strain rate distributions in a mid-ventricular slice in a normal volunteer. Venc was set at 20cm/s.	144
Figure 5.23 Circum-ferential strain rate distributions in the same slice in the same volunteer calculated at a venc of 13cm/s.....	144
Figure 5.24 Radial strain rate distribution, after further processing, in a normal subject in a mid-ventricular slice using venc 20cm/s. Radial thickening can be seen in systolic frames.	145
Figure 5.25 Radial strain rate distribution in the same normal subject in the same mid-ventricular slice using venc 13cm/s. The radial strain pattern can now be clearly distinguished in systole when radial thickening, <i>i.e.</i> , contraction, is occurring.....	146
Figure 5.26 Circumferential strain rate distribution in the same normal subject at the same location using venc 20cm/s. The diastolic circumferential lengthening can be clearly seen in frame 7.	147
Figure 5.27 Circumferential strain rate distribution in the same subject and same slice using venc 13cm/s. Now the circumferential lengthening during diastole can be seen from frame 5 through to frame 8 and the regional pattern can also be determined.	148
Figure 5.28 Mean radial strain rate for five normal subjects in the (a) anterior, (b) anterolateral, (c) inferolateral, (d) inferior, (e) inferoseptal and (f) anterosseptal regions.	

The solid line shows the strain rate measured using venc 20cm/s and the dashed line shows that at venc 13cm/s.....	149
Figure 5.29 Mean circumferential strain rate for five normal subjects in the (a) anterior, (b) anterolateral, (c) inferolateral, (d) inferior, (e) inferoseptal and (f) anteroseptal regions. The solid line shows the strain rate measured using venc 20cm/s and the dashed line shows venc 13cm/s.....	150
Figure 6.1 Flowchart showing method adopted to calculate the strain rate magnitude.	157
Figure 6.2 Flowchart showing the normalisation process used to find the mean strain rate for all normal subjects.	161
Figure 6.3 Plot of divergence against number iterations for the first-order technique for different step sizes with the starting λ set at 100.	163
Figure 6.5 Plot of total cost against number of iterations for different values of λ	164
Figure 6.6 Plot of divergence for different values of λ	165
Figure 6.7 Comparison of restored velocity and derived strain rate for different techniques. First column shows the result from simple smoothing (a, e, i), second column using the vector restoration described in Section 4.2.6 (b, f, j), third column from the divergence free algorithm (c, g, k) and last column shows the original noise free dataset for comparison (d, h, l).	166
Figure 6.8 The strain rate magnitudes and divergences obtained for the simulation dataset using different values of Lamda. (a) $\lambda=1$, (b) $\lambda=10$, (c) $\lambda=100$ and (d) original noise free dataset for comparison.	167
Figure 6.9 Strain rate distribution in a typical normal subject. Ten time frames showing the (c,d) systolic and (g) diastolic behaviour of the myocardium. The active recoil of the myocardium in early diastole is especially prominent.....	170
Figure 6.10 Mean normalised strain rate magnitude for 11 normal subjects in the (a) anterior, (b) anterolateral, (c) inferolateral, (d) inferior, (e) inferoseptal and (f) anteroseptal regions. The strain rate was normalised over time and space, <i>i.e.</i> , over the myocardial ring.....	171
Figure 6.11 Standardised strain rate for 11 normal subjects, calculated using the scheme illustrated in Figure 6.2. The diastolic frames can be clearly spotted as (i-k).....	172
Figure 6.12 Strain rate maps for a patient with DCM. The overall strain rate is similar to that found in normal subjects. The corresponding normal strain rate is shown in the bottom right hand corner. The colour map is the same as Figure 6.11.	173

Figure 6.13 Strain rate distributions for a patient with Eisenmenger complex. It can be seen that there is septal deviation due to the pressure balance between the right and left sides, (a), (b), (m) and (n). There is also inferolateral motion to compensate for the septal deviation. The bottom right hand corner of each image shows the corresponding strain rate for the normal mean dataset. The colour map used is the same as that in Figure 6.11. 174

Figure 6.14 Strain rate distribution for a patient with ischaemic heart disease. The normal mean strain rate corresponding to the same frame is shown in the bottom right hand corner of each image. The colour map used is the same as Figure 6.11. 175

Figure 6.15 Strain rate maps for a patient having undergone a pericardiectomy. The overall strain rate is similar to that found in normal subjects. The normal mean strain rate corresponding to the same frame is shown in the bottom right hand corner of each image. The colour map is the same as Figure 6.11..... 176

Figure 7.1 A schematic illustration of different configurations that can be used for virtual tagging, where (a-b) represent uniform polar grids with different densities, (c) Cartesian grid, and (d) polar grid with non-uniform grid density..... 180

Figure 7.2 The design of the silicon gel phantom used for *in vitro* validation of the current study. (a) The overall system configuration, (b) the silicon gel assembly which allows both twisting and compression, and (c) the driving motor located away from the magnet. 187

Figure 7.3 A numerically simulated data set based on Equations (7.9)–(7.11) for simulating the motion of the heart. Top row: virtual tag results at increasing time points of the motion cycle with a noise free data set. Mid and bottom rows: results for a data set with an SNR of 16.32 dB calculated with and without mass conservation, respectively. The colour coding represents the radial strain ϵ_r , within the range of -0.6 and 0.6 189

Figure 7.4 The same numerical results corresponding to Figure 7.3, but with colour coding representing the in-plane shear strain $\gamma_{r\theta}$ in the range of -0.6 and 0.6 190

Figure 7.5 The influence of the values of the weighting factor λ on the accuracy of the virtual tagging result. All calculations were performed by using the numerically simulated data set used in Figures (7.3)–(7.4) with an SNR of 16.32 dB. 192

Figure 7.6 A comparison of the performance of different optimisation algorithms used and the effect of different weighting factors used for introducing the mass conservation constraint. Three simulation data sets, ranging from noise free, to an SNR of 28.07 dB and 16.32 dB, were used. 192

Figure 7.7 The *in vitro* results demonstrating the accuracy of the virtual tagging in tracking material over time, (a-c) velocity components along the *x*, *y*, and *z* axes where mid-grey value represents zero velocity, (d) the derived virtual tagging grid at three different times of the motion cycle (increasing down each column) superimposed on a conventional tagging image of the same phantom with a SPAMM sequence. 193

Figure 7.8 The manually measured absolute tracking error at two mid-slices of the phantom throughout the motion cycle, where the peak gel velocity is provided as a reference. It is evident that there is a slight increase in the tracking error during peak acceleration, which can be partially avoided by increasing the temporal resolution of the velocity sequence..... 194

Figure 7.9 A 3D representation of the virtual tagging result for the phantom at six different time instances of the motion cycle, where the colour coding represents the longitudinal strain in the range of $-0.3 \sim 0.3$. The time increases across each row, with the phantom deforming and then returning to its original position. The top and bottom rows show, respectively, the results calculated with and without the mass conservation constraint. 195

Figure A.1. A sequence diagram for a simple SPAMM sequence. Two $+90^\circ$, $+90^\circ$ RF pulses are separated by a gradient in the *y*-direction, which produces horizontal tags in the image. The tagging is followed by a standard FLASH imaging sequence.205

Figure A.2. MR tagged image of the heart, short axis view. Horizontal and vertical tags can be applied separately or a grid can be produced by applying both directions of tagging in one acquisition.206

Figure A2.1 Effect of gradient field on the phase of a spin. The moving spin will acquire a phase shift directly proportional to its velocity during the second half of the bipolar gradient.210

Figure A2.2 Schematic sequence diagram of through-plane velocity encoding sequence. The bipolar gradient pulse is played in the slice-select/through-plane direction. It can be played on the different axes to enable velocity mapping in different directions.....211

Figure A2.3 The concomitant gradient terms are due to the non-zero *x* and *y* components of the gradient field.212

Figure A3.1. Short axis image of the heart with horizontal tagging and (b) its corresponding Fourier transform. As this is the second frame in the cardiac cycle, the spectral peaks are quite bright. Later on in the cardiac cycle as the tags fade the spectral peaks become dimmer and the central peak dominates the Fourier image.214

Figure A3.2. CPAMM magnitude image of the same short axis slice as in Figure A3.1 at the same point in the cardiac cycle. The corresponding Fourier transform shows how the DC peak has been suppressed and the spectral peaks are considerably enhanced.216

Figure A3.3. Change in phase as the tissue deforms. A particular mass point, $P(x,y)$, will carry its phase with it as it moves, changing the phase slope.218

Figure A3.4. The tag plane intersects the image plane along the dotted line. As the tissue deforms, point O moves to point T. However, only the point where the tag plane intersects the image plane, A, is recorded.221

Figure A3.5. Data flow diagram for HARP processing. After acquisition, the magnitude and phase images are converted to real and imaginary and Fourier transformed. They are then subtracted to obtain the CSPAMM images in frequency space. These are then filtered and inverse Fourier transformed to obtain the HARP images which can then be used to calculate strain and/or velocity.223

Figure A3.6. Velocity displayed in the HARP software. Pictures 1 and 2 are the velocities in the x and y directions respectively. Picture 3 is the magnitude of the velocity vector and Picture 4 is the direction. The software allows zooming in to the region of interest.224

Figure A3.7. Strain displayed in the HARP software. Pictures 1 and 2 are the maximum and minimum principal strains respectively. Pictures 3 and 4 display their corresponding eigenvectors. The left ventricle has been selected after drawing contours around the myocardium and creating a mask which the software allows you to save for use later.225

1 Introduction

Heart failure due to coronary artery disease is one of the biggest killers in the Western world with 63,000 new cases every year in the UK and 38% of those dying within one year of diagnosis. An understanding of the underlying mechanics governing myocardial contraction is a prerequisite for interpreting and predicting changes induced by heart disease. To this end, different imaging techniques have been used for quantitative assessment of intrinsic myocardial motion quantitatively. Most of these techniques have not, however, been fully extended to clinical environment albeit being valuable for research purposes. Thus far, the main functional imaging methods for myocardial contractility are ultrasound and magnetic resonance (MR) imaging. Recently, tissue Doppler ultrasound has broken new ground as it allows the direct measurement of myocardial velocities *in vivo* with reasonably high temporal resolution. The main disadvantages of this technique, however, are the limited acoustic windows into the body, which only allow velocity in certain directions to be measured, and low spatial resolution, which limits accuracy of strain rate information. The clear advantages of ultrasound are that it is relatively inexpensive, portable and does not use ionising radiation, making it ideal for routine clinical use.

As an alternative approach, Cardiovascular Magnetic Resonance (CMR) allows full flexibility in imaging oblique planes, and hence permits access to the intrinsic cardiac axes. It has the added advantages of measurements being anatomically correct and allowing a range of functional indices to be measured including ejection fraction, wall thickness, perfusion and blood flow. CMR is an established technique with a proven track record in diagnosing a

variety of disorders, ranging from valvular disease and congenital heart disease to the more common ischaemic heart disease.

For measuring myocardial contractility, CMR offers a number of possibilities by exploiting the intrinsic properties of CMR imaging. The technique currently being applied routinely for measuring myocardial motion in clinical environment is CMR tagging. Tagging involves saturating bands of tissue as fiducial markers that follow the motion of the heart as it contracts and expands. This technique, however, does not permit high resolution imaging of the motion. This is limited by the paucity of tags across the myocardium and the tag fading that occurs during the cardiac cycle due to saturation recovery. It also requires time-consuming post-processing steps that often require extensive user intervention to ensure accurate tag tracking. For qualitative assessment, however, the technique allows direct visual assessment of myocardial deformation and has been proven to be effective clinically.

The recent development of HARP imaging, which exploits the phase properties of MR tagging, bodes well for the transfer of strain into a clinically useful functional index of contractility. Tagging entails the modulation of the MR signal in the spatial, *i.e.*, image, domain, causing spectral peaks in the frequency domain. These spectral peaks can be isolated to obtain the phase properties of the tags. The phase of a material point is carried with it as it deforms during the cardiac cycle, and thus can be used to track the tags automatically. New HARP imaging techniques are approaching almost real-time visualisation of contractility. It remains to be seen whether these techniques will be viable in clinical settings and whether they provide accurate and robust assessment of changes in contractility due to disease.

CMR phase contrast velocity mapping, an alternative to tagging, employs the phase shifts introduced by the gradient magnetic field to directly encode the velocity of moving tissue. It permits improved motion sensitivity and potentially requires less extensive post-processing. Up until recently, however, CMR velocity mapping sequences cannot be readily applied to myocardial contractility assessment as a comprehensive scan of the whole left ventricle (LV) with velocity encoding in all three directions would require too long an acquisition time. This typically involves a scanning time of up to an hour, which is intolerable for very ill patients. Despite the advantages of myocardial velocity being recognised for many years, its practical application has also been hindered by the low signal-to-noise ratio (SNR) in in-plane velocity components due to their relatively low velocity magnitude and artefacts arising from the ventricular flow patterns. An improved imaging strategy combined with effective velocity vector rectification needs to be developed before the full strength of myocardial velocity mapping being realised.

The purpose of this thesis is to develop a clinically viable platform for functional correlation with other measures such as myocardial perfusion and diffusion, and to serve as an aid for further understanding of the links between intrinsic cardiac mechanics, localised genesis and progression of cardiovascular disease. This involved the development of robust and fast MR imaging sequences and protocols, and a 3D analysis and visualisation technique that would allow assessment of intrinsic myocardial mechanics. The different techniques available at present were explored and further developed. Validation and comparison of the techniques was conducted on numerically simulated, *in vitro* and *in vivo* data. A novel complementary analysis framework, named Virtual Tagging, was also developed which used velocity data in all directions combined with a finite element mesh by incorporating geometrical and physical constraints. The Virtual Tagging framework allows velocity measurements, either derived from HARP or directly measured from myocardial velocity imaging, to be effectively visualised and quantified in terms of overall strain distribution.

This thesis presents a detailed write-up of the imaging techniques used, the virtual tagging framework developed and the experiments carried out to validate the work. Chapters 2 and 3 provide a comprehensive overview of the background to the described work, illustrating the primary motivation behind the measurement of myocardial contractility. Chapter 2 gives a review of the anatomy and physiology of the normal and diseased heart. It presents a summary of the anatomical models proposed to describe myocardial fibre architecture and their relationship to the dynamics of the beating heart. Disease processes and the significance of non-invasive imaging in early and accurate diagnosis are highlighted. A literature review of the existing CMR techniques used for evaluating myocardial motion is presented in Chapter 3. This includes the CMR sequences developed over the years, the various post-processing techniques used, a summary of the clinical research conducted, and the current state-of-the-art.

The two main CMR techniques used currently are tagging and velocity mapping. The CMR tagging sequences developed during the course of this work are detailed in Chapter 4. The imaging sequence and the HARP processing are described herein, and the application of this technique to measure changes in contractility during free-breathing and cardiomyopathy are explored to highlight the importance in controlling respiration for consistent myocardial strain measurement. It is assumed that the reader is familiar with the basic concepts of MR imaging, therefore no details about the basic physics of MR imaging is elaborated. However, details on CMR tagging, phase contrast velocity mapping and HARP imaging are provided in accompanying appendices.

Chapter 5 describes the CMR phase contrast velocity mapping sequence used. The advantages of the sequence over other imaging methods are outlined. The effectiveness of the sequence at reducing blood flow artefacts was investigated. The velocity data acquired with this sequence was found to be useful in describing the overall trend of the velocity distribution, however accurate strain rate calculation was limited as the velocity-to-noise ratio (VNR) is too low. The consistency of the 3D velocity distribution required further improvement. An iterative optimisation scheme incorporating the incompressibility constraint was developed to improve the consistency of the in plane velocity data and is described in Chapter 6. This allowed accurate assessment of in-plane and through-plane strain rate components. Comparison between normal subjects and ischaemic patients demonstrated the practical value of the technique.

CMR velocity mapping does not allow direct visualisation of motion as each velocity component is acquired separately and displayed as a grey scale image. Thus, visualisation requires the combination of different velocity directions to allow visualisation of 3D myocardial motion. The principles behind a novel Virtual Tagging framework used to derive and display deformation based on the measured velocity field are explained in Chapter 7. Virtual Tagging allowed direct visualisation of motion by using a virtual grid superimposed on the velocity data, which deformed according to the velocities contained within each element subject to geometrical and physical constraints. The experiments carried out on simulated and *in vitro* data, and the results obtained are included in this chapter. Chapter 8 concludes the thesis with a discussion about the existing work and suggestions for future directions.

Most parts of this thesis are published in peer-reviewed academic journals and conference proceedings, which include the following:

- ? J. X. Gao, S. Masood, B. Jung, F. Deligianni, G. Z. Yang. Reconstruction of 3D deformation from 2D MR velocity data using incompressibility constraints. Proc. of 4th Annual IEEE Conf on Information/Technology in Biomedicine, UK, April 2003, pp.134-137.
- ? S. Masood, J. Gao, G. Z. Yang. Virtual tagging: numerical considerations and phantom validation. IEEE Trans Med Imaging 2002 Sep 21(9), pp. 1123-31.

- ? S. Masood, P. D. Gatehouse, D. N. Firmin, G. Z. Yang, The Effect of Respiratory Motion on the Accuracy of HARP Imaging. ISMRM 10th Annual Scientific Meeting, Hawaii USA, May 2002.
- ? S. Masood, G. N. Estcourt, P. D. Gatehouse, D. N. Firmin, G. Z. Yang. Virtual tagging for cardiac deformation. Proc. of IEEE International Workshop on Medical Imaging and Augmented Reality, Hong Kong, 2001, pp 61-66.
- ? S. Masood, G. N. Estcourt, D. N. Firmin, P. Gatehouse, S. Collins, G. Z. Yang. Virtual Tagging: a novel method for evaluating myocardial function. ISMRM 9th Annual Scientific Meeting, Glasgow UK, May 2002, pp. 603.
- ? S. Masood, G. Z. Yang. Macroscopic Structure and Physiology of the Normal and Diseased Heart. Technical Report Series, 2001, Dept. of Computing, Imperial College, London.
- ? S. Masood, G. Z. Yang, D. J. Pennell, D. N. Firmin. Investigating intrinsic myocardial mechanics: the role of MR tagging, velocity phase mapping and diffusion imaging. Journal of Magnetic Resonance Imaging 2000 Dec 12(6), pp. 873-83.

2 Macroscopic Structure and Physiology of the Normal and Diseased Heart

2.1 Introduction

The structure of the heart and its relation to myocardial function is a challenging problem that has troubled anatomists and physiologists for centuries¹. The heart is a “complex three-dimensional fibre-wound structure with mechanical properties that are non-linear, anisotropic, time varying and spatially inhomogeneous”². The heart consists of four chambers, four valves and various vessels bringing blood to and carrying it away from the heart by veins and arteries as illustrated in Figure 2.1. The *superior* and *inferior vena cavae* are the veins that bring blood from the rest of the body to the *right atrium*. The blood then enters through the *tricuspid valve* to the *right ventricle* (RV). From there it is pumped through the *pulmonary valve* entering the *pulmonary artery* and then through to the lungs to be re-oxygenated. Once re-oxygenated, the blood is carried back to heart through the *pulmonary veins* to be circulated to the rest of the body. It enters the *left atrium* and once that is filled, the blood is pushed through the *mitral valve* into the *left ventricle* (LV). The *left ventricle* does the majority of the work by then pumping the blood through the *aortic valve* to the *aorta* and hence out to the rest of the body³.

Although the microscopic structure of the heart can be explored relatively easily, the macroscopic muscle structure has remained an unresolved problem, dependent on how

dissection is performed^{2,4}. Despite this, studies have verified the relation of dissection techniques to conclusions on architecture using non-invasive imaging techniques^{5,6}. From previous studies in this field, two different families of macroscopic myocardial models can be distinguished. In the first, the arrangement of myocardial fibres is given by analogy with the description of the arrangement of the muscular skeletal fibres. Thus, the fibres are considered to gather in distinct bundles and muscles with each fibre retaining a close individual relationship with the cardiac fibrous skeleton. These models distinguished from one to four systems of myocardial bundles⁷⁻¹¹. In the extreme case, Robb and Robb proposed an arrangement of four myocardial bundles anchoring on the fibrous trigones and the aortic and pulmonary roots, while Torrent-Guasp, in contrast, considered only one bundle, which is described in further detail in this chapter. The other models consider the fibres to be in layers in the ventricle, with each layer having a different orientation, *e.g.* in Sanchez-Qunitana¹² *et al*'s model, the ventricle is considered to consist of three layers: the subepicardial, the mid and the subendocardial, all of which change in orientation throughout the ventricle.

The limitations of these models are that they are primarily based on dissection; some researchers cast the heart in acrylic resins and then consider histological sections and superficial fibre angles¹² while others prepare the heart by boiling and then unrolling the muscle along its main orientation¹³. The major flaw in the concept of layers arises from the fact that they describe fibres as running exclusively inside their layer whereas it has been shown that fibres can run between layers^{14,15}.

The second family of models views the myocardium as a specialisation of the vascular musculature, with myocardial fibres branching from one to another, rather than taking their origin or insertion from the fibrous skeleton. This approach was initiated by Krehl¹⁶ at the end of the 19th century. It has been notably reinforced by significant advances that, by means of photonic and electronic microscopy, showed the myocardial fibres to be a network of preferentially oriented and branched myocardial cells forming end-to-end cellular junctions¹⁷⁻¹⁹. There is considerable work ongoing in this field where the fibre orientation is being measured using non-dissection techniques such as polarised light microscopy^{20,21} and MR diffusion imaging techniques. This field of research is relatively new and results are limited at present, however, it shows considerable promise in elucidating myocardial architecture in normal and diseased hearts.

Studies into the structure of the heart are at different levels. One of these is at the cellular level, or histological studies. These usually explore the myocyte structure, alignment and ionic pathways or overall fibre architecture². The next level, the muscle level, is what we are

particularly interested in. This level of study can give us clues to how the heart functions and hence an indication of where and how things go wrong in disease.

This chapter briefly describes the general micro and macro structure of the heart, the changes in muscle structure in disease, and the measures currently used to define function. The first family of macroscopic models is discussed, particularly the model proposed by Torrent-Guasp. The relationship between myofibre architecture and ventricular dynamics are elucidated and the changes in disease are discussed briefly.

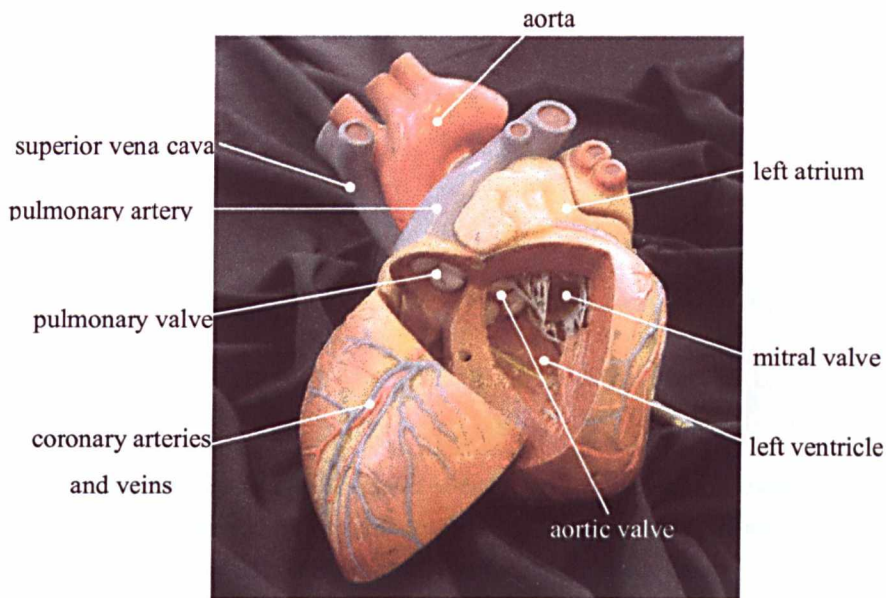


Figure 2.1 The anatomy of the heart. The arteries carrying blood away from the heart, from the LV, are marked in red while the veins carrying blood to the heart, to the right atrium, are in blue.

2.2 Histology and Cellular Structure

To understand how the myocardium functions, we first need to understand the muscle structure at a basic level. Cardiac muscle tissue is unlike any other muscle in the body. Cardiac fibres consist of elongated cells with central nuclei and branching attachments²². About 75% of the total volume of the myocardium is composed of cardiac myocytes, representing about one third of all cells in the myocardium²³. They are smaller than skeletal muscle fibres measuring around 110 μ m long and 15 μ m wide.

Figure 2.2 is a histological photograph of a slide of cardiac muscle. It can be seen that cardiac myocytes are connected to each other end to end by intercalated discs which are usually at

right angles to the long axis of the cardiac myofibres (a myofibre is defined as a group of myocytes connected by collagen.) These are specialised cell-cell junctions that form regions of low electrical resistance, hence providing not only mechanical but also electrical coupling between cells. This leads to a branching network of interconnected muscle fibres. Thus, the entire tissue can theoretically be treated as a single muscle cell, called a functional syncytium.

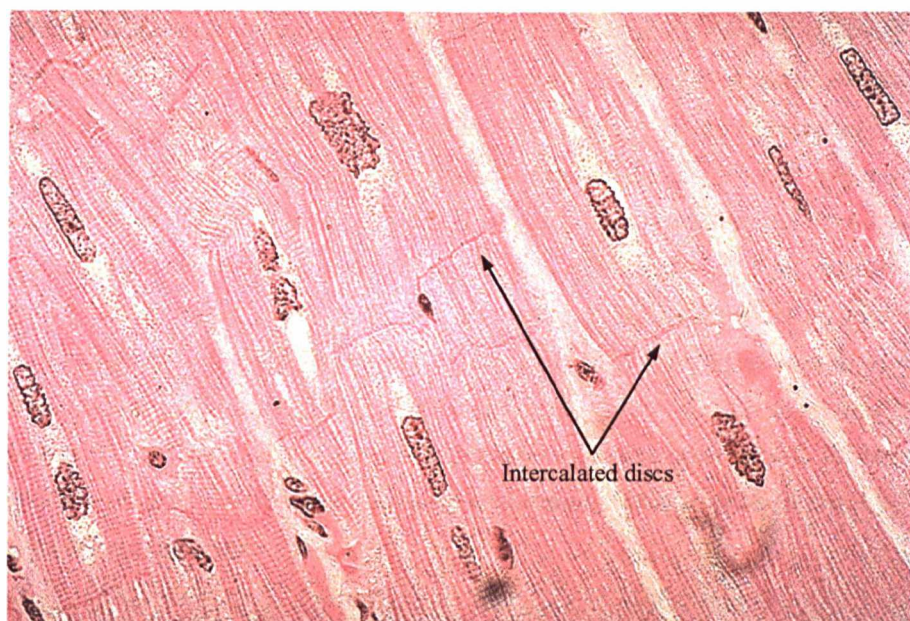


Figure 2.2 Cardiac muscle tissue is striated with the myocytes containing usually just one central nucleus and being connected to each other by intercalated discs. [Image courtesy of Dr R Wagner, Biological Sciences, University of Delaware]

Cardiac myocytes are also unique in their contraction properties. They contract without neuronal stimulation, instead, specialised cardiac pacemaker cells establish a regular rate of contraction. The action potentials in cardiac muscle fibres are also very different to those established in axons and skeletal muscle. In cardiac muscle, the action potential lasts much longer, 200 – 350 ms in the ventricles. This means the refractory period, *i.e.*, the period when the cell will not respond to a second stimulus, is quite long, thus preventing any further contraction from taking place and keeping the whole muscle in synchrony.

Cardiac muscle cells are bounded by the cell membrane, the sarcolemma, and filled with rodlike bundle of myofibrils, which are the contractile elements. The sarcolemma extends to form an extensive network, the extensions are known as T-tubules. The cell also contains mitochondria that are interspersed between the myofibrils and usually located immediately beneath the sarcolemma. The main function of the mitochondria is to produce adenosine triphosphate (ATP). Proper function of the myocardium requires highly controlled regulation

of the calcium concentration within the cardiac myocytes. Contraction is initiated by calcium ions, discharged by the sarcoplasmic reticulum in response to electrical stimulation. The major molecules involved in contraction are the proteins actin and myosin. The thin actin filament and the thick myosin filament contract by sliding over each other, not by actual shortening. This is commonly called “cross-bridge cycling”. The actin filament is actually composed of actin and tropomyosin, which in turn consists of the three proteins troponin I (TnI), troponin C (TnC) and troponin. Calcium binding induces a conformational change in TnC, causing it to elongate. This causes the TnI to close up to TnC and the normal inhibition of the TnI on the actin-tropomyosin is released, allowing the repositioning of tropomyosin in relation to actin and hence contraction²⁴. This relationship between electrical stimulation and intracellular calcium release is called excitation-contraction coupling²⁵. The “calcium cycle” is integral to the regulation of contractility of the myocardium. Perturbations of either release (systolic) phase of the cycle or reuptake (diastolic) phase of the cycle can contribute to heart failure and sudden cardiac death²⁵. During heart failure, the force of contraction is reduced and there is an abnormal delayed pattern of relaxation. Unlike other muscle tissue, cardiac myocytes are incapable of dividing and hence cardiac muscle tissue once damaged by injury or disease cannot regenerate.

2.3 Macroscopic Muscle Structure

A picture of the muscle structure on the macroscopic scale can be obtained by dissecting the heart. Researchers have studied the structures of different mammalian hearts extensively²⁶. Results obtained from these studies are dependent on the dissection method employed by the researchers. These include histological dissection on hearts preserved in resin to obtain their models or peeling methods to peel away the layered architecture of the heart²⁷. Ideally results from different methods, including imaging techniques, should be combined to obtain an overall picture of myocardial fibre architecture. The following section discusses the results obtained from one such dissection method. It should be noted that this does not provide a complete description of the architecture and results from other research groups should be included to obtain a complete picture of the complex myocardial fibre architecture.

One established dissection method used consists of firstly boiling the hearts in water to soften the connective tissue and then performing a blunt dissection of them using fingers with the help of non-toothed forceps, scalpel and scissors, after first removing the atria, aorta and pulmonary artery. This blunt dissection method is used as it was found to be the best way of

identifying the direction of the laminar pathways followed by the muscle bands, *i.e.*, the cleavage planes. By using this dissection method, the natural cleavage planes of the muscle can be examined, and a clearer picture of the macroscopic muscle fibre architecture obtained^{4,10,26,28,29}. Firstly, we need to clarify the nomenclature of the different regions of the heart. The base is at the top of the heart, *i.e.*, where the ventricles connect to the atria, and the apex is the bottom tip of the heart. To make the explanation of the anatomy easier, the heart can then be divided up into four regions, the LV apical and basal halves, and the RV apical and basal halves. The apical halves of the ventricles describe the lower half of the heart, whereas the basal halves describe the upper half, *i.e.*, from base to midway.

2.3.1 Left Ventricle Apical Half

To examine the apical half of the LV, a transverse cut made between the middle and apical third of the heart was found to be useful. Pulling on the fibres revealed a cleavage plane showing that the muscle layer always took a helical path from the periphery to the centre. Torrent-Guasp *et al* found that the sub-epicardial fibres undergo a twist turning into sub-endocardial fibres around a central tunnel, bounded by the endocardium on the inside and the epicardium on the outside. They concluded that, looking from the apex up towards the base, all fibres pass clockwise from the sub-epicardium to the sub-endocardium.

2.3.2 Left Ventricle Basal Half

The free wall of the basal half of the LV is similar to the apex in that the muscle layers take a helical path from the periphery to the centre. The fibres of the basal half pass beneath, but do not insert into, the mitral ring. The study showed that the fibres of the free wall of the base, passed anti-clockwise, again looking from the apex up towards the base, from the sub-epicardium to the sub-endocardium.

The basal and apical halves of the LV may seem similar but there are four differences worth noting:

- The apical orifice is virtual while the basal orifice is real.
- The edges of the apex had structural uniformity, while the base had two segments, *i.e.*, the free wall and the interventricular septum.
- The basal superficial fibres are in contact with a fibrous ring, *i.e.*, the mitral annulus, while the apical superficial fibres are at a distance from the mitral fibrous ring.

The most fundamental and probably anatomically the most important difference is that the fibres at the base pass in an opposite direction, from periphery to centre, than those at the apex.

2.3.3 Right Ventricle Apical Half

The free wall of the RV displays two groups of fibres. The sub-endocardial fibres run from the posterior interventricular sulcus to the pulmonary artery in an ascending course to the basal region. The sub-epicardial fibres run from the posterior interventricular sulcus to apical regions in a descending course. There is also a third group of fibres whose path runs from the direction of the first to the direction of the second group. This explains why dissection reveals a series of circularly overlapping muscle layers in the apical border of the free wall.

In conclusion, the apical half of the free wall of the RV consists of myocardial fibres which pass from a sub-epicardial to a sub-endocardial position in a clockwise helical course (looking from apex to base).

2.3.4 Right Ventricle Basal Half

The myocardium around the tricuspid orifice can be divided into three segments: the free wall, the supra-ventricular bridge and the interventricular septum. It was found that the free wall segment at the base corresponded well with the free wall at the apex but, as in the LV, at the apex the fibres pass in an opposite direction to those at the base.

2.3.5 One Muscle Band

This method of dissection shows the heart to be a helically wound structure. It also shows that there is a clear difference between the structures at the base and apex, since at the base the muscle fibres, in their helical course from the epicardium to the endocardium, run in an opposite direction to those at the apex. A rubber mould of a real heart is shown in Figure 2.3. Through unwinding, it reveals the helical winding of the muscle band to create the different chambers. Two loops can now be defined, the basal and apical loops. The basal loop can be further divided into the right and left segments and the apical loop into descendent and ascendant segments, as illustrated in Figure 2.5.

This model also helps to explain the differences in thickness of ventricular walls. It is known that the RV wall is much thinner than the LV wall, and the double loop model illustrates that this is due to the fact that the LV wall is made up of two windings of the muscle band and hence thicker. It can be concluded that “the ventricular myocardium consists of a singular muscle band twisted on itself as a rope, that, extending from the origin of the pulmonary artery to the root of the aorta, define, while describing two turns in a helical fashion, two cavities, the right and left ventricles”^{4,10}.

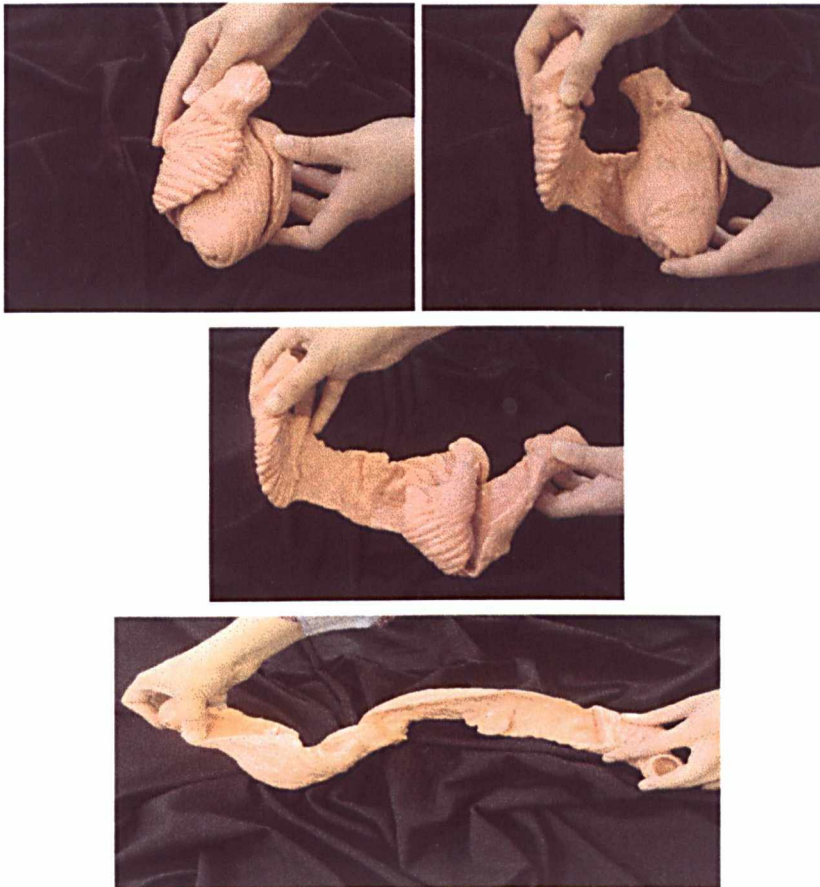


Figure 2.3 A rubber mould of the heart reveals it to be a single muscle band which can be unwound to reveal the helical structure of the fibres making up the ventricles. There is a “double twist” in 3D if using a single muscle band as the basic structure of the model.

2.3.6 Other Models

Although this model presents a simple view of myocardial architecture it does not address some of the findings of other research groups. The differences in interpretation of myocardial architecture arise from the methods of dissection and of observation. Other groups have used histological dissection on hearts preserved in resin to obtain their models or a peeling method to peel away the layered architecture of the heart²⁷. A number of models have developed over

the years, which distinguish from one, *i.e.*, the Torrent-Guasp model, to four, Robb and Robb's model, muscle bands²¹.

Histological studies have always shown the fibre angles of the muscles change from epicardium to endocardium, with the angles at the endocardium being directly opposed to those at the epicardium and transmural angles varying between the two². These studies lead to different models depicting the myocardium as a three-layered structure or a nested set of geodesics. Advances in imaging techniques, such as electron and photon microscopy and MR diffusion tensor imaging (DTI), are allowing further elucidation of this structure leading to the current trend which is to regard the muscle structure as an extension of the vascular musculature with myocardial fibres branching from one to another as in the blood vessels³⁰. Examples of these different models are further illustrated in Figure 2.4, where four models are described in more detail. MR DTI is a particularly powerful technique as it is potentially capable of investigating *in vivo* fibre architecture and linking this to local strain³¹⁻³³. It would be especially useful in tracking changes in diseases such as cardiomyopathy and changes after surgery.

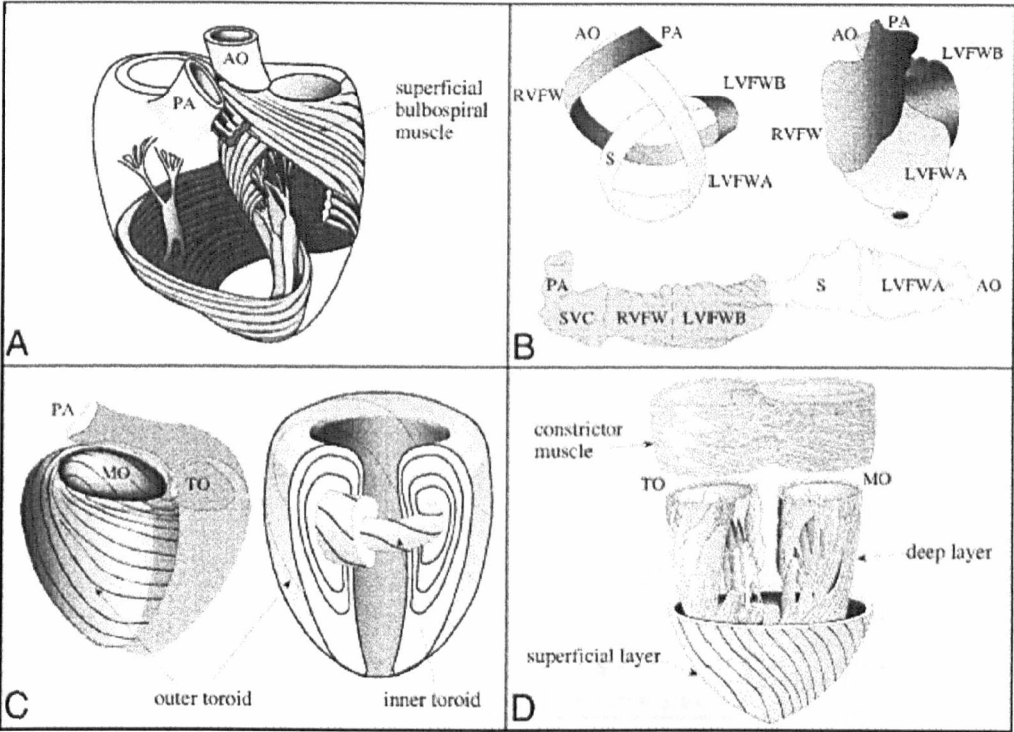


Figure 2.4 (A) One of the bundles, *i.e.*, the superficial bulbospiral muscle, described by Robb and Robb is shown. (B) Torrent-Guasp’s one muscle band model represents the myocardium as a ribbon wound in a double helix. (C) The left hand side shows Krehl’s (1891) model and the right hand side Streeter (1979) and Chadwick’s (1982). In Streeter’s model of the LV the myocardial fibres run like geodesics on toroidal surfaces. These surfaces or layers are nested within one another with the trajectories of fibres in each layer changing to more circumferential further into the myocardium. (D) Rushmer (1953) describes three layers, with the superficial layer, the middle layer or constrictor muscle and the deep layer. [Image courtesy of Dr PS Jouk, UF Biologie du developpement et Genetique clinique, Centre Hospitalier Universitaire de Grenoble, France]

2.4 The Cardiac Cycle and Ventricular Dynamics

The cardiac cycle was fully assembled by Lewis³⁴, but the idea was first conceived by Wiggers³⁵. In their view, the cardiac cycle consists of three basic events: LV contraction, LV relaxation and LV filling.

The characteristics of the cardiac cycle can be explained by the pressure curve shown in Figure 2.5. The LV pressure starts to build up when the arrival of calcium ions at the contractile proteins triggers actin-myosin interaction. This is followed by the closure of the

mitral valve leading to isovolumic contraction. This period of contraction refers to a time when the volume of the LV is constant as both the aortic and mitral valves are closed. When LV pressure reaches a point where it is greater than aortic pressure, the aortic valve opens and rapid ejection ensues. LV pressure then starts to fall and calcium ion concentration also falls causing the myofibres to enter a state of relaxation. As LV pressure falls the aortic valve closes and the LV goes into isovolumic relaxation. Finally, when LV pressure reaches a point when it is lower than atrial pressure, the mitral valve opens and filling begins.

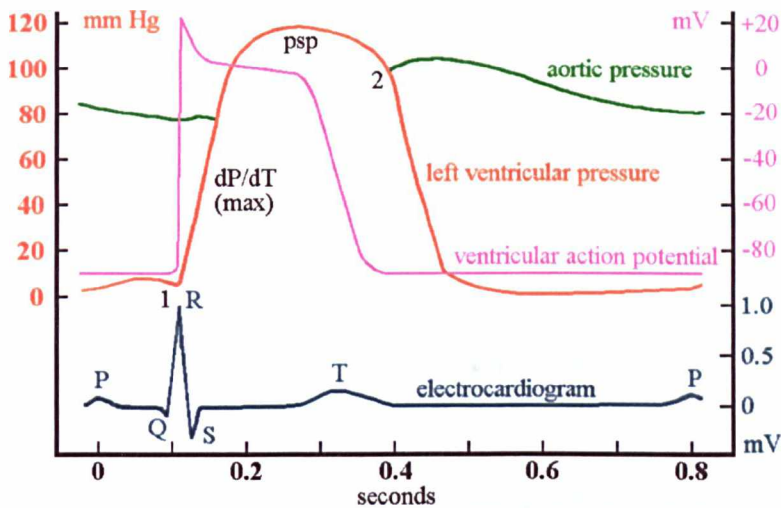


Figure 2.5 Cardiac pressure variation throughout the cardiac cycle. The blue line shows the echocardiogram trace, in mV, whilst the purple line is the ventricular action potential, *i.e.*, the electrical stimulus to the ventricle. The red line, a trace of the ventricular pressure, rises rapidly after the mitral valve closes until the aortic valve opens to allow rapid ejection of the blood into the aorta. The green line is the aortic pressure, which rises in systole and then decreases slowly as flow slows due to ventricular pressure decreasing. [Image courtesy of Dr JA Illingworth, Dept of Biochemistry and Molecular Biology, University of Leeds, UK]

In terms of overall muscle motion, it can be seen that at diastole there is a dilation of the ventricles resulting in a drop in pressure which leads to filling and at systole the ventricles contract to increase the interventricular pressure, hence expelling the blood into the arteries. In addition to this motion there is a lengthening and shortening in the longitudinal direction, which entails the base of the heart moving down towards the apex. Observation of the beating heart using CMR imaging or echocardiography shows that the apex remains motionless while the base moves up and down. This is a strange phenomenon considering the fact that the apex of the heart is free and unattached while the base is fixed and attached to the pulmonary artery, aorta and atria. These motions involve radial and circumferential stress development, leading early anatomists to assert that myocardial fibres are aligned parallel and tangential to

ventricular surface³⁰. However, this theory has been disproved by both histological and morphological studies. There is also the additional torsion of the heart³⁶ consisting of the base twisting in one direction while the apex twists in the opposite direction, making the motion of the heart something like the wringing of a wet towel^{10,14}. The physiologic and pathophysiologic function of this twisting is not well understood. It is known that the angles involved are too small to contribute to the expulsion of blood from the ventricular chambers, but observations have shown measurable changes during disease³⁰.

One way of explaining these motions is using Torrent-Guasp's model. It attempts to explain the four main motions involved in a beating heart and how they arise from the muscle structure, elucidating the way that the ascent and descent of the base and the torsion of the heart occur. This model, however, is incomplete in addressing the results obtained from different dissection methods. Other researchers contend that the results obtained using this blunt dissection technique are artifactual and do not fully explain the architecture or function of the heart³⁷. Dissection techniques such as the fibre strand peel-off technique give a picture that shows the heart to consist of multiple, entwined, spiralling fibre layers³⁷. This gives an alternative picture of how the motions involved in the cardiac cycle proceed, with an emphasis on different layers contributing to the main motions. Hence, the layers aligned in a longitudinal direction would contribute to the lengthening and shortening in that direction, while the obliquely aligned fibres would contribute to the twisting of the ventricle. Thus, it becomes necessary to not only look at histological and morphological studies but to combine these results from data obtained using functional techniques such as MR DTI, tissue Doppler ultrasound and CMR tagging and velocity mapping. Although, the following section explains the motions the heart undergoes during a cycle in the context of Torrent-Guasp's model, it should not be taken as the only explanation but rather as one theory that needs to be validated using the functional imaging techniques that are becoming increasingly available.

The contraction of the heart is controlled by electrical impulses that travel through its pacemaker cells. Figure 2.6 illustrates the journey of the impulse through the heart. The impulse begins at the sino-atrial (SA) node, which is located in the wall of the right atrium near the entrance of the superior vena cava. The SA node is also known as the cardiac pacemaker. The impulse takes about 50ms to travel from there to the atrio-ventricular (AV) node. The conduction through the AV node is quite slow, about 100ms, causing the atria to start contracting before the ventricles. The impulse then travels down through the Bundle of His, also known as the atrial bundle, in the interventricular septum to the Purkinje fibres, which then fan out throughout the ventricles. By this time, around 225ms into the cycle, atrial

contraction is complete and ventricular contraction begins. The Purkinje fibres conduct action potentials very rapidly hence allowing a smooth contraction of the whole ventricle.

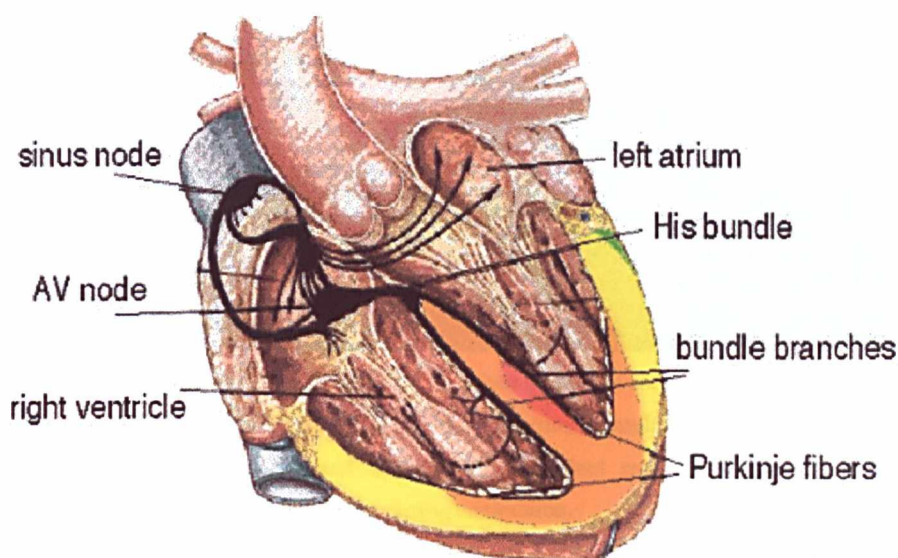


Figure 2.6 The electrical activation of the heart starts at the sino-atrial or sinus node, continues through the atria to the atrio-ventricular (AV) node. It then proceeds through the interventricular septum and out to the ventricles through the Purkinje fibres. Source: The Physiome Project (<http://physiome.org/>). [Image courtesy of Dr F Prinzen, Dept of Biomedical Engineering, Technische Universiteit Eindhoven, The Netherlands]

The electrical activation of the different sections of the muscle band should correspond to the different motions. The four main motions are two longitudinal and two transversal motions that occur in the following order: narrowing of the base, shortening in the longitudinal direction, lengthening in the longitudinal direction, and widening of the base. The last two motions are in a sense opposing motions to the first two. The experimental observations of Armour and Randall³⁸ supplement the model proposed by Torrent-Guasp. Armour and Randall observed the electrical activation to proceed as follows: right ? left ? descend ? ascendant. Figure 2.7 schematically illustrates the definition of these segments.

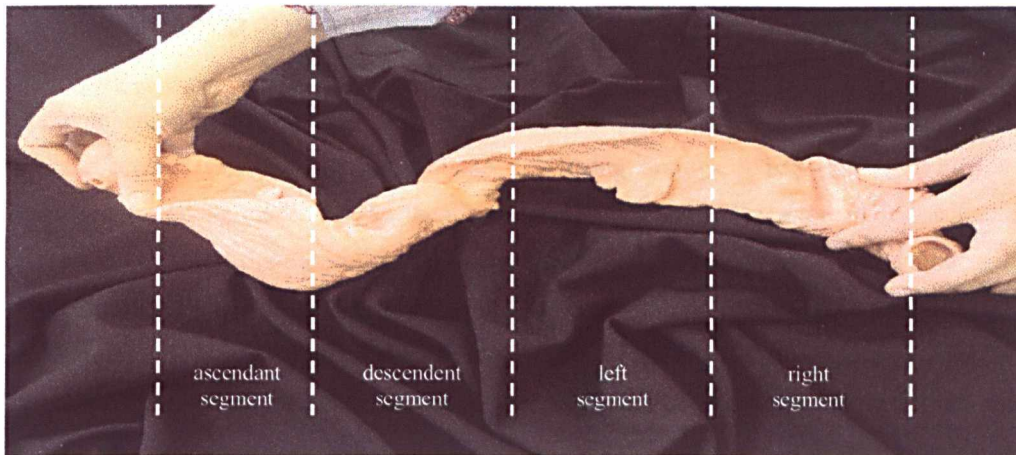


Figure 2.7 The muscle band can be divided up into four segments; ascendant, descendent, left and right depending on the orientation of the muscle fibre. Electrical stimulation has been shown to proceed from right to left to descendent and lastly to the ascendant segment, from right to left in this photograph, giving rise to the torsion seen during contraction.

2.4.1 Narrowing of the ventricles

This can be explained by looking at the way that the contraction proceeds. When the right and left segments receive electrical activation, they cause the muscle in the basal loop to contract forming a “stiff outer shell” inside which then occurs “the subsequent contraction of the bulk of the myocardium”¹⁸. This contraction of the basal loop causes a slight reduction in the diameter of the ventricles at the isovolumic phase of systole (no blood is being ejected as the valves are closed at this stage). The almost horizontal fibres of the basal loop prevent the spreading of the almost vertical fibres of the apical loop. This can be further evidenced by the fact that in the diseased state of dilated cardiomyopathy, the belt of the basal loop fails.

2.4.2 Shortening of the ventricles

The electrical activation continues immediately into the descendent and ascendant segments of the apical loop. Due to the way the two segments cross each other, two contrary rotations also occur; looking from apex to base (this convention is used from here onwards), a counter clockwise rotation at the base and a clockwise rotation at the apex. These rotations obviously imply a shortening of the ventricles as in a towel being wrung dry as shown in Figure 2.8.

2.4.3 Lengthening of the ventricles

The lengthening of the ventricles is not so obviously explained. However, if we look closely at the ascendant segment and the motions it is going through it becomes clear how the lengthening is taking place. The segment's contraction is preceded by a forced distension due to the contraction of the descendent segment. So when the ascendant segment contracts, its muscular fascicles stiffen, as happens with the paravertebral musculature of snakes when they attack going up. This stiffening gives rise to the rapid ascent of the base of the ventricles, and the clockwise rotation of the base and a counter clockwise movement of the apex, thus leading to the lengthening of the ventricles. The theory being that the shortening and lengthening of the ventricles is actually due to a torsion and untorsion of the myocardium around its longitudinal axis, as revealed by using CMR tagging^{36,39}.

2.4.4 Widening of the ventricles

To explain the widening of the ventricles we need to again consider the ascendant segment of the apical loop. Coming from the anterior aspect of the LV, the fibres of the ascendant segment divide, when they arrive at the interventricular sulcus, into the aberrant fibres and the intraseptal fibres. The aberrant fibres are named thus due to the unusual pathway they take. They, after jumping onto the interventricular sulcus, pass to cover subepicardially the free wall of the RV. This pathway is considered unusual as most of the fibres of the ascendant segment run intraseptally to terminate in the root of the aorta.

If we now consider the contraction of the ascendant segment, it can be seen that the widening of the ventricles is initiated by the untwisting motion caused by the contraction and is helped along by the contraction of the aberrant and intraseptal fibres. The untwisting motion implicates the development of a centrifugal force that will tend to the spreading of the ventricular mass. Models proposed by other researchers also point towards passive elastic forces acting in the transmural myocardial fibres that restore the myocardium into its initial, diastolic, position^{15,30}.

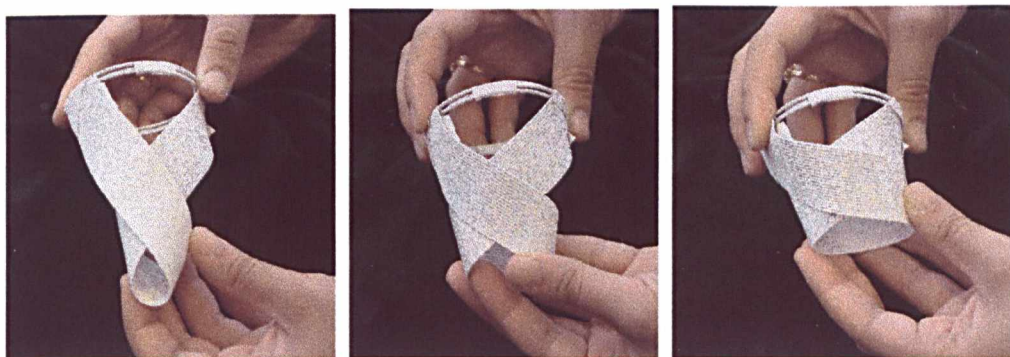


Figure 2.8 Lengthening and shortening of the ventricles is produced by the torsion involved. Two counter rotations occur; a counter clockwise one at the base and a clockwise one at the apex (looking up from the apex towards the base), causing the muscle band to behave as a towel being wrung dry.

2.5 Coronary Circulation and Myocardial Mechanics

The energy used by the heart is provided by the nutrients carried by the coronary circulation. The blood supply to the myocardium is via large epicardial coronary arteries. The main coronary arteries are depicted in Figure 2.9. They are the left main coronary artery (LEFT MAIN), right coronary artery (RCA), left anterior descending (LAD), circumflex (LCX) and posterior descending (PDA) coronary arteries. The LEFT MAIN and RCA branch out from the aorta. The LEFT MAIN then divides into the LAD and LCX, and the RCA, LAD and LCX form three clinically significant vessels. Anatomically, the major coronary arteries lie in grooves that separate the heart chambers. The LEFT MAIN, which branches into the LAD and LCX, provides virtually all of the blood supply to the LV, and hence these are clinically significant.

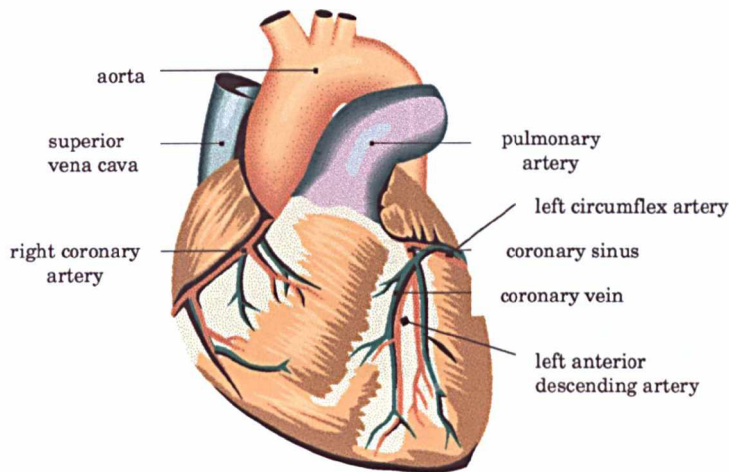


Figure 2.9 The major coronary arteries supplying blood to the myocardium and their anatomical locations.

The heart is usually divided into four distinctive regions to ease classification of perfusion and dysfunction. If looking at a short axis view, as in Figure 2.10(d), the anterior of the LV is the part facing the chest wall, the septal region is the side connected to the RV and the posterior and lateral are their opposites respectively. The LAD supplies blood to the anterior septum, the anterior wall, and in most cases apex. It might wrap around the apex and supply the most apical portion of the posterior and lateral wall as shown in Figures 2.9 and 2.10. The LCX supplies the lateral wall and the RCA, which runs down the groove connecting the LV and RV, supplies the posterior lateral segments, the inferior segments, and the posterior septum. The delivery of the blood to the myocardium is determined by intramyocardial pressure, *i.e.* when the intramyocardial pressure is low the blood can flow into the myocardium. Hence, almost all the nutrient coronary flow takes place during diastole. Occlusion of the coronary arteries can lead to “one-vessel”, “two-vessel” or “three-vessel” disease depending on which major arteries are occluded. Sudden occlusion of a major coronary artery causes ischaemic infarct with sharply demarcated borders. Venous drainage of the coronary circulation is via the coronary sinus and the anterior cardiac veins.

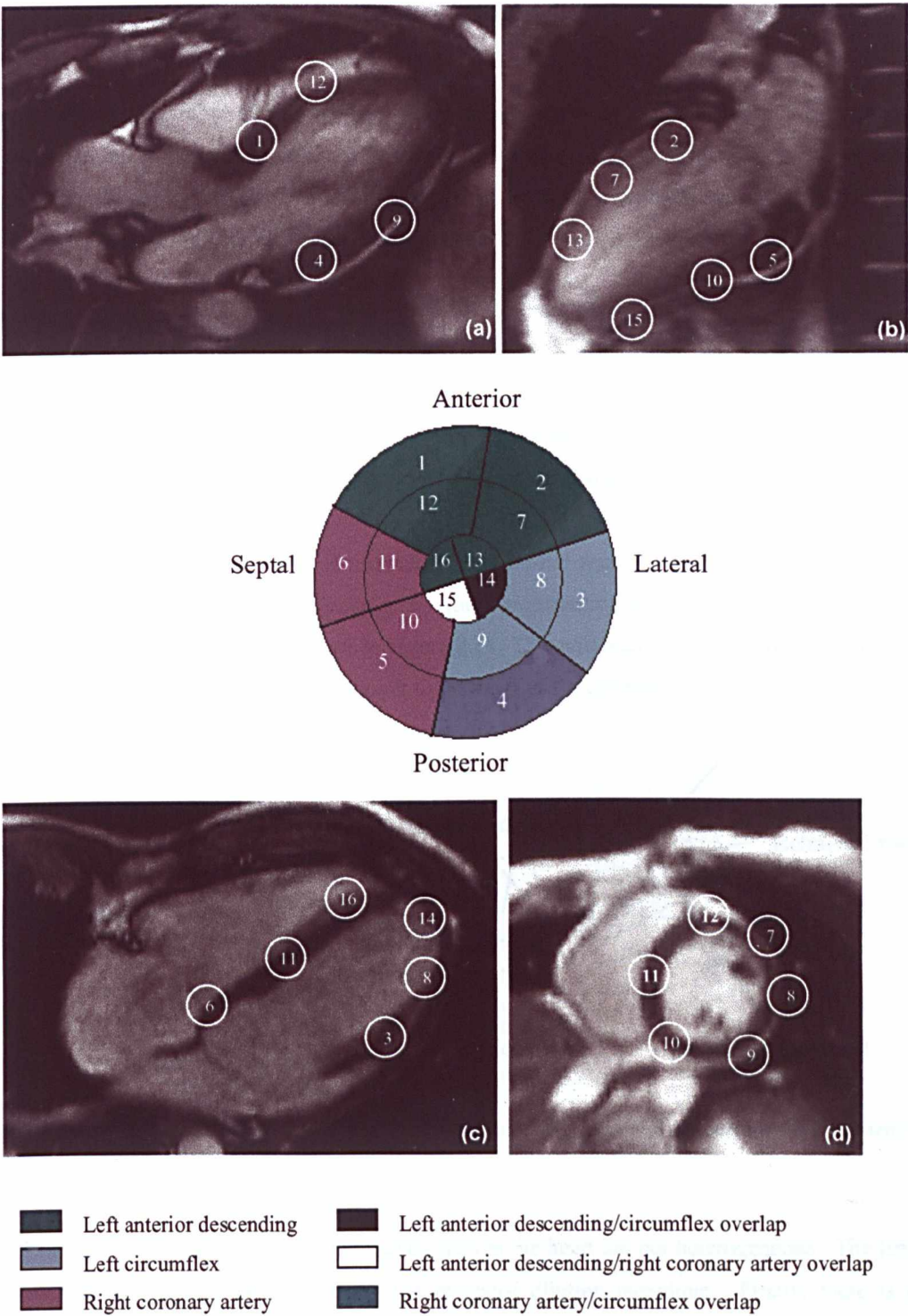


Figure 2.10 Schematic illustration of the perfusion of the heart. The main regions supplied by the three main coronary arteries are described. (a and c) Four chamber views of the heart. (b) A two chamber view of the LV and (d) a short axis view showing the LV ring. The bull's eye plot in the centre can be used to quantify the perfusion to different regions.

2.6 Perfusion

The constant activity of the beating heart means there is a high demand on oxygen consumption at about 5 to 10 ml/min/100g (higher than brain, 4ml/min/100g, and skeletal muscle, 0.2 ml/min/100g.) The Fick principle can be used to calculate an organ's metabolic rate from the blood flow. So for the heart it is:

$$\text{Metabolic Rate} = Q(C_a - C_v)$$

where Q is the blood flow and C_a and C_v are the arterial and venous constants respectively. At rest, myocardial oxygen extraction is nearly maximal which implies that coronary flow rate has to increase during stress to keep up with the increased oxygen consumption. Hypoxia and ischaemia stimulate vasodilatation to allow increased coronary flow rates.

Collateral circulation can arise in ischaemic myocardial regions to reduce the effect of a stenosed artery. Collateral vessels can grow from neighbouring arteries to perfuse the regions with low or no blood flow as shown in Figure 2.11. This will lead to a late perfusion response in those regions, as the blood takes longer to go through the collateral network.

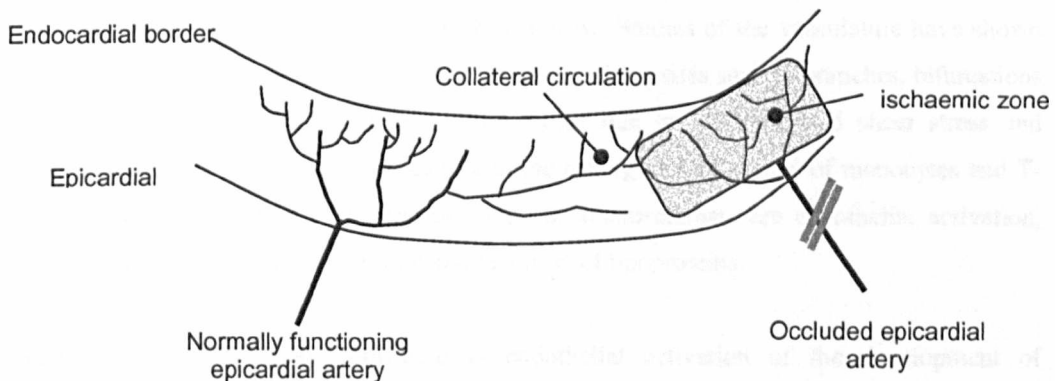


Figure 2.11 Collateral circulation arising from a normal artery to supply a neighbouring ischaemic zone.

It has been shown that perfusion and metabolism in the heart are not heterogeneous. The first evidence for this was obtained using the indicator dilution technique. Firstly, there is a transmural gradient of perfusion, where the subendocardium has 20%-40% greater perfusion than the subepicardium. Then there is spatial and temporal heterogeneity of flow. However, it is not clear whether heterogeneity of contractile function of the myocardium echoes this perfusion heterogeneity.

2.7 Atherosclerosis

Atherosclerotic disease is the leading cause of death in most of the developed world. It is a complex disease process involving the development of plaque composed of variable amounts of connective tissue matrix (collagen, proteoglycans, glycosaminoglycans), vascular smooth muscle cells, lipoproteins, calcium, inflammatory cells (monocyte-derived macrophages, T-lymphocytes and mast cells), and new blood vessels. Figure 2.12 illustrates the morphology and the formation of an atherosclerotic plaque. The transitional thrombus zone is where the lipid-filled plaque has ruptured and caused thrombus to develop in the artery. The causes and pathogenesis of atherosclerosis are so far not completely understood. The emerging theories state that atherosclerosis may reflect a chronic inflammatory response to vascular injury caused by a variety of agents that activate or injure endothelium and promote lipoprotein infiltration, lipoprotein retention and lipoprotein oxidation.

In relation to heart disease, atherosclerosis affects the aorta, and large- and medium-sized elastic and muscular arteries of the heart, predisposing the heart to ischaemic injury. Specific sites in the circulation predisposed to atherosclerosis are characterised by increased influx or prolonged retention of lipoproteins, evidence of endothelial activation with expression of leukocyte adhesion molecules, and low shear stress. Studies of the vasculature have shown that alterations in blood flow appear to be critical, making sites such as branches, bifurcations and curvatures naturally susceptible. This being due to the decreased shear stress and increased turbulence at these sites leading to the rolling and adherence of monocytes and T-cells. Studies suggest that the earliest steps in atherosclerosis are endothelial activation, injury or dysfunction with infiltration and retention of lipoproteins.

Various factors that may contribute to endothelial activation or the development of endothelial injury or dysfunction including risk factors associated with atherosclerosis are elevated and modified LDL/VLDL (low density lipoprotein/very low density lipoprotein) cholesterol (reduced high-density lipoprotein cholesterol, oxidant stress caused by cigarette smoking, hypertension, diabetes mellitus), genetic alterations, elevated plasma homocysteine concentrations, infectious micro organisms, estrogen deficiency, and advancing age. Vascular remodelling can occur in atherosclerotic disease leading to enlargement of the vessel, termed positive remodelling, to try and restore blood flow. Once this process stops, the lumen will start to narrow as the plaque grows. Luminal narrowing can also occur as a result of adventitial restriction or contraction, termed negative remodelling.

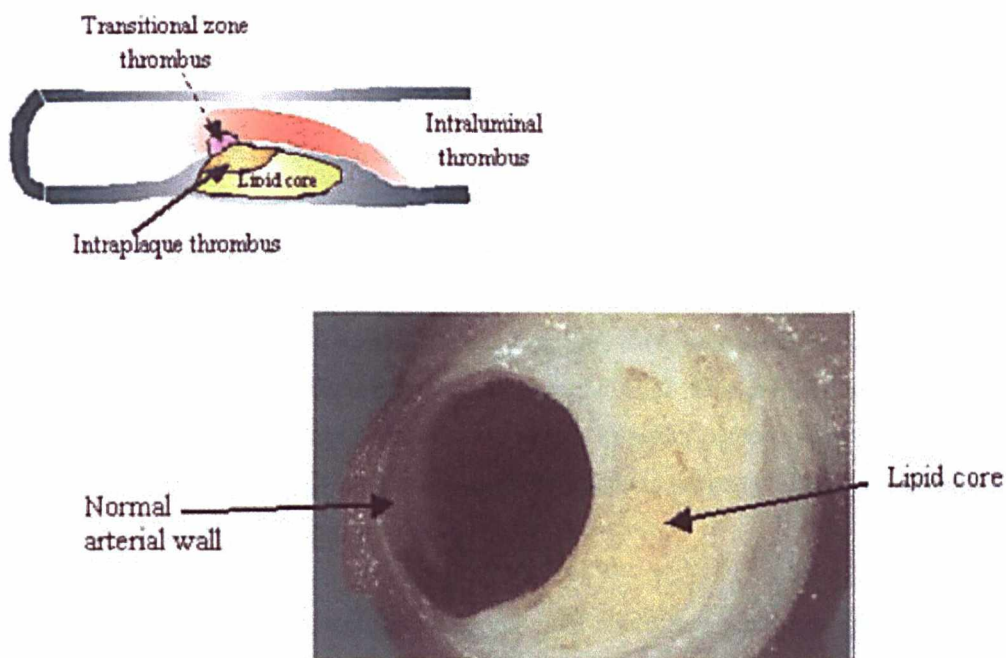


Figure 2.12 Illustration of an atherosclerotic plaque. The transitional thrombus zone is where the lipid-filled plaque has ruptured and caused thrombus to develop in the artery.

The atherosclerotic plaque can be unstable with a risk of thrombosis developing as a result of uneven thinning and rupture of the fibrous cap of the lipid-filled plaque. This can lead to acute ischaemic syndromes such as unstable angina, myocardial infarction and sudden cardiac death.

2.8 Myocardial Ischaemia: Causes and Effects

Myocardial ischaemia occurs when there is an imbalance between the supply of oxygen and other essential myocardial nutrients, and the myocardial demand for these substances. Causes of myocardial ischaemia include reduced coronary blood flow to a region, decrease in flow of oxygenated blood due to decreased coronary perfusion pressure, and an increased demand for oxygen resulting from an increase in cardiac output or myocardial hypertrophy. Reduced coronary blood flow can be a consequence of atheroma, thrombosis, spasm, embolus or coronary artery stenosis.

Myocardial ischaemia is characterised by an imbalance between myocardial oxygen supply and demand. On a macroscopic level, the effects of this include myocardial stunning, hibernation and necrosis, which will be explained in further detail later. Ischaemia can be

explained by the fact that coronary blood flow is closely linked to myocardial oxygen consumption in normal hearts. This linkage is needed as a) the myocardium depends almost entirely on aerobic metabolism, b) the oxygen saturation of coronary venous blood is low, permitting little additional oxygen extraction, and c) oxygen stores in the heart are meagre.

Ischaemia caused by a reduction of blood flow and oxygen supply due to increased vascular tone, intracoronary platelet aggregation or thrombus formation, is termed supply or low-flow ischaemia. The other form of ischaemia, demand or high-flow, is caused by the fact that increased coronary flow is insufficient to meet oxygen demand. This can be introduced by chronic coronary obstruction combined with exercise, tachycardia (an excessively increased heart rate) or emotional stress. Typically, a myocardial infarct is the result of both an increase in oxygen demand and a fall in oxygen supply.

Low-flow ischaemia is further characterised by not only inadequate oxygen supply but also by inadequate removal of metabolites. The build-up of metabolites can lead to the reduction of calcium sensitivity of myofilaments hence leading to diminished contractility. As coronary flow and perfusion pressure supplement LV systolic performance and reduce LV diastolic distensibility, LV systolic performance is lower and LV diastolic distensibility higher in low-flow ischaemia.

The subendocardium is most susceptible to ischaemia. Epicardial coronary stenoses cause a reduction in the subepicardial to subendocardial flow ratio, hence making the endocardium predisposed to ischaemia. It should be noted however, that after total or near-total occlusion of a coronary artery, perfusion of ischaemic myocardium occurs by way of collaterals – vascular channels that interconnect epicardial arteries, as shown in Figure 2.11.

Ischaemia can lead to myocardial stunning, hibernating myocardium or cell death. Stunned myocardium has been described as prolonged myocardial dysfunction with a gradual return of contractile activity after a brief episode of severe ischaemia. This condition has been observed in patients with coronary artery disease and after exercise-induced ischaemia. Studies have shown that a number of factors converge in the pathogenesis of stunning, including a) generation of oxygen derived free radicals, b) calcium overload, and c) reduced sensitivity of myofilaments to calcium and loss of myofilaments. These mechanisms interact together to result in stunned myocardium. Clinical treatment involves using inotropic agents, agents which affect the force or energy of muscle contractions, to reverse the stunning.

Hibernating myocardium is muscle that at rest has impaired function, due to poor coronary blood flow, but its function can be restored to normal after revascularisation. Hibernation was first noted in patients with coronary artery disease whose systolic LV function was improved after coronary bypass graft. Hibernating myocardium is present in about one third of patients with coronary artery disease. Recovery of hibernating myocardium can be from days to months; this is thought to be dependent on the period of hibernation. Observations of hibernating myocardium have led to the notion that the myocardium can reduce its contractility to match reduced perfusion, preserving its viability. Detection of hibernating myocardium is of utmost importance as the earlier it is caught, the more likely the chances of restoring function. Methods used to detect hibernating myocardium include stress echocardiography, thallium-201 redistribution study, imaging with technetium-99m sestamibi, positron-emission tomography with agents that detect residual metabolic activity, and, more recently, CMR perfusion studies at rest and stress combined with Gd-DTPA late enhancement and contractility assessment⁴⁰.

As was mentioned earlier, the subendocardium is most vulnerable to ischaemia due to low collateral flow and high myocardial oxygen consumption. In a normal heart, thickening and shortening are greater in the subendocardium, as is wall stress, accounting for the greater energy requirements. Higher metabolic activity, lower tissue oxygen tension and greater oxygen extraction have also been found in this area, which is consistent with the fact that the energy requirements are high. Consequently, the subendocardial cells are the first to undergo necrosis due to the likelihood of severe ischaemia occurring there first. So the 'wavefront of necrosis' travels from the subendocardium towards the epicardium gradually involving the less ischaemic outer layers. However, it can be slowed down by residual blood flow if the coronary occlusion is incomplete and by collaterals forming in the region²⁵.

2.9 Myocardial Remodelling

Myocardial remodelling is a consequence of structural and functional changes accompanied by molecular changes that affect multiple signalling pathways. It is an adaptive mechanism including LV enlargement, hypertrophy and distortion of regional and global geometry. Remodelling can be due to ischaemic^{41,42} or non-ischaemic heart disease, as in the case of familial cardiomyopathies. In ischaemic heart disease, acute myocardial infarction can lead to changes in left ventricular chamber volume, regional function and geometry, with remodelling continuing for months or years following the initial ischaemic injury. The

process of events is as follows. Necrosis of tissue leading to thinning of the myocardial wall, followed by dilatation of the thinned tissue eventually leading to hypertrophy of the non-ischaemic tissue. This is a result of the non-ischaemic tissue adapting to the extra load being placed on it⁴². The final stage is global LV dilatation as seen in dilated cardiomyopathy (DCM). In this context, surgical techniques have been employed that hope to achieve reverse remodelling of the LV by means of reduction of ventricular diameter, synchronization of myocardial activity, passive support of diastolic ventricular shape, and active support of systolic ventricular constriction. More recently, surgical intervention such as implantation of LV assist devices (LVAD) is being combined with pharmacological therapies to produce maximal reverse remodelling⁴³.

Remodelling associated with non-ischaemic heart disease includes changes in chamber dimensions due to diseases such as pulmonary hypertension and genetic disorders such as hypertrophic cardiomyopathy (HCM). Pulmonary hypertension results in hypertrophy of the RV due to the extra load placed on it, so that the chamber dimensions of the RV become similar to, or sometimes even greater than, those of the LV. HCM is explained in more detail in Section 4.4.

Functional changes in the heart due to heart disease are closely linked to the fact that structural remodelling of the ventricle occurs at macro and microscopic levels. Features of remodelling are hypertrophy (the enlargement or overgrowth of an organ or part due to an increase in size of its constituent cells), disruption of the extracellular matrix and LV dilation. The myocardial components involved in remodelling include the cardiac myocytes, endothelial cells and fibroblasts⁴⁴. By Laplace's law, the increased diameter of the ventricle places a greater mechanical burden on the myocytes. It has been shown that the myocytes change their phenotype with marked enlargement in their size, with the long axis being the most distorted^{44,45}. In addition, there is a complex gene response involving the genes encoding and handling proteins, metabolic enzymes, ion channels, secreted cytokines and growth factors. Thus, structural remodelling leads to reduced efficiency of contraction, due to greater wall stress and increased work.

Chronic changes in hemodynamic load can cause changes in chamber size and shape in the heart. Remodelling, in the context of coronary artery disease is described as ventricular enlargement and distortion of regional and global geometry as a result of an infarct. Thinning and stretching of the infarcted area (infarct expansion) are usually the first changes seen. On the cellular level, there is myocyte slippage, myocyte cell lengthening, and alterations in the intercellular matrix.

As time goes on, eccentric hypertrophy of non-infarcted myocardium, progressive LV dilation, and increased chamber sphericity develop. Remodelling may progress even with the lack of further ischaemia and can produce heart failure several months after the initial injury. Remodelling in other disease, such as hypertension and valvular disease, tends to produce global rather than regional changes.

At the myocyte level, remodelling may result in apoptosis, or in hypertrophy due to increased haemodynamic load. In concentric hypertrophy (the ventricular cavity becomes more spherical), cell surface area increases while in eccentric hypertrophy cell length tends to increase. Myocyte slippage is thought to be the cause of chamber dilation, and myocyte disarray has been found to be a characteristic feature of hypertrophic cardiomyopathy, but has also been found in cases of other myocardial hypertrophies, ischaemic heart disease and even in normal, healthy hearts.

The collagen interstitial matrix has many functions in heart muscle including transmitting force, maintaining alignment of myocytes and muscle bundles, preventing over-distention of the myocardium, and determining the shape and architecture of the heart. It also supports the intramural coronary arteries, stores energy in systole and repairs myocardial damage and responds to stress. Failing hearts have shown an increase in the collagen content from 4% (normal) to 25% (worst cases), which causes progressive functional impairment. The increased collagen content can impair both diastolic relaxation and systolic contraction. There can also be breakdown of the fibrillar collagen matrix that runs perpendicular to the myocytes, causing myocyte slippage, the cause of ventricular thinning in the remodelling process.

On a functional level, the contraction properties of myocytes have been found to be impaired in failing hearts. It is thought that irregularities in important cellular processes explain these contractile changes. The overall effect of these irregularities is that the action potential is prolonged, the duration of contraction is increased, reducing both the rates of contraction and relaxation.

2.10 Myocardial Infarction

Myocardial infarction (MI) is defined as the death of myocardial tissue due to lack of oxygen. The exact events leading up to infarction are not clearly understood. However, it is clear that coronary artery occlusion has a large part to play. It has been found that nearly all cases of MI occur in patients with already existing atherosclerosis. It is thought that there is a continuum of events, from stable plaque to plaque rupture and thrombus formation, leading to MI. Examination of patients reveals that it is not always so clear and in some cases the later stages of thrombus formation *etc.* are not evident.

Previous research has shown that the subendocardium is most vulnerable to ischaemia; hence necrosis usually begins there, with a “wavefront of necrosis” travelling to the subepicardium. In experimental animals, it has been observed that within the first hour of occlusion, patches of irreversibly injured myocytes develop in the subendocardial third. By three to four hours, fingers of the necrotic wavefront extend into the middle third of the myocardium. By twelve to twenty-four hours, the entire wall thickness is involved in the necrosis⁴⁶.

The body exhibits its natural inflammatory response on detection of necrotic tissues, which leads to some healing by fibrosis. Immune cells are dispatched to destroy the necrotic tissue. Macrophages destroy the necrotic myocytes and interstitial cells. The remaining interstitium, of collagen and reticulin, is used as the scaffolding to build fibrous scar tissue. Fibroblasts then proceed to manufacture dense and collagenous scar tissue; this usually consists of extracellular collagen²⁴. This fibrous tissue can help to restore some of the lost function of the myocardium as it is linked to the healthy tissue and moves with it.

The amount of impairment of LV function can be a good indicator of survival rates for the patient. However, we have to remember that myocardial stunning can also take place and that tissue that may look damaged on preliminary examination may actually be functioning at a later stage. Hence, making re-vascularisation therapy, *i.e.*, surgery, the best option for treatment.

2.11 Myocardial Contractility: a Basic Representation

Contractility is defined as the “inherent capacity of the myocardium to contract independently of changes in the preload or afterload”¹. It is associated with the heart’s inotropic state, *i.e.*,

its contractile state. Increased contractility of the heart refers to an increased rate of contraction, to reach a greater peak force. Contractility is an important regulator of myocardial oxygen uptake. Factors that increase contractility include exercise, adrenergic stimulators, digitalis and other inotropic agents. Contractility is usually measured using generalised quantities such as stroke volume, cardiac output, and ejection fraction.

Myocardial oxygen uptake is closely linked to the work done by the heart and hence the contractility. Increases in heart rate, preload or afterload cause an increase in oxygen demand.

$$\begin{aligned} \text{cardiac output} &= \text{mass moved} \\ \text{blood pressure} &= \text{resistance} \\ \text{minute work} &= \text{systolic blood pressure} \times \text{stroke volume} \times \text{heart rate} \end{aligned} \quad (2.1)$$

So it can be seen that an increase in ventricular radius or pressure will cause an increase in wall stress, as defined in Equation (2.2) below, leading to increased myocardial oxygen uptake as more ATP is consumed by the myofibrils to develop greater tension.

In principle, changes in contractility should be independent of loading conditions. However, we first need to define preload and afterload. Preload is the load present at end-diastole before contraction starts. This reflects the venous filling pressure that fills the atrium and consequently the LV. If preload increases, the LV becomes distended and stroke volume rises according to Starling's Law. The heart rate also rises as the arterial mechanoreceptors are stimulated making the rate of the SA node discharges increase. This has the effect of increasing cardiac output, which is the product of stroke volume and heart rate. The wall stress at end-diastole is a direct measure of preload. Laplace's law to calculate wall stress is the following:

$$\text{wall stress} = \frac{\text{pressure} \times \text{radius}}{2 \times \text{wall thickness}} \quad (2.2)$$

However, measurement of wall stress *in vivo* is difficult as measurements of LV radius ignore the complex anatomy of the LV.

The afterload is the systolic load on the LV after it has started to contract. Clinically, the arterial blood pressure is usually taken to represent the afterload. In a normal heart, the LV can overcome any physiological acute increase in afterload. However, in a chronically

increased afterload as in sustained arterial hypertension or significant stenosis, the LV must hypertrophy.

Starling's Law of the heart, formulated by Starling in 1918, is used to describe the effect of volume and pressure changes on the cardiac cycle. It states that the greater the volume of the heart, the greater the energy of contraction and the amount of chemical change at contraction. The modern version of this law states that stroke volume is directly related to end-diastolic volume. The graph in Figure 2.13 can be used to illustrate this relationship, end-diastolic pressure is used as an indicator of LV volume. As systolic pressure rises, the heart operates further up the graph, causing end-diastolic pressure to increase as well.

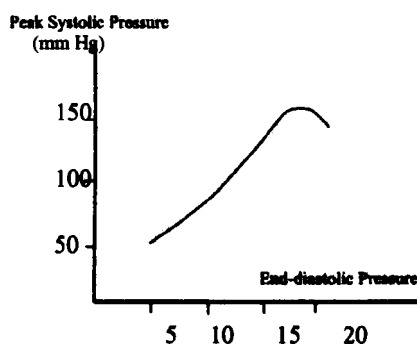


Figure 2.13 Starling's Law: the end-diastolic pressure reflects the initial passive 'stretch' of the myocardium in response to systolic pressure. The relationship is not fixed and the shape of the curve depends on the outflow resistance.

Frank, in 1895, reported that the greater the initial LV volume, the more rapid the rate of rise, the greater the peak pressure reached and the faster the rate of relaxation¹. Hence he was able to describe both a positive inotropic effect and an increased lusitropic (relaxation) effect of increased cardiac volume at onset of contraction. Combining the Frank and Starling laws gives us the Frank-Starling law, which illustrates the link between preload and afterload. It states that an increased LV volume leads to increased contractility, which in turn leads to an increased systolic blood pressure and hence afterload¹.

2.11.1 The Need for Non-Invasive Imaging Techniques

Measuring the heart's contractility is not an easy task. Currently, pressure-volume curves are among the best approaches. However, major criticisms arise when trying to use the slope of the curve as an index of "absolute" contractility. Also, the ventricular pressure needs to be measured invasively to obtain the full pressure-volume loop, making it an impractical

technique. It has also been found that the contractility is affected by the heart rate and loading conditions *in vivo*, although in theory it shouldn't be. Therefore, different indices of contractility have been used instead as indicators of the healthiness of the heart, these include wall thickening and shortening, ejection fraction and stroke volume²⁵.

Imaging techniques may be used to assist the evaluation of ventricular function, and hence contractility. The most commonly used imaging techniques are radionuclide scintigraphy, echocardiography, electron beam CT and MRI. LV ejection fraction (LVEF) is the most widely used index of LV function. It is defined as the ratio of the difference between end-diastolic and end-systolic volume to the total volume of the LV. Research has shown that LVEF is decreased in dilated and ischaemic cardiomyopathy, with most cases eventually leading to LV failure.

Echocardiography is useful for detecting ventricular hypokinesis and dilatation of the left atrium and ventricle. Examination of the patient with stress induced, using exercise or drugs, can be employed to observe changes in ventricular function. Nuclear imaging is extensively used in perfusion studies. Perfusion imaging, again combined with physical or drug-induced stress, has been found to be very useful in determining myocardial viability. For studying LV function using nuclear imaging, the most commonly utilised technique is equilibrium radionuclide angiocardiology. With this technique, ECG gated images in three views are acquired and used to assess LV wall motion and LVEF. Time activity curves can be plotted reflecting LV volume changes, and the ejection fraction can be calculated from the curve. Peak ejection and peak filling rates can also be calculated from the slopes of the curve. Additional information that can be obtained includes LV end-diastolic, end-systolic and stroke volumes. Recently, the technique was enhanced by using a forearm Doppler-based device for indirect measurement of aortic pressure, hence allowing pressure volume curves to be obtained. These curves can then be used to calculate the heart's contractility²⁵.

Electron beam CT, on the other hand, allows assessment of coronary artery calcification and general morphology of the heart and major vessels and useful measurement indices such as chamber volumes. A contrast agent has to be used to allow demarcation of the chamber borders. This then allows ejection fraction, myocardial mass and the chamber volumes to be measured. MR imaging has also been used for assessing global and regional RV and LV performance. It is also useful for evaluating abnormal morphology of congenital heart disease, for characterising myocardial tissue and measuring wall thickness and ventricular volume. Actual ventricular function can be assessed using cine MR, especially when combined with rapid imaging. MR velocity mapping and MR tagging have already proven

their usefulness in assessing ventricular function and eventually providing an index of contractility.

2.12 Conclusion

The heart has a complex anatomy that is closely linked to its function. Different levels of study can be performed to elucidate the intrinsic relationship between its anatomy and function. At the cellular level, cardiac myocytes are quite different from skeletal or smooth myocytes having a prolonged refractory period to stop contractions from interfering with each other, and not being able to repair on injury. They are also uniquely connected by intercalated discs, junctions that allow chemical, electrical and mechanical linkage between cells, allowing the cardiac muscle to be described as a functional syncytium.

At the macroscopic scale, different models of the myocardium have been proposed, ranging from a multi-layer approach to a single muscle band model. The differences between these models arise mainly from dissection and imaging techniques used. Dissection after preparation by boiling the heart reveals that following the natural cleavage planes of the muscle allows a “ventricular band” to be identified. This is a helically wound structure that winds twice to form the left and right ventricles. This double-winding also explains the thickness of the ventricles, *i.e.*, the fact that the LV wall is almost twice as thick as the RV wall, and the orientation of the muscle fibres from endocardium to epicardium. This muscle band model also explains the dynamics of the LV during the cardiac cycle. Although the single muscle band model is convenient, it does not fully explain the histological data that shows a trend of changing fibre orientations transmurally, giving rise to more complex models of myocardial architecture developed by other research teams.

The cardiac cycle can be divided into four basic motions: narrowing of the base, shortening in the longitudinal direction, lengthening in the longitudinal direction, and widening of the base. The work done by the heart, and hence the mechanics of the heart, is directly related to myocardial oxygen consumption which in turn is related to the coronary circulation. Defects in perfusion of the myocardium can lead to ischaemia and eventually infarction leading to impairment of ventricular function. Contractility, defined as the inherent ability of the myocardium to contract, can be used to measure LV function. However, it is not easy to measure this non-invasively and different quantities, such as ejection fraction and stroke volume, are used as basic indices of contractility. Recently, methods such as MR tagging and

velocity mapping have allowed non-invasive measurement of strain, which can also be used as an index of contractility. It is hoped that these techniques will allow a much more sensitive measure of contractility and hence the ability to predict and model disease.

3 MR Techniques for Measuring Myocardial Motion and Fibre Architecture

3.1 Introduction

In order to understand intrinsic myocardial mechanics, it is important to develop techniques for interpreting and predicting changes in the diseased heart. It has already been established that regional contractile motion may be used to assess myocardial viability after myocardial infarction, and CMR is one technique which is of great value to this end⁴⁷. It would also be valuable to assess contraction abnormalities at rest or during stress prior to irreversible damage.

The earliest developed technique for quantifying myocardial motion was based on radio-opaque fiducial markers. These had the disadvantages of being invasive and restricted by the paucity of the physical markers. A similar technique used ultrasonic crystals and ultrasound imaging, but suffered from the same disadvantages and also the fact that the ultrasound images had a relatively low SNR. Even when these imaging methods work well for determining the position and movement of the endocardial and epicardial contours, they do not enable assessment of the intrinsic contractility of the myocardium. Nevertheless, their use has led to the development of a general mathematical formulation for describing heart mechanics. The kinematics of the heart can be described using rotation and strain tensors, the

eigenvalues and eigenvectors of which allow the quantification of the maximum shortening and lengthening.

CMR techniques have been developed to allow not only accurate measurement of epi- and endocardial motion but also give an insight into the intramural myocardial function including regional contractile function, perfusion and diffusion. CMR offers the capability of combining functional and anatomical measures to obtain a more comprehensive assessment of cardiac function. There are three main approaches used for investigating intrinsic myocardial mechanics. Tissue motion can be assessed with CMR by using either tissue tagging or velocity encoding techniques, while tissue fibre architecture can be evaluated by diffusion sensitive imaging.

MR tagging normally uses a grid of magnetic saturation produced by applying a sequence of radio frequency (RF) pulses, either with the magnetic field gradients switched on whilst they are applied⁴⁸ or separated by magnetic field gradients⁴⁹. This grid provides landmarks that can be used to track the myocardial motion. They can be processed in the same way as the fiducial markers used in the ultrasound and X-ray techniques, hence providing regional strain measures. The advantage of CMR tagging compared to the older techniques is that it allows a higher density of markers and full functional imaging of intramural myocardium.

On the other hand, MR velocity imaging uses motion induced phase shifts for measuring myocardial motion^{50,51}. The phase of the signal is directly related to the velocity of the material within each voxel. The velocity field can then be integrated to yield displacements, which in turn can be used to calculate the strain tensor. Velocity imaging has the advantage of enabling the strain tensor to be calculated for each pixel, hence allows a greater degree of sensitivity than tagging, as there is a higher density of points being tracked.

As a complementary technique, MR diffusion tensor imaging (DTI) has been used to measure the fibre orientation of the myocardial muscle, which can be used to provide an insight into the relationship between the distribution of strain across the myocardium and the fibre architecture⁵²⁻⁵⁵. Recent advances in MR DTI allow interpretation of fibre shortening *in vivo*, showing promise in elucidating myocardial fibre architecture and its link to function in normal and diseased hearts.

This chapter compares these three CMR techniques and their relative strengths and weaknesses. The pitfalls associated with each technique are addressed and the clinical applications and future development are highlighted.

3.2 Mathematical Description of Myocardial Motion

During each cardiac cycle, the heart undergoes complex, non-linear deformation, which varies regionally. Mathematically, a small triangle of fiducial markers, such as the one defined in Figure 3.1, can be used to identify such a region of the myocardium. If it is assumed that the movement inside the triangle is homogeneous, then the deformation of the whole region can be described by the displacement of its centroid.

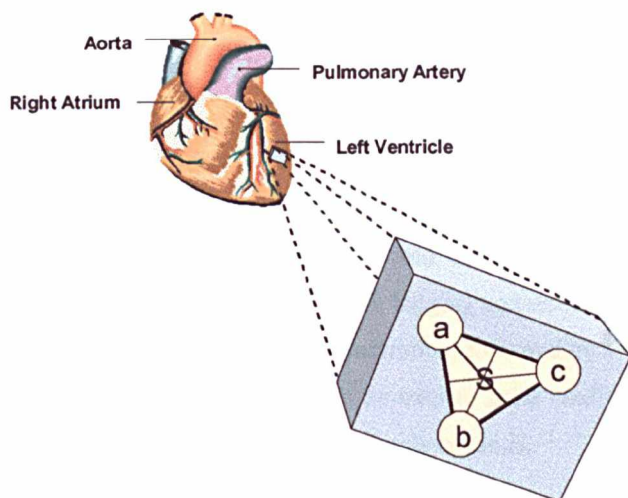


Figure 3.1 The triangle defines a region of the heart, bounded by the markers a, b and c, assuming that the properties of the centroid (S) apply homogeneously to all the material inside the triangle. The eigenvectors of the rotation and strain tensors associated with the centroid can be used to assess the contraction of the region.

Within each cardiac cycle, the centroid undergoes deformation which can be described by a tensor transformation⁵³⁻⁵⁵. This tensor is known as the deformation gradient tensor and is composed of two parts; the rotation and the stretch tensors. The rotation tensor rotates every point in the myocardial region by some angle around one of the axes. The stretch tensor reflects the way that the myocardial region lengthens, or shortens, by three factors, called eigenvalues, along the associated directions, called eigenvectors. The eigenvalues of the stretch tensor are called principal strains, which correspond to the maximal shortening and lengthening of the triangle. The associated eigenvectors are the directions in which they act. These deformation characteristics can be shown to be mathematically unique. This formulation applies for all times throughout the cardiac cycle, and consequently offers the most concise description of regional cardiac mechanics. Several studies have been conducted using CMR tagging or velocity encoding with this mathematical formulation aiming to quantify the function of normal and diseased hearts^{53,56-60}.

Another approach to quantifying myocardial motion is to use physics-based models. A deformable surface model was used by Nastar and Ayache⁶¹ to analyse cardiac ultrasound

data and MR human head data. A Fourier analysis of the surface's deformation over time can be used to describe the motion of the model, by using only the main excited modes and main Fourier harmonics. They also developed a 4D polar transformation, defined in 3D planispheric co-ordinates, which can be used to describe LV motion⁶². This was applied to cardiac SPECT data but has the potential to be applied to other modalities including MR tagging. Park *et al*^{63,64} used volumetric deformable models rather than surface models to quantify the motion information. These were applied to tagged MR images, and Lagrangian dynamics and finite element theory was used to convert the volumetric primitives into dynamic models.

3.3 MR Tagging

MR tagging was developed more than ten years ago as a technique to track the motion of moving tissues^{49,65}. The basic MR tagging sequence consists of using RF pulses to produce regular dark bands of selective saturation, followed by a conventional imaging sequence. The motion of the material can then be tracked quite readily, as the movement of the material is reflected by the deformation of saturation bands.

3.3.1 Sequence Design

One of the earliest and most popular tagging sequences is the Spatial Modulation of Magnetisation (SPAMM) sequence^{49,66}. The simplest form of tagging requires the application of two 90°, -90° non-selective RF pulses separated by a gradient waveform pulse applied in the direction of the final image plane, *i.e.*, if the slice select gradient is applied in the *z*-direction, the other pulse is either in the *x* or *y* direction. The direction of the applied gradient determines the direction of the tag lines. The first RF pulse turns some of the longitudinal magnetisation into transverse magnetisation, depending on the flip angle. The gradient pulse then causes a linear modulation of the phases of the spins in the transverse plane along the direction of the gradient. The second RF pulse mixes the modulated transverse magnetisation with the longitudinal magnetisation causing the total longitudinal magnetisation to be sinusoidally modulated, hence producing dark bands of magnetisation in the final image.

This sequence was further modified to improve the definition of the tags by using more than two RF pulses whose relative amplitudes are distributed according to binomial coefficients, and are separated by gradient waveforms⁶⁶. This has now become one of the standard tagging

sequences used in most clinical studies. The biggest disadvantage of SPAMM tagging is that the tag lines are not very well-resolved, especially in the later frames of the cardiac cycle, as tag-fading occurs due to the relaxation of the magnetisation. So the contrast between the tissue and the tags falls considerably during the later phases of the cardiac cycle. One advantage of SPAMM is that it can be easily extended to all three dimensions by tagging planes in three orthogonal directions⁶⁷.

Fischer *et al*⁶⁸ improved the tag contrast obtained from the SPAMM sequence naming the technique Complementary Spatial Modulation of Magnetisation (CSPAMM). It was realised that the contrast between the tags and the anatomy could be improved by separating the component of the magnetisation with the tagging information from the relaxed component. This could be done by subtracting two measurements, the first with a positive tagging grid and the second with a negative one. This greatly improved the tagging contrast especially in the later phases of the cardiac cycle. The tagging grid became the predominant signal with hardly any contribution from the anatomical background. The contrast was further improved by optimising the flip angle of the RF pulse of the imaging sequence. The angle can be optimised according to the tissue that needs to be imaged, which in this case is the myocardium. This suppresses the deformation of the tag lines due to T_1 relaxation and also the displacement due to fat. Even though there was a marked improvement in tag contrast, the contours of the tag lines were comparable to normal SPAMM tagging. The contrast provided by CSPAMM tags was further improved by employing a slice-following technique, as has been illustrated in Figure 3.2⁶⁹. However, only a 1-1 SPAMM sequence can be used for CSPAMM, which means that more detailed tagging cannot be obtained. But the improvement in contrast greatly enhances the possibility of using automatic tracking techniques.

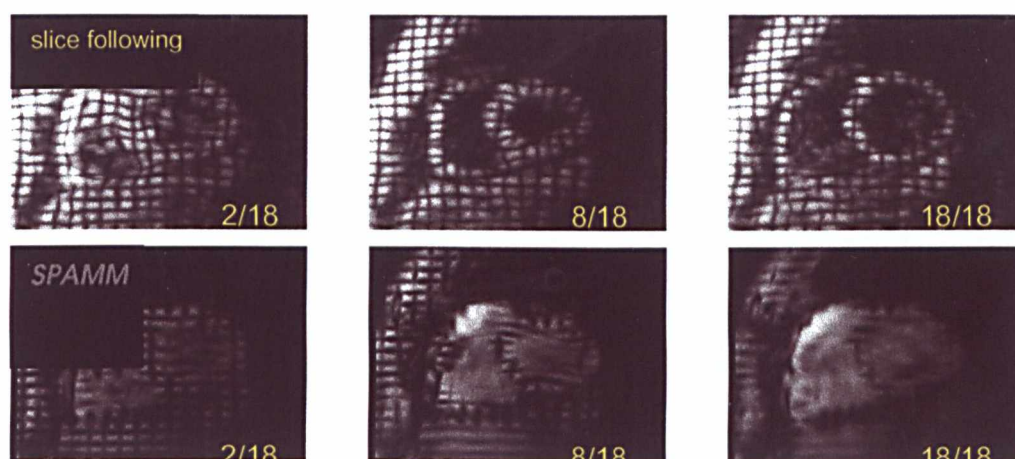


Figure 3.2 The effect of slice-following CSPAMM on the quality of myocardial tags. The top three figures are short-axis images obtained using slice-following CSPAMM, whereas the bottom three figures are the same slice obtained using conventional SPAMM. It can be seen that the contrast has been greatly improved using CSPAMM, and that the slice-following has helped overcome tag-fading⁶⁹. [Image courtesy of Prof P Boesiger, Institute of Biomedical Engineering, University and ETH Zurich, Switzerland]

Another popular tagging sequence is the Delays Alternating with Nutations for Tailored Excitations (DANTE) pulse sequence developed by Mosher *et al*⁴⁸. This sequence causes selective excitation at the frequency of the scanner and at the DANTE harmonic frequencies. This results in parallel planes of excitation orthogonal to the applied gradient. Varying either the DANTE interpulse delay or the tagging magnetic field gradient controls the thickness and spacing of the tag lines. This flexibility of tag spacing and thickness and the high resolution of tags is an added advantage of DANTE tagging. It also allows the tagging magnetic gradients to be left on during the application of the RF pulse train. This reduces the RF exposure to the patient, reduces eddy current effects, and minimises the strain on the gradient coils. As shown in Figure 3.3, the biggest advantage of the DANTE tagging sequence is the resolution of the tags and the ability to get more closely spaced tag lines⁷⁰.

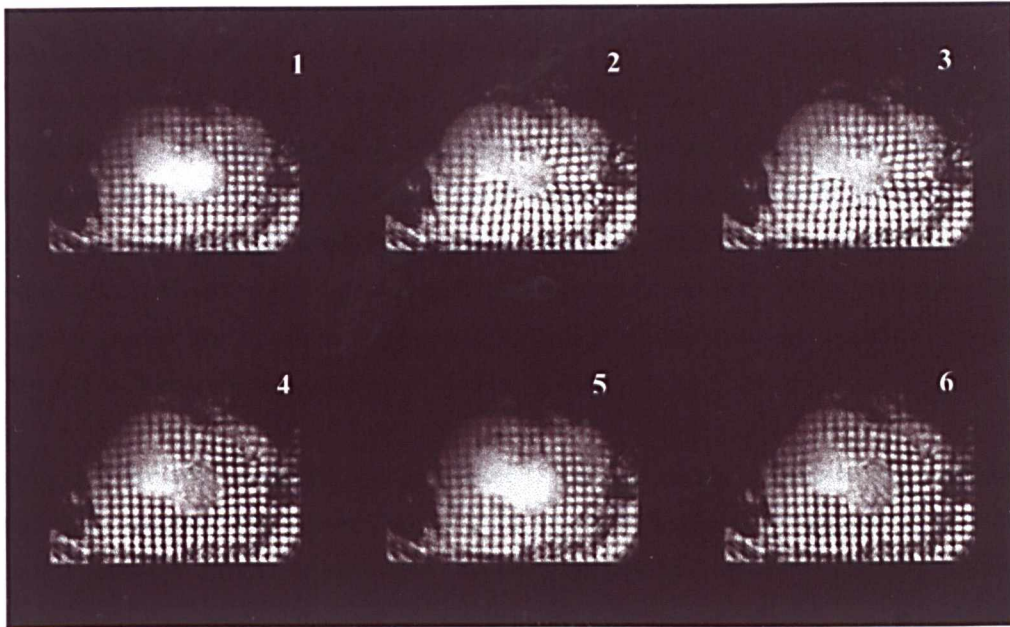


Figure 3.3 Short apical-view tagged images at 4.7 Tesla of a canine heart, using the adiabatic DANTE inversion sequence, showing six phases of one cardiac cycle. The deformation of the 4?4mm grid clearly demonstrates translational and rotational motion of the myocardial wall⁷⁰. [Image courtesy of Prof K Ugurbil and Dr N Tsekos, Department of Radiology, University of Minnesota, USA]

Recent developments in tagging include 3D CSPAMM⁷¹ and tagging with steady-state free precession (SSFP) sequences^{72,73}. 3D CSPAMM uses the basic principles of CSPAMM but tagging pulses are applied in all three directions and a 3D volume acquisition is used rather than the standard 2D slice imaging. Preliminary work shows promise with a spatial resolution of 2mm x 2mm x 2mm, in a volume of 256 x 256 x 80mm⁷¹. The processing was done using a 3D HARP formulation. However, the sequence has inherent problems as acquisition time is quite long requiring a complicated breath-hold technique. It is also not possible at the moment to verify the 3D strain results.

Tagging with SSFP sequences has only become possible with the developments in scanner hardware allowing ever faster gradient switching and hence the ability to interrupt the steady-state to apply the tagging saturation pulse without inducing too many artefacts. Initial studies are showing increased tag contrast-to-noise ratio (CNR) and tag persistence⁷². The reduced imaging time needed for SSFP imaging allows flexibility in a reduced breath-hold, or increased temporal and/or spatial resolution. This flexibility was exploited by Zwanenburg *et al*⁷³ to improve the temporal resolution to 14ms, which is comparable to tissue Doppler ultrasound. They have also conducted preliminary clinical studies looking at asynchrony in contraction in the LV and found differences between normals and patients⁷⁴.

3.3.2 Image Analysis

Once the tagged images have been obtained, the displacement of the tag lines needs to be measured for calculating the strain in different regions of the heart. Hence, the first part of the image analysis involves the tracking of the tag lines. Two different approaches can be taken, either the intersections of the tag lines are tracked or the whole line is tracked. The intersections or the lines can be found using either manual marking or semi-automated tracking software, relying on the active contour model⁵⁶.

There are different techniques for calculating the displacements of these points once they have been marked. The first is a model-based approach developed by Young and Axel^{56,75}. In this approach, the left ventricle (LV) is represented as a finite element model that deforms to fit the displacements of the tag intersection points. Alternatively, Kerwin and Prince⁷⁶ have used thin-plate splines, *i.e.*, spline surfaces, to represent the tag surfaces and then used an iterative algorithm to detect the intersections of the planes. The intersections are then regarded as material markers and their displacement can be measured. One of the disadvantages of these approaches is that the displacement measurement is based only on the tag intersection points rather than the whole tag line.

An approach that does use the whole tag line to calculate the displacement, the field-fitting approach, was developed by O'Dell *et al*⁷⁷. The deformed tag lines in each consecutive slice of the heart are treated as part of a surface that is described by a series expression. This series expression describes the displacement field. Using the co-ordinates of the undeformed and deformed tag lines, the coefficients of the series expression can be found. This enables the calculation of the strain from the displacement field. Spline surface interpolation has also been used to find the three-dimensional displacement field in a similar fashion⁷⁸. Here each tag surface is treated as third order B-spline curve. Once the equation of the curve is known it can be used to calculate the strain field as in the field-fitting method.

More recently, Young⁷⁵ modified their finite element technique to use model tags within the model of the whole ventricle. A substantial improvement in post-processing time was achieved, with tracking of tags and ventricular contours relying on only a few guide points. Denney and McVeigh⁷⁹ have proposed a model-free reconstruction of the displacement field. This method decomposes the myocardial volume into a fine mesh and then uses finite difference analysis and a smoothness constraint to reconstruct the displacement field. The strain field is then obtained by numerically differentiating the displacement field. An optical flow method has also been tried by Dougherty *et al*⁸⁰ and proven to be as fast as the snakes (or

splines) method but more accurate as it allows tracking of every single pixel. Optical flow describes the movement of points from one frame to the next, and hence can be a useful tool in detecting myocardial motion. This method uses a fully automated tracking technique, which computes the flow field between sequential images and uses this to compute the displacement field. The tracking of the tag intersections takes less than 5 seconds per slice per phase of the cardiac cycle. Also, due to the fact that the process is fully automated, every pixel in the image can be tracked. This improves the accuracy without an increase in processing time.

Koerkamp *et al*⁶¹ have developed a histogram modification technique to improve the tag contrast. The developed algorithm uses the intensity histogram of the first image, which has the best tag contrast, and normalises the later images in the cardiac cycle to this. A novel tag tracking technique was also developed which applied filtering in the Fourier domain to track the tags. The method was validated by applying a mathematical model of LV motion to images of the thigh muscle.

Recently, Osman *et al*^{62,63} have developed a rapid image processing technique for tracking tags. This method uses the fact that SPAMM tagging modulates the underlying images, and filters the spectral peaks in the raw data domain to obtain the motion data. A semi-automated method is then used to calculate the Lagrangian strain. This technique enables rapid analysis and visualisation of myocardial strain within 5-10 minutes after the scan is complete. An HARP-MRI sequence developed by Sampath *et al*⁶⁴ allows imaging of both tag directions in two heartbeats, allowing a “real-time” assessment of myocardial strain. This is especially useful in CMR stress testing and could be implemented on a clinical scanner with some simple modification of reconstruction software. The usability was proven in an animal study examining the effectiveness of HARP in detecting the onset of ischaemia⁶⁵. One of the limitations of HARP is that it only allows measurement of motion in two dimensions. Work carried out by Ryf *et al* extends the HARP technique to 3D using a 3D CSPAMM method⁷¹. Although initial *in vivo* results are promising, the image acquisition is long and thus requires a complicated breath-holding technique, which makes it clinically unsuitable.

Other recent 3D work includes that of Huang *et al*⁶⁷ who have used a four-dimensional (4D) time-varying B-spline model for analysing the data. This model enables the reconstruction of tag surfaces, 3D material point localisation, and displacement reconstruction. They later improved the registration of the method by coupling the B-splines in the different orthogonal planes⁶⁶. Chandrashekara *et al*⁶⁷⁻⁶⁹ have used non-rigid image registration for tag tracking. Diastolic tagged images are used as the target image and the transformation needed to register

systolic images back to the initial diastolic ones can be used to calculate the tag deformation. They have validated their method using a cardiac motion simulator and normal subjects.

For the purpose of visualisation, research groups have used arrows imposed onto 2D or 3D images to show the displacement of the tag points. The strains and rotation angles have been encoded in colours superimposed onto the 2D images. This allows quick assessment of patterns in different regions of the heart. Also, regions that are thickening and/or twisting more than others can be readily spotted. Axel *et al*^{63,56} have used cross hairs imposed onto a 3D picture of the LV to show the principal strains and their directions. This enables the user to visualise the motion of the entire heart wall.

3.3.3 Clinical Applications

A number of clinical studies have been carried out using tagging since its development in 1988 by Zerhouni *et al*⁶⁵ and, separately, by Axel and Dougherty^{49,66}. Tagging has been found to be an easy to employ method of assessing myocardial function. However, further development needs to be carried out to establish it as a standard clinical tool.

One of the first studies for measuring myocardial shortening in the human LV was conducted by Clark *et al*⁶⁰ using SPAMM. Results were found to agree well with echocardiographic data. Rogers *et al*⁶¹ measured long axis shortening and displacement of the LV using the tagging method developed by Zerhouni. In 1993, Young *et al*⁶³ built a database of normal LV function so that it could be used as a baseline to assess disease. SPAMM was used to study 12 normal human volunteers and values of displacement, rotation, torsion and principal strains in different regions of the heart were acquired. This database was subsequently used to compare the function of the LV in patients with hypertrophic cardiomyopathy (HCM) with that of normals. Dong *et al*⁶² also studied patients with HCM and found that the circumferential shortening and fractional thickening were good indicators of disease. Tagging enabled accurate measurement of both these measures. Dong *et al*⁶³ subsequently investigated LV function in patients with right ventricular pressure overload and found that septal thickness and function were changed in patients.

Park *et al*^{63,64} used volumetric deformable models to track tags and measure the changes induced by HCM. The volume primitives were defined by a few parameters, which are locally varying functions across the LV. The parameters could be used to quantify radial and longitudinal contraction, axial twisting and long-axis deformation. A marked difference was found between the function of a normal heart and that with HCM.

Tagging has also been used to study ventricular-ventricular interaction characterised by the regional wall motion and strain measures⁹⁴. MacGowan *et al*⁹⁵ have used strain data obtained from tagging to assess the directions of principal strain in relation to the directions of the fibres of the myocardial muscle. Myocardial viability has also been assessed using tagging in conjunction with a stress test using dobutamine⁹⁶. It was shown that myocardial function, which was depressed at rest but improved with isotropic stress could recover its function after re-vascularisation. Recent work using tagging includes Stuber *et al*'s⁹⁷ work on patients with aortic stenosis. Using CSPAMM, it was found that torsion is increased and diastolic untwisting is prolonged in patients compared with normals. Other studies have used tagging to look at the effect of pacing on the mechanical function at different sites of the heart^{98,99}. Marcus *et al*¹⁰⁰ have successfully used SPAMM to study contraction in the perfusion bed of the left anterior descending coronary artery.

Tagging has already made a mark in the clinical assessment of ventricular function. It has also shown potential in its application to other chambers of the heart, such as the right ventricle. New tagging sequences are being developed to improve tag contrast, number of tags per image, and reduce tag spacing to enable better spatial resolution of the myocardial motion. As tagging allows assessment of the transmural function of the wall, it remains an important tool for assessing normal and diseased LV function.

3.4 MR Velocity Encoding Using Phase Shifts

The measurement of motion via MR imaging can also be accomplished using velocity phase mapping. This is based on the principle that the spins of hydrogen nuclei inside a magnetic field are precessing at a frequency dependent on the strength of the field. If these spins are placed inside a magnetic field gradient and they move into another part of the gradient, the frequency of precession changes due to the variation of the net magnetic field strength experienced by these spins during motion. This frequency shift multiplied by the time during which it acts results in an accumulated phase shift relative to the unshifted spins¹⁰¹. Hence, this phase shift is directly related to the velocity of the moving particle. This phenomenon was first applied by van Dijk⁵⁰ and, separately, by Bryant *et al*⁶¹ to achieve MR velocity mapping of the heart wall and blood flow measurements. Nayler *et al*¹⁰² developed the method for cine blood flow imaging enabling measurement throughout the cardiac cycle.

The standard way of encoding velocity is to incorporate a bipolar gradient with a conventional MR image. This bipolar gradient causes the phase shifts of the stationary tissues to cancel out, whereas the moving tissues will acquire a phase shift due to their motion¹⁰³. To obtain the velocity in different directions, the bipolar gradient has to be applied in each direction. This means that for each velocity encode direction another image has to be taken. Hence, a total of four images have to be taken; three velocity encoding ones and one reference image. The velocity window of the imaging sequence is dependent on the gradient and has to be chosen so as to prevent phase wrapping, as the phase range is 2π radians, and to obtain the range of myocardial velocities rather than other moving tissues. However, phase-unwrapping techniques have also been developed to allow accurate measurement of velocity¹⁰⁴.

3.4.1 Pulse Sequences Design

The pulse sequences used to produce velocity encoded images comprise of bipolar velocity-encode gradients perpendicular to the required velocity direction, followed by a fast imaging sequence, either using echo planar or spoiled gradient echo sequences. It has been shown that due to the high velocity sensitivity needed to encode the myocardial motion, blood flow artefacts can have a significant effect on image quality¹⁰⁵. The phases of the spins are used to encode one of the image axes and consequently the blood can show up as an artefact in the phase-encode direction. The blood artefact can be reduced by a number of different methods. Probably the most successful approach has been the use of spatial presaturation pulses prior to the velocity encoding sequence. Drangova *et al*¹⁰⁵ investigated the use of such an approach by applying presaturation to slices adjacent to the slice to be imaged. It was found that even though there was an increase in repeat time (TR), the average root mean square error in trajectories was improved by a factor of two. To date, most research groups rely on segmented breath-hold gradient echo sequences with spatial presaturation to reduce the blood artefact^{106,107}, ECG-gated single-shot EP spin-echo⁶⁰, and other fast sequences to perform CMR myocardial velocity mapping.

3.4.2 Image Analysis

The basic aim of image analysis, carried out on velocity encoded images, is to obtain the strain tensor for all the velocity points. The first part of this process is to convert the velocity measured in the stationary co-ordinate system, to the Eulerian velocity. This is the local velocity of a material point and does not include the bulk motion of the heart as it is in a moving frame of reference.

Hennig *et al*¹⁰⁶ achieved this by firstly semi-automatically segmenting the myocardial wall, then the centre of mass of the LV was calculated and used as the origin of a polar co-ordinate system. The “velocity twist” was defined as the apical-to-basal rotation velocities in each plane. It was not considered important to use the processed velocity data to calculate the strain tensor. The velocity data was found to be reliable enough to predict abnormality in the function of the heart. Van Wendeen¹⁰³, however, attempted to forgo this type of calculation and directly convert the velocity gradient into the strain-rate tensor. This factors out the bulk motion, as it is a measure of the velocity gradient across the image rather than the true velocity.

Zhu *et al*¹⁰⁷ calculated the displacement from the velocity data and then computed the strain tensor from the trajectories. The first technique used to integrate the velocity data was the forward-backward technique. This method recursively computes the trajectory by computing the position in any time-frame, using the position in a neighbouring frame and the inter-frame velocity. Then, a weighted sum of trajectories is obtained by integrating first forwards and then backwards. This technique minimises the noise and eddy-current effects, but tends to underestimate motion and does not compensate for cine interpolation effects.

The forward-backward technique was extended into a Fourier tracking technique¹⁰⁸. The new method considers the trajectories as a sum of Fourier harmonics. It starts by using the forward-backward method as a coarse estimate of the trajectory and then refines it by taking its Fourier transform (FT), filtering it, then taking its inverse FT and repeating the process until convergence is reached. The Fourier tracking technique gave more accurate results than the forward-backward method but is more susceptible to noise and eddy-current effects.

Zhu *et al*¹⁰⁹ then used the calculated trajectories to derive the strain. This work was also extended to three dimensions using volumetric CMR data. The scan times of this data were quite long (half an hour for one image), but there is room for improvement as any of the currently available ultra-fast imaging sequences could be used. Recently, Arai *et al*¹¹⁰ applied a rigid body correction, hence simplifying the velocity vectors. Then the strain rates were calculated and the data was used to look at myocardial ischaemia in canines. However, this work has not been extended to human studies as yet. An interesting approach was adopted by Robson and Constable¹¹¹. The fact that the magnitude of the signal contains information about the range of velocities in a voxel was used to calculate the velocity in the slice direction, *i.e.*, perpendicular to the image plane. Good results were obtained on phantoms as well as *in vivo* on a human volunteer. Meyer *et al*¹¹² took a different approach, using a deforming mesh

placed on the myocardium. The velocity field was computed with a Kalman filter to track the motion of the mesh over the cardiac cycle.

It is difficult to visualise the strain tensor as it is a three-dimensional quantity, or 2D if only looking at the (x, y) plane. Many scalar quantities have been defined to try and deal with this problem, as a scalar could easily be visualised using a colour map. Hennig *et al*¹⁰⁶ overcame this difficulty by only visualising the velocities as separate colour-coded images. Plots of the velocity versus time were also constructed and found to be a helpful means of looking at the data.

Van Wedeer *et al*¹⁰³ have used ellipses to represent the strain-rate tensor. The major and minor axes of the ellipse represent the principal strains, *i.e.*, the eigenvalues of the strain-rate tensor. The ellipse is supposed to characterise the deformation of a circle of myocardial tissue during the cardiac cycle after the strain-rate tensor has been acting for a number of seconds. It was found that it is more useful to represent the ellipses as rhomboids. The axes of the rhomboids were defined using the time the strain rate tensor acts as a scale factor and the eigenvectors of the two-dimensional strain rate tensor as the directions. A scalar quantity was also used as a colour hue superimposed onto the anatomical images. This scalar quantity is chosen such that it acts like a magnitude for incompressible materials. Hence, an underlying assumption is made that the myocardium is incompressible.

A limited number of clinical studies have been carried out using CMR velocity mapping. It has still not been developed or applied as much as CMR tagging. The few studies that have been carried out include those of Karwatowski *et al*^{67,58}. These studies looked at the long axis function of the LV during diastole and compared results to echocardiographic data, and were able to demonstrate changes in long axis velocity caused by ischaemia during dobutamine stress. The studies showed the potential of CMR velocity mapping for the analysis of ischaemic heart disease. Figure 3.4 illustrates how velocity mapping can be used to study the function of the myocardium.

More recently, van der Geest *et al*^{113,114} have used velocity mapping to look at the function of both ventricles. They explored the function of the left ventricle by dividing it into three regions and measuring the radial, circumferential and through-plane velocities for each. It was found that radial velocity and strain rate as functions of time were more sensitive indicators of myocardial dysfunction than wall thickening. Markl *et al*⁶⁹ utilised global motion parameters to describe rotation and contraction in 20 patients suffering from myocardial infarction. They reported significant localised motion deficits in patients as compared to normal volunteers.

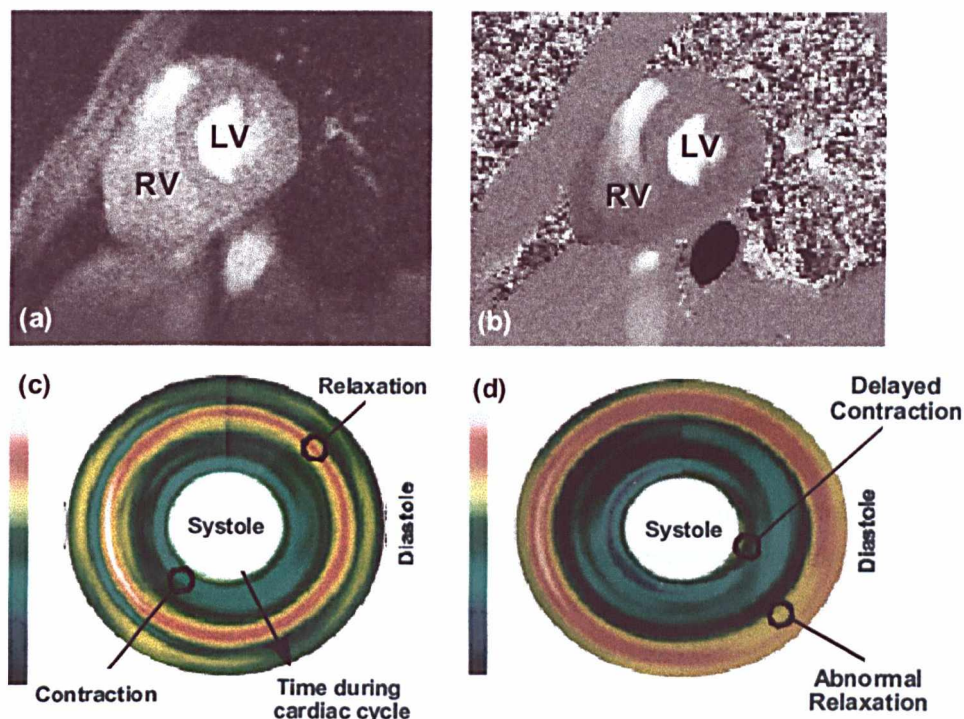


Figure 3.4 Assessment of myocardial contractility with high sensitivity MR velocity imaging. (a) The anatomical structure of the image plane, (b) the MR velocity measurement, (c) the reconstructed longitudinal contractility mapping showing uniform contraction (sky blue) during systole and relaxation (red) during diastole for a normal subject. (d) The contractility mapping for a patient with ischaemic heart disease, showing delayed contraction during systole and abnormal contraction (broken and broadened red strip) during diastole.

3.5 MR Diffusion Imaging

MR can also be used to image the diffusivity of different tissues¹¹⁵. This is useful because the diffusion anisotropy of tissues has been found to correlate to their fibre orientation. MR diffusion imaging has been extensively used in brain function studies and has also been applied to renal function and studies of tongue fibre architecture. In the last five years or so, it has also been used to study the fibre architecture of the myocardium.

The diffusion co-efficient of tissues is measured by estimating the mean free path of water molecules as a function of time. However, in biological systems we can only measure Apparent Diffusion Coefficients (ADCs) as the measurement of the diffusion coefficient is affected by other factors such as bulk motion, intracellular streaming, temperature and

magnetic susceptibility variations⁵². MR can be used to measure diffusivity by making the sequence phase sensitive to motion. Diffusion results in phase dispersion within a voxel with a resultant signal loss. This enables us to measure the diffusion tensor of that particular region. It has been found that the fibre orientation is defined by the eigenvector of diffusion, which is the eigenvector corresponding to the maximal eigenvalue of the diffusion tensor⁵².

3.5.1 Pulse Sequence Design

Different pulse sequences have been employed to measure the ADCs of the myocardium. Diffusion imaging requires the diffusion sensitising gradient to be switched on for a long period of time, as diffusion is a slow process. Also, the echo time needs to be long, as the signal is relatively weak. This poses additional problems when applied to the heart. The heart is plagued with respiratory and muscle motion which means that imaging the same slice after the long period of time which is needed for diffusion imaging is almost impossible. The heart motion involves the need for a gated and possibly a breath-held sequence. Different approaches have been employed to get around this problem.

Edelman *et al*^{62,116} have used stimulated echo-EPI pulse sequences which have proved quite successful. The stimulated echoes decay according to T1, hence allowing a long period of time for diffusion sensitising. This sequence was successfully used on human volunteers providing good results. The sequence incorporated gating and breath-holding hence allowing ultra-fast acquisition of the data and factoring out bulk motion, improving the image resolution. The breath-holding improved accuracy but resulted in an increased imaging time.

The diffusion sensitivity of such a pulse sequence can be calculated and gives an indication of how useful it will be for any specific application. The sensitivity of the sequence can be altered by adjusting the timing and/or the gradients according to the experiment.

Other groups like Hsu *et al*¹¹⁷, Scollan *et al*¹¹⁸ and Trouad *et al*¹¹⁹ have used spin-echo and fast spin-echo pulse sequences for diffusion imaging. Results that are comparable to histological fibre angle data, have been obtained³². Recent studies are starting to define the relationship between fibre shortening using strain data from MR velocity mapping combined with diffusion tensor imaging to elucidate the relationship between fibre angle and cardiac contraction^{31,33}.

There is a need for strain correction to be applied to diffusion data as tissue motion affects the diffusion measurement process and the diffusivity tensor. This is due to the fact that when

material is stretched along a certain direction, the phase modulation in that direction is reduced proportionally. Hence, the observed diffusion is lower than it would be in a stationary sample^{52,120}. This means that the above mentioned methods are not sufficient to measure the diffusion anisotropy of the myocardium accurately.

Two different approaches have been used to get the strain correction. The first approach is to incorporate it into the image analysis¹¹⁵. The true diffusion tensor can be gained by obtaining the deformation gradient tensor and assuming that the diffusion tensor is only affected by the rotation. This calculation then becomes part of the data processing.

The other approach is to try to forego the strain correction by imaging at points in the cardiac cycle where the strain is equal to the average strain¹²⁰. These are called “sweet spots” and can be estimated using a periodic time-dependent scaling function to represent the myocardial strains. It was found that there are two such “sweet spots” during the cardiac cycle, and that they occur at mid-ejection and in mid-filling.

The visual representation of the diffusion tensor needs to somehow correlate to the fibre orientation. Tseng *et al*¹²⁰ have used colour maps, octahedra and boxes with different coloured sides to represent the diffusion tensor, as shown in Figure 3.5. Each box points along the direction of the first eigenvector of the diffusion tensor and the colours represent the fibre helix angle. Hsu *et al*¹¹⁷ have used lines to represent the eigenvectors of the diffusion tensor and hence the fibre orientation. Scollan *et al*¹¹⁸ have used colour maps of diffusion anisotropy to enable comparison between normal and diseased hearts. It is difficult to indicate which method works best and there is still a need for standardisation of diffusion-weighted images.

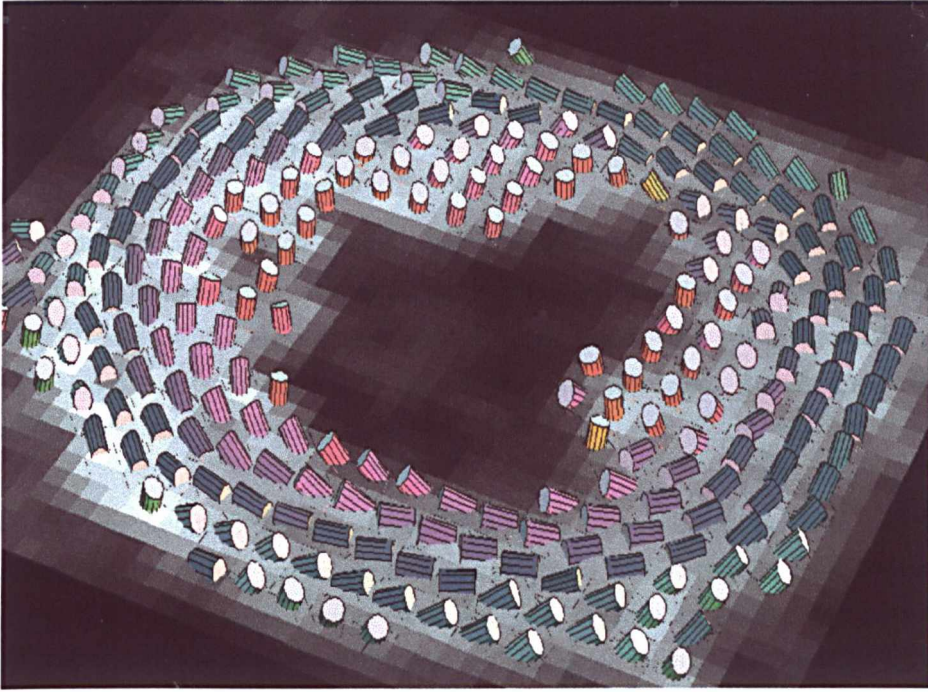


Figure 3.5 Diffusion tensor MRI of the myocardial fibre orientation in the beating heart. 3D fibre orientation is represented at each pixel by a cylinder pointing along the first eigenvector of the diffusion tensor, and colour-coded according to the fibre helix angle¹²⁰. [Image courtesy of Prof Van J Wedeen, NMR Centre and Department of Radiology, Massachusetts General Hospital and Harvard Medical School, USA]

3.5.2 Cardiac Diffusion Studies

Even though MR diffusion imaging has been extensively used in brain studies, it has had limited application in cardiac studies as it is still in the early stages of development. The majority of studies have been in an effort to validate the accuracy and usefulness of cardiac diffusion imaging. Studies have been carried out comparing the diffusion data with the fibre angles obtained from histological data from canine and rabbit hearts^{32,117,118}. It has been shown that there is a clear correspondence between the eigenvector of the diffusion tensor measured using MR and the orientation of the local fibre angles. Edelman *et al*⁵² have measured the ADC's of the interventricular septum of 12 healthy subjects and tried to compare them with those from 10 patients with cardiomyopathy. Other studies have tried to validate the method using normal volunteers¹²⁰. All of these studies show the potential of MR diffusion imaging for analysing intrinsic cardiac mechanics. However, the imaging

techniques need to be improved to account for respiratory motion and allow faster data acquisition.

3.6 Discussion and Conclusions

Myocardial mechanics, though complex and difficult to measure, can be accessed using CMR. This information is important for determining the extent of disease and myocardial viability. There are two main techniques that enable measurement of myocardial motion, which include CMR tagging and CMR velocity mapping techniques. Both of these methods have their advantages and disadvantages.

CMR tagging, despite being easy to use and faster than velocity mapping, involves a significant amount of post-processing to obtain the strain data. A large amount of work has been, and is still being, carried out in CMR tagging to improve tag contrast and persistence. A range of techniques including CSPAMM and histogram modification have already been developed and tested. They have shown good prospects to be used clinically. However, the post-processing techniques are not trivial and tend to be time-consuming. Even though extensive work has been conducted on finite element analysis of the motion data, there is also a necessity for a fast, robust image processing method, which could calculate the strain field from the tagged images. More development is required to enable the tracking to become fully automated. This would allow the technique to move from being a research to a routine clinical tool enabling on-line assessment of myocardial function.

Velocity encoded images are slower to acquire as they require four scans to measure the velocity in all three directions. Research is being carried out to improve the acquisition time of velocity imaging, such as the work of Firmin *et al*¹²¹. This technique uses a novel echo-planar *k*-space sampling scheme combined with selective excitation to obtain 3D cine blood flow data. Even using the conventional flow imaging techniques, the post-processing of the images is faster and less tedious than with tagging as it has the potential to be fully automated. Nevertheless, the problem of segmenting the myocardium by detecting the contours remains. Velocity mapping has also shown the possibility of an extension to three-dimensional volumetric data sets. New ultra-fast imaging techniques such as hybrid EPI could allow both of these methods to become more efficient, reliable and relatively accurate by allowing breath-hold data acquisition.

Diffusion CMR, although not used for direct measurement of myocardial motion, could be used to elucidate the relationship between fibre architecture and strain. It has been shown to be very useful in brain and renal studies, yet remains to be fully exploited in cardiac imaging. It has not yet been extended to the clinical environment due to the problems associated with imaging the heart. However, research is being carried out to assess the importance, accuracy, and applicability of diffusion imaging to the myocardium. It is expected that the fast imaging techniques will play an important role in the development and application of diffusion imaging clinically. It is hoped that diffusion CMR will enable measurement of fibre architecture to obtain a more complete picture of myocardial function.

Assessment of myocardial mechanics can be a valuable tool for understanding, predicting and evaluating disease. However, research and development in CMR needs to continue to make full use of the recent availability of higher performance gradients and post-processing computers. The most efficient method of determining strain tensors needs to be ascertained and validated. A database needs to be constructed of normal healthy volunteers to allow for comparison with diseased hearts. The myocardial motion data obtained by using CMR could present us with an invaluable key. Not only would it allow an insight into the onset of disease, it will also assist researchers in unlocking certain physiological mysteries of *in vivo* cardiac function.

4 Measuring Myocardial Motion *In Vivo*

Using HARP Imaging

4.1 Introduction

As discussed in Chapter 3, the current techniques for assessing myocardial motion with CMR are tagging and velocity mapping. CMR tagging is based on the principle of magnetically saturating bands of tissue that follow the motion of the heart, thus allowing measurement of the deformation. MR tagging allows flexibility in the density of tags placed, within physical limits governed by the scanner hardware, and thus the spatial resolution. As tags only need to be applied at the beginning of each cardiac cycle, the temporal resolution can also be adjusted allowing good assessment of different stages of contraction and dilatation. However, as the tags fade during the cardiac cycle, it is probable that the diastolic motion cannot be measured accurately. Improved hardware performance and CMR sequences have enabled tags to persist for a longer period and it is now possible on most scanners to assess diastolic motion as well.

The main obstacle towards using tagging for measuring contractility is that the post-processing can be time-consuming and tedious. Quantitative study of myocardial motion using tagging requires software that allows tag detection and tracking. This is difficult to achieve fully automatically, and thus often requires extensive human intervention. Researchers have been working towards developing a clinically feasible system since the 1980s, but to date this has not been possible mainly due to the computational difficulties.

HARP imaging, on the other hand, exploits the information content of CMR tagging and allows the estimation of myocardial motion in near real-time. It makes use of a simple SPAMM tagging sequence for assessment of myocardial motion and processing is done in frequency space (*k-space*) with spectral filtering and reconstruction. The technique has shown promise in application to different clinical settings particularly for the on-line assessment of stress induced contractility changes.

To implement HARP for myocardial motion quantitation, the first step is the development of a fast imaging sequence and appropriate clinical protocols. In CMR imaging, the image acquisition time *in vivo* is always limited by the motion of the heart, which is a combination of the heart's intrinsic motion and respiration induced distortion. The use of ECG gating allows the synchronisation of data acquisition with cardiac motion except for patients with irregular ECGs. The respiratory motion, however, is more difficult to deal with but can be removed in one of the following two ways. The first is to ask the subject to hold their breath, which is routinely used and end-expiratory breath holds have been shown to be highly reproducible. This, however, is problematic for patients particularly for those with heart failure or coronary artery disease. In these cases, some form of respiratory gating is needed. This can be done by using a physical system such as a belt attached to the patient's chest or by using navigator echoes, either retrospectively or prospectively¹²².

This chapter describes the use of CSPAMM tagging and HARP processing for myocardial motion quantification. A CMR sequence was developed which could be easily used *in vivo*. The sequence was further developed to incorporate respiratory gating with navigator echoes. We further demonstrate the effect of free-breathing on strain measurements by using HARP imaging. The practical value of the proposed method was evaluated with application to the assessment of myocardial motion for patients with cardiomyopathy.

4.2 Extracting Myocardial Motion

4.2.1 MR Sequence Design

The basic principles of MR tagging are well established and those relevant to this thesis are explained in Appendix I. A SPAMM sequence is typically used but in this thesis we used a CSPAMM segmented FLASH sequence with a reduced phase encode *k-space* acquisition for improved tag quality and efficiency. In essence, the tagging sequence can be thought of as

four separate image acquisitions, with two acquisitions each for the vertical and horizontal tags. The two acquisitions are required for each direction of tagging to get the $+90^\circ, +90^\circ$ tagged images and the $+90^\circ, -90^\circ$ tagged images needed for CSPAMM subtraction. The segmented FLASH sequence consisted of acquiring eight phase encode lines per segment (cardiac cycle) as shown in Figure 4.1. By choosing an image matrix of 256 by 32, each image could be acquired in 4 cardiac cycles, allowing the complete acquisition to take place in 16 heartbeats, which is considered a reasonable breath-hold even in a clinical environment. It was found that 32 phase encode lines were sufficient to capture the tag motion providing the phase encoding direction was oriented in line with the tag direction. As the main information regarding the motion is contained within the low frequency components of the spectral peaks, acquiring the central 32 k -lines is adequate for delineation of the myocardial motion.

Figure 4.2 illustrates an example of short axis CSPAMM tagged images of a normal heart. It can be seen that the CSPAMM subtraction significantly reduces the central peak thus reducing artefacts that can be introduced into the HARP processing.

The tags were designed to have variable tag spacing. The image matrix was set to 256 in the read direction and 32 in the phase encode. The phase encoding direction was switched so as to correspond to the tag direction. In the Fourier frequency space, k -space, the tag information is contained primarily in the centre of k -space. This allowed the reduction of phase encode lines acquired to 32 to cover just the centre of k -space, without loss in spectral peak, and hence motion, resolution. The tag spacing was set to 8mm as default but could be varied. However, there is a balance to be found between tag spacing and spatial resolution as having a low spatial resolution in the read direction will make having finer tags redundant. The field-of-view was typically set at 300mm but could be varied if necessary. For the long axis images, only one set of CSPAMM images was acquired with the tags running perpendicular to the long axis of the heart to capture the longitudinal shortening.

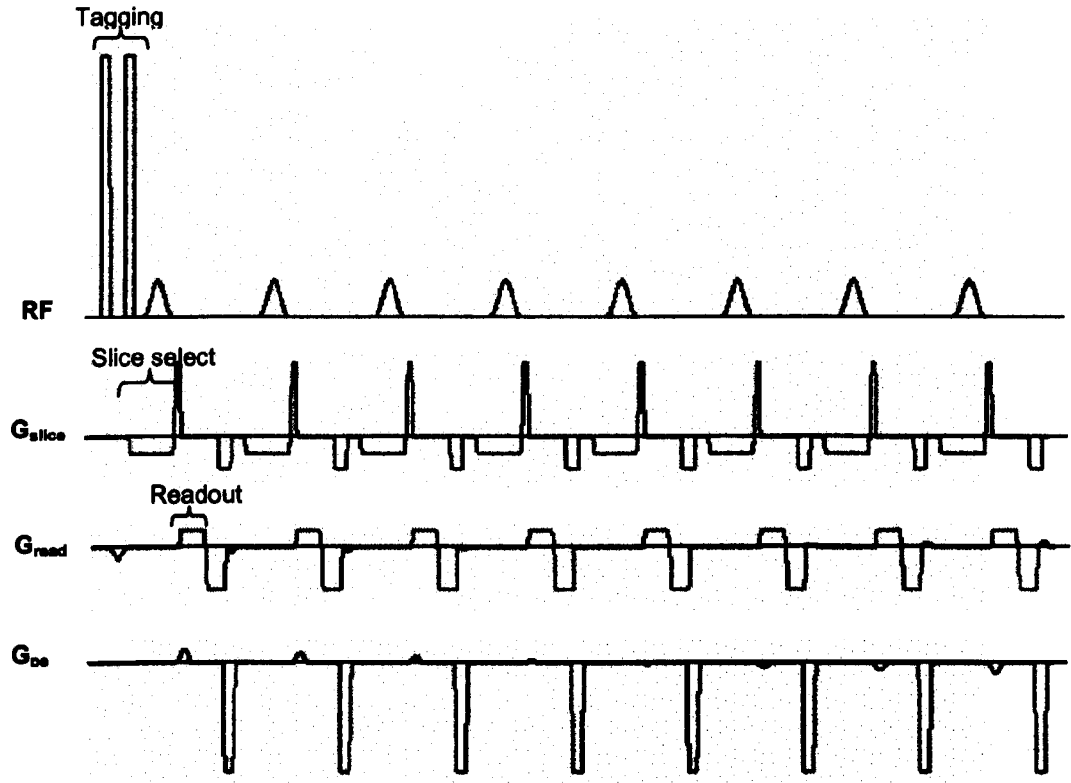


Figure 4.1 The basic sequence diagram. The sequence consisted of four such acquisitions. The first with $+90,+90$ tagging pulses, with the tagging gradient played in the x (phase encode) direction. The second acquisition with $+90,-90$ tagging pulses with the tagging gradient played again in the x (phase encode) direction. The whole process is then repeated with the phase encode direction switched and the tagging gradient played in the y (phase encode) direction. The tagging gradient has to be in the same direction as the phase encode to enable satisfactory resolution of the tags.

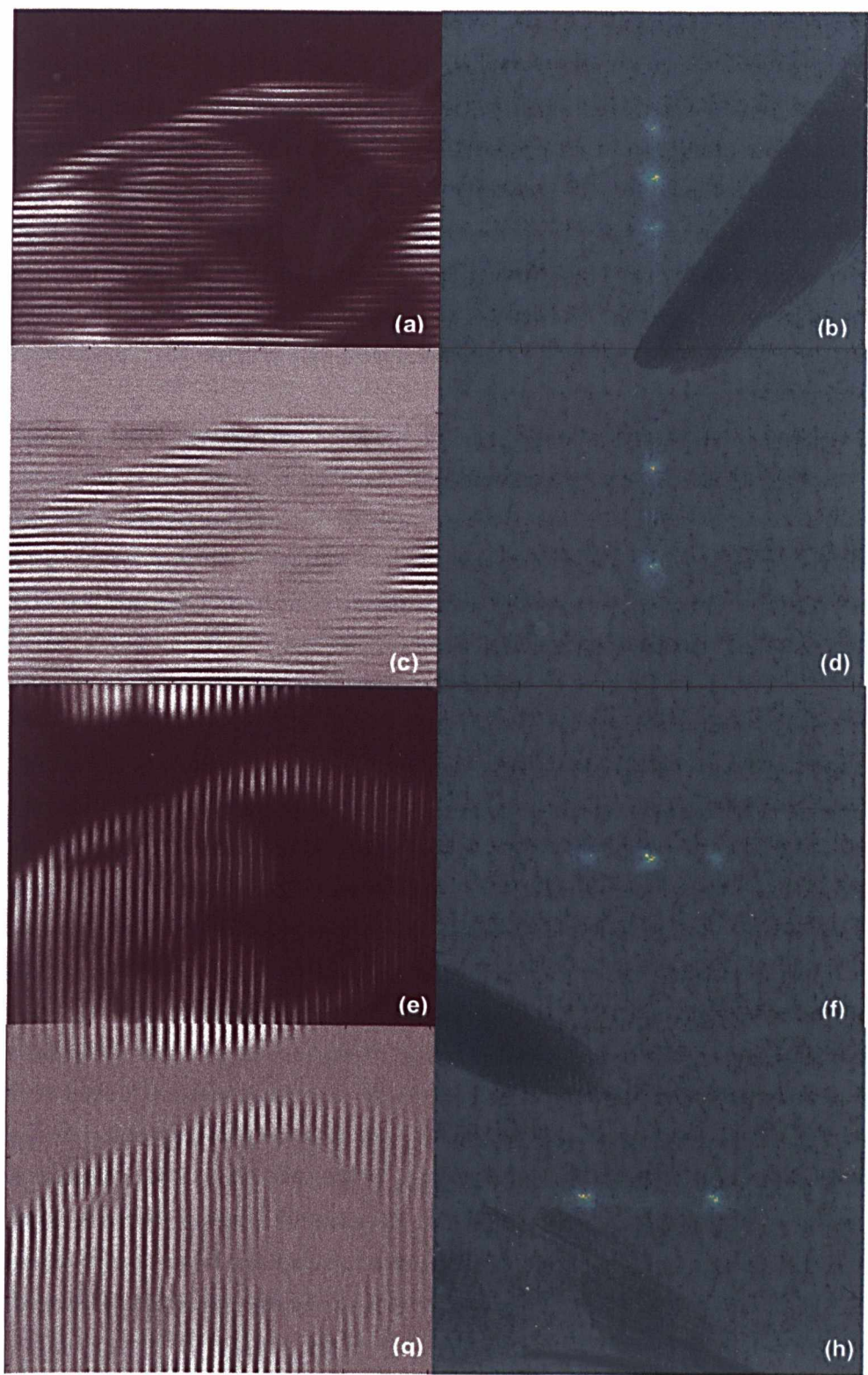


Figure 4.2 *k-space* representation of horizontal and vertical (a, e) SPAMM and (b, g) CSPAMM tagged images. As can be seen the central peak in *k-space* is significantly reduced in the CSPAMM images thus reducing possible artefacts in the HARP processing.

4.2.2 Respiratory Gating using Navigator Echoes

Thus far, multiple breath-holds have been employed to acquire the different directions of motion. For CMR tagging with high spatial resolution, this would entail two breath-holds acquiring both the vertical and then the horizontal tags. This can potentially introduce mis-registration errors in the strain calculation because of the different breath-holds used. For example, for the in-plane strain a radial and circumferential representation of strain would require the combination of the horizontally and vertically tagged images, and inconsistency in breath-holds could introduce significant artefacts.

The developed sequence in this thesis requires approximately 16-20 seconds for each acquisition which can be problematic for patients with impaired ventricular function or respiratory disease. This can result in a poor quality image due to respiratory motion. Even for normal subjects, however, consistent breath-holds between scans have proven to be difficult. Effective respiratory motion management is therefore essential to the practical application of HARP. For this study, prospective navigator echoes were used, because the method allows data acquisition under normal physiological conditions.

The idea of monitoring motion using navigator echoes was first introduced by Ehman and Felmlee¹²³. The principle is to use the signal from a column oriented parallel to the direction of motion. After Fourier transforming this signal a well-defined edge of the moving structure can be seen and used to monitor the motion. Navigators can be employed in one of the following two ways, either using two intersecting slices, one 90° the other at 180° so that a spin-echo is formed in the intersecting column, or using a 2D selective RF pulse in the cylindrical shape. Each method has its own advantages and disadvantages. The 90°-180° pulse is robust but cannot be repeated rapidly due to the involvement of 180° pulses. Care also has to be taken that the navigator slices do not impinge on the region of interest as otherwise a saturation band can be introduced. The 2D selective RF pulse method, on the other hand, considerably reduces this problem by using only a small flip angle, and thus the pulse sequence can be repeated. However, the method is prone to shimming errors, which can result in poor spatial localisation. Furthermore, if a large excitation field-of-view is to be ensured, the 2D RF pulse can be considerably long.

Another issue to consider for the use of navigator echoes is the positioning of the column. The dome of the right hemi-diaphragm is higher than that of the left, and the motion of the diaphragm is greater posteriorly than anteriorly. Nonetheless, the dome is a good place to

position the column as it is perpendicular to the direction of motion over a wide range of motion and provides a sharp edge, which can be easily detected.

In practice, the timing of the navigator can be positioned in the scanning in four ways; pre-imaging, pre and post-imaging, post-imaging or at a pre-determined frequency. The precision of the navigators is determined by the SNR attained and the spatial resolution of the navigator column. Spatial resolution is usually 1mm, with a 256mm field-of-view and a read-out of 256. The quality of the edge determines the effectiveness of the respiratory gating, which requires a small column cross-sectional area combined with careful positioning of the navigators. In practice, edge-detection can be achieved by using simple edge-detection, correlation or least squares fitting. If the navigator is well-positioned and the SNR is high, a sharp edge is obtained which can be easily detected even using a simple edge-detection algorithm^{122,124}.

Using prospective navigators for respiratory gating assumes that the feedback from the reconstruction computer is fast enough to follow the sequence. This requires a computer architecture that is able to cope with fast reconstruction of the signal read out from the column and is able to feedback to the image acquisition computer whether the phase encode line needs to be reacquired or not. At present, new scanner hardware is able to cope with this feedback loop and allows navigator acquisition and feedback in less than 50ms. Once acquired, the navigator information can be used either for monitoring the reproducibility of multiple breath-holds, or for prospectively controlling the acquisition of different k -lines during free-breathing. Retrospective or prospective navigators can be used in free-breathing acquisition. Retrospective respiratory gating entails over-sampling, *i.e.*, repeating the scan four or five times, and then sorting the data acquired according to the diaphragm positions. Free-breathing acquisition using prospective navigators entails the use of respiratory gating algorithms, the simplest of which is the accept-reject algorithm first used by Sachs *et al*¹²⁵ and Oshinki *et al*¹²⁶. In this method, a navigator acceptance window is defined and everything outside it is rejected. Typically a window size of ~5mm gives reasonable scan efficiency and accuracy. Respiratory drift, a translation of the diaphragm, during the scan can be a problem in this type of algorithm.

To resolve this problem, Sachs *et al* developed the diminishing variance algorithm¹²⁷. This method does not require a specific acceptance window to be defined. One complete scan is taken with the navigator positions saved for each phase encode line. The most frequent position is found and the scan is begun again. The data is reacquired until the range of diaphragm positions reduces to the required variance. More adaptive ordering of k -space developed by Jhooti *et al*¹²⁸ increases scan efficiency while retaining image quality. This is

achieved by using different acceptance windows for the central and outer lines of k -space, as it is known that the central lines of k -space are the most susceptible to motion artefact. The central lines are acquired within a 5mm window while the outer lines can be within the 10mm window. This allows higher scan efficiency with the same image quality. This method was refined by guiding the image acquisition to acquire certain lines of k -space when it detects a certain diaphragm position¹²⁹. This allows full use of the scan time while retaining image quality. Yang *et al* exploited the varying spatial resolution contained within an image to optimise the phase encoding by assigning an adaptive window dependent on the relationship between phase encode line and the image the reconstruction function, $r(y)$ ¹³⁰. As an example, Figure 4.3 shows the image reconstruction function, the covariance matrix and the selection of optimal locations of k_y lines using the back selection algorithm, whereas Figure 4.4 shows the corresponding normalised weighting function used to adapt the respiratory gating window.

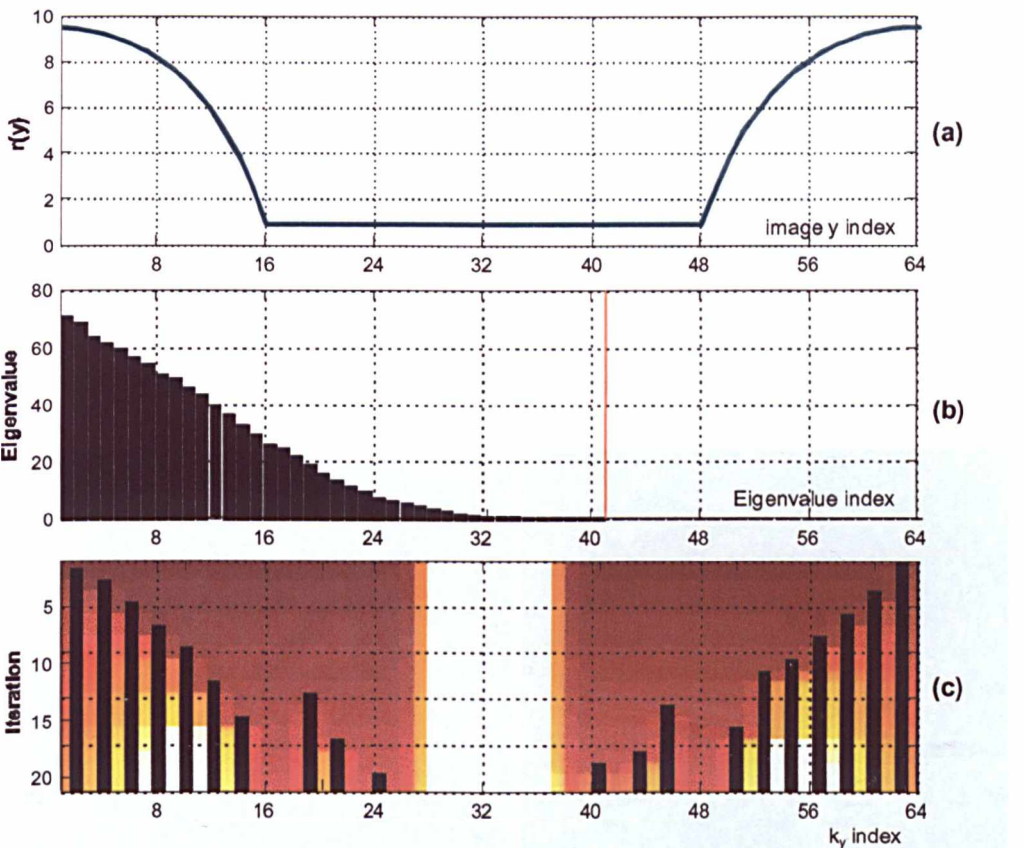


Figure 4.3 (a) The applied resolution constraint $r(y)$, and (b) the corresponding distribution of eigenvalues of the covariance matrix. (c) The selection of near optimal locations of k_y phase encoding steps using the sequential back selection algorithm. In (c), the deleted encoding steps are represented as black strips. [Image courtesy of Prof. GZ Yang]

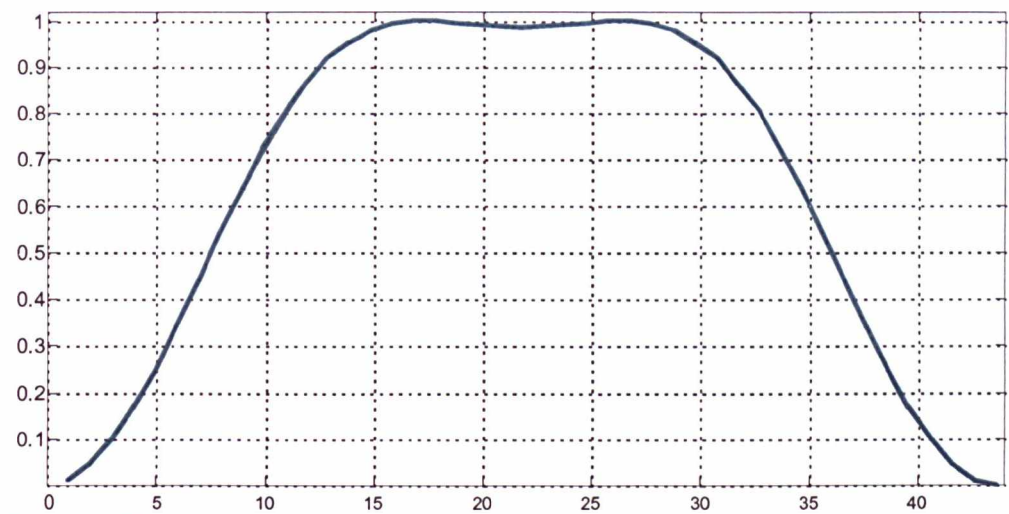


Figure 4.4 The normalised weighting function conforming to the spatial constraint prescribed by Figure 4.3. The horizontal axis denotes the k_y line to be acquired and the vertical axis the value of the weighting function. [Image courtesy of Prof GZ Yang.]

Another related algorithm is that developed by Sinkus and Bonert¹³¹. They used a tailored acceptance window that progressively increases in size in a defined manner to the edge of k-space. In most of the techniques developed so far, navigators are generally placed at end-expiration, as illustrated in Figure 4.5(b), as this is sustained for longer and thus increases scan efficiency and image resolution.

4.2.3 CSPAMM Sequence with Navigator Echoes

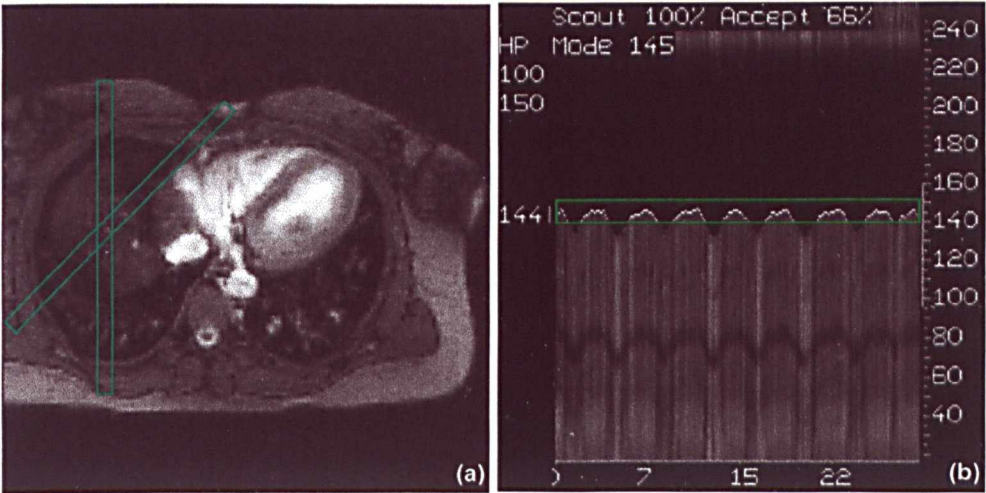


Figure 4.5 (a) The navigators are positioned on the dome of the diaphragm using a transverse slice of the heart. (b) A scout scan shows the respiratory motion of the diaphragm which can be used to gate the imaging. The green box is the acceptance window used for the scan. End-expiration is at the crests while end-inspiration is the troughs in the waveform.

For the proposed HARP imaging of myocardial contractility, a CSPAMM sequence developed for single-breath-hold imaging was used to incorporate navigator echoes. A 90° - 180° navigator echo pulse with a column size of $10 \times 10 \text{ mm}^2$ was used to sample the movement of the dome of the right hemi-diaphragm. A gating window of $\pm 4 \text{ mm}$ and $\pm 2.5 \text{ mm}$ was used for the end-expiratory and end-inspiratory gating respectively. Prospective navigator echoes were used, so they were only applied at the beginning of each cardiac cycle with a simple accept/reject algorithm. The timing diagram for the sequence is shown in Figure 4.6.

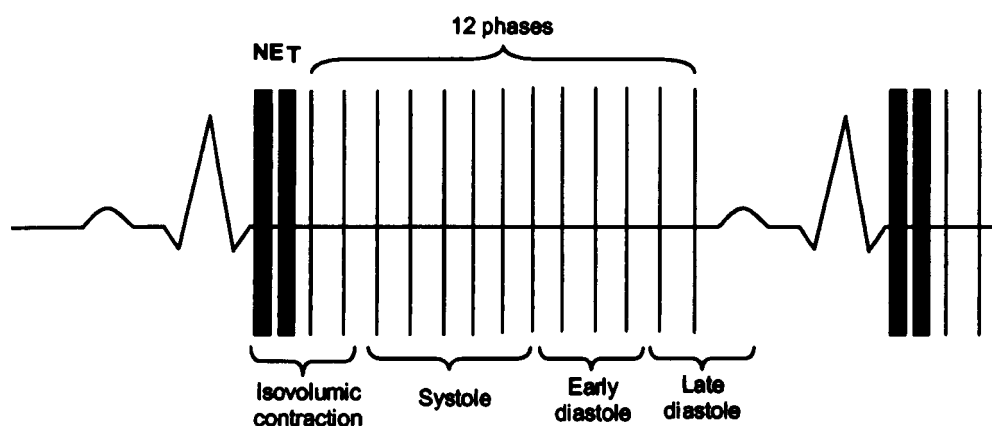


Figure 4.6 This diagram shows the timing of the navigators. The navigator echoes, NE, are played out right after the R-wave, followed by the tagging pulse, T. The imaging sequence then follows, typically 12 phases are acquired but this varies according to the subject's heart rate.

Unless otherwise stated, all MR data for this thesis was acquired on a Siemens Sonata 1.5T system with a peak slew rate of 200 mT/m/s and peak amplitude of 40 mT/m . A segmented FLASH sequence was used to acquire the CSPAMM data with a segment size of 8 k -line encodings. A TR of 52 ms , flip angle of 20° , image matrix of 256×64 , field-of-view of $300 \times 300 \text{ mm}^2$ and a slice thickness of 8 mm were used to obtain a cine sequence of 12 image frames. The phase encode direction was switched according to the tag direction as in the breath-hold sequence.

A study designed to compare the effect of free-breathing on strain measurements was carried out. A comparison between free-breathing and breath-held acquisition is needed to assess the physiological relevance of the strain data. Breath-holding is not a normal physiological condition and thus it is expected that there will be changes to regional myocardial contractility during breath-holding.

4.2.4 *In Vivo* Imaging Protocol

Five normal subjects were recruited for this study with informed consent. The same mid-ventricular short axis slice was imaged three times for each subject, using a single breath-hold at end-expiration, free-breathing with respiratory gating at end-inspiration and end-expiration. A complete CSPAMM data set was acquired with $+90^\circ$, $+90^\circ$ and $+90^\circ$, -90° vertical and horizontal tagging pulses. A gating window of $\pm 4\text{mm}$ and $\pm 2.5\text{mm}$ was used for the expiratory and inspiratory gating respectively. By using the breath-hold data as the baseline measurement, the percentage changes in strain due to respiratory motion were measured.

The imaging protocol for a clinical study consisted of acquisition of 3 short axis slices and two long axis slices: basal, mid-ventricular and apical short axis and vertical long axis (two chamber) and horizontal long axis (four chamber). Figure 4.7 illustrates the imaging protocol used to find the long axis and short axis views. Acquisition of a complete 3D LV volume was not feasible in clinical studies as it would require acquisition of about 10 short axis slices when patient time inside the scanner is limited. Hence, only the four chamber and two chamber long axis views, and basal mid-ventricular and apical short axis views were acquired resulting in just 5 slices being imaged as shown in Figure 4.8. This imaging protocol allowed study of the radial, circumferential and longitudinal myocardial motion. Thus, an assessment of 3D myocardial motion could be made.

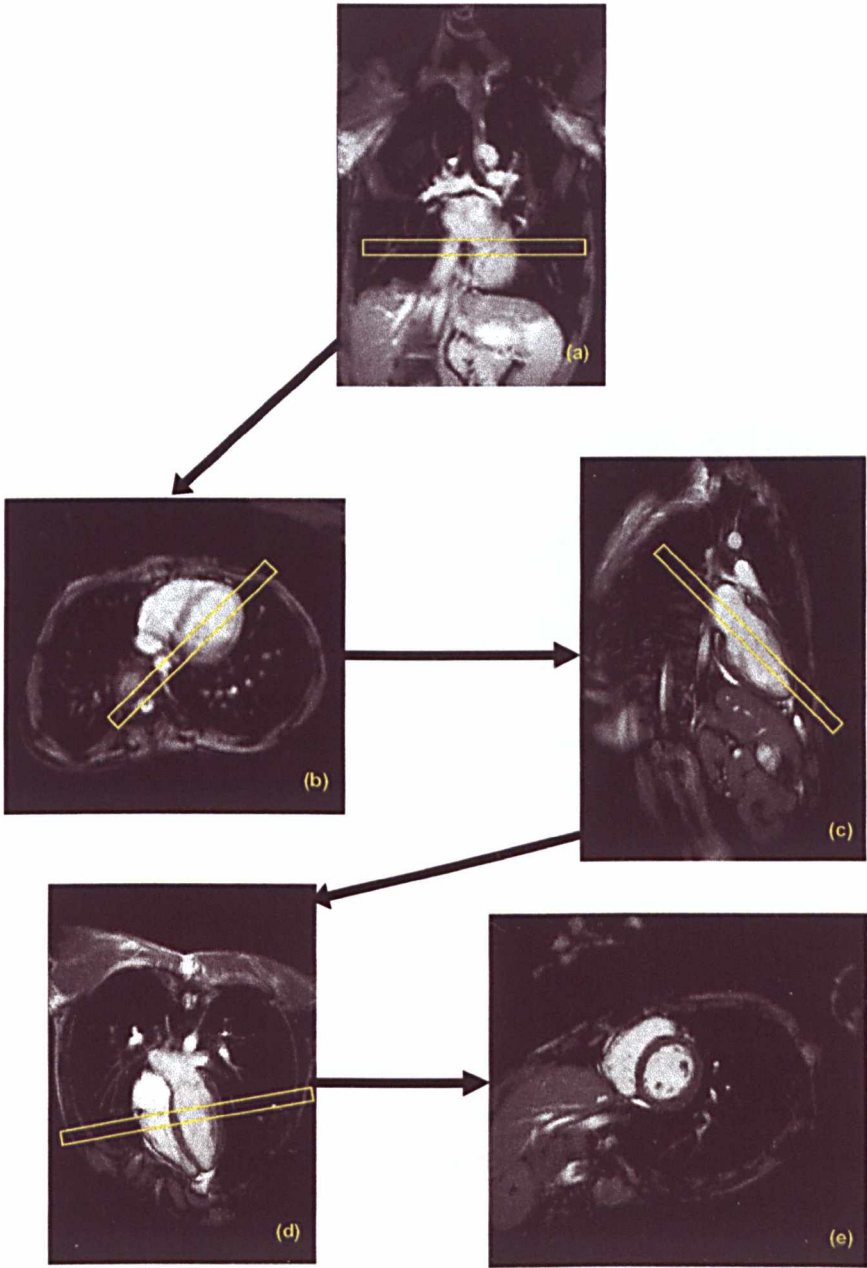


Figure 4.7 Piloting protocol for obtaining (c) the vertical long axis (two chamber view) and (d) the horizontal long axis (four chamber view) and subsequently (e) the short axis view. (a) A coronal image of the whole body is acquired followed by (b) a transverse cut through the heart, this is used to obtain the (c) vertical long axis and the subsequent views are piloted from there.

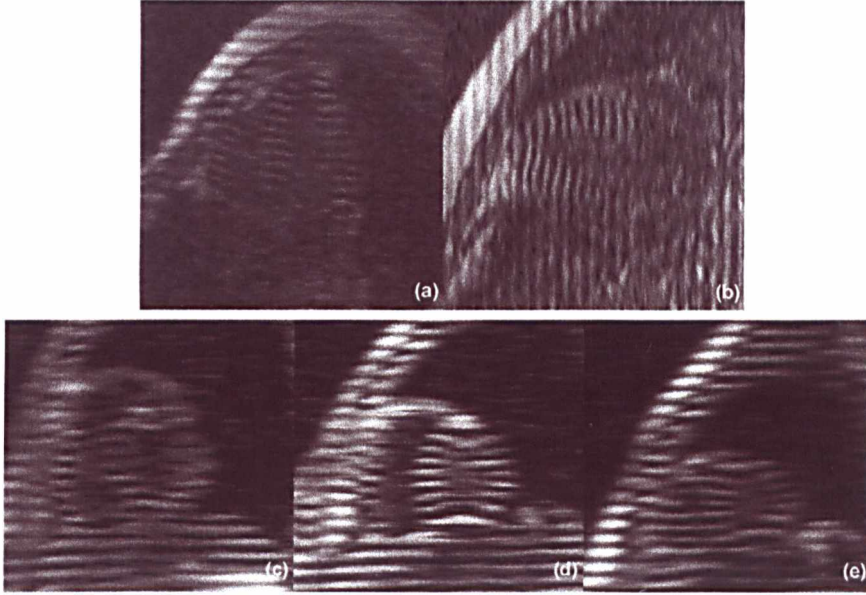


Figure 4.8 Imaging protocol used when acquiring images in a clinical setting. (a) Four chamber view, (b) 2 chamber view, (c) (d) and (e) basal, mid-ventricular and apical short axis images of the heart. For (a) and (b), only the horizontal tagged images are acquired while for (c-e) both horizontal and vertical tagged images are acquired.

4.2.5 Calculating Strain and Velocity using HARP processing

HARP processing utilises the phase of the tags to extract the myocardial motion¹³². Hence, care has to be taken to store the complex signal from the scanner and not just the reconstructed magnitude images. The phase data is used for calculating the strain and velocity while the magnitude images can be used to segment the myocardium. The principle is that as the tags move, they carry their phase with them, hence changing the phase slope within the spectral peak. This change in phase slope can be used directly to calculate the instantaneous strain. The velocity of the myocardium can also be estimated using an optical flow technique on the harmonic phase images.

Velocity and strain can be calculated from HARP images using the fact that as a material point moves, it carries its phase, Φ , with it⁸³. To calculate the velocity for any material point, \bar{y} , the following assumption is made:

$$\frac{d\Phi(\bar{y}, t)}{dt} = 0. \quad (4.1)$$

This can be rewritten using the chain rule:

$$\frac{\partial \Phi(\bar{y}, t)}{\partial \bar{y}} \underbrace{\frac{d\bar{y}}{dt}}_{u(\bar{y}, t)} + \frac{\partial \Phi(\bar{y}, t)}{\partial t} \frac{\partial t}{\partial t} = 0 \quad (4.2)$$

So the velocity can be written in terms of the harmonic phase:

$$u(y, t) = - \left[\frac{\partial \Phi(\bar{y}, t)}{\partial \bar{y}} \right]^{-1} \frac{\partial \Phi(\bar{y}, t)}{\partial t} \quad (4.3)$$

We do not have Φ_k , where the subscript k denotes the direction of the tags, rather we have the wrapped version of the phase, a_k . In the case that the time difference between successive images is sufficiently small we can assume the phase difference to be in the range $[-\pi, \pi]$.

$$|\Phi(y, t_{n+1}) - \Phi(\bar{y}, t_n)| < \pi \quad (4.4)$$

Therefore, the partial time derivative of the phase is approximately equal to the wrapped difference of the wrapped phase. It can be shown that the wrapping function W maps the difference of the wrapped phases back onto the real phase difference $\Delta\Phi$.

So Equation (4.3) can be turned into its discrete form, which can be solved using the harmonic phase information as follows:

$$\frac{\partial \Phi(y, t_n)}{\partial t} \approx \frac{1}{\Delta t} W[a(y, t_{n+1}) - a(y, t_n)] \quad (4.5)$$

$$u(y, t_n) = - \frac{1}{\Delta t} \nabla^* a^{-1}(y, t_n) W[a(y, t_{n+1}) - a(y, t_n)] \quad (4.6)$$

where

$$a = W(\Phi) = \arctan\left(\frac{\text{imag}(I)}{\text{real}(I)}\right) \quad (4.7)$$

and the $*$ denotes the unwrapped version of a .

W is the wrapping function given by:

$$W(\varphi) = \text{mod}(\varphi + \pi, 2\pi) - \pi \quad (4.8)$$

The strain tensor can be obtained using the changes in phase slope that occur as the tags move.

$$F = \begin{bmatrix} \frac{\partial x}{\partial x_0} & \frac{\partial x}{\partial y_0} \\ \frac{\partial y}{\partial x_0} & \frac{\partial y}{\partial y_0} \end{bmatrix} = \left[\frac{1}{k_{10}} \nabla \phi_{11}, \frac{1}{k_{20}} \nabla \phi_{21} \right]^{-T} \quad (4.9)$$

For modulation with equal frequency in vertical and horizontal directions, $k_{10}=k_{20}=k_l$ giving

$$F = k_1(\nabla^* a)^{-1}$$

where F is the deformation gradient tensor and $\nabla\Phi$ is related to the wrapped phase $\nabla^* a$ as follows:

$$\nabla\Phi = \nabla^* a = \begin{bmatrix} \nabla a_1 \\ \nabla a_2 \end{bmatrix} \quad (4.10)$$

$$\nabla^* a = \begin{cases} \nabla a & \|\nabla a\| \leq \|\nabla W(a + \pi)\| \\ \nabla W(a + \pi) & \text{otherwise} \end{cases} \quad (4.11)$$

To obtain the Eulerian strain the deformation tensor has to be decomposed into the rigid-body rotation, R , and the stretch tensor, U .

$$F = RU$$

$$F = \begin{bmatrix} a & b \\ c & d \end{bmatrix} = \underbrace{\begin{bmatrix} \cos(\theta) & \sin(\theta) \\ -\sin(\theta) & \cos(\theta) \end{bmatrix}}_R \cdot \underbrace{\begin{bmatrix} t_x & t_{xy} \\ t_{yx} & t_y \end{bmatrix}}_U \quad (4.12)$$

The strain tensor can now be calculated from the deformation tensor as follows:

$$E = U - I = \begin{bmatrix} t_x - 1 & t_{xy} \\ t_{yx} & t_y - 1 \end{bmatrix} \quad (4.13)$$

The eigenvalues of the strain tensor indicate stretching, positive values, or shortening, negative values. Their corresponding eigenvectors indicate the direction the strain is acting in. The two eigenvectors are always orthogonal to each other. In the cardiac case, this usually implies radial thickening coupled with circumferential shortening or vice versa.

Strain and velocity can thus be calculated within seconds after image acquisition using HARP imaging. Full details of this processing and the in-house software developed are described in Appendix III.

4.2.6 Velocity Vector Field Restoration

De-noising and restoration of the in-plane velocity fields calculated using HARP was carried out using a vector restoration method. The method restores the vector direction without affecting the velocity magnitude. The technique used here for vector restoration is based on Chan and Shen's theoretical model¹³³. This framework provides a systematic way for constructing the energy function, which is an extension of the classical total variational (TV) model¹³⁴⁻¹³⁶. The method used here was first developed by Ng and Yang¹³⁷ for CMR velocity images.

If \vec{u}_0 denotes the direction field of the noisy velocity images, \vec{u} denotes the clean direction field we want to restore the velocity to, where $\vec{u}_0 = \vec{u} + \vec{n}$, \vec{n} being the additive noise. Assuming the variance of the noise \vec{n} is σ^2 and that its value is known, the restoration of the direction field of a velocity field can be formulated as a constrained optimisation problem by minimising the following term

$$E^{TV}(\vec{u}) = \int_{\Omega} e(\vec{u}; \alpha) \quad (4.14)$$

subject to the constraint $h(\vec{u})$:

$$h(\vec{u}) = \frac{1}{2} \left(\int_{\Omega} (\vec{u} - \vec{u}_0)^2 - |\Omega| \sigma^2 \right) = 0 \quad (4.15)$$

where E^{TV} denotes the total variation (TV) energy of the whole image, $e(\vec{u}; \alpha)$ denotes the energy at pixel α , Ω denotes the image domain and $|\Omega|$ the size of the image domain.

The strength function $e(\vec{u}; \alpha)$ at voxel α can be defined as:

$$e(\vec{u}; \alpha) = \left[\sum_{\beta \in N_{\alpha}} d_i^2(\vec{u}_{\beta}, \vec{u}_{\alpha}) \right]^{\frac{1}{2}} \quad (4.16)$$

where N_{α} denotes the neighbourhood of pixel α , d_i denotes the embedded Euclidean distance in S^2 . This reduces the problem to a constrained optimisation problem, which is further simplified to a relatively simple iterative scheme as follows:

$$\begin{aligned} u_{\alpha}^{n+1} &= u_{\alpha}^n + \Delta t \cdot \prod_{u_{\alpha}} \left[\sum_{\beta \in N_{\alpha}} w_{\alpha}^{\beta} u_{\beta} + \lambda^n u_{\alpha}^0 \right] \\ \lambda^{n+1} &= \lambda^n + \Delta t \cdot \frac{1}{2} \left[\sum_{\alpha \in \Omega} d_i^2(u_{\alpha}, u_{\alpha}^0) - |\Omega| \sigma^2 \right] \end{aligned} \quad (4.17)$$

where

$$w_{\alpha}^{\beta} = \left(\frac{1}{e(u; \alpha)} + \frac{1}{e(u; \beta)} \right) \quad (4.18)$$

u is the velocity vector to be calculated, λ is the regularisation parameter and w_{α}^{β} is the weighting term for each adjacent pixel. Using this iterative scheme the restored velocity fields can be calculated within seconds even for a large number of iterations. The limitation of this technique is that it can only be used for two-dimensional vectors. It also does not affect the magnitude of the pixel and does not take into account the magnitude of the surrounding pixels. A simple median filter can be used to make sure the magnitudes of the noisy pixels are also restored. Figure 4.9 shows the effectiveness of the vector restoration algorithm on a

synthetic dataset, and the convergence behaviour over iterations. It has been shown that the restored velocity field is much more consistent without losing any critical features of the original velocity field.

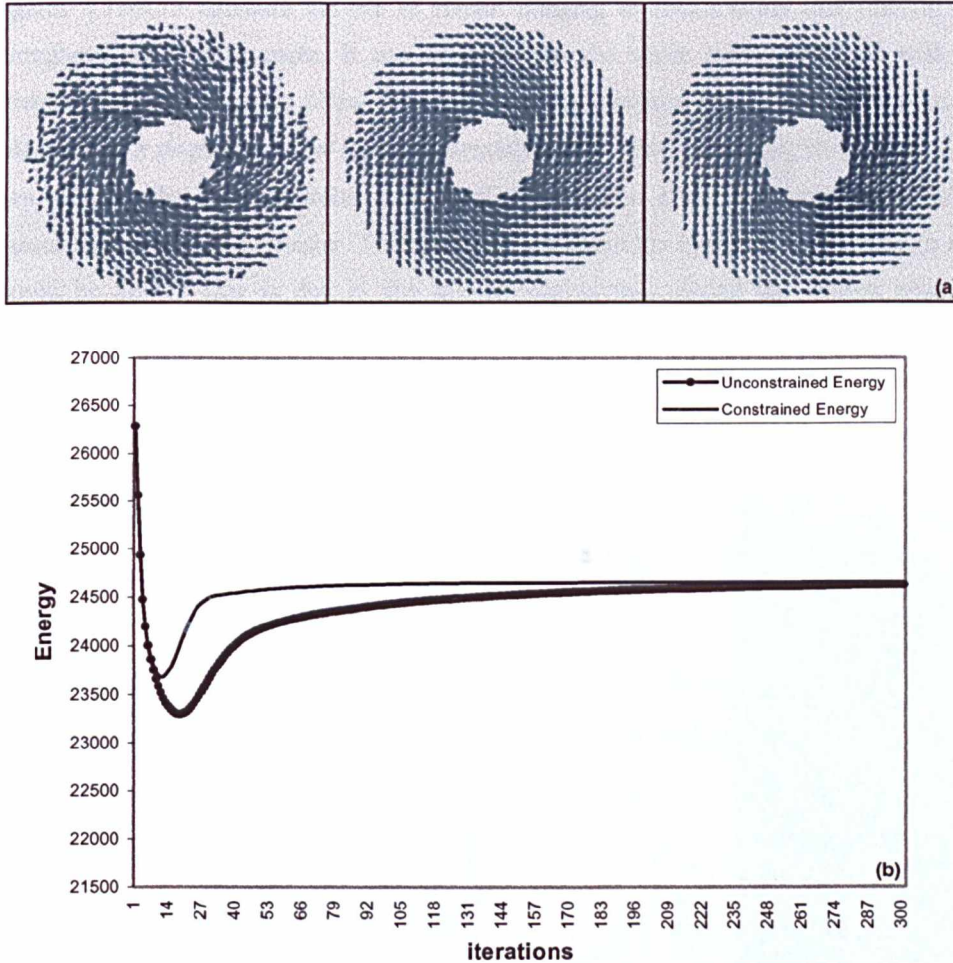


Figure 4.9 The effectiveness of the vector restoration algorithm. (a) From left to right, original noisy dataset with 50% noise, restored vector map and original dataset without noise for comparison. (b) The convergence of the energy terms against number of iterations. The minimum energy is reached in around 10 iterations.

4.3 *In Vivo* Strain and Velocity Measurements using HARP Imaging

The CSPAMM sequence has been used to acquire data on normal and symptomatic subjects. Some examples of the strain and velocity maps obtained are illustrated in Figure 4.11–4.17. It was found that CSPAMM tagging, as opposed to SPAMM tagging significantly reduced the artefacts found in the HARP strain maps. This is due to the fact that the signal from the

central peak can interfere with the spectral peaks, especially in the later phases of the cardiac cycle due to tag fading as can be seen in Figure 4.10.

Figures 4.11–4.17 illustrate the use of HARP imaging to obtain strain and velocity maps throughout the cardiac cycle. It can be seen that the strain maps combined with their corresponding eigenvectors allow fast and easy visualisation of myocardial motion. The velocity vector maps also allow easy representation of myocardial motion. However, it can be seen that in the later diastolic frames of the cardiac cycle, the strain and velocity measurements tend to be noisier. The velocity wrap around in Figure 4.16 and 4.17 (h and i) should be noted. This is due to the overlapping of tags during the frames where the myocardial tissue is moving quite quickly. The optical flow technique used to calculate velocity is unable to cope with this causing wrap-around in the velocity range. The velocity scale is chosen arbitrarily and is directly proportional to the tag spacing.

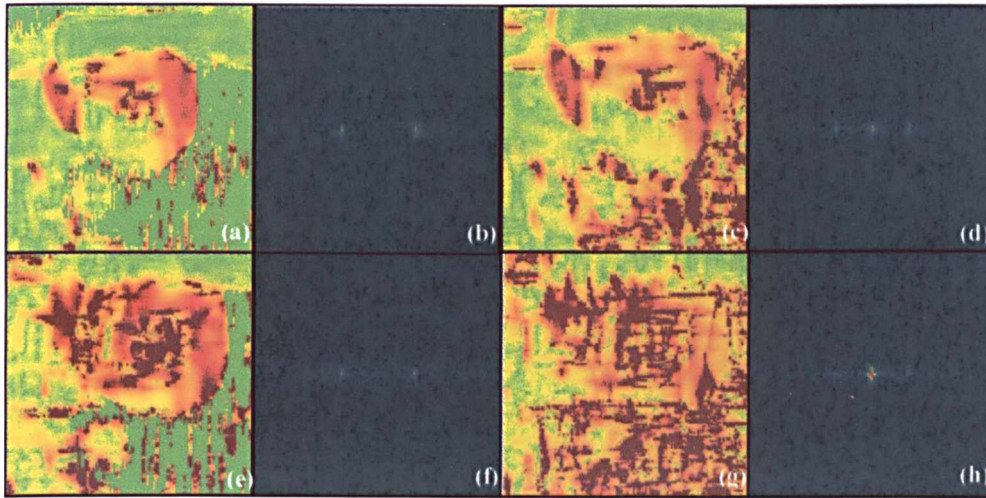


Figure 4.10 Velocity magnitude maps obtained using (a) and (e) CSPAMM and (c) and (g) SPAMM for frames 2 and 9 respectively, *i.e.*, near the beginning and end of the cardiac cycle. As can be seen from the *k-space* representation of the original images (b,d,f,h), the central peak is enhanced in the SPAMM images causing considerable artefact in the HARP velocity images especially in the later frames of the cardiac cycle.

Figure 4.11 Maximum principal strain maps in a mid-ventricular slice in a normal volunteer throughout the cardiac cycle. A positive value of strain indicates thickening of which, as can be seen from Figure 4.12, occurs in the radial direction.

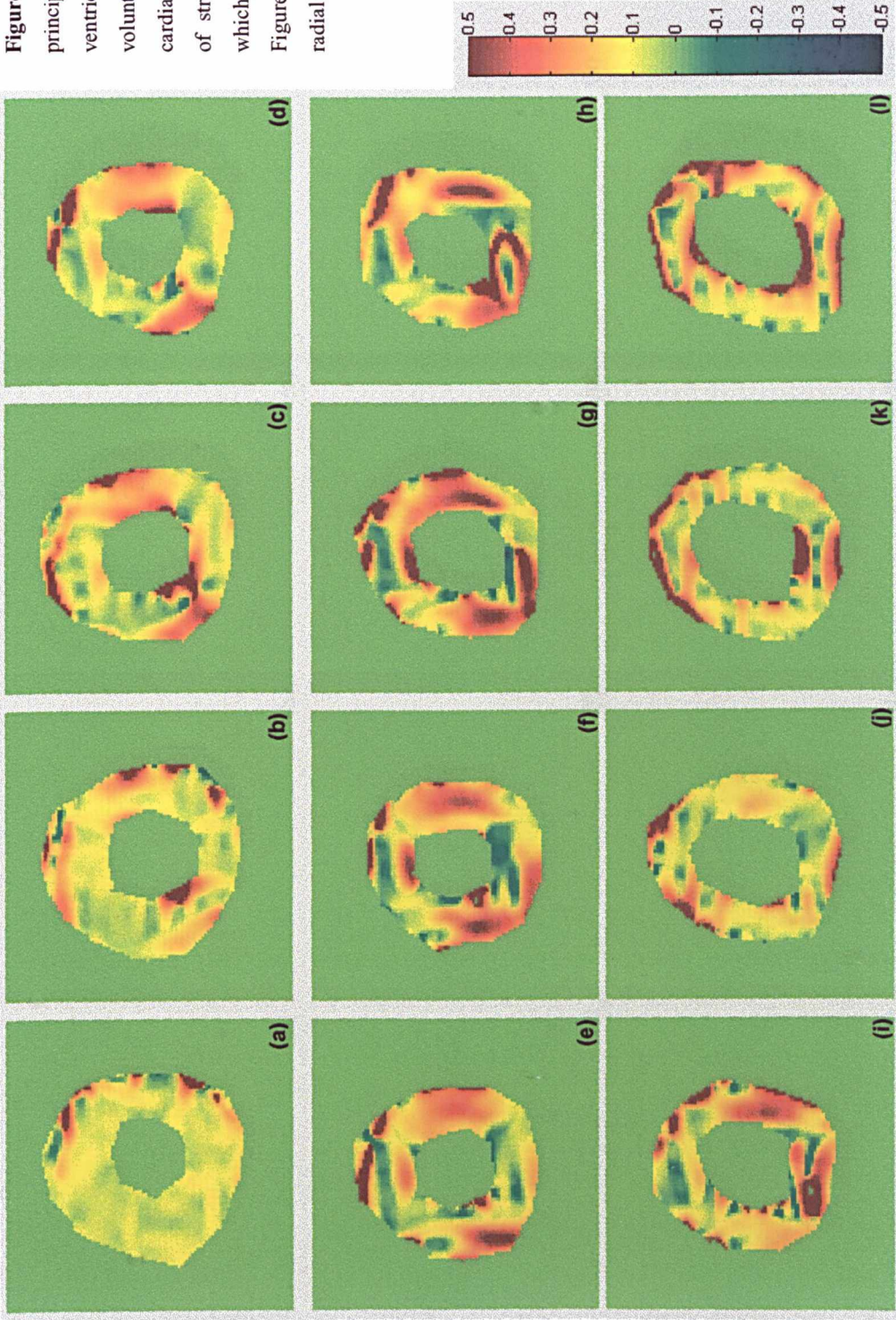


Figure 4.12 Eigenvector corresponding to the maximum principal strain maps shown in Figure 4.11.

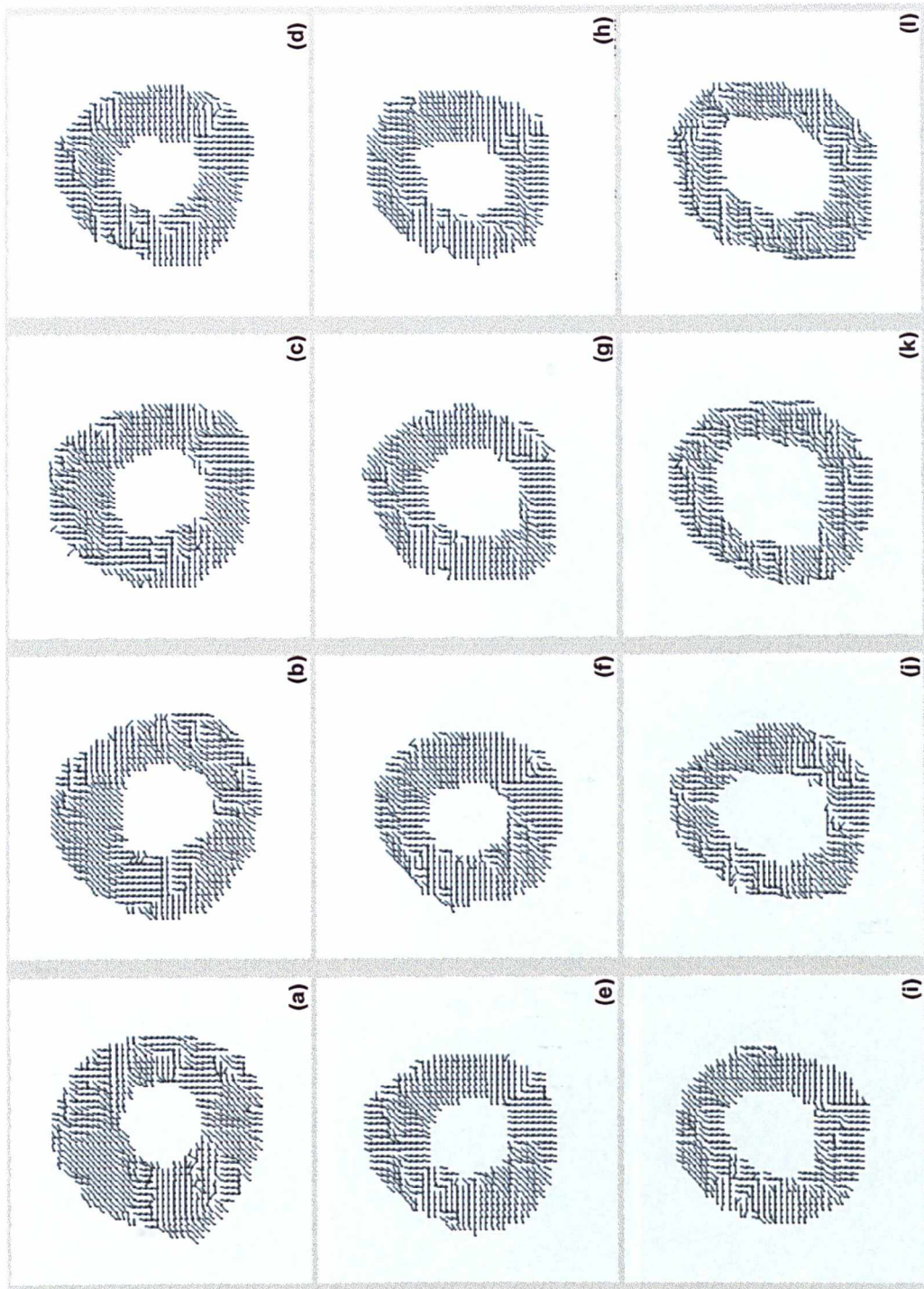


Figure 4.13 Minimum principal strain maps at a mid-ventricular slice in a normal volunteer. The negative values indicate circumferential shortening during systole.

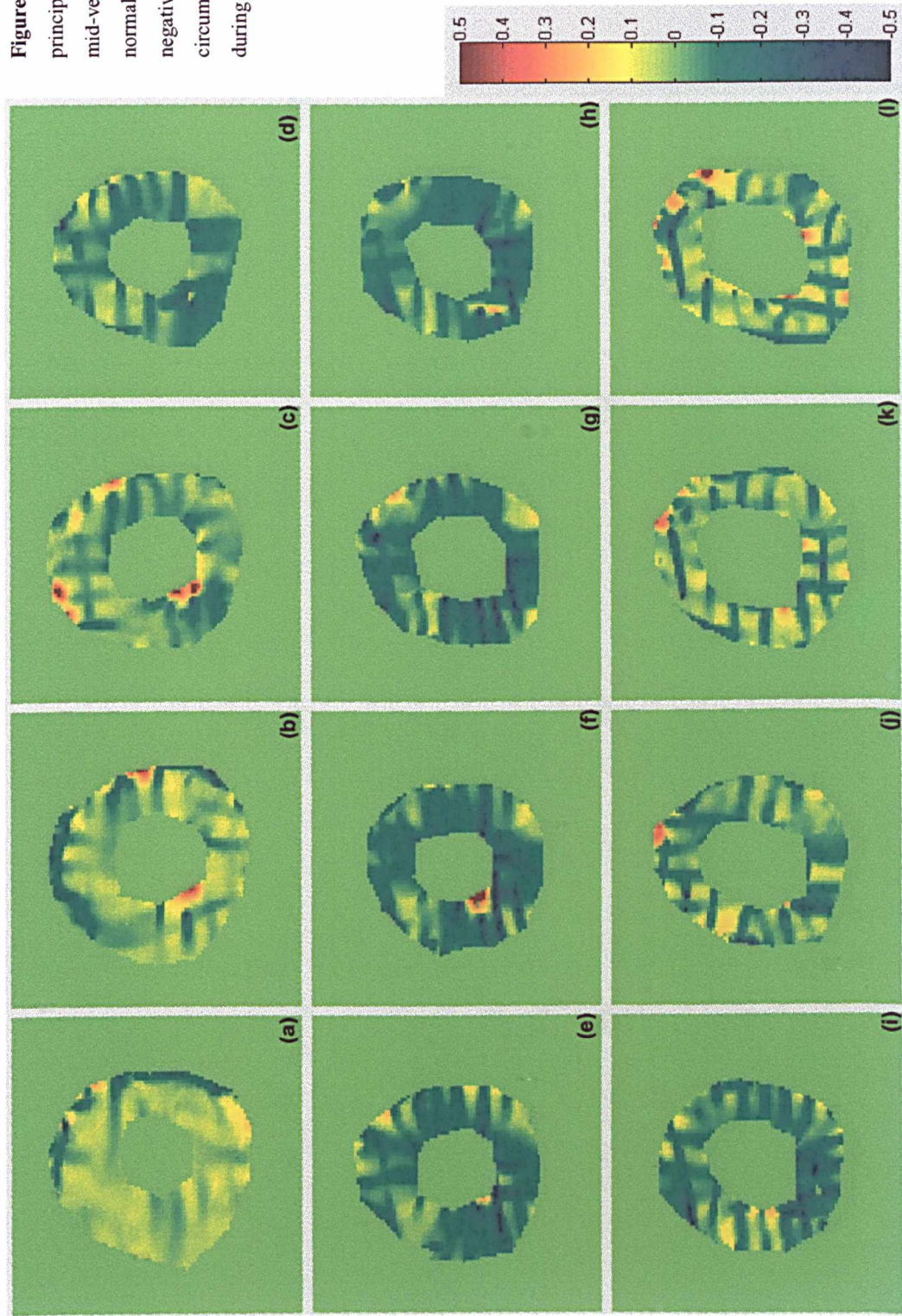


Figure 4.14 Eigenvector corresponding to minimum principal strain maps shown in Figure 4.13. It can be seen that this acts primarily in a circumferential direction throughout the cardiac cycle.

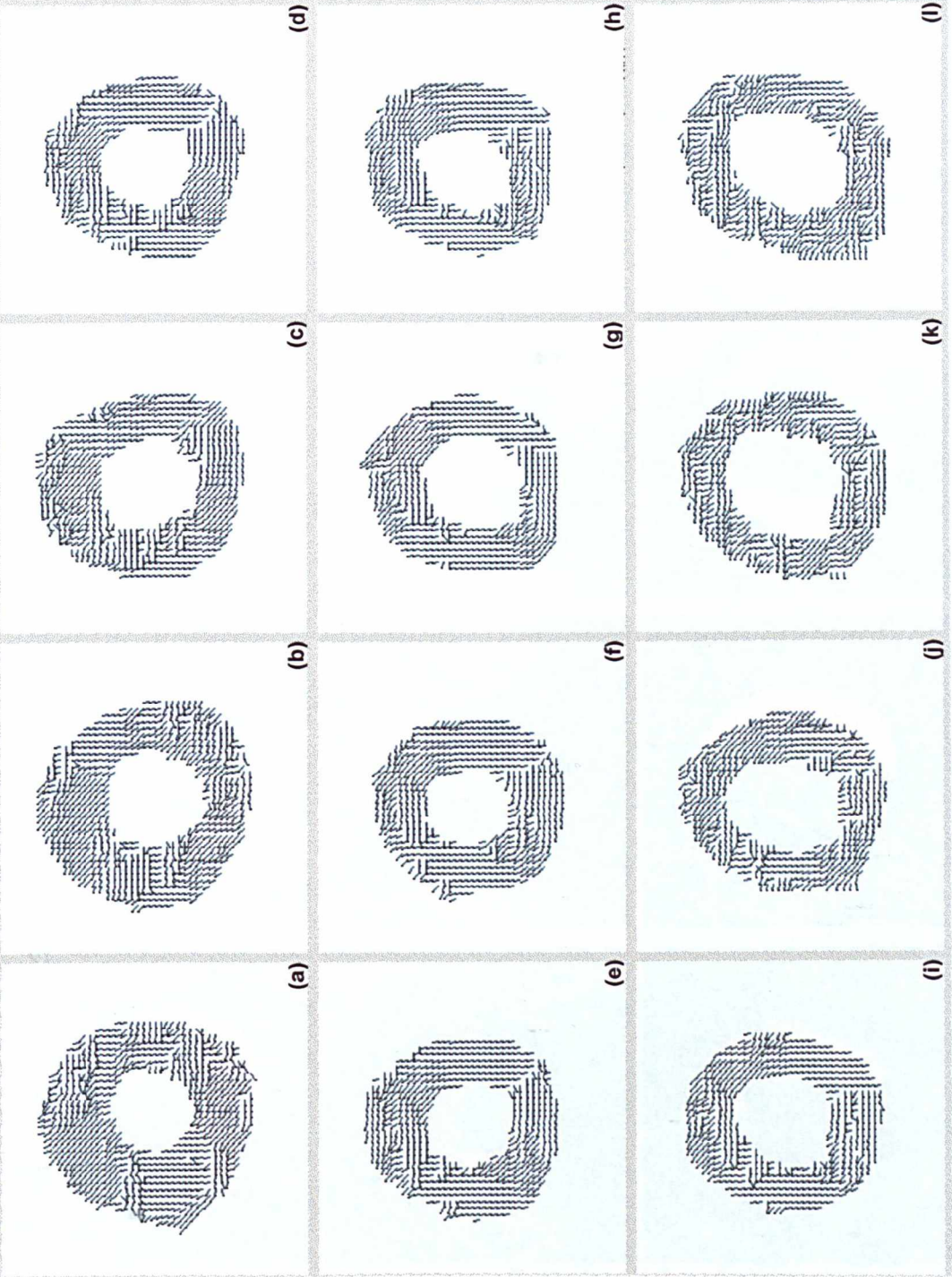


Figure 4.15 Colour map showing v_x in normal subject at the same mid-ventricular slice. The pattern in diastole (i and j) can be seen to oppose that in systole (a and b).

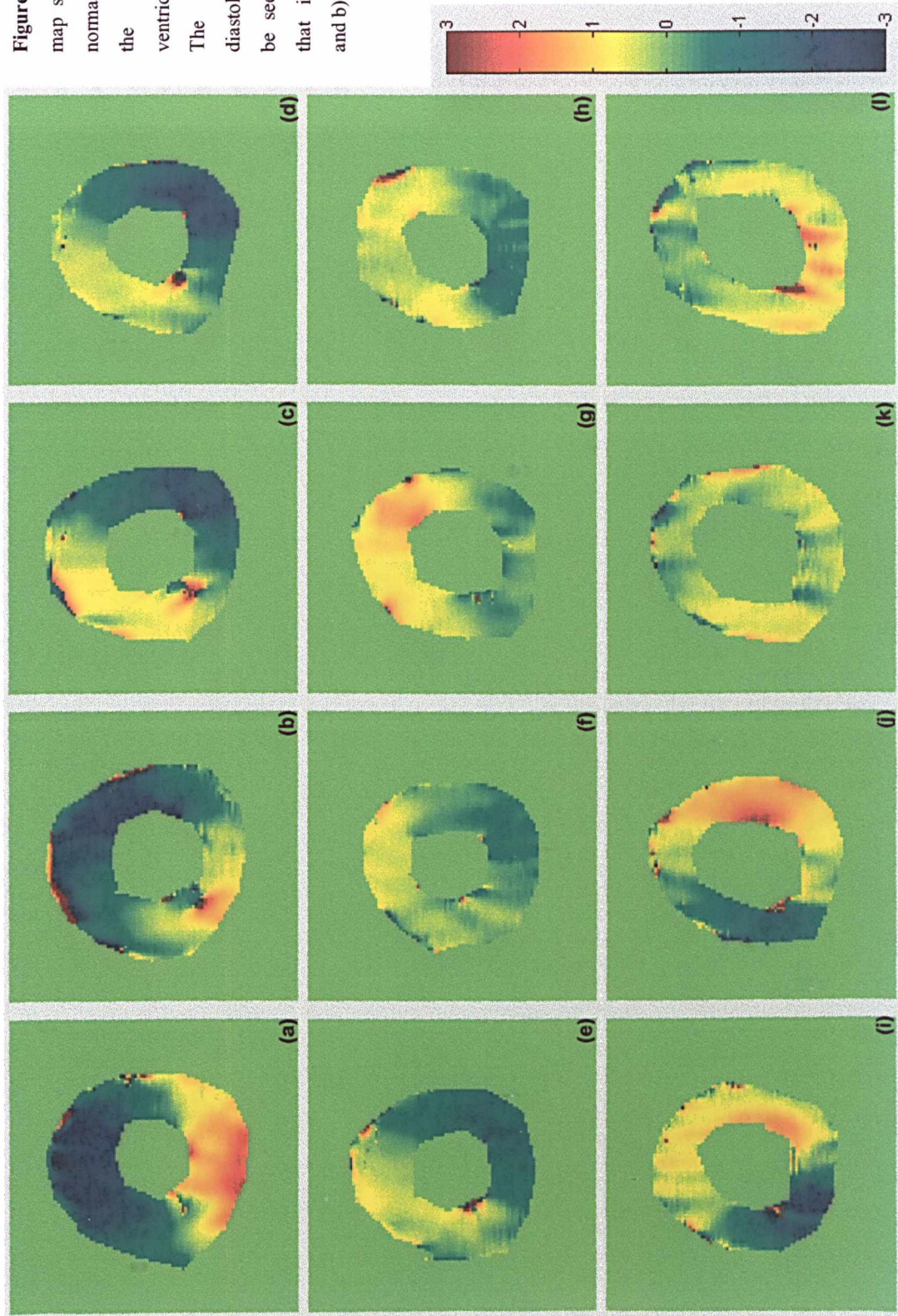


Figure 4.16 Colour map showing v_y in normal subject at the same mid-ventricular slice. Some wrap-around in the velocity range can be seen in (h) and (i). This is confirmed by looking at the vector maps in Figure 4.17.

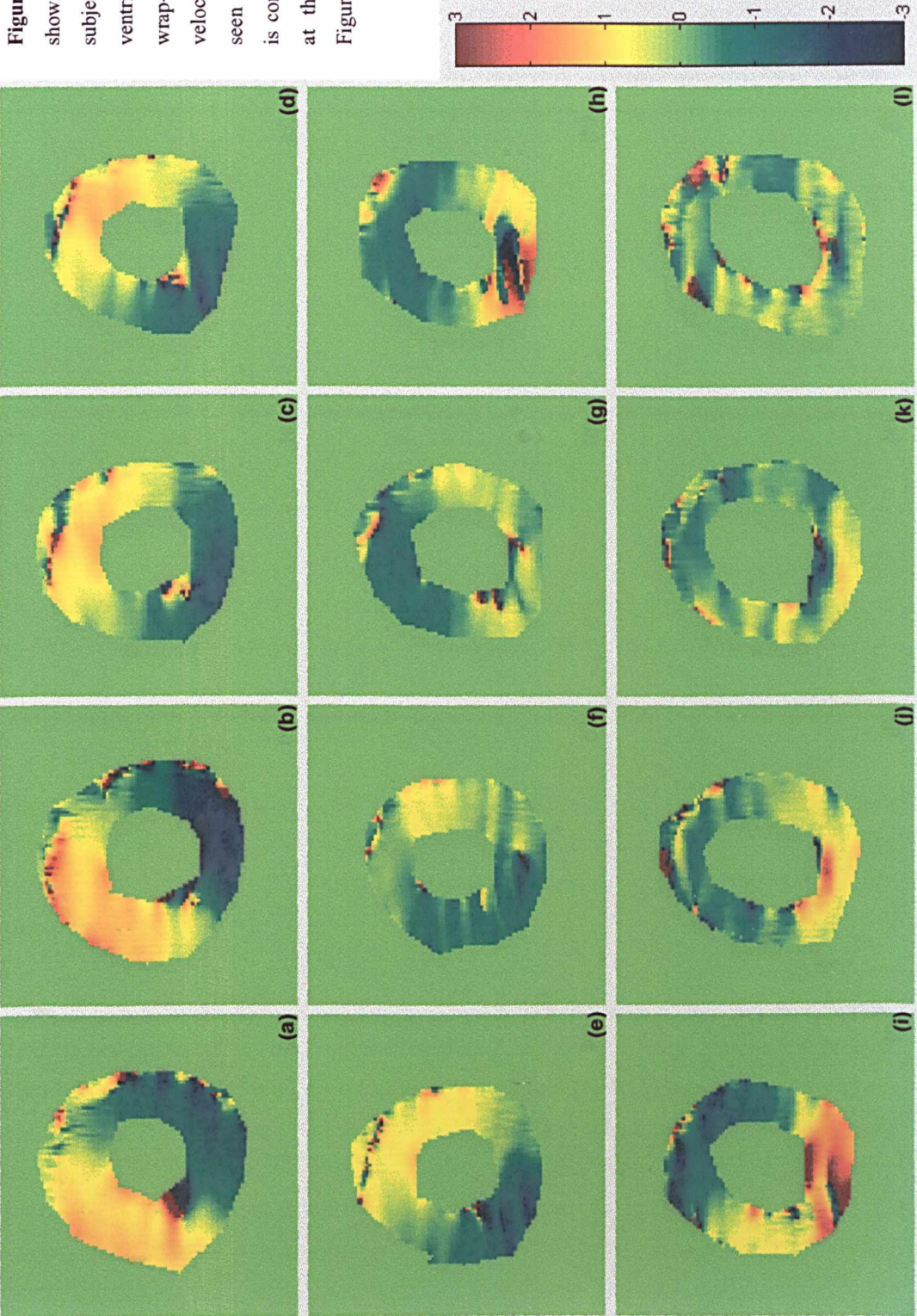
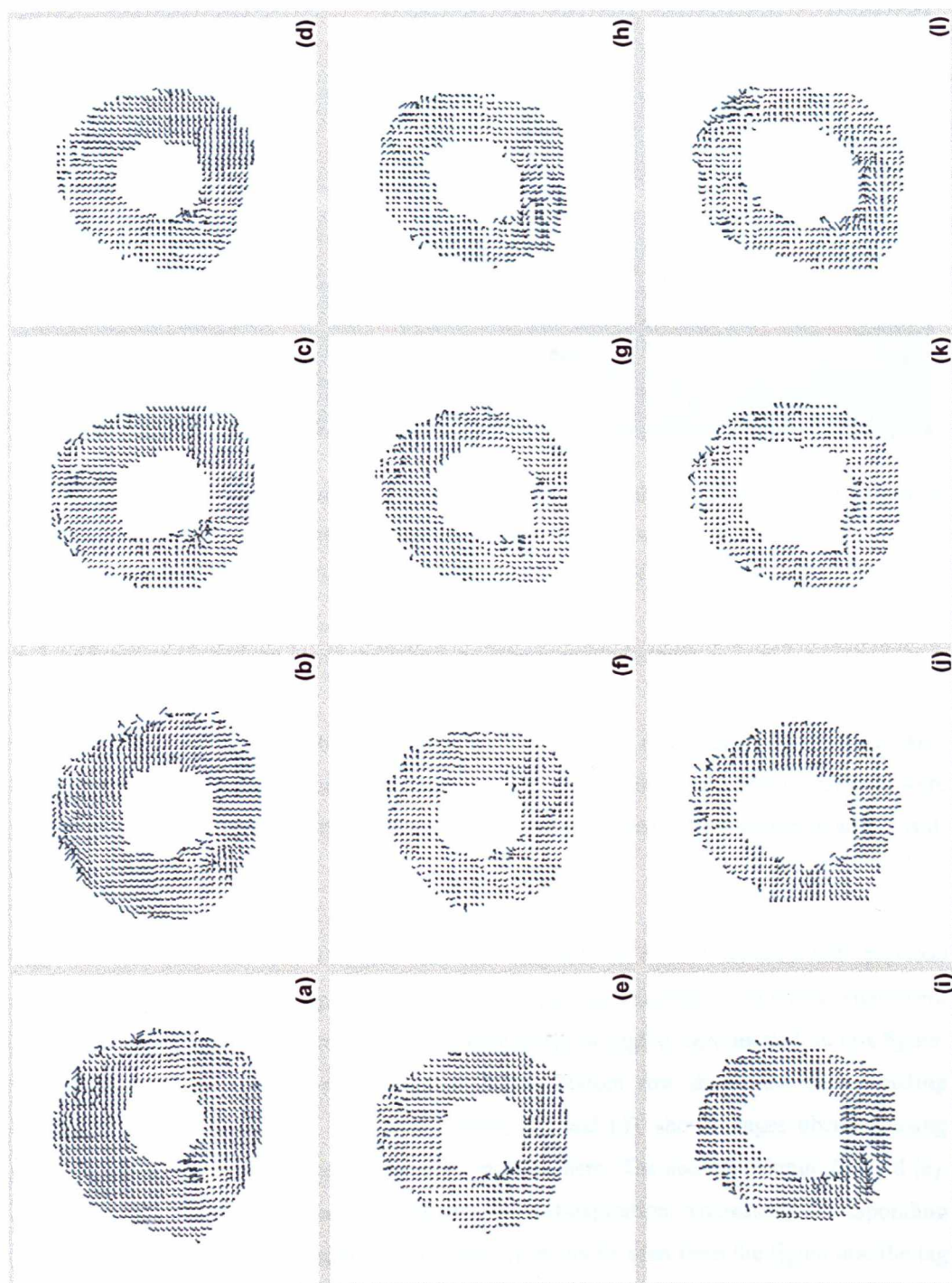


Figure 4.17 Velocity vector map combining Figures 4.15 and 4.16. The pattern of torsion described by other researchers can be seen.



The framework also allowed analysis of longitudinal strain. Only the shortening was measured rather than both directions of in-plane motion. This allowed the image matrix to be increased to 256x64 while keeping the breath-hold to 16 cardiac cycles. Figure 4.18 shows examples of longitudinal strain at diastole and systole in the four-chamber and two-chamber views.

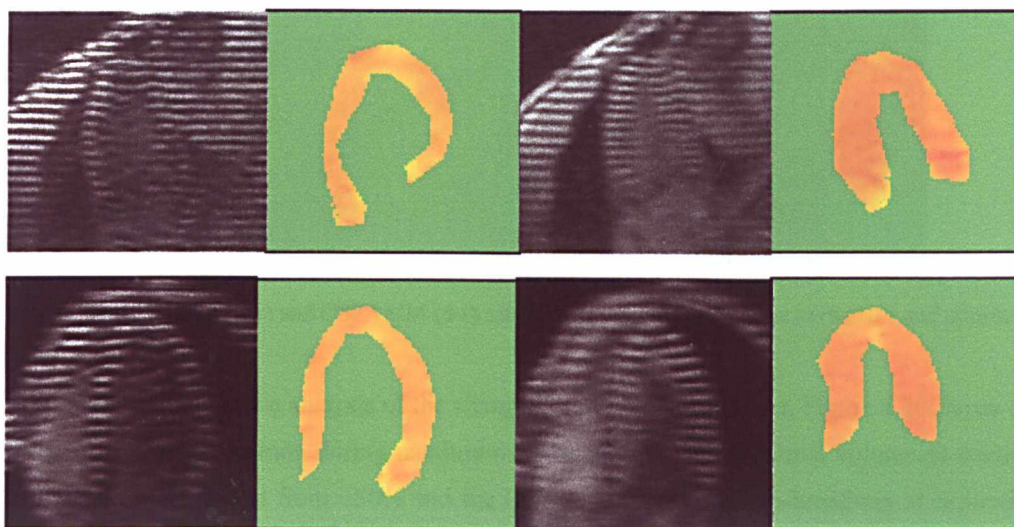


Figure 4.18 Longitudinal shortening in a normal volunteer. Top row shows the two-chamber, or vertical long axis, view showing the posterior and anterior walls at diastole and systole. Bottom row is the four-chamber, or horizontal long axis, view showing the lateral and septal walls at diastole and systole.

4.3.1 Effect of Variation in Respiration on Myocardial Strain

Breath-holding can introduce changes in myocardial strain that as yet remain unexplored. As a preliminary study into the effect of respiration on myocardial strain five normal subjects were imaged at end-expiration and end-inspiration using the respiratory gated sequence and at end-expiratory breath-hold.

Figure 4.19 illustrates SPAMM tagged short axis images of the heart. Consistent with previous findings in coronary imaging, respiratory gating at end-inspiration involves significant respiratory jitter¹³⁸, and therefore the quality of the image is slightly deteriorated. In this figure, the top row shows just one set of tags while the bottom row shows the corresponding subtracted CSPAMM images. The first column, (a) and (d), show images obtained using breath-holding, which is used as the baseline measurement. The second column, (b) and (e), shows images obtained with free breathing gated at end-expiration, whereas the corresponding result for end-inspiration is illustrated in (c) and (f). It can be seen from the figure that the tag

line deformation in each of the three imaging protocols is noticeably different even though the same short axis slice has been acquired each time.

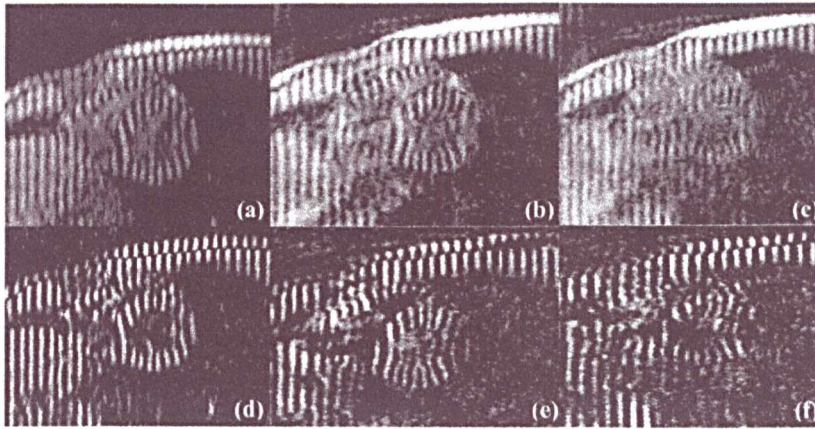


Figure 4.19 SPAMM (a-c) and CSPAMM (d-f) subtraction images of the heart in diastole and systole.

To provide a quantitative analysis of the changes in strain measurement, Figure 4.20 shows the percentage change in strain during maximum contraction for the 5 normal volunteers studied. The y-axis scale ranges from $\pm 50\%$ and the light grey represents free-breathing at expiration and black at inspiration. The calculations were carried out for four separate regions of the heart, (a) septal, (b) posterior, (c) lateral, and (d) anterior segments. The mean and standard deviation, represented in percentile strain changes, for the four segments are 5.2 ± 16.5 , -1.1 ± 14.2 , 4.4 ± 6.1 and 7.0 ± 5.7 at end expiration, and 1.4 ± 5.7 , 5.1 ± 7.7 , 5.9 ± 6.1 , and 19.5 ± 14.0 at end inspiration, respectively. Figure 4.21 illustrates an example of the maximum principal strain maps derived from the different imaging protocols.

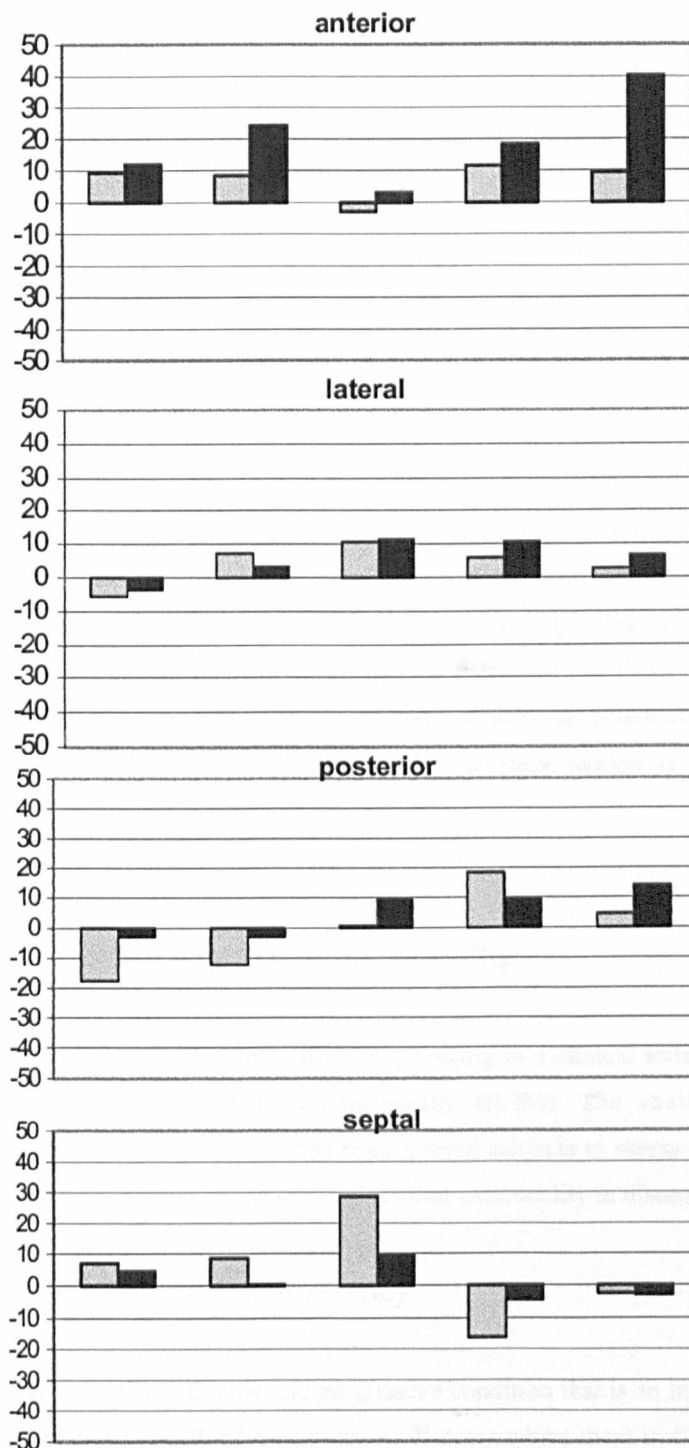


Figure 4.20 Percentage strain in the anterior, lateral, posterior and septal regions in a mid-ventricular short axis slice in five normal subjects at maximum contraction during free-breathing at (grey) end-expiration and (black) end-inspiration.

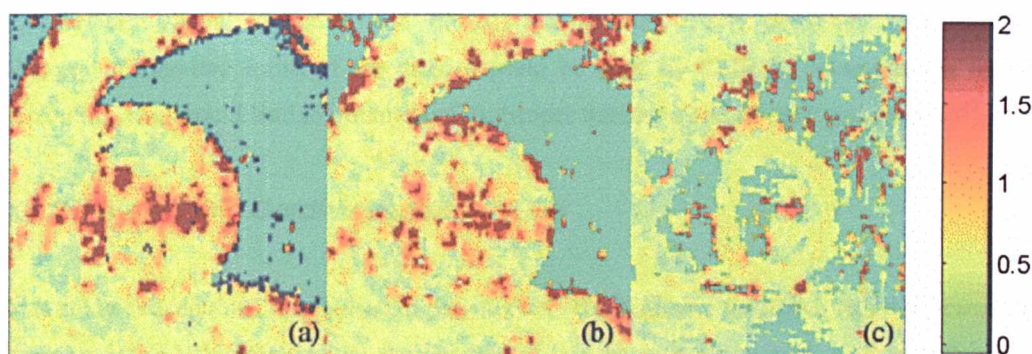


Figure 4.21 Maximum principal strain maps at a mid-ventricular short axis slice in a normal volunteer during free-breathing at (a) end-inspiration, (b) end-expiration and (c) during breath-hold.

It is evident that respiration can have a significant effect on the absolute strain values derived. For the five subjects studied, the changes in strain ranged from -17.4% to 40.0% compared with data calculated from breath-holding. This highlights the importance of using real-time navigator echoes for performing HARP imaging so that physiologically correct strain distributions can be calculated. Existing study also indicates that the effect of respiration on different segments of the myocardium is not uniform, which can potentially interfere with assessment of regional contractile abnormalities if respiratory motion is not consistently monitored.

4.4 Changes in Contractility in Cardiomyopathy

To evaluate the accuracy and robustness of HARP imaging in a clinical setting, we studied a group of patients with hypertrophic cardiomyopathy (HCM). The strain measurements obtained were compared with those obtained from normal subjects to assess the effectiveness of HARP in determining changes in regional myocardial contractility in disease.

4.4.1 Relevance of CMR in Cardiomyopathy

Cardiomyopathy is generally a chronic and progressive condition that is an important cause of morbidity and mortality. It is defined by a group of diseases where there is direct involvement of the muscle in the disease process¹³⁹. CMR is especially well-suited in the diagnosis of cardiomyopathy as it makes no assumptions about the left or right ventricle geometries which can be greatly changed in disease. CMR imaging is accurate and reproducible¹⁴⁰, and static and dynamic images of the anatomy can be obtained allowing evaluation of morphology and function. Specific CMR techniques can also be employed to evaluate infiltrative processes,

myocardial oedema, perfusion, and fibrosis and scarring. Early detection of phenotypic changes in inherited forms of the disease could be done by CMR by incorporating family screening. This would lead to initiation of the proper treatment and a better prognosis.

4.4.2 Hypertrophic Cardiomyopathy (HCM)

This study concentrated on a subset of patients with the genotype for HCM. HCM manifests as inappropriate LV hypertrophy in the absence of any obvious cause such as hypertension or aortic stenosis. Patients with HCM display impaired diastolic function, although myocardial function is usually preserved until late in the disease. Histologically, HCM results in myocyte disarray. An incidence of 1 in 500 is found in the general population. It usually presents as dizziness and shortness of breath, and is the most common cause of sudden death in the young¹⁴¹. A key challenge is to identify the subset of patients in HCM that are at increased risk of sudden cardiac death.

Typically, diagnosis of HCM is made through a combination of echocardiography and abnormal ECG. CMR has considerable advantage over echocardiography, however, as it allows the whole myocardium to be visualised clearly including the epi- and endo-cardial borders, apex and inferior wall whereas with echo the apex can be problematic and the acoustic windows limit the views obtainable. CMR has been found to be ideal for determining phenotype and hence finds application in relative studies for assessing family risk. As can be seen from Figure 4.22 the anatomy of the LV is well delineated using CMR SSFP sequences allowing functional and anatomical indices to be measured accurately.



Figure 4.22 Anatomy of a hypertrophied heart using CMR SSFP imaging. Two chamber, four chamber and mid-ventricular short axis views at peak systole show the myocardium to be abnormally thickened.

CMR features associated with HCM are, depending on the genotype, a heterogeneous pattern of myocardial thickening, increase in end-systolic and end-diastolic wall thickening and an increase in ratio of septal to lateral wall thickening. The overall LV mass can also significantly

increase with dilation of both atria. Using high resolution steady-state free-precession (SSFP) cines and appropriate image processing software, the peak filling rates and time to peak filling rate can be calculated. These are markers of diastolic function and in HCM reveal a restrictive filling pattern due to reduced compliance. Mitral regurgitation and outflow tract obstruction can also be observed using CMR, manifesting as a loss in signal in the jet flow or as a marked difference in velocities using CMR velocity mapping. Abnormal regional contractility with reduced septal wall motion and impaired radial and circumferential strain patterns have also been shown in HCM patients using CMR tagging. Reduced long axis function and increased ventricular torsion has also been observed. Imaging late gadolinium enhancement in the myocardium has displayed patchy and diffuse areas of increased signal intensity. The role of CMR in early detection of phenotypic abnormalities is well-documented, with much interest being shown in tagging and better markers of diastolic dysfunction.

4.4.3 Measuring Contractility in HCM

This study explored early detection in familial HCM. Due to the heterogeneity of clinical presentation, patients in the genotype characterised group were studied. HARP imaging was carried out as part of a thorough CMR exam on subjects to study the phenotypic presentation of the disease. Eight subjects who carried the genotype for troponin mutation were studied, mean age 35 (± 16), 6 male. Five normal subjects were also studied for comparison, mean age 42 (± 11), 4 male. The imaging protocol used was as described in Figure 4.8. The standardised 17 segment model was used to analyse data¹⁴². Basal, mid-ventricular and apical slices HARP data was acquired on all subjects. Vertical and horizontal long axis images were also acquired on all the normals and on the patients when time permitted.

The sequence used to acquire the slices consisted of a segmented FLASH CSPAMM sequence. Image matrix was 256 by 32, slice thickness 8mm, field-of-view 300 to 360mm, depending on the subject. Only 32 phase encode lines were acquired in each tag direction reducing acquisition time to just 16 cardiac cycles for both tag directions. This was found to be a reasonable breath-hold for all subjects.

Data for each subject was used to delineate the epi- and endo-cardial borders manually, as were the segments of the left ventricle. The maximum and minimum principal strain values in the myocardium were averaged for each segment to produce the segmental analysis. The maximum and minimum principal eigenvalues of the strain tensor were used in conjunction with their eigenvectors, rather than the radial and circumferential strains as these were found to be highly dependent on choice of origin of the co-ordinate system. However, using the

corresponding eigenvector direction, we were able to infer whether the strain was acting in a radial or circumferential direction.

4.4.4 Comparison of Hypertrophied to Normal Hearts

Maximum and minimum principal strains at peak systole were measured for each subject. The mean and standard deviation values for normal and HCM patients were plotted for each segment in all three slices, basal, mid-ventricular and apical as shown in Tables 4.1 to 4.4. The longitudinal strain was calculated for all time frames for the five normals. The trend of the strain was found to be similar in all normals and comparable to that found in ultrasound and is shown in Figure 4.29.

Figures 4.23 to 4.25 visually illustrate the results from Tables 4.1 to 4.4. The basal slice showed that the maximum principal strain for the HCM patients was higher throughout the myocardium. In the mid-ventricular slice, the maximum principal strain was lower in the HCM patients for all segments except the anterior and the infero-septal segments. In the apical slices, the maximum principal strain was lower in the HCM population than in the normals. However, the minimum principal strain for the HCM patients was consistently lower than normal in both the basal and mid-ventricular slices for all segments, but it was found to be higher in the apical slices. It is also important to look at the direction the strain is acting in as this is either radial or circumferential, and combining this directional information with the strain value can determine whether there is lengthening or shortening. The two eigenvectors are always orthogonal and can be displayed with their corresponding eigenvalues as shown in Figures 4.26 to 4.28. It was found that in systole the maximum principal strain acted in a radial direction, while the minimum principal strain acted in an orthogonal direction to this, *i.e.*, it was circumferential, as illustrated in Figures 4.26 to 4.28. This was found to be the case in all slices, basal, mid and apical, and in all subjects, normal and HCM.

The longitudinal shortening was measured in all four walls of the left ventricle. The shortening for six normals and their mean and standard deviation is plotted in Figure 4.29. The general trend agreed well with previously published ultrasound data^{143,144}. Edvardsen *et al* showed longitudinal shortening during systole in normal subjects in all four walls of the LV using tissue Doppler imaging of around -20%. This corresponds well to our observed longitudinal strain in five normal subjects as shown in Figure 4.29. It should be noted that a setting of zero strain needs to be set for frame 1 to obtain strain plots similar to Edvardsen *et al*.

	Segments					
	Anterior	Anterolateral	Inferolateral	Inferior	Inferoseptal	Septal
Base	36 ? 48	17 ? 32	19 ? 42	17 ? 32	17 ? 38	21 ? 38
Mid	29 ? 26	35 ? 21	25 ? 28	24 ? 35	11 ? 25	32 ? 48
Apex	38 ? 30	51 ? 8 (lateral)	-----	42 ? 42	-----	31 ? 20

Table 4.1. Maximum principal strain in normals. This was found to act in a radial direction.

	Segments					
	Anterior	Anterolateral	Inferolateral	Inferior	Inferoseptal	Septal
Base	-11 ? 28	-18 ? 20	-18 ? 19	-16 ? 23	-14 ? 21	-17 ? 20
Mid	-19 ? 13	-14 ? 13	-16 ? 13	-21 ? 15	-21 ? 16	-18 ? 14
Apex	-11 ? 7	-5 ? 2 (lateral)	-----	-8 ? 16	-----	-8 ? 9

Table 4.2. Minimum principal strain in normals. This was found to act in a circumferential direction.

	Segments					
	Anterior	Anterolateral	Inferolateral	Inferior	Inferoseptal	Septal
Base	38 ? 28	43 ? 34	54 ? 45	22 ? 21	27 ? 38	19 ? 27
Mid	33 ? 35	30 ? 20	25 ? 23	23 ? 26	20 ? 21	26 ? 28
Apex	32 ? 18	28 ? 22 (lateral)	-----	23 ? 26	-----	28 ? 18

Table 4.3. Maximum principal strain in HCM patients. This was found to act in a radial direction.

	Segments					
	Anterior	Anterolateral	Inferolateral	Inferior	Inferoseptal	Septal
Base	-15 ? 11	-11 ? 16	-12 ? 10	-14 ? 13	-15 ? 12	-15 ? 9
Mid	-11 ? 14	-12 ? 13	-12 ? 11	-10 ? 13	-12 ? 13	-11 ? 12
Apex	-13 ? 12	-13 ? 9 (lateral)	-----	-12 ? 13	-----	-10 ? 12

Table 4.4. Minimum principal strain in HCM patients. This was found to act in a circumferential direction.

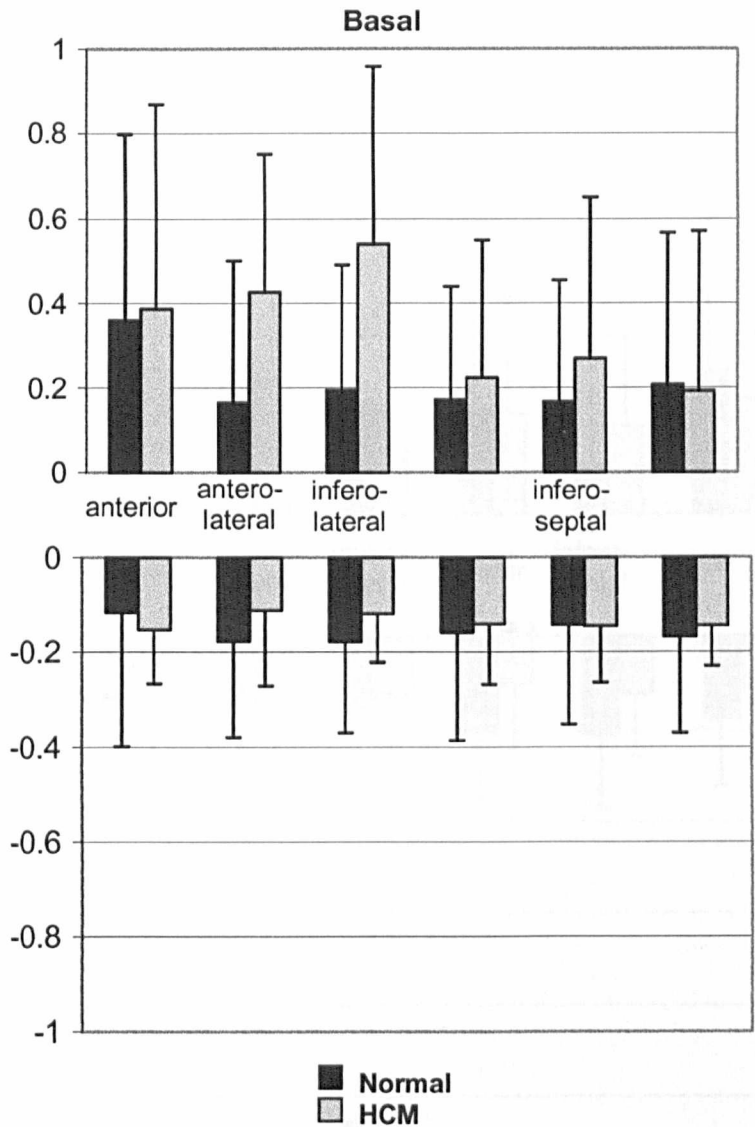


Figure 4.23 Maximum and minimum principal strain in normals (black) and HCM patients (grey) in the basal slice. It can be seen that the difference was considerable, even though some of the patients did not display the phenotype using standard diagnosis techniques.

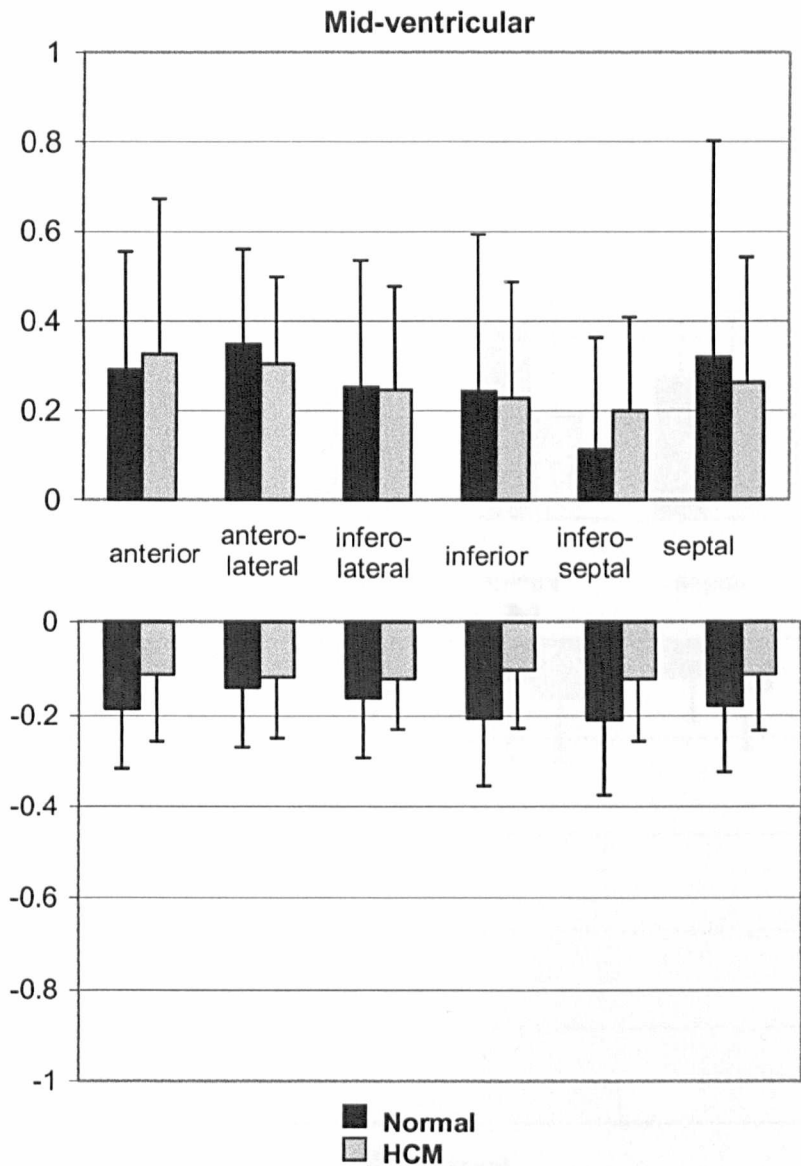


Figure 4.24 Maximum and minimum principal strain in normals (black) and HCM patients (grey) in the mid-ventricular slice.

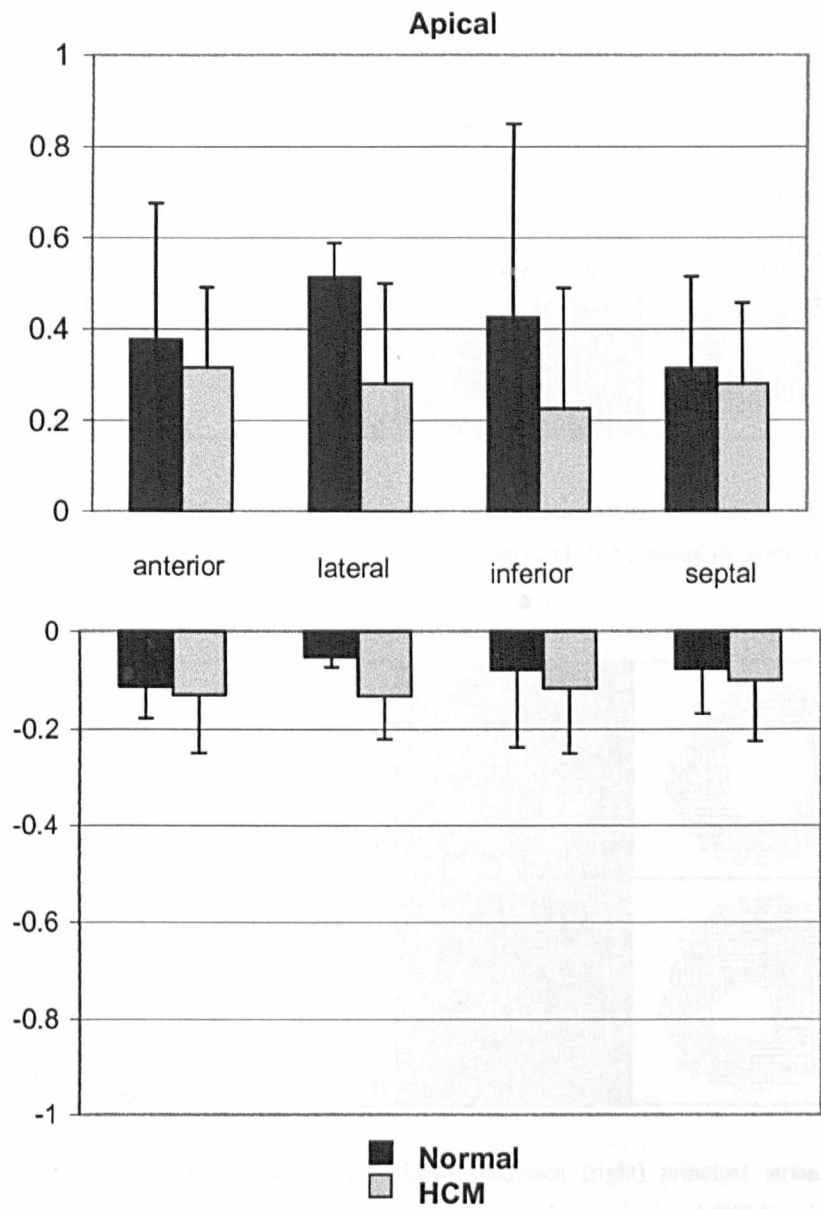


Figure 4.25 Maximum and minimum principal strain in normals (black) and HCM patients (grey) in the apical slice.

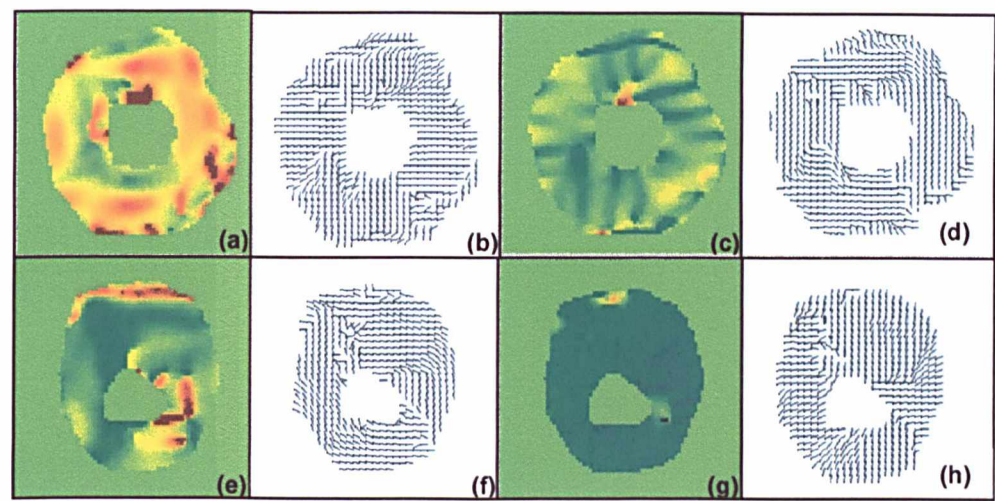


Figure 4.26 (a,b,e,f) Maximum (left) and (c,d,g,h) minimum (right) principal strain and their corresponding directions in the basal slice in a normal (top row) and HCM patient (bottom row).

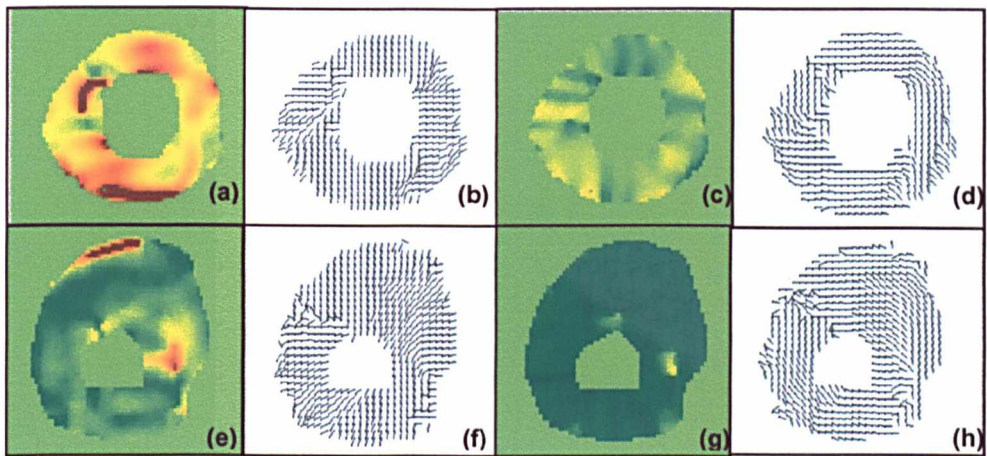


Figure 4.27 (a,b,e,f) Maximum (left) and (c,d,g,h) minimum (right) principal strain and their corresponding directions in the mid-ventricular slice in a normal (top row) and HCM patient (bottom row).

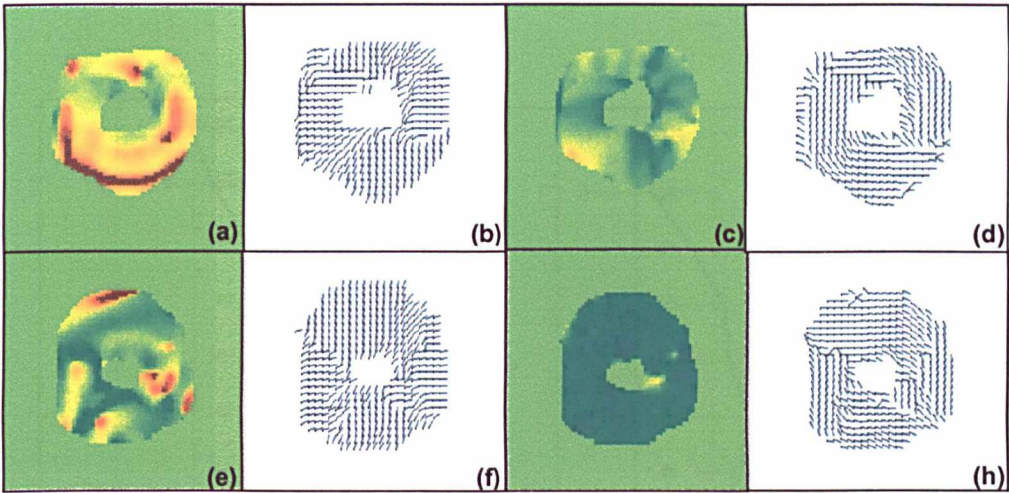


Figure 4.28 (a,b,e,f) Maximum (left) and (c,d,g,h) minimum (right) principal strain and their corresponding directions in the apical slice in a normal (top row) and HCM patient (bottom row). It can be seen that the maximum principal strain acts in a radial direction while the minimum acts in the circumferential direction.

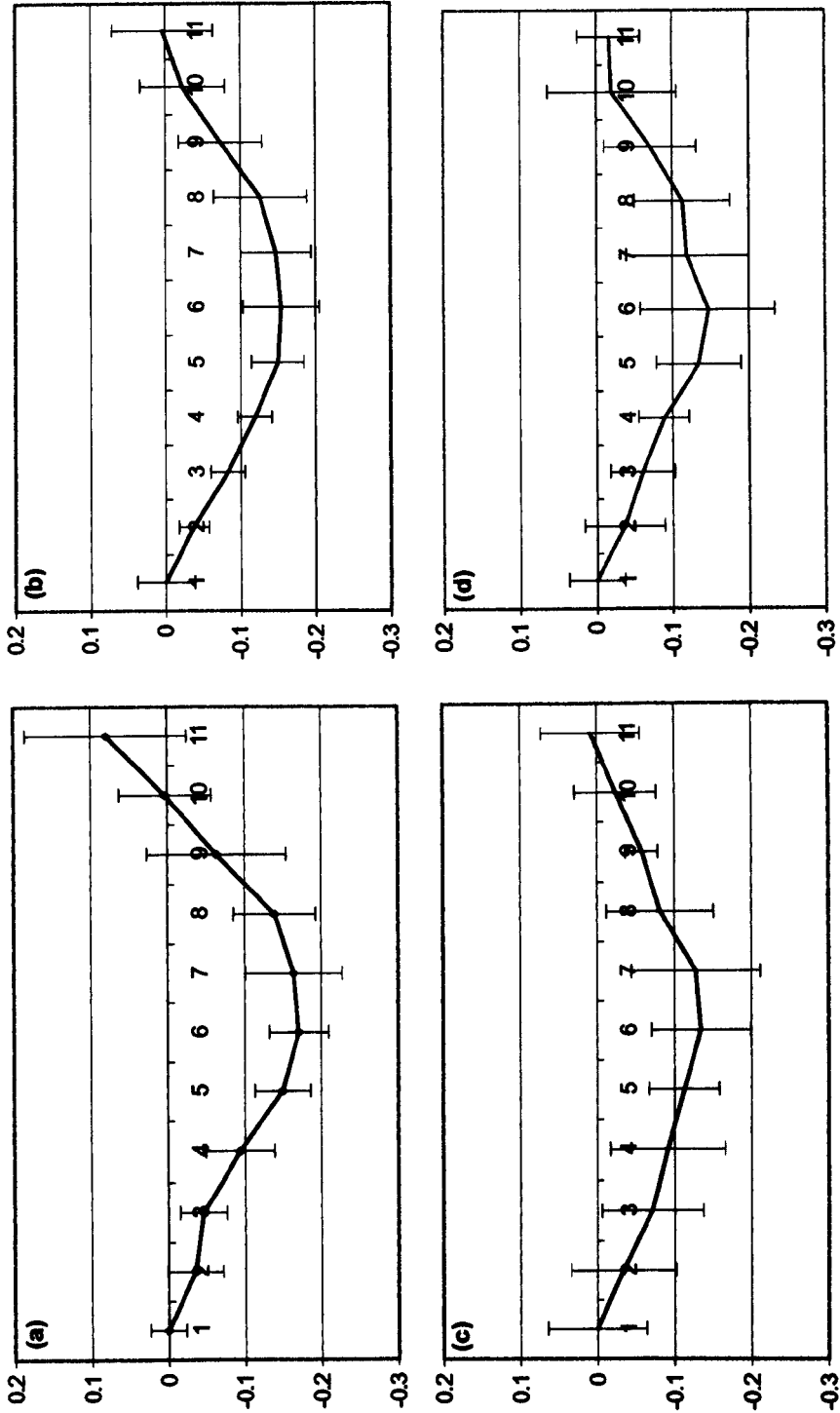


Figure 4.29 Strain in the longitudinal direction in (a) lateral, (b) septal, (c) anterior and (d) posterior regions. The trend is for the strain to reduce as the ventricle shortens and then increase as it lengthens out again. The lateral and septal walls show that the standard deviation across the subjects increases in the later frames of the cardiac cycle. This could be due to the decreased SNR caused by tag fading.

4.5 Discussion and Conclusion

HARP imaging allows an alternative to the lengthy processing generally needed for obtaining strain data from tagged images. It can be seen that HARP imaging is a potentially powerful technique for online assessment of myocardial contractility. It has already been demonstrated that it can delineate between normal and abnormal function¹⁴⁵. This chapter outlines the image acquisition and processing used to measure strain *in vivo* using HARP. The technique was used to study the effect of breathing on regional strain. It is evident from this study that respiration can have a significant effect on the absolute strain values derived. For the five subjects studied, the changes in strain range from -17.4% to 40.0% compared with data calculated from breath-holding. This highlights the importance of using real-time navigator echoes for performing 3D HARP imaging so that physiologically correct strain distributions can be calculated. Although there were differences found between end-inspiration and end-expiration, these were not found to be predictable and varied greatly between subjects. This study also indicates that the effect of respiration on different segments of the myocardium is not uniform, which could interfere with assessment of regional contractile abnormalities if respiratory motion is not consistently monitored.

4.5.1 HARP for Evaluating HCM

Regional contractile motion is thought to be a sensitive indicator of disease, *e.g.* single artery coronary disease will only affect one region of the heart. In many disease processes, such as cardiomyopathies, it is important to assess regional motion to evaluate onset of disease. Although studies using conventional tagging have been used to evaluate changes in myocardial motion in HCM, this study is the first to use HARP to do this. To evaluate the role of HARP imaging in early diagnosis of HCM a study was carried out on patients with the HCM genotype. This chapter presents some preliminary results comparing strain in normal subjects to that in patients with HCM. Initial results suggest that there is a marked difference in strain magnitude between the two sets. However, the direction of acting strain at peak systole remains the same with maximum principal strain acting in a radial direction indicating lengthening and minimum principal strain acting in the circumferential direction indicating shortening.

In the basal slices it was noted that the maximum principal strain was higher in the HCM patients, while the minimum principal strain was lower (*i.e.*, less negative) than normal. This

indicates how due to the extra muscle growth the myocardium contracts in the radial direction but cannot shorten in the circumferential direction due to the extra mass. This trend could be explained by the fact that the hypertrophy usually starts in this region of the heart. In the mid-ventricular slice, the trend varied with maximum principal strain in HCM patients being lower than normals except in the anterior and inferoseptal regions. This could be explained by the interaction of the right ventricle with the left ventricle. However, as in the basal slice, the minimum principal strain was reduced in HCM. In the apical slice, the trend was reversed with the HCM patients displaying a lower radial strain (maximum principal), *i.e.*, less lengthening, but a higher circumferential strain (minimum principal) than normals, *i.e.*, more shortening.

This preliminary study shows the potential of using HARP for measuring contractility in the LV. It is important to further validate this technique and expand the normal database for all ages. This technique could also be used to study contractile changes in other diseases such as dilated cardiomyopathy and ischaemic heart disease. It could be especially useful in studying ventricular-ventricular interaction in diseases such as pulmonary hypertension and Arrhythmogenic Right Ventricular Cardiomyopathy (ARVC). Loss of contractile function could be used as an early marker in disease. Stunned or hibernating myocardium could be detected using stress testing. In a CMR environment, this entails the use of drugs such as dobutamine to induce stress. By causing the heart to work harder, changes in contractility can indicate where there may be hibernating or stunned myocardium. This would have significant impact on the therapeutic course chosen to treat disease. The next step in this would be to link HARP with CMR perfusion imaging to examine the relationship of coronary blood flow and scarring to contractile function. It is expected that increased scarring and decreased perfusion should be directly linked to reduced contractility.

The HCM study indicates the usefulness of HARP imaging in measuring contractility. HARP imaging could become part of the standard CMR exam to assess anatomy and function. Due to the simplicity of the calculation involved, strain calculation could be incorporated within an image-processing toolbox, allowing the clinician to a variety of indices including ejection fraction, time-volume curves, perfusion and strain.

4.5.2 Conclusions

The respiratory-gated CSPAMM sequence potentially offers a much higher spatial and temporal resolution. This would enable detailed study into regional contractile motion of the normal heart. Volunteer and animal studies could be used to elucidate the relationships between physiological factors such as coronary blood flow, electrical excitation and regional

contractility. The tag spacing could be reduced while increasing the resolution, allowing a greater number of tags to cover the myocardium hence improving the strain measurement. Studies of the complete 3D volume of the LV could be carried out with detailed analysis of regional contractility. The higher spatial resolution would also allow study of RV contraction which is not possible robustly using any other modality. A full 3D model of heart function could be built incorporating RV and LV electrical excitation, coronary blood flow and contraction.

A fully integrated MR system with online HARP MRI would have the added advantage of standard CMR tools, such as being able to measure ejection fraction, LV mass and volume, and perfusion. This would enable the technique to become an integral part of the MR heart function clinic, allowing near real-time assessment of contractility.

4.5.3 Limitations of HARP Imaging

It must be noted, however, HARP has certain drawbacks including the limited temporal resolution of the segmented FLASH sequence. In practice, this could be overcome by using the respiratory gated sequence, which would mean a longer total image acquisition time, or by using SSFP tagging sequences. Another drawback of the technique is that with HARP, it is difficult to assess 3D motion as only the apparent in-plane motion is measured. Assessment of 3D motion using HARP requires full 3D coverage of the myocardium, involving a long scan time to cover multiple short and long axis slices. A full 3D volume scan of the heart may not be possible in a clinical environment. This can be partially overcome by increasing the scan efficiency of the respiratory-gated CSPAMM sequence. One possible method for doing this is using the phase reordering techniques discussed earlier^{146,147}. This data would then have to be transformed back onto a 3D geometric model to enable easy visualisation of the strain in all three directions.

As in conventional tagging the spatial resolution is restricted by the tag spacing possible. This is illustrated in Figure 4.14(h and i) where velocity wrap-around occurs due to the tags merging into one another. To avoid this, either a bigger field of view or a larger tag spacing has to be chosen. Tagging also does not allow clear delineation of motion in diastolic frames due to tag fading. CSPAMM helps by increasing tag contrast but later frames tend to have a lower SNR. This can be overcome by delaying image acquisition but this would entail acquiring the same image plane twice, resulting in the doubling of the total scan time.

On the other hand, CMR phase contrast velocity mapping has the ability to measure all three directions of motion for any imaging plane and for all time frames, giving 7D data *i.e.*, 3 spatial dimensions, 3 directions of motion and time. The SNR is the same for all time frames allowing delineation of motion for all phases of the cardiac cycle, and the field of view is not restricted by the velocity range. Velocity imaging also circumvents the need for complicated processing allowing fast strain rate calculation, allowing easy discrimination of regional myocardial contractility.

5 MR Phase Contrast Myocardial Velocity Mapping

5.1 Introduction

CMR phase contrast velocity mapping is a powerful technique already in routine use for blood flow imaging. It allows measurement of velocity in all three directions and is valuable in assessing blood flow in the major vessels and ventricular chambers of the heart. It is an important research and clinical tool, but has found limited application in myocardial velocity imaging. The main reason for this is the long acquisition time needed to obtain images with adequate velocity sensitivity. The velocity sensitivity has to be reasonably high for myocardial velocity imaging as typical peak velocities of the myocardium in normal subjects are in the range of $\pm 14\text{cm/s}^{38}$, as compared to the high blood velocities found in the aorta and ventricular chambers, which are around $\pm 100\text{cm/s}$. In practice, the velocity sensitivity achievable is limited by the image acquisition time, which needs to be squeezed into either a single breath-hold or multiple breath-holds for each velocity encoding direction. The maximum gradient strength and peak slew rate of the scanner are therefore the determining factors of both acquisition time and velocity sensitivity. The limited velocity sensitivity physically possible on the scanner restricts the accuracy of the derived strain rate and strain calculations.

The main advantage of velocity mapping over conventional MR tagging is that it potentially allows fast calculation of strain rate. The processing would consist of simply taking spatial derivatives in all three directions and combining the information to give a suitable 3D representation of strain rate. With accurate and robust myocardial velocity measurement, processing to produce strain rate results would be a matter of seconds. Vector maps could also be plotted to show the trend of the velocity distribution giving an immediate visualisation of myocardial function. With reasonable temporal resolution, strain and displacement in any direction could be calculated using integration methods. Although HARP imaging overcomes the processing limitations of conventional tagging, it only allows measurement of apparent in-plane myocardial deformation. Measurement of longitudinal motion using HARP would require additional long axis scans of the LV as illustrated in Figure 4.16. CMR velocity mapping overcomes this limitation as it allows all three velocity directions to be acquired in a single scan, allowing accurate delineation of motion in all directions. Thus, a complete volume scan of the heart, using just short axis slices, could be used to reconstruct the 3D motion of the heart.

Measuring myocardial velocities directly using CMR is not an easy task. The complications involved include the high velocity sensitivity required to encode the comparatively slow myocardial velocities. The highest velocities recorded in the myocardium are around $\pm 14\text{cm/s}$ with the velocities dropping significantly for diseased hearts³⁷. Therefore, the velocity sensitivity required to capture myocardial motion accurately should be in the range of $\pm 15\text{cm/s}$. This requires a high system hardware performance to enable the encoding in a short enough period of time for one breath-hold. Previous research in the area has only allowed acquisition of the velocity encoded images in different directions in multiple breath-holds, *i.e.*, reference scan and *x*-encoding in one breath-hold, reference scan and *y*-encoding in the next breath-hold and reference scan and *z*-encoding in the third breath-hold. However, this can introduce errors due to mis-registration in the velocity distributions and thus the final strain calculation.

Another factor to be considered when performing any CMR imaging is the effect of flowing spins. If we consider only one voxel that contains spins with many different velocities within it, the phases of these different velocities can cancel out, producing a null signal for the voxel. This type of signal nulling can be eliminated or reduced by using flow compensation gradients. These are gradient pulses incorporated into the sequence to ensure that the zero and first moments of the sequence are nulled at time of readout. To this end, the CMR velocity mapping sequence used in this work incorporated flow compensation within the bipolar gradients used for velocity encoding.

Probably the most important problem in myocardial velocity mapping is the blood flow related artefact. The fast flowing blood in the left ventricle during certain phases of the cardiac cycle can cause considerable artefacts in the phase encode direction. As the signal from blood is a periodic function of time due to varying inflow, then the measured k -space signal will vary from one phase encoding line to the next, leading to ghosting^{148,149}. This can effectively contaminate signal from the myocardium and render the data in those regions useless as shown in Figure 5.2. As blood flow varies from one cardiac cycle to the next, the blood flow artefact is unpredictable.



Figure 5.2 This short axis image shows the blood flow artefact in a magnitude image. As the blood signal has a phase shift proportional to velocity and variable flow during each phase encode, it is encoded in a different part of k -space than where it should be, producing a streaking artefact in the phase encode direction, destroying signal in parts of the myocardium.

The aim of this chapter is to develop a high spatial resolution and velocity sensitivity sequence by the use of black-blood saturation and view-sharing.

5.2. Principle of Phase Contrast Velocity Mapping

In MR velocity mapping, the received MR signal is a complex signal with a magnitude and a phase. The phase of the signal is directly related to the gradients applied and can be used to calculate the velocity of the spins as follows.

The frequency of precession is given by:

$$\omega(r, ts) = \gamma B(r, t) = \gamma B_0(r, t) + \gamma r(t)G(t) \quad (5.1)$$

where γ is the gyromagnetic ratio, B is the local magnetic field and r is the spatial position of the particle. Where B is composed of the static magnetic field B_0 and G the gradient magnetic

field $G(r)=(G_x, G_y, G_z)$. The phase of the signal can be calculated by integrating this expression with respect to time.

$$\phi(t) = \gamma B_0 (ts - t) + \gamma \int G(t)r(t)dt \quad (5.2)$$

For stationary spins this equation yields a simple expression known as the zero gradient moment.

$$\phi(t) = \gamma_0 \int G(t)dt \quad (5.3)$$

However, for spins moving at a constant velocity the expression becomes:

$$\phi(t) = \gamma_0 \int tG(t)dt \quad (5.4)$$

where v_0 is the spin's constant velocity. This expression is known as the first moment of the gradient.

If the spins are undergoing higher orders of motion, these can be derived using the power series expansion for displacement, s :

$$s(t - t_0) = s_0 + \int \left(\frac{ds}{dt} \right)_0 dt + \left(\frac{d^2 s}{dt^2} \right) \int t dt + \left(\frac{d^3 s}{dt^3} \right) / 2! \int t^2 dt + \dots \quad (5.5)$$

This relationship between the gradient applied and the phase can now be used to measure the velocity of the moving spins. Thus, if a balanced bipolar gradient is applied before image acquisition, stationary tissues will not experience a phase change. However, spins moving at a constant velocity will experience a phase change, directly proportional to their velocity, as determined by Equation 5.4. By subtracting the phase images from a scan with and without the bipolar pulse, a direct measurement of the velocity can be obtained.

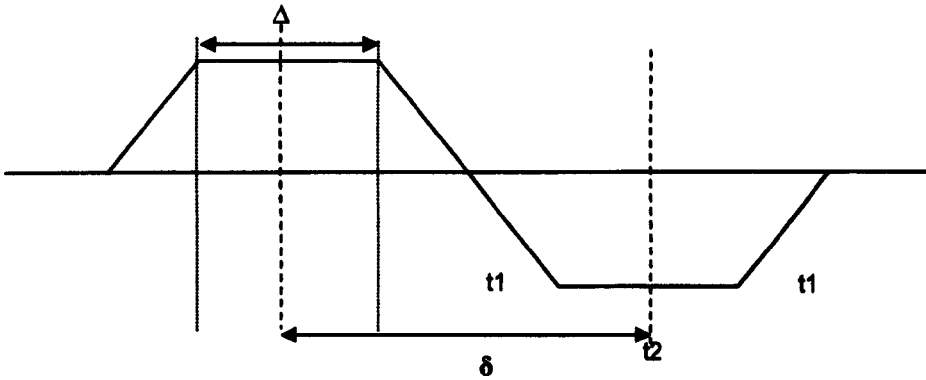


Figure 5.1 Bipolar gradient pulse. The timings and gradient amplitude can be used to calculate the velocity sensitivity of the sequence.

The velocity sensitivity of a bipolar gradient pulse can be easily derived using Equation 5.4.

$$\begin{aligned}
 \phi(t) &= \gamma_0 \int tG(t)dt \\
 &= \gamma_0 2G(t-t_0)(t_1+t_2) \\
 &= 2\gamma_0 G \delta\Delta
 \end{aligned} \tag{5.6}$$

If the phase is set to π we can easily calculate the velocity sensitivity (venc) of the gradient applied, or the gradient needed to achieve a particular venc. Designing such a sequence, however, does not take into account higher orders of motion such as acceleration. This can potentially lead to signal loss due to intravoxel phase dispersion when imaging turbulent flows. The principle behind phase contrast velocity mapping can be derived from basic MR principles and is explained in more detail in Appendix 2.

5.3 CMR Phase Contrast Velocity Mapping Sequence

The most common technique of overcoming the blood flow related artefacts is using black blood sequences. The basic idea behind these sequences is to magnetically saturate the blood in the region adjacent to the slice being imaged. This is done by saturating the signal in those regions just prior to the imaging part of the velocity encoding sequence, as shown in Figure 5.3. This can be accomplished using a number of different techniques. The easiest way is to select the two regions above and below the slice just as a normal slice would be selected, *i.e.*, a 90° RF pulse and a slice select gradient. However, the time required to do this for two regions can be quite long making it unfeasible to repeat several times during the cardiac cycle. A faster way of accomplishing the blood saturation, in use since the late 80s, is using spectrally shaped RF pulses that selectively saturate the regions adjacent to the slice being imaged¹⁵⁰. RF pulses can be effectively designed to saturate any shape, just as a sinc pulse gives us a slice with a square profile. This principle can be used to design a pulse with a zero profile in the middle, where the imaging slice is to be located, with two regions of high saturation to either side. Figures 5.4 and 5.5 illustrate the relationship between RF pulse shape and excitation profile. Figure 5.4 shows the excitation (slice) profile, *i.e.*, time domain representation, of a sinc, $\left(\frac{\sin x}{x}\right)$, pulse and Figure 5.5 shows the black blood pulse used in this sequence.

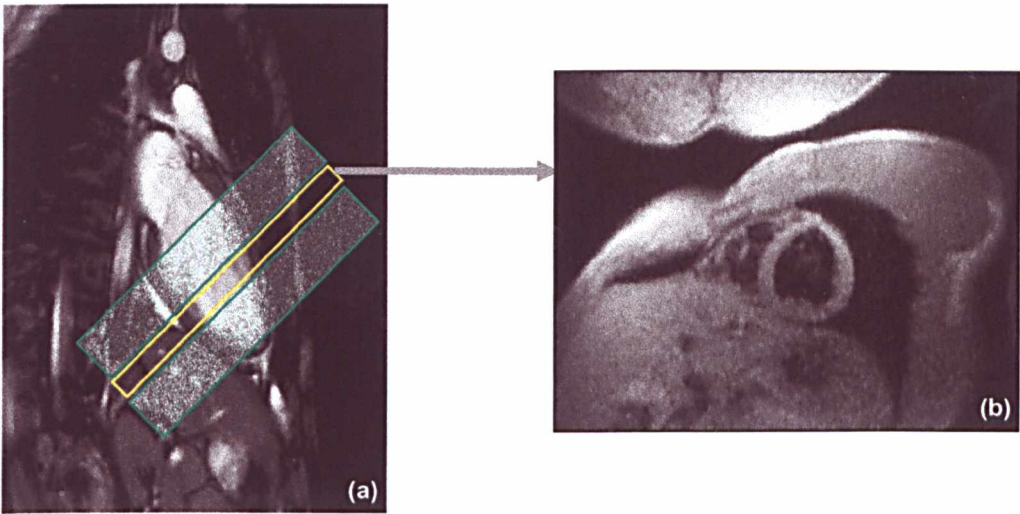


Figure 5.3 (a) The blue slices denote the saturation pulses and the yellow slice is the slice being imaged. This sort of scheme nulls the blood signal in (b) the short axis image. Giving an image with high signal intensity in the myocardium and “black blood”.

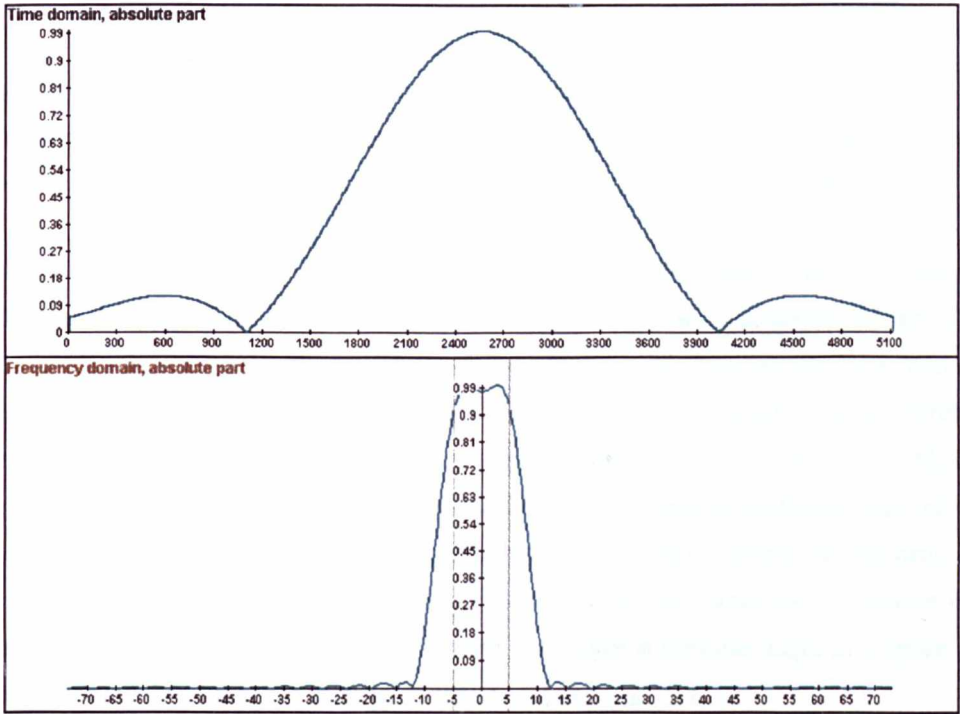


Figure 5.4 The frequency domain shows a truncated sinc pulse which translates into a rectangular excitation profile once played out on the scanner. As can be seen the slice profile contains some ringing as it is physically impossible to use a non-truncated sinc RF pulse.

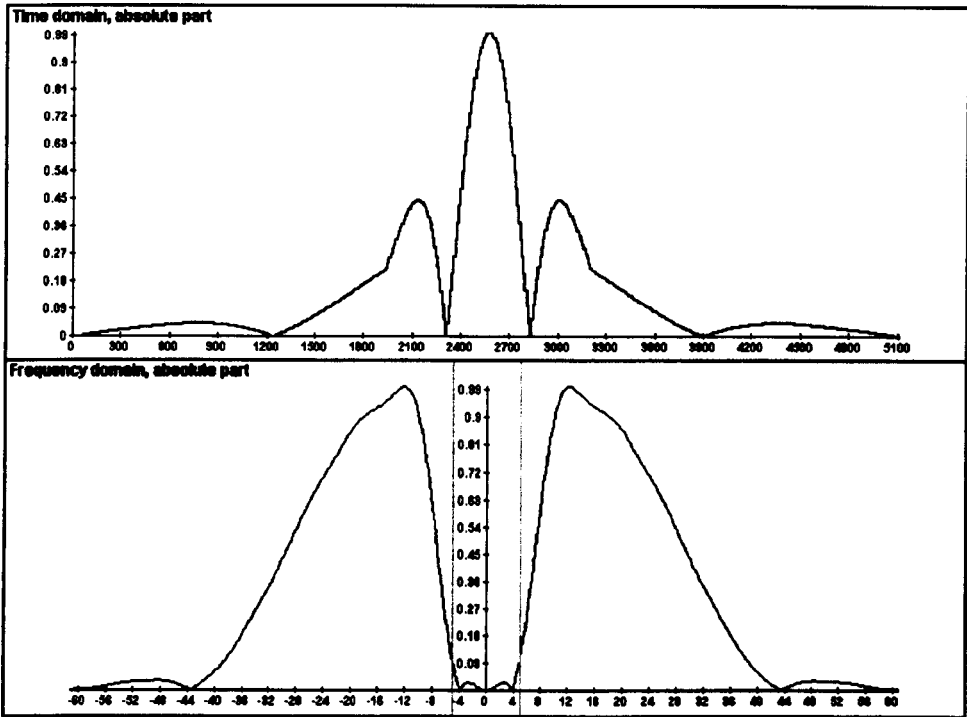


Figure 5.5 RF pulse design used to produce the black blood saturation. The time domain is the RF pulse transmitted producing the frequency domain profile in the image, *i.e.*, saturation bands next to the slice being images. The pulse was only 5.1ms long allowing repetition at every other phase.

In order to further reduce the acquisition time view-sharing can be used to reduce the number of *k*-lines needed per cardiac cycle. A view-sharing scheme was implemented as part of the velocity mapping sequence. The principle of view-sharing uses phase encode lines from two adjacent time frames to build up an “extra” time frame in between allowing an increased temporal resolution. The velocity mapping sequence was based on a segmented FLASH sequence. The segment size could be varied according to the temporal resolution required. For a typical temporal resolution of 62ms 16 phase encode lines were acquired per segment. The view-sharing was implemented by acquiring 16 lines for the first frame and 10 lines for each subsequent frame. The last 6 lines of each frame were taken at the outer edges of *k*-space, and shared with the next frame. This scheme is illustrated in Figure 5.7.

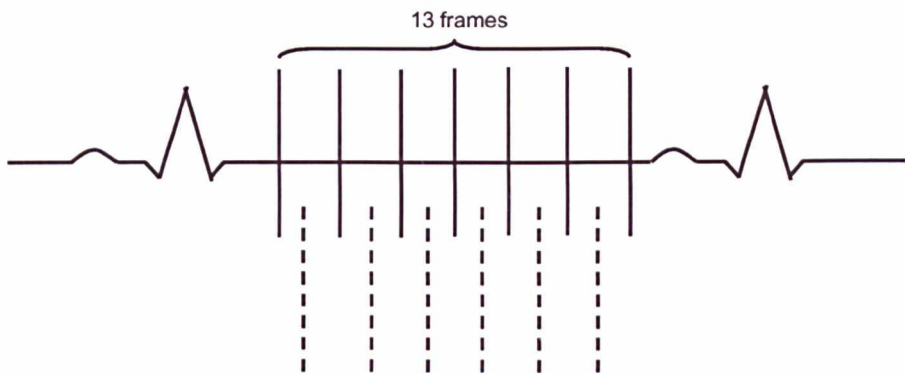


Figure 5.6 This diagram illustrates the principle of view-sharing. Echoes are acquired for seven time frames, however by sharing the data between adjacent frames extra frames can be reconstructed resulting in 13 frames covering the cardiac cycle.

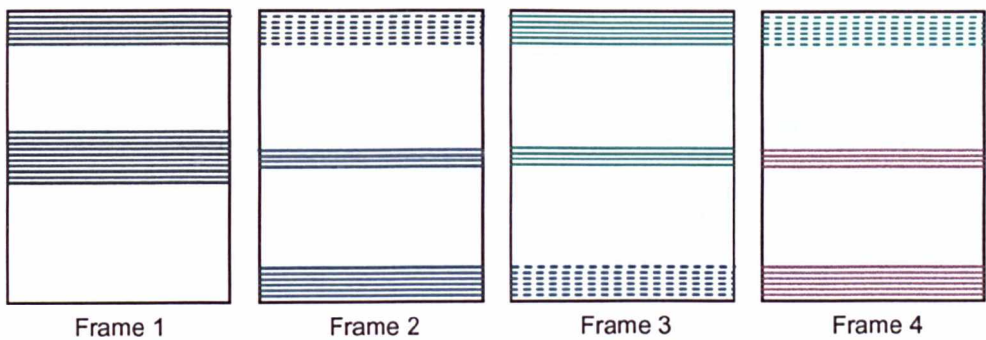


Figure 5.7 16 phase encode lines are acquired for the first frame, and 10 for each subsequent frame. 6 lines are acquired at the outer edges of k-space and shared with the next frame. This illustration shows how the image would be built up for the first four frames in the cardiac cycle. The dotted lines are the k-space lines shared from the last frame.

In summary, the sequence consists of a black blood pulse, repeated for every other phase, followed by the slice select, the velocity encoding gradients and then the image acquisition. This is repeated three times for the three velocity encoding directions¹⁵¹. The imaging parameters were set to 256x96 image matrix with a typical FOV of 400x300mm to reduce the imaging time needed. This gave a pixel size of 1.6x3.1mm². The velocity encoding was ± 20 cm/s, giving a range of 40cm/s. This was too large a range to acquire the in-plane myocardial velocities accurately, giving a low VNR. Temporal resolution was 62ms although this could be reduced to 49.6ms at the expense of losing spatial resolution in the phase encode direction and increasing the breath-hold duration. The image acquisition took 25 cardiac cycles for the reference, *x*, *y* and *z* encodings. It was desirable to improve the spatial and velocity resolutions. This was done by incorporating navigator echoes into the sequence so

that data acquisition was no longer limited by the length of breath-hold possible by the subject.

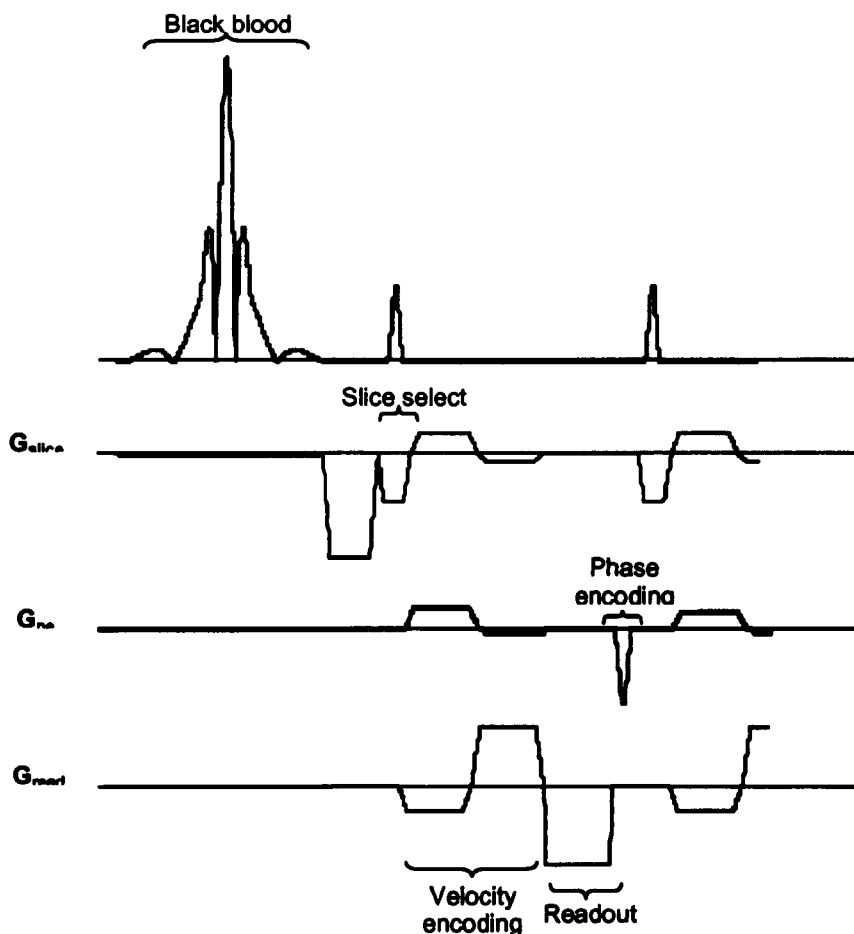


Figure 5.8 The sequence diagram showing the black blood pulse followed by slice selection and velocity encoding in the slice (through-plane) direction. The phase encode and readout gradients are then followed by spoilers to destroy any signal left in the transverse plane. The black blood pulse is repeated before every other frame, *i.e.*, 1, 3, 5, 7 and so on, at the beginning of each segment.

5.3.2 CMR Velocity Mapping with Respiratory Gating

It is important to image myocardial motion under normal physiological conditions to obtain an accurate assessment of regional contractility as shown by the study conducted using HARP imaging in Section 4.3.1. It was shown that the effect of breathing on strain measurements was variable and unpredictable. Thus, it becomes necessary to incorporate navigator echoes into the velocity mapping sequence. Breath-hold imaging, although robust and reproducible, also carries a penalty of limited spatial and temporal resolution. It is difficult to use long

breath-holds, 25 cardiac cycles in the case of 3D velocity mapping, in patients with respiratory problems or severe heart disease.

Respiratory gating was incorporated into the sequence in the form of navigator echoes, as in the case of the CSPAMM imaging sequence. A 90°-180° spin echo prospective navigator was applied at the beginning of each cardiac cycle. This was found to be adequate for free-breathing acquisition. However, if this sequence were to be used to monitor multiple breath-holds it would need modification to either pre and post navigators or regular navigators applied throughout the cardiac cycle to avoid registration errors.

Each navigator has a column area of approximately 10x10mm². The column is positioned at the dome of the right hemi-diaphragm, same as that shown in Figure 4.3. The gating window of ±4mm was set at end-expiration. Prospective navigator echoes were used, so they were only applied at the beginning of each cardiac cycle. If the position of the diaphragm was within the required window all the data acquired in that cardiac cycle was accepted, however, if the position of the diaphragm was outside this window all the data acquired within that cycle was discarded, *i.e.*, a simple accept/reject algorithm was used. The timing diagram for the sequence is shown in Figure 5.9. This is similar to that used for the CSPAMM sequence described in the previous chapter.

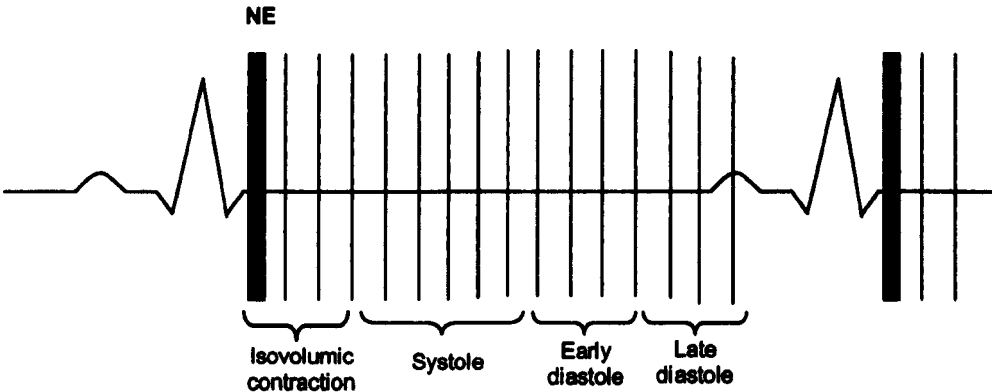


Figure 5.9 Timing diagram for the respiratory gated velocity mapping sequence. The navigator echo is applied at end-diastole and is 50ms long including the time needed to feedback to the pulse sequence.

Adding navigators to the sequence allows the spatial and temporal resolution of the sequence to be improved. Improving spatial resolution entails prolonging the ramp times of the readout and phase encode gradients, as the sequence was already running at the peak slew rate of 200mT/m/s, to allow higher gradients and hence smaller fields of view. For improving

temporal resolution, the segments can be shortened so that fewer phase encode lines are acquired per segment, hence reducing the time between phases. By using navigator echoes for respiratory gating, it is also possible to improve the SNR by acquiring the same image more than once and averaging the multiple measurements. However, the phase of the image is not as severely affected by the SNR as the magnitude. It would be more beneficial, in terms of measuring myocardial motion, to increase the velocity sensitivity by prolonging the time of the bipolar gradient.

5.3.3 Velocity to Noise Ratio

The velocity-to-noise ratio (VNR) is a key factor in determining the usability of velocity images. The relationship between phase noise, σ_ϕ and magnitude SNR was explored fully in Conturo and Smith¹⁵². The phase noise was found to be inversely proportional to SNR, $\sigma_\phi(\text{radians}) = 1/\text{SNR}$. Therefore, subtracting two phase images to obtain the velocity map will have a noise level of $\sigma_v = \sqrt{2}\sigma_\phi$. The VNR can thus be calculated as follows:

$$\begin{aligned} \text{VNR} &= \phi_v / \sigma_\phi \\ &= \left(\frac{\pi}{\sqrt{2}} \right) \left(\frac{v}{v_{\text{enc}}} \right) \text{SNR} \end{aligned} \quad (5.7)$$

where v is the instantaneous measured velocity, and $\phi_v = \left(\frac{v}{v_{\text{enc}}} \right) \pi$ is the velocity related phase shift. Equation 5.7 reveals that although SNR is an important factor in determining noise levels in velocity images, it is equally important to set the velocity sensitivity, v_{enc} , close to the expected measured velocities. The respiratory gated velocity mapping sequence allowed the v_{enc} to be increased to $\pm 13\text{cm/s}$, close to the expected peak myocardial velocities giving an increase in VNR of 54% allowing more robust calculation of in-plane strain rates. The VNR can be further improved by improvements in SNR using data averaging, *i.e.*, averaging multiple acquisitions of the same image plane. Although the respiratory gated velocity mapping sequence has the flexibility to incorporate data averaging, image acquisition time spent on increasing velocity sensitivity is a much more efficient use of time in terms of improvement of VNR rather than the doubling or tripling of acquisition time for data averaging to improve SNR.

5.3.4 Errors due to Phase Shifts

Errors can be introduced into the velocity field from background phase shifts due to eddy currents when the gradients are switched rapidly and/or by concomitant gradient terms. Eddy currents are caused by imperfections in the active shielding of the magnet and gradient fields, and vary from frame to frame in a non-steady state cine. They are difficult to predict and hence can only be corrected by using software which corrects background phase errors for each frame of a cine.

Concomitant non-linear magnetic fields result whenever a linear gradient is switched on¹⁵³. These are a consequence of Maxwell's equations for the divergence and curl of a magnetic field, and can cause artefacts in the velocity image. The principles behind this and ways of overcoming the errors are covered in more detail in Appendix 2. The background phase error was not found to be a problem in this experiment. However, if velocity sensitivity is enhanced by increasing the gradient strength, concomitant gradient terms can be significant. The background phase shifts should then be calculated for the velocity maps and rectified as necessary. This could be solved either by employing sequence design principles, or using software that is able to correct the background phase shift. A simple background correction can be achieved by fitting a polynomial to the final velocity images using the stationary material, such as the chest wall, as points of zero velocity. The offset can then be calculated and subtracted from the image by fitting a 2D surface to the background phase error.

Another potential error in velocity mapping is partial volume effects. These occur at the edges of the myocardium at the tissue-tissue interfaces. As the phase of a voxel is the phase of the complex average of all the spins within it, at the tissue-tissue interfaces, the phase is the average of the moving and stationary spins. Thus velocity measurements of edge voxels depend on the relative magnitudes of static and moving spins¹⁵⁴. This will introduce errors into the strain rate calculation at the epicardial and endocardial borders of the myocardium. One way of overcoming this is to segment the myocardium carefully, however this may result in underestimation of myocardial pixels and hence loss of useful contractility information.

5.4 Experimental Method

5.4.1 Artefact Reduction

Figure 5.10 shows the effectiveness of the black blood pulse at nulling the blood signal. The velocity data obtained from the breath-hold and navigator sequence was processed using software written in MatLab (MathWorks Inc.). The phase subtraction to obtain velocity was done automatically in this software when the data is loaded in. The myocardium was segmented semi-automatically and the data was displayed as magnitude images with the in-plane velocity shown in a vector map and the through-plane in a colour map. Figure 5.11 shows the corresponding myocardial velocity vector and colour maps obtained using this software.

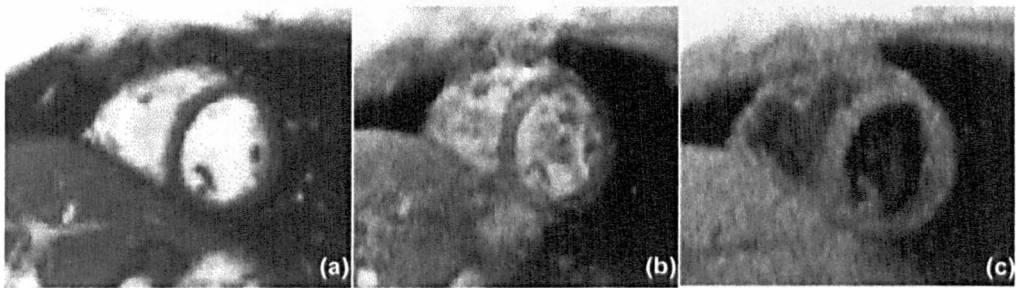


Figure 5.10 Mid-ventricular short axis image. (a) True FISP image, segmented FLASH velocity mapping sequence (b) without and (c) with blood saturation.

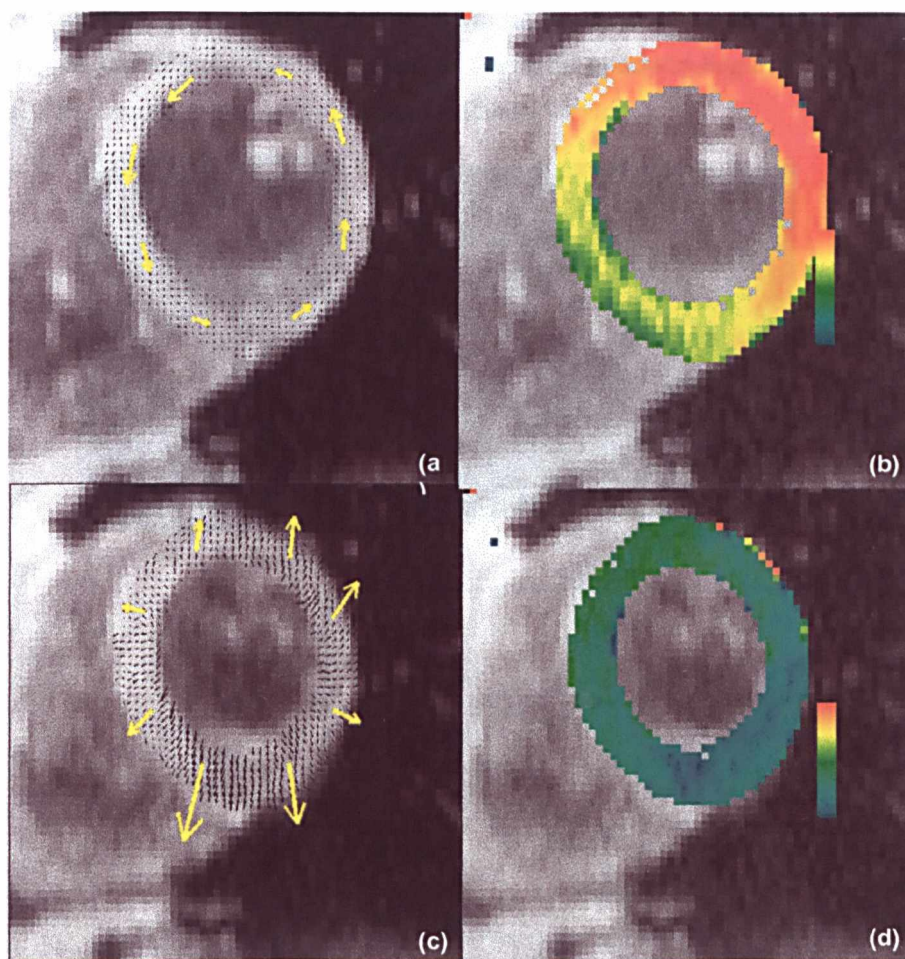


Figure 5.11 Vector maps showing in-plane (x,y) velocities at (a) end-diastole and (c) start diastole. (b) and (d) show the corresponding through-plane (z) velocity. The colourbar represents velocities from +10cm/s to -10cm/s.

The effect of blood saturation on the velocity signal was examined by comparing mean velocities in the myocardium with and without the black blood pulse. Short axis slices at the mid-ventricular level slice were imaged in five normal subjects with and without the black blood pulse. All other parameters were kept the same including the timing of the sequence. Image matrix was 256x96, field of view 400x300mm, flip angle 15°, slice thickness 8mm, v_{enc} of 20cm/s with a temporal resolution of 62ms. A regional analysis was carried out by dividing a mid-ventricular slice into six segments: anterior, anterolateral, inferolateral, inferior, inferoseptal and anterosseptal as shown in Figure 5.12. By plotting the in-plane velocities for each region, it was shown that the error in velocities obtained without blood saturation was variable, not only for the five subjects but also for the different myocardial regions. Figures 5.13 and 5.15 show in-plane velocities for one subject in each region. Figure 5.14 and 5.16 show the absolute differences in velocities for all subject for each myocardial

region. These were averaged over time as it was found that the differences were variable for each region and for each time. This agrees well with the understanding that the ghosting due to blood flow artefacts is unpredictable and randomly varying.

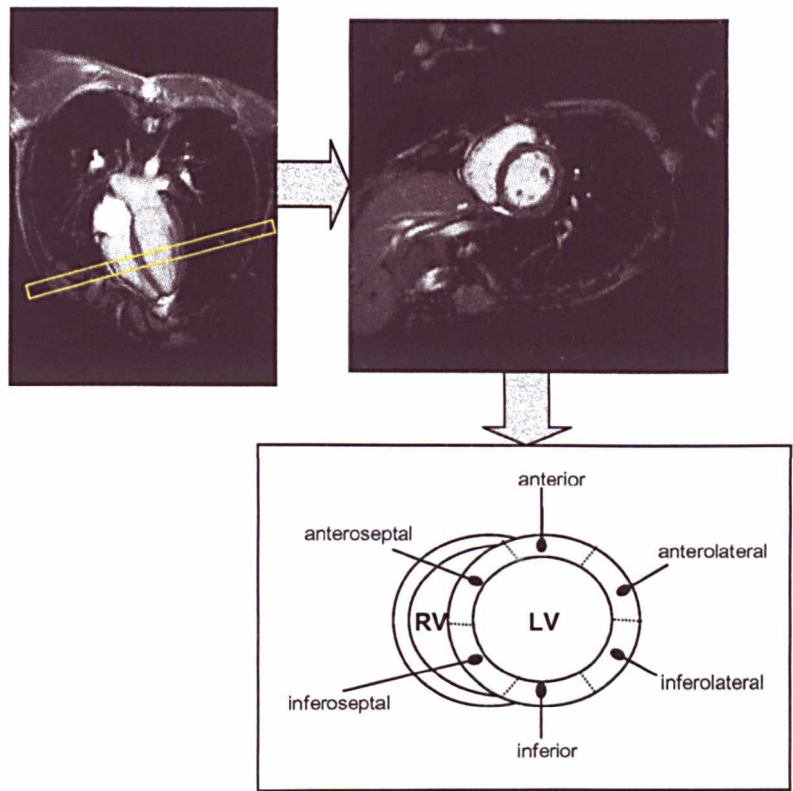


Figure 5.12 Segmentation of the mid-ventricular slice according to the standardised model as recommended by the American Heart Association Writing Group on Myocardial Segmentation and Registration for Cardiac Imaging¹⁴².

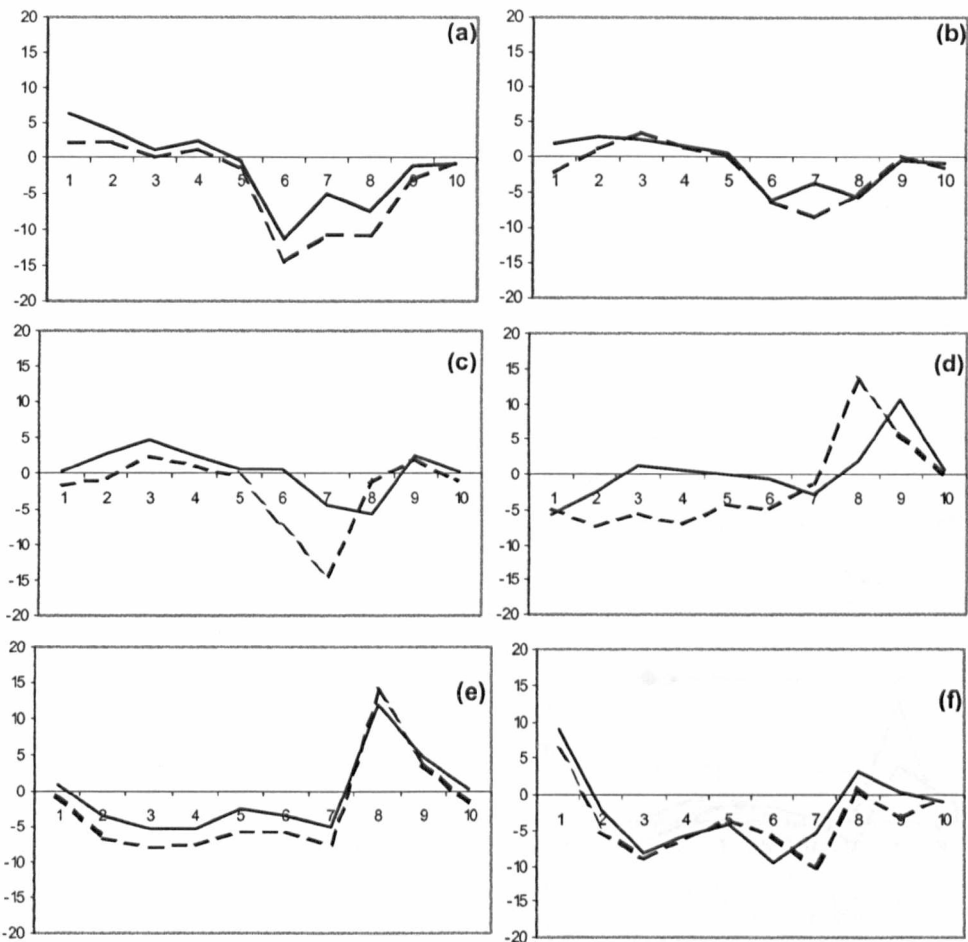


Figure 5.13 Mean velocity in the read (x) direction in the (a) anterior, (b) anterolateral, (c) inferolateral, (d) inferior, (e) inferoseptal and (f) antero-septal regions of the same slice for one subject. The dashed line shows the scan without blood saturation and the solid line with the blood saturation.

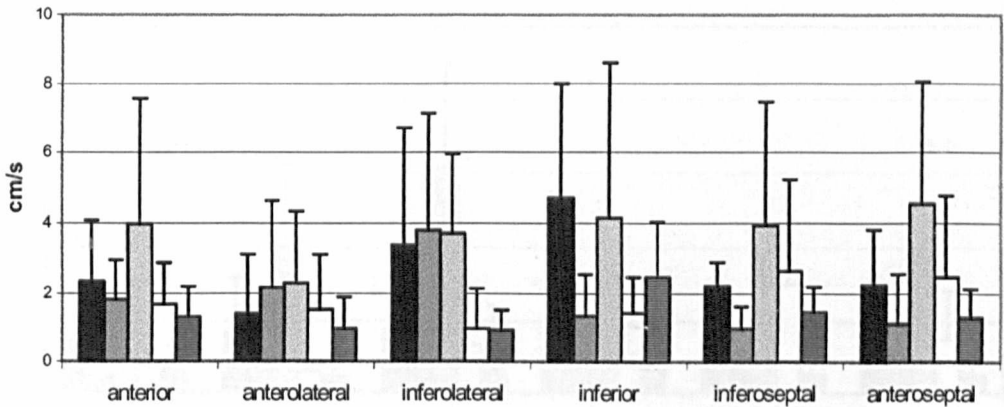


Figure 5.14 Absolute difference in v_x between velocities measured in different regions with and without the blood saturation pulse for five different subjects.

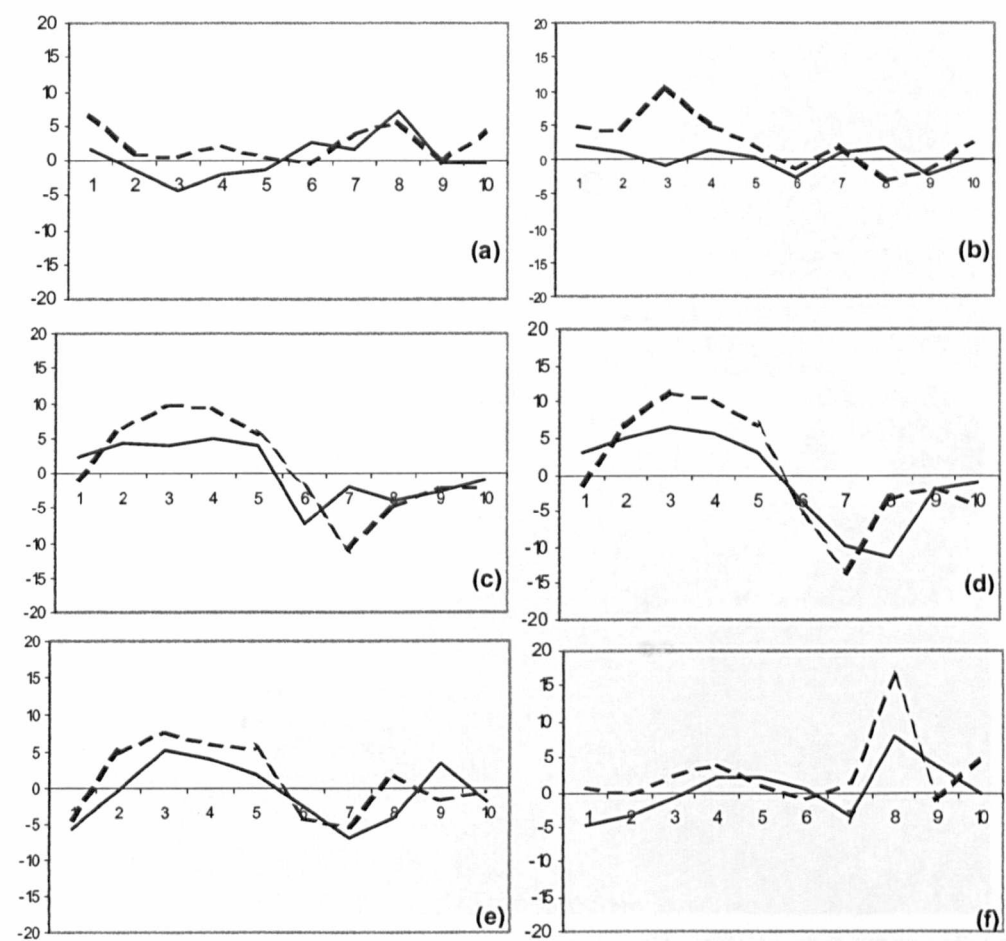


Figure 5.15 Mean velocity in phase encode (v_y) direction in the (a) anterior, (b) anterolateral, (c) inferolateral, (d) inferior, (e) inferoseptal and (f) anteroseptal regions for the same subject. Again the dashed line is the scan without blood saturation and the solid line is with blood saturation.

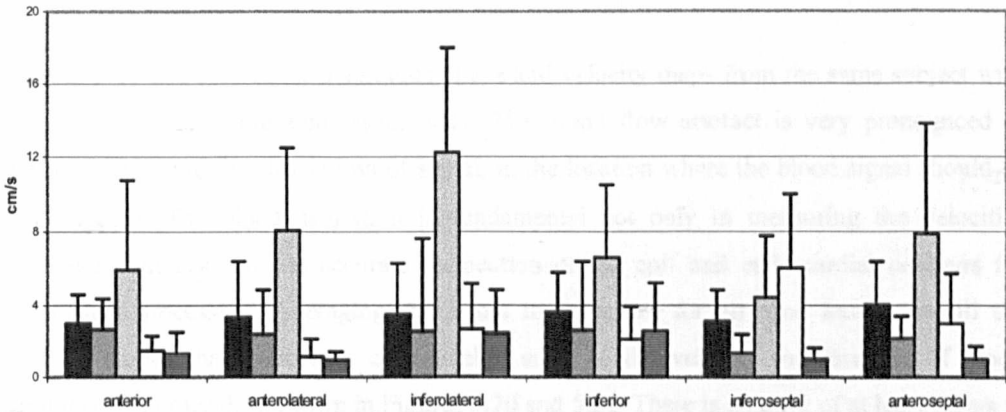


Figure 5.16 Absolute difference in v_y in different regions of the myocardium between the scan with and without blood saturation for five different subjects.

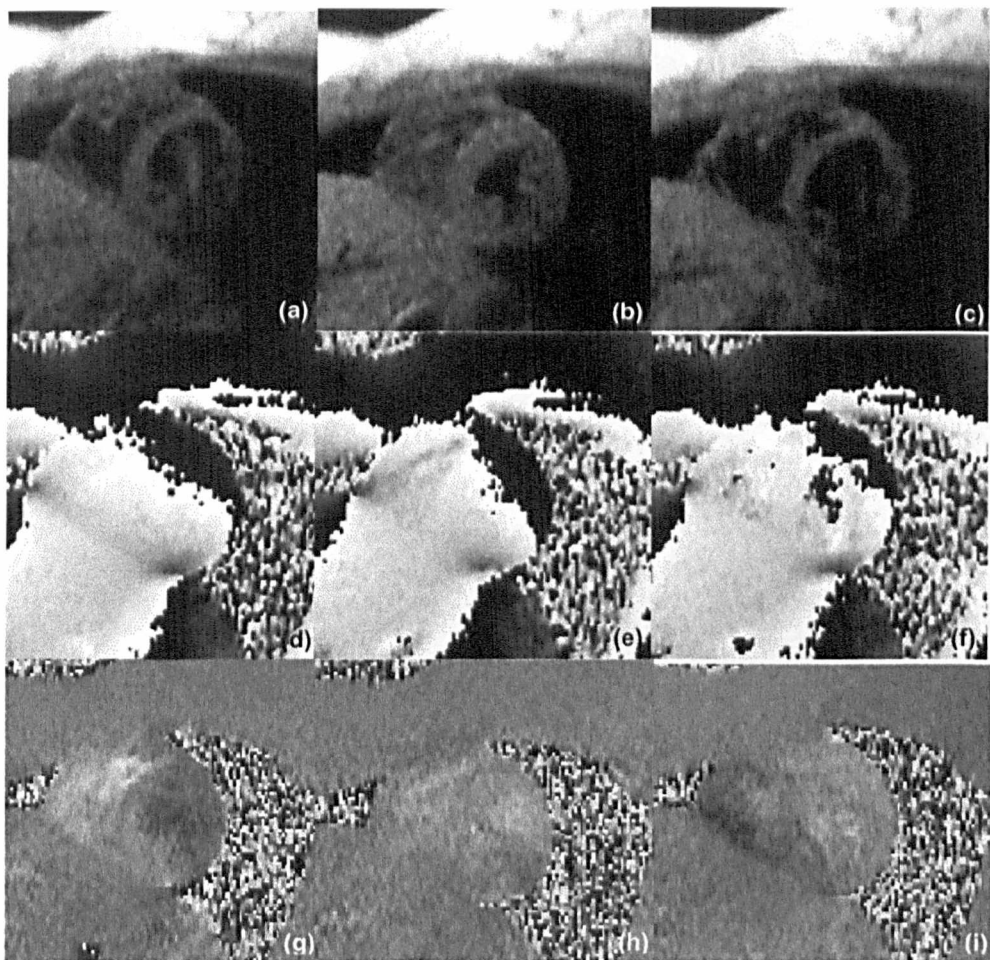


Figure 5.18 Magnitude, phase and velocity images for the mid-ventricular slice corresponding to Figures 5.14-5.17. These images correspond to the scan with black blood saturation. (a, d, g) End-diastole which is the first frame, (b, e, h) systole which is the fifth frame, and (c, f, i) early diastole which is the last frame.

Figures 5.18 and 5.19 show magnitude phase and velocity maps from the same subject with and without blood saturation respectively. The blood flow artefact is very pronounced in Figure 5.19(c) and the classic loss of signal, in the location where the blood signal should be seen. The blood saturation is fundamental not only in measuring the velocities accurately but also for the accurate delineation of the epi- and endo-cardial contours for subsequent processing. Averaging the errors in velocities for all time frames for all the subjects shows that there is a considerable error in the velocity measurement if blood saturation is not used, as shown in Figures 5.20 and 5.21. There is an error of at least 2cm/s in all regions of the heart. This, however, changes during the cardiac cycle and varies from subject to subject.

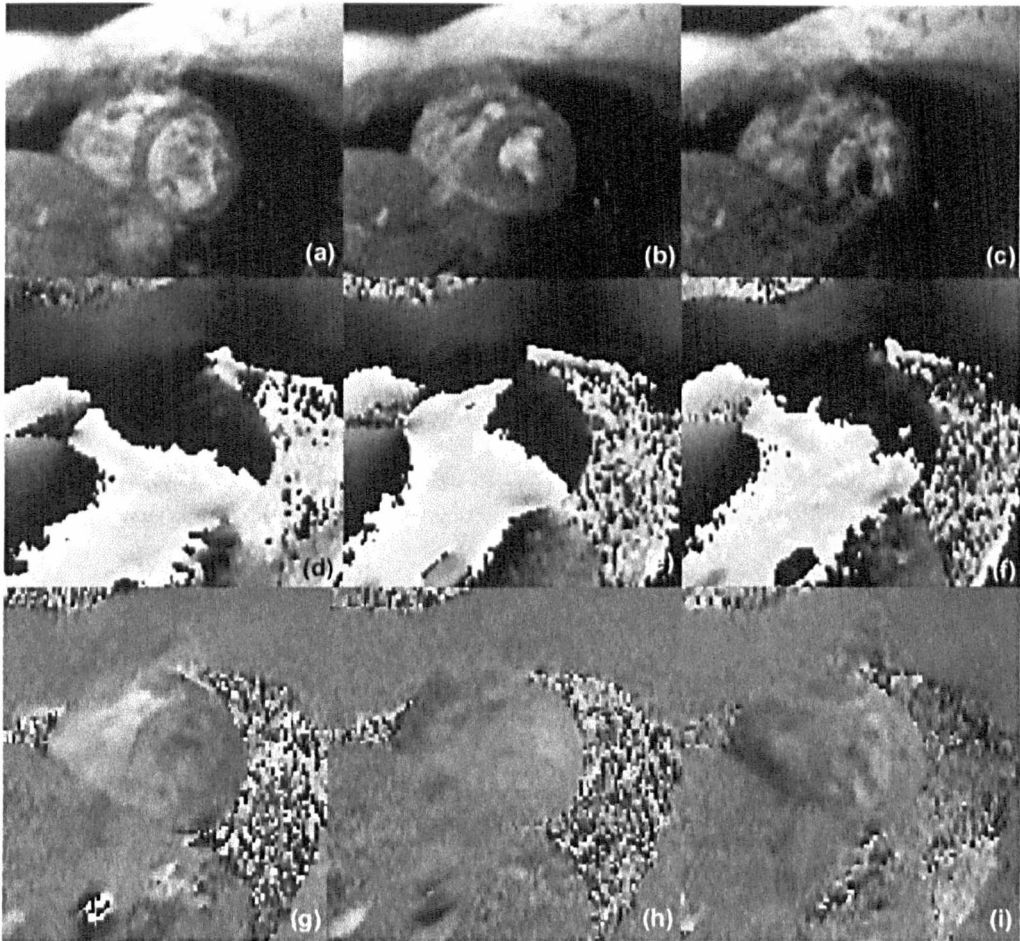


Figure 5.19 Magnitude, phase and velocity images for the mid-ventricular slice corresponding to Figures 5.14-5.17. These images correspond to the scan without black blood saturation. (a, d, g) End-diastole which is the first frame, (b, e, h) systole which is the fifth frame, and (c, f, i) early diastole which is the last frame. The blood flow artefact can be clearly seen on the diastolic images.

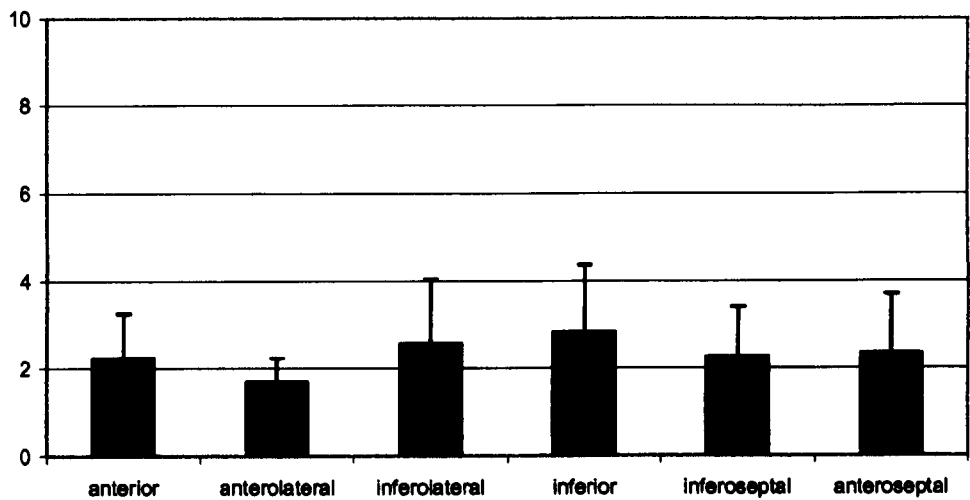


Figure 5.20 Absolute error in v_x averaged over all five subjects for all time frames in the different regions of the heart.

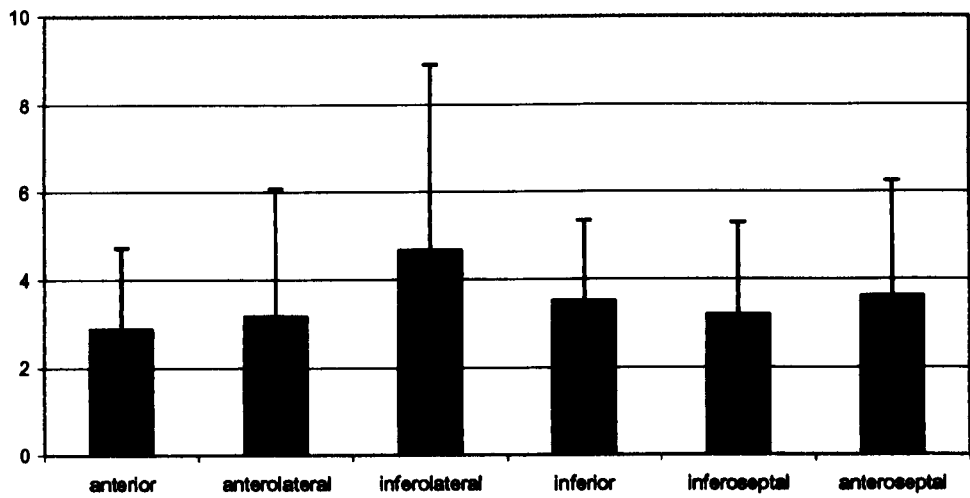


Figure 5.21 Absolute error in v_y averaged over all time frames for all five subjects in different regions of the heart.

5.4.2 Derivation of Strain Rate from MR Velocity Data

One of the most straightforward ways of deriving mechanical indices is the calculation of myocardial strain rate as it allows comparison of function in hearts with different geometries and is not affected by rigid body motion. Strain rate is defined as the spatial derivative of velocity and indicates the rate of change of deformation. The three dimensional Cartesian, Lagrangian strain rate components are calculated as follows:

$$\dot{\epsilon}_{ij} = \frac{1}{2} \left\{ \frac{\partial \dot{u}_i}{\partial x_j} + \frac{\partial \dot{u}_j}{\partial x_i} \right\}, \quad i, j = 1, 2, 3; \quad (5.8)$$

The corresponding components in a cylindrical polar, (r, θ, z) co-ordinate system can be calculated directly as follows, given an origin has been defined for the myocardial ring:

$$\begin{aligned} \dot{\epsilon}_r &= \frac{\partial \dot{u}_r}{\partial r} \\ \dot{\epsilon}_\theta &= \frac{\partial \dot{u}_\theta}{r \partial \theta} + \frac{\dot{u}_r}{r} \\ \epsilon_{r\theta} &= \frac{\partial \dot{u}_r}{r \partial \theta} + \frac{\partial \dot{u}_\theta}{\partial r} \end{aligned} \quad (5.9)$$

Alternatively, they can be calculated by transforming the Cartesian strain components to the polar system:

$$\begin{aligned} \dot{\epsilon}_r &= \dot{\epsilon}_x \cos^2 \theta + \dot{\epsilon}_y \sin^2 \theta + 2\dot{\epsilon}_{xy} \sin \theta \cos \theta \\ \dot{\epsilon}_\theta &= \dot{\epsilon}_x \sin^2 \theta + \dot{\epsilon}_y \cos^2 \theta - 2\dot{\epsilon}_{xy} \sin \theta \cos \theta \\ \dot{\epsilon}_{r\theta} &= (\dot{\epsilon}_y - \dot{\epsilon}_x) \sin \theta \cos \theta + \dot{\epsilon}_{xy} \cos 2\theta \end{aligned} \quad (5.10)$$

Five normal subjects, 2 male, 3 female, mean age 27 ± 5 , were scanned with two versions of the MR velocity mapping sequence. The first was an end-expiratory breath-hold scan as described earlier in Section 5.4.1. Image matrix was 256×96 , field of view 400×300 mm, flip angle 15° , slice thickness 8 mm, venc of 20 cm/s and temporal resolution of 62 ms. The second scan was a respiratory gated version of the same sequence but with a venc of 13 cm/s. The respiratory gating allowed the VNR of the scan to be increased by 54% by increasing the duration of the velocity encoding bipolar gradients. The flexibility in imaging time also allowed the addition of dephase gradients after the readout gradient to destroy any residual transverse magnetisation left from the previous RF pulses, which was found to be a problem on stationary phantom scans. All five subjects were scanned with the respiratory gated sequence with the following parameters: image matrix was 256×100 , field of view 400×300 mm, flip angle 15° , slice thickness 8 mm, venc of 13 cm/s and temporal resolution of 60 ms. The temporal resolution could not be changed due the view-sharing scheme employed.

Radial, circumferential and longitudinal strain rates were calculated for a mid-ventricular slice in each subject from velocity measurements from both sequences. A segmental analysis was carried out to compare the accuracy of the strain rates obtained. As before, the standardised model as recommended by the American Heart Association Writing Group on Myocardial Segmentation and Registration for Cardiac Imaging¹⁴² was used, see Figure 5.12.

Longitudinal strain could be calculated with reasonable accuracy as the long axis motion is much more pronounced. It was found that trends could be seen even with slice thickness of 8mm. The breath-hold sequence did not give adequate in-plane velocity sensitivity to obtain reasonable strain maps. Figures 5.22-5.23 show the circumferential strain rate maps in a normal volunteer at venc 20cm/s and 13cm/s respectively. It can be seen that the diastolic circumferential stretching can be clearly seen in Figure 5.23(g) but is not as clear in Figure 5.22. As the strain rate calculation requires differentiation of the original velocity field, the noise is always magnified producing the effect seen in Figures 5.23 and 5.24. Thus, to improve the visual appearance of the strain maps it becomes necessary to use further processing before display. Figure 5.24-5.27 show the radial and circumferential strain rate in a normal subject using the two sequences, *i.e.*, venc 20cm/s and venc 13cm/s. the higher velocity sensitivity produced more robust in-plane strain rate distributions. Figures 5.28 and 5.29 show a comparison of regional radial and circumferential strain rates averaged for five subjects using the two sequences. It can be seen that although the trend of the strain rate throughout the cardiac cycle is similar in both cases, the values are quite different. The radial strain rate curves especially show a marked change when imaging at venc 13cm/s. The changes could either be due to the increased VNR, leading to an improvement in the strain rate measurement, or they could be due to changes in strain due to respiration as explored in Chapter 4, Section 4.3.1. It should be noted, however, that although the overall trend of the strain rate may be measured accurately in normal subjects, in patients with motion abnormalities this becomes much more difficult. Regional velocities can be much lower depending on the disease process reducing the measured VNR and thus the accuracy of the measured strain rate.

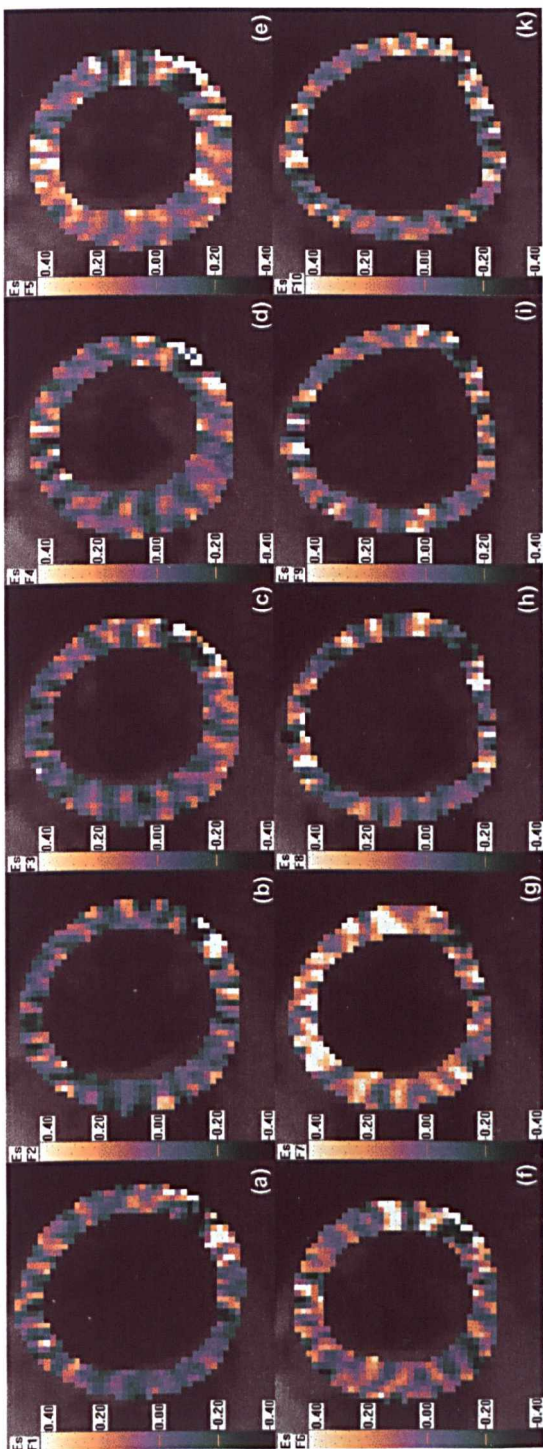


Figure 5.22 Circumferential strain rate distributions in a mid-ventricular slice in a normal volunteer. Venc was set at 20cm/s.

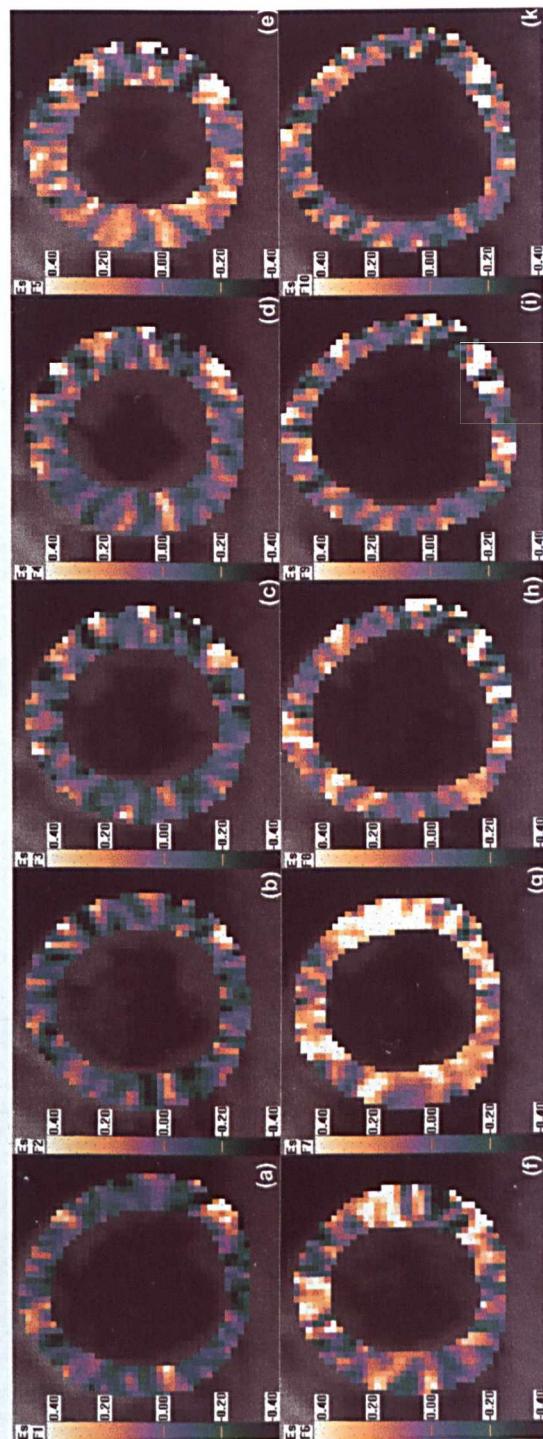


Figure 5.23 Circumferential strain rate distributions in the same slice in the same volunteer calculated at a venc of 13cm/s.

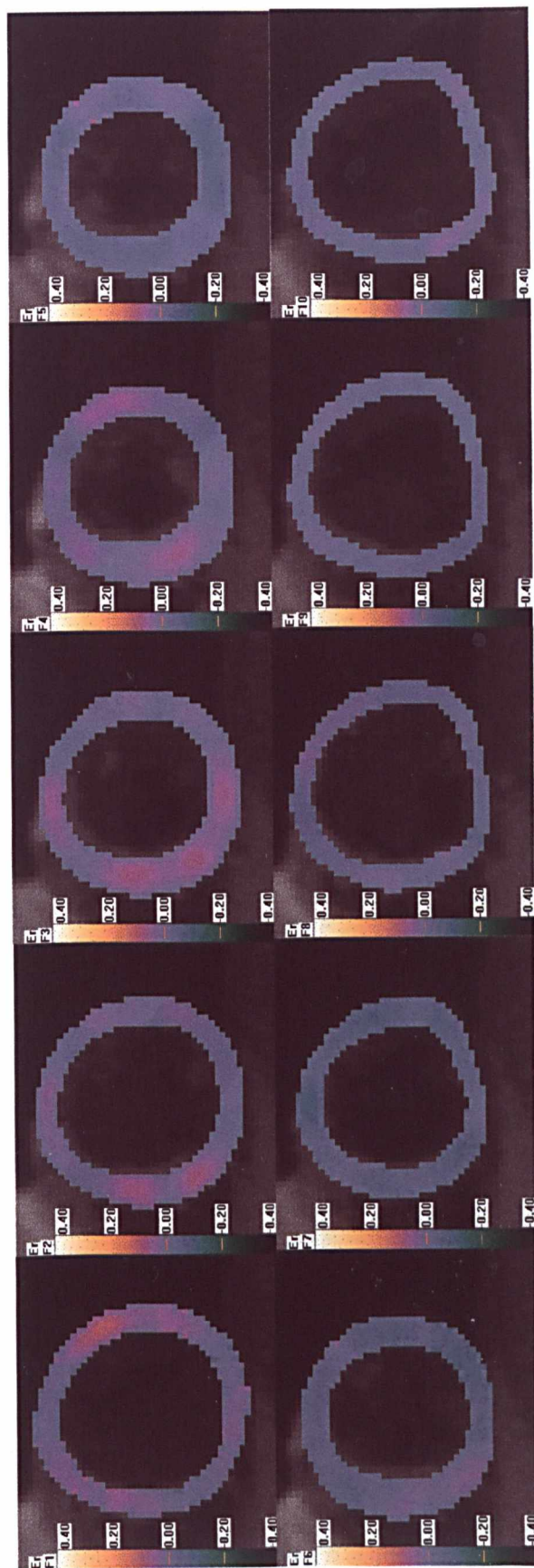


Figure 5.24 Radial strain rate distribution, after further processing, in a normal subject in a mid-ventricular slice using $v_{enc} = 20\text{ cm/s}$. Radial thickening can be seen in systolic frames.

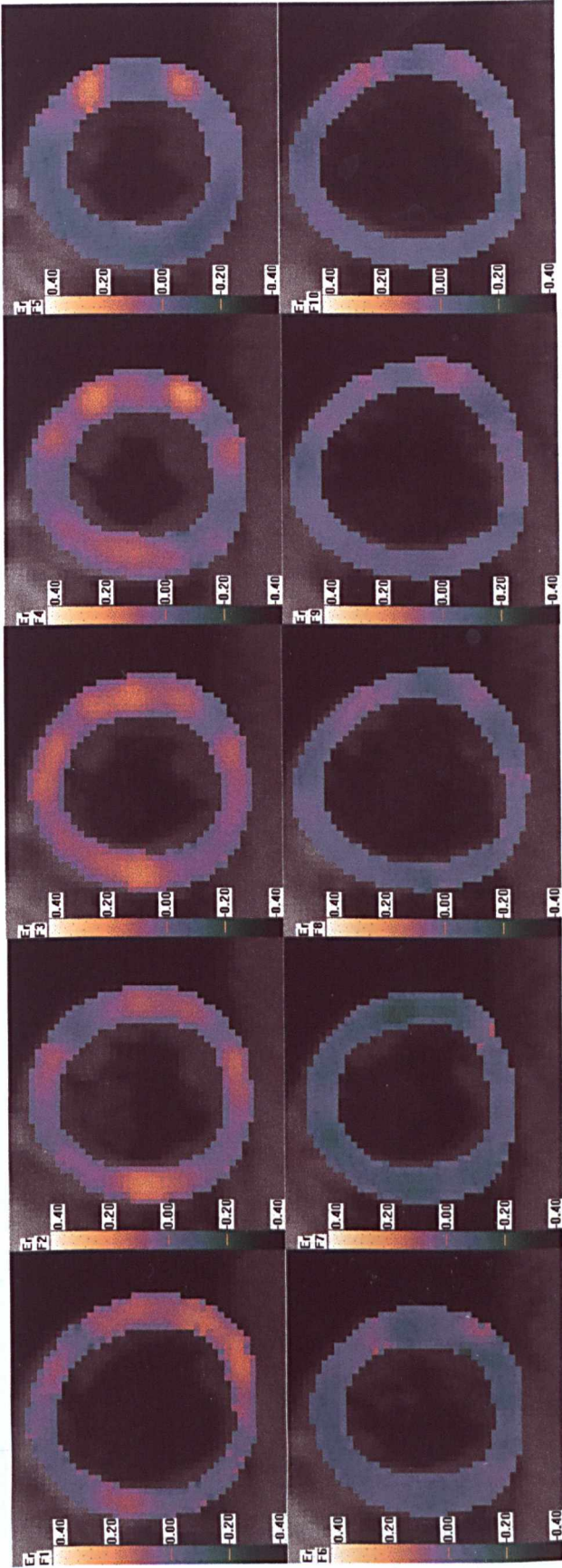


Figure 5.25 Radial strain rate distribution in the same mid-ventricular slice using v_{enc} 13cm/s. The radial strain pattern can now be clearly distinguished in systole when radial thickening, *i.e.*, contraction, is occurring.

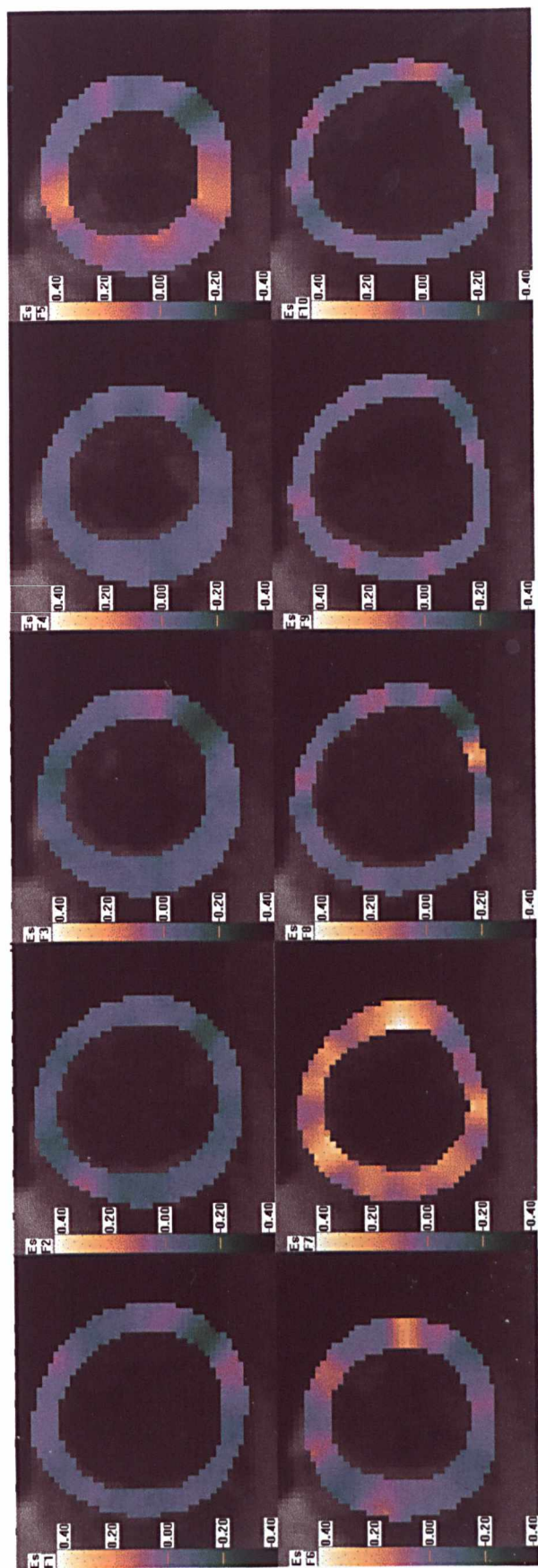


Figure 5.26 Circumferential strain rate distribution in the same normal subject at the same location using v_{enc} 20cm/s. The diastolic circumferential lengthening can be clearly seen in frame 7.

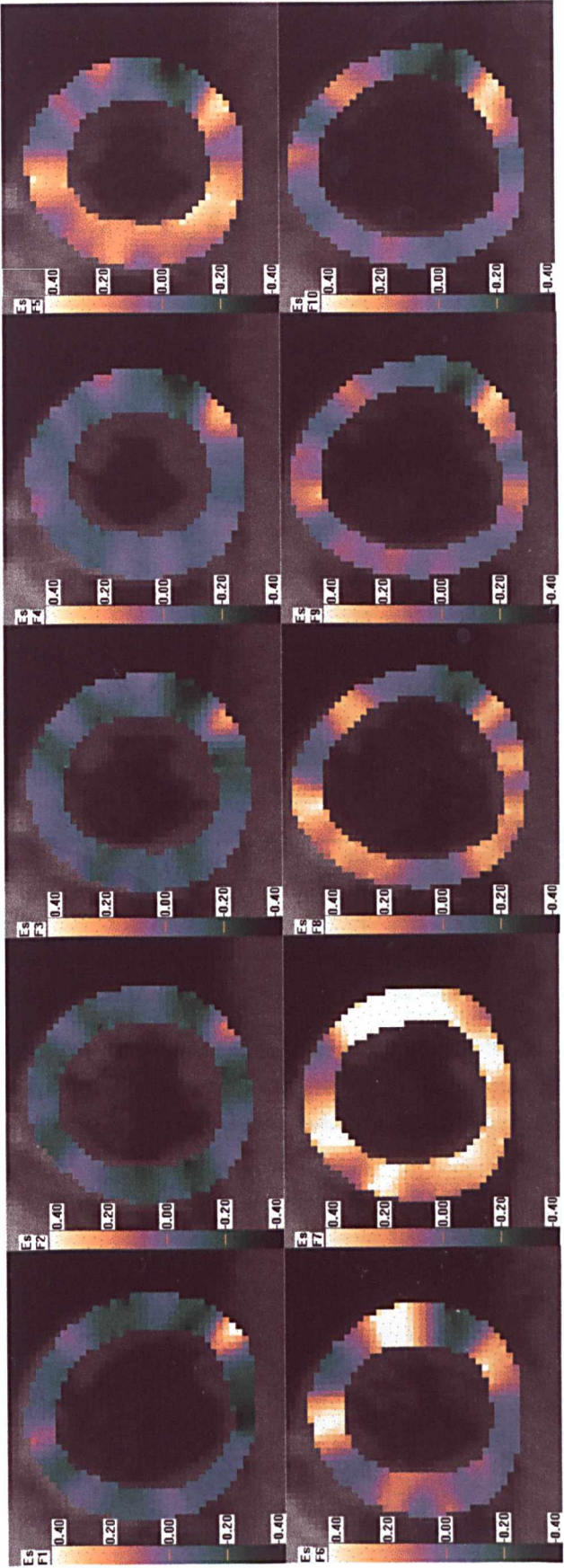


Figure 5.27 Circumferential strain rate distribution in the same subject and same slice using v_{enc} 13cm/s. Now the circumferential lengthening during diastole can be seen from frame 5 through to frame 8 and the regional pattern can also be determined.

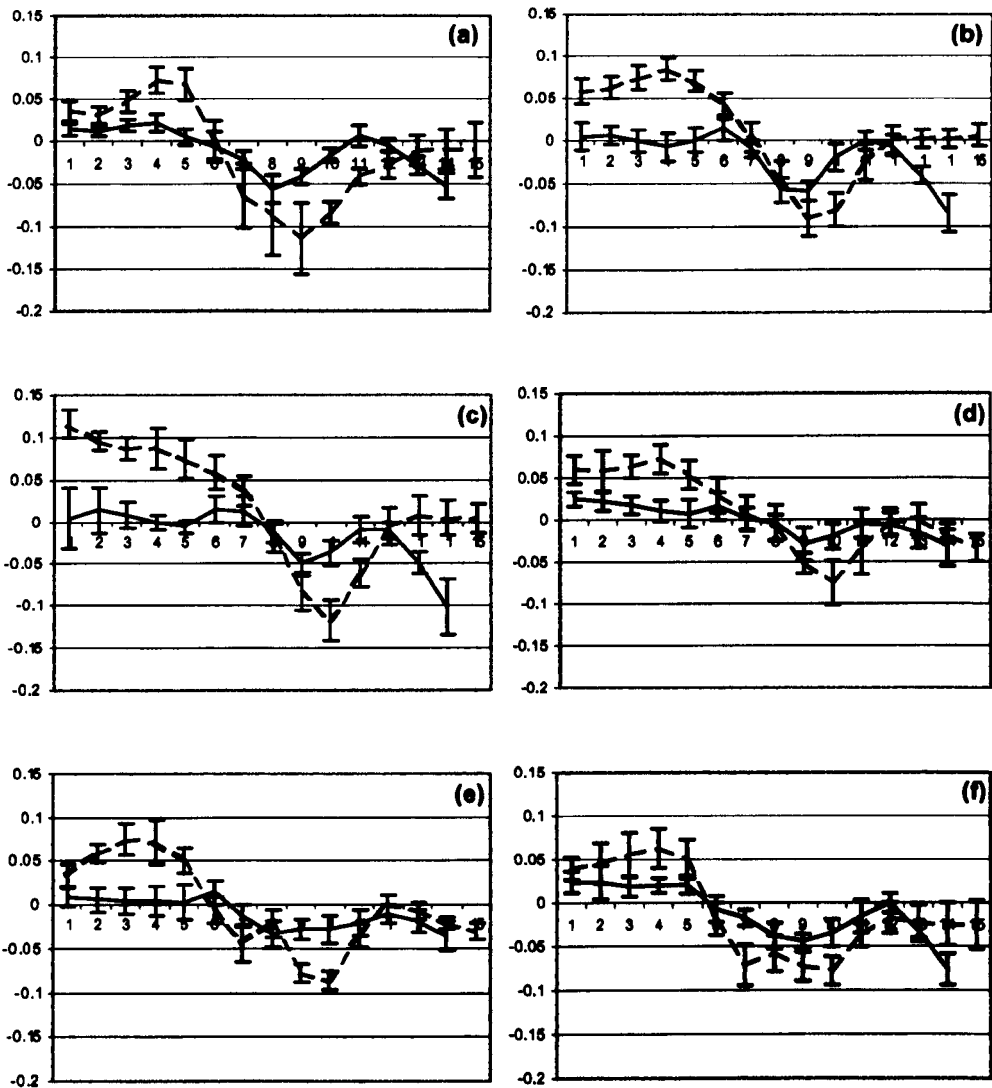


Figure 5.28 Mean radial strain rate for five normal subjects in the (a) anterior, (b) anterolateral, (c) inferolateral, (d) inferior, (e) inferoseptal and (f) anterosseptal regions. The solid line shows the strain rate measured using venc 20cm/s and the dashed line shows that at venc 13cm/s.

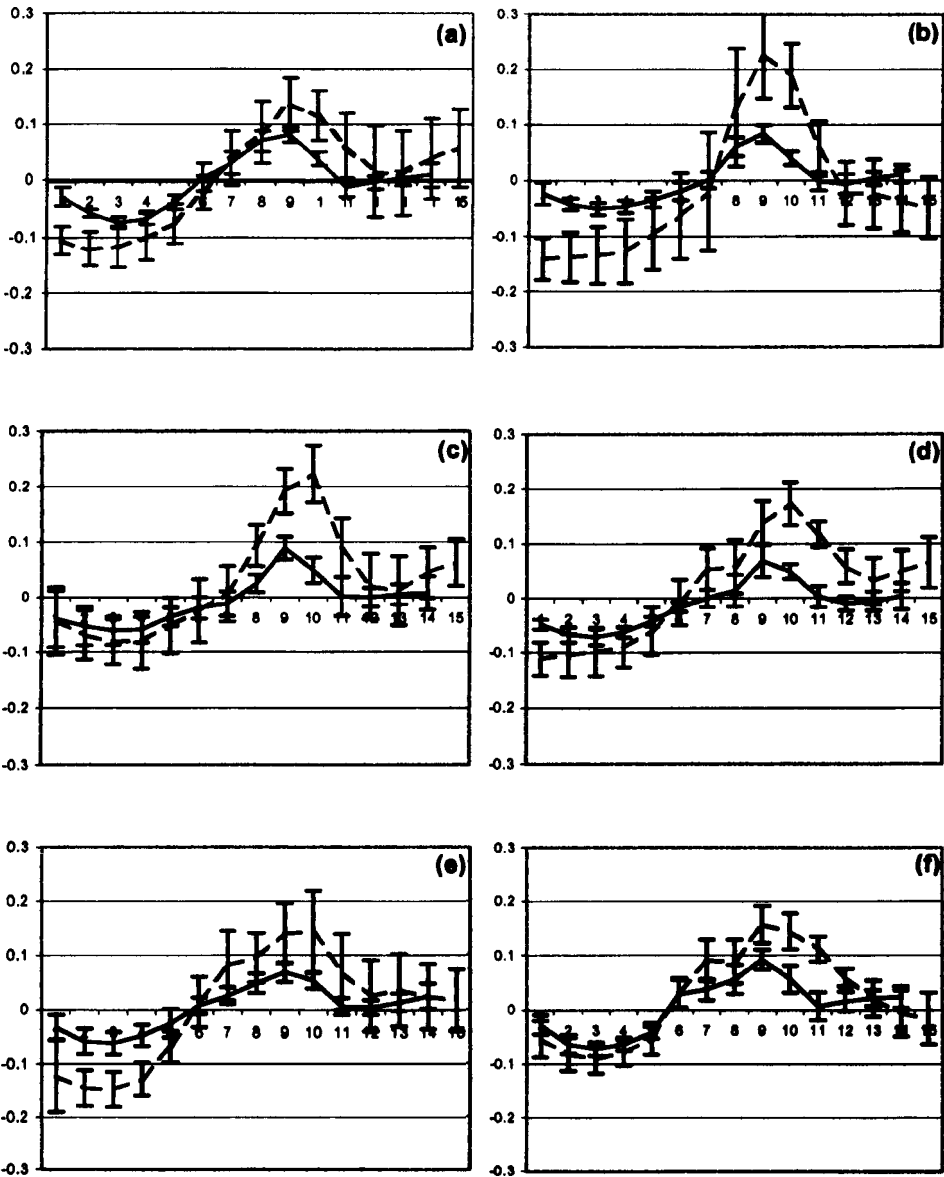


Figure 5.29 Mean circumferential strain rate for five normal subjects in the (a) anterior, (b) anterolateral, (c) inferolateral, (d) inferior, (e) inferoseptal and (f) anterosseptal regions. The solid line shows the strain rate measured using venc 20cm/s and the dashed line shows venc 13cm/s.

5.5 Discussion and Conclusion

Measuring myocardial motion *in vivo* is not an easy task. Although CMR tagging overcomes the difficulties associated with blood flow artefacts, it does not allow a full 3D evaluation of motion and tag-fading makes evaluation of diastolic motion prone to error. Phase contrast velocity mapping allows measurement of 3D motion at all times during the cardiac cycle but is prone to blood flow artefact and has additional limitations due to the velocity sensitivity required. This chapter describes a velocity mapping sequence that overcomes some of these limitations. The sequence employed a spectrally shaped RF pulse to implement blood saturation quickly and efficiently. As the RF pulse only took 6ms to run, it could be applied every other time frame. The efficiency of the pulse in saturating the blood was explored by comparing scans of the same slice with and without blood saturation. It was found that in the diastolic frames, when the blood is flowing rapidly into the LV, there is a distinct difference between the saturated and unsaturated velocity scans. Qualitatively, the effectiveness of blood saturation can be clearly seen in Figure 5.10. Regional analysis of in plane velocities measured in a mid-ventricular slice revealed a distinct difference in the velocities measured with and without blood saturation, strengthening the argument that blood saturation is necessary for accurate measurement of myocardial velocities.

By implementing view-sharing and segmentation, the scan with all four velocity encodings could be fitted into a single breath-hold of 25 heartbeats. This was done by reducing the phase encode matrix to 96. If a higher temporal or spatial resolution was required the breath-hold would become too long. To overcome this limitation, respiratory gating was added to the sequence. This allows a much longer scan time without the introduction of registration errors and thus the potential for higher spatial and temporal resolutions. The velocity sensitivity was also increased to improve the in-plane VNR. This allowed better delineation of radial and circumferential strain rate. Further *in vitro* and *in vivo* validation is however needed to fully explore the potential of this technique.

Velocity mapping potentially allowed higher spatial resolution than tagging as all pixels in the myocardium could be included in calculating the strain rate. Initial strain rate results were calculated and compared for 5 normal subjects. Longitudinal, through-plane, strain rate was calculated robustly due to the higher velocities, and thus higher VNR, in that direction. It was found that radial and circumferential strain rates were subject to noise and did not show any clear trend. Respiratory gating using navigator echoes was incorporated into the sequence to

allow higher velocity sensitivity and imaging under normal physiological conditions. Regional radial and circumferential strain rate was compared in five normal subjects in a mid-ventricular slice using v_{enc} 20cm/s and 13cm/s. Although the trends in circumferential strain rate were similar, those for radial strain rate were not, with the radial strain rates calculated using the higher v_{enc} showing a much clearer trend of thickening during systole and thinning during diastole.

The navigator sequence allowed much higher velocity resolution, however the scan time was lengthened to around one minute per slice, which would not be feasible for a clinical CMR exam. Thus, it becomes necessary to use the breath-hold sequence with a lower velocity resolution. As can be seen from Figure 5.22, this does not give sufficient VNR for reliable strain rate calculation, thus making it necessary to improve the consistency of the in-plane velocity data using post-processing techniques. To achieve this, Chapter 6 describes a novel restoration strategy for extracting the underlying trend of the derived strain rate data.

6 Improving the Consistency of Velocity Data

6.1 Introduction

In Chapter 5, we have shown that it is clinically desirable to obtain strain rate data from the velocity distribution to assess regional myocardial contractility as it is not affected by rigid body motion. Furthermore, it is a percentage measurement, which allows easy comparison between subjects with different cardiac geometries and pathologies. However, current technology does not permit acquisition of robust *in vivo* myocardial velocity data that could be processed to obtain viable strain rate measurements. Although the sequence described in Chapter 5 overcomes a number of problems associated with CMR velocity imaging, it still has some significant limitations. Despite the use of blood saturation to reduce the blood flow artefact and view-sharing to improve the temporal resolution, the velocity data has relatively low VNR for consistent strain rate calculation as demonstrated at the end of Chapter 5. Further processing for improving the consistency of the velocity data needs to be explored.

Since with the current sequence design the hardware performance has already been pushed to the limit, post-processing is the only means of further improving the consistency of the velocity data. Obvious processing methods are smoothing by using simple averaging techniques. This, however, cannot guarantee the physical meaning of the data. Furthermore, it is difficult, in practice, to control the convergence behaviour of the smoothing process. To

circumvent these problems, this chapter introduces a new technique for improving the intrinsic consistency of the velocity data. The method uses the divergence-free constraint and the different VNRs of the three velocity components to improve accuracy of the in-plane velocity distribution. This is achieved by using an optimisation process where the divergence and the error between measured and estimated velocity data are minimised. Results from both simulated and *in vivo* data were used to validate the proposed algorithm. Eleven normal subjects and five ischaemic patients were scanned by using the CMR velocity sequence described in Chapter 5, and regional strain rate was compared by using the normalised strain rate, both in time and space.

6.2 Principle and Methods

Incompressibility is an ideal state of a material, either solid or liquid, under any stress conditions. In reality, the myocardium can be compressed to a certain extent, corresponding to the coronary blood flow changes during the cardiac cycle. However, the actual volume change due to the compressibility of the material can be considered negligible as compared to the apparent volume change produced by the inconsistent velocity distribution. This means that the error due to the incompressibility assumption is always less than that caused by noise in the original velocity dataset. The through-plane velocity data is known to be more robust than the in-plane velocity data. The motion of the heart in the longitudinal direction has been shown to be in the range of $\pm 14\text{cm/s}$, hence the velocity sensitivity of $\pm 20\text{cm/s}$ is adequate to capture it. Therefore, the incompressibility constraint can be used to improve the in-plane velocity by assuming that the longitudinal strain rate is relatively immune to noise.

It should be noted that the incompressibility constraint is generally suitable for analysing the behaviour of fluids. For solids, the corresponding constraint is mass conservation, which is expressed by the strain components rather than the strain rate components. It is the final state of the material that is assessed to see whether the mass is conserved or not. When the displacement or deformation field is not large, the incompressibility constraint is equivalent in nature to the mass conservation constraint because the strain and strain rate are all expressed in linear formats. This kind of geometric linearity will ensure that, if incompressibility holds for each incremental behaviour of a material, its overall behaviour will keep incompressibility (mass conservation) too. However, when the material deforms sufficiently largely into geometric non-linearity, the strain components must be expressed in non-linear formats containing higher order terms of displacement gradients. The incompressibility constraint will

no longer be equivalent to the mass conservation constraint. Thus, even though the strain rate components at each time interval comply with the incompressibility constraint, the resulting integrated displacement and strain field will no longer obey the mass conservation constraint.

6.2.1 Iterative Velocity Field Restoration using the Incompressibility Constraint

By using the relationship derived for the VNR in Section 5.3.3, we can calculate the relative VNR for the through-plane and in-plane velocities. It is known that maximum longitudinal velocity in the heart is in the range of $\pm 15\text{cm/s}$ while in-plane velocities are much lower for most frames of the cardiac cycle, (in the range of $\pm 10\text{cm/s}$), although they may reach up to 14cm/s in peak diastole in healthy young subjects. Based on Equation 5.7 and by setting the SNR to be a constant, the relative VNR of v_z is 0.75 while that of v_x and v_y is 0.5. It is worth noting that the value of 0.5 is only in the radial direction by assuming uniform contraction. In practice, VNR for v_x and v_y is much smaller. Therefore, if we assume that the through-plane motion is measured with a high VNR we can use it to improve the consistency of the in-plane velocity field by using the incompressibility constraint.

The incompressibility of a velocity field $(\dot{u}, \dot{v}, \dot{w})$ is expressed as

$$\frac{\partial \dot{u}}{\partial x} + \frac{\partial \dot{v}}{\partial y} + \frac{\partial \dot{w}}{\partial z} = 0 \quad (6.1)$$

This can be used to improve the consistency of the in-plane data by optimising the following cost function:

$$\text{Cost} = \sum (\tilde{u}_0 - \tilde{u})^2 + \lambda \sum \left(\frac{\partial \dot{u}}{\partial x} + \frac{\partial \dot{v}}{\partial y} + \frac{\partial \dot{w}}{\partial z} \right) \quad (6.2)$$

where \tilde{u}_0 is the error between the measured and calculated in-plane velocities. The purpose of this optimisation is to achieve a balanced improvement in terms of both the velocity distribution and its corresponding divergence. In Equation (6.2), λ is a weighting factor that controls the relative importance of mass conservation and the conformance of the restored and original velocity data. A small weighting factor tends to produce results closer to that of simple smoothing, while an excessive value will ignore the original velocity distribution to suppress the divergence and will finally lead to a flat distribution. The cost function in Equation (6.2) consists of both velocity and its derivatives. An iterative optimisation process is implemented by using a simple steepest descent algorithm.

6.2.2 3D Strain Rate Computation

After velocity restoration, the improved velocity field is then used to compute the three dimensional Cartesian Lagrange strain rate components at each pixel:

$$\dot{\epsilon}_{ij} = \frac{1}{2} \left\{ \frac{\partial \dot{u}_i}{\partial x_j} + \frac{\partial \dot{u}_j}{\partial x_i} \right\}, \quad i, j = 1, 2, 3; \quad (6.3)$$

where the subscript $i, j = 1, 2, 3$ correspond to the x, y and z axes, respectively. In short axis images, the myocardium generally takes the shape of a ring, thus it is reasonable to use a cylindrical co-ordinate system (r, θ, z) instead of the Cartesian co-ordinate system (x, y, z) . The radial and circumferential strain rate components can be obtained to show the expansion and contractility of the myocardium along its circular region. They are more useful in clinical settings as radial and circumferential strain rate are more intuitive measures of function than ϵ_x and ϵ_y . In practice, the computed radial and circumferential strain rate components are dependent upon the location of the origin of the cylindrical co-ordinate system, in this thesis the origin of the coordinate system is defined to be at the centre of the myocardial mass.

Therefore, the radial and circumferential strain rate components are derived from the following equations:

$$\begin{aligned} \dot{\epsilon}_r &= \frac{\partial \dot{u}_r}{\partial r} \\ \dot{\epsilon}_\theta &= \frac{\partial \dot{u}_\theta}{r \partial \theta} + \frac{\dot{u}_r}{r} \\ \epsilon_{r,\theta} &= \frac{\partial \dot{u}_r}{r \partial \theta} + \frac{\partial \dot{u}_\theta}{\partial r} \end{aligned} \quad (6.4)$$

When mapped back to the Cartesian coordinates, we have:

$$\begin{aligned} \dot{\epsilon}_r &= \dot{\epsilon}_x \cos^2 \theta + \dot{\epsilon}_y \sin^2 \theta + 2\dot{\epsilon}_{xy} \sin \theta \cos \theta \\ \dot{\epsilon}_\theta &= \dot{\epsilon}_x \sin^2 \theta + \dot{\epsilon}_y \cos^2 \theta - 2\dot{\epsilon}_{xy} \sin \theta \cos \theta \\ \dot{\epsilon}_{r,\theta} &= (\dot{\epsilon}_y - \dot{\epsilon}_x) \sin \theta \cos \theta + \dot{\epsilon}_{xy} \cos 2\theta \end{aligned} \quad (6.5)$$

To simplify inter and intra subject comparisons, we introduced a scalar index to measure the overall strain rate magnitude defined by:

$$|\dot{\epsilon}| = \sqrt{\dot{\epsilon}_r^2 + \dot{\epsilon}_\theta^2 + \dot{\epsilon}_z^2} \quad (6.6)$$

Figure 6.1 illustrates the overall approach of the proposed method where the first step is the smoothing of the velocity field to be used as a starting point of the iterative optimisation process. The proposed algorithm leads to a physically plausible and spatially consistent 3D velocity field, which can subsequently be used to calculate the contractility of the myocardium.

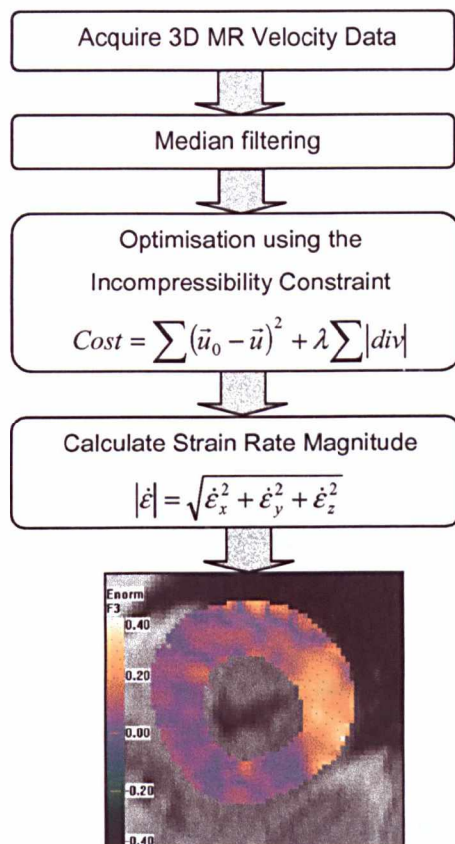


Figure 6.1 Flowchart showing method adopted to calculate the strain rate magnitude.

6.3 Validation

6.3.1 Simulation Dataset

To evaluate the accuracy of the proposed method, a 3D simulation dataset was produced which corresponded to a cylindrical structure under cyclic deformation involving expansion, contraction and torsion. All of the three velocity components were simulated with the incompressibility constraint. The dataset aimed to simulate cardiac motion and the actual CMR imaging set-up where the imaging planes were fixed in space while the mass points moved cyclically.

The velocity components are:

$$\begin{aligned}\dot{u} &= K_x(x, y) \cos \varpi t \\ \dot{v} &= K_y(x, y) \cos \varpi t \\ \dot{w} &= K_z(x, y, z) \cos \varpi t\end{aligned}\tag{6.7}$$

The displacement components are the summation of velocity components for the same mass point over time, *i.e.*,

$$\begin{aligned}u &= K_x(x, y) \frac{\sin \varpi t}{\varpi} \\ v &= K_y(x, y) \frac{\sin \varpi t}{\varpi} \\ w &= K_z(x, y, z) \frac{\sin \varpi t}{\varpi}\end{aligned}\tag{6.8}$$

where ϖ is the simulated cyclic speed. The in-plane kernel functions K_x and K_y are predefined 2D functions that are independent of the longitudinal axis z , and K_z is the longitudinal kernel function derived from K_x and K_y based on the divergence free constraint. That is,

$$K_z(x, y, z) = -\left(\frac{\partial K_x}{\partial x} + \frac{\partial K_y}{\partial y}\right) \cdot z + K_0(x, y)\tag{6.9}$$

where $K_0(x, y)$ is a constant 2D function. For the sake of simplicity and without losing generality, we chose $K_0(x, y) = 0$.

In the cylindrical co-ordinate system, the in-plane kernel velocity functions are defined as

$$\begin{aligned}K_r(r, \theta, z) &= A\left[1 - \left(\frac{r}{b}\right)^2\right] + B\left[\left(\frac{r}{a}\right)^2 - 1\right] \\ K_\theta(r, \theta, z) &= C\left[1 - \left(\frac{r}{b}\right)^2\right] + D\left[\left(\frac{r}{a}\right)^2 - 1\right]\end{aligned}\tag{6.10}$$

where A, B, C, D are constants, and a, b are the inner and outer radius of the cylinder. The corresponding longitudinal kernel function of (6.9) can now be defined as:

$$K_z(r, \theta, z) = -\left(\frac{\partial K_r}{\partial r} + \frac{1}{r} \frac{\partial K_\theta}{\partial \theta} + \frac{K_r}{r}\right) \cdot z\tag{6.11}$$

In this study, the cyclic speed ϖ in (6.7) was chosen as

$$\varpi = \frac{2\pi}{16}\tag{6.12}$$

which resulted in sixteen cine frames per repetition cycle.

It should be noted that, because the mass points are constantly moving in 3D while the imaging planes are spatially fixed during data acquisition, certain numerical considerations must be observed. That is, we cannot calculate and record the values at each pixel by substituting the initial coordinates in (6.10) and hence (6.11). Otherwise, we will be effectively assuming that the imaging planes are following the material over time. An algorithm based on backward propagation was used to avoid this problem. That is, given a current mass point of interest $P_t(x, y, z)$, its retrospective origin, $P_{t0}(x_0, y_0, z_0)$, is backward tracked. If it is within a predefined mass region, *i.e.*,

$$a \leq r(x_0, y_0) \leq b \quad (6.13)$$

the velocity components are recorded. Otherwise, it means that the current mass point is coming from a point that is outside the predefined mass region. This forms an inverse search problem, *i.e.*, at the current mass point $P_t(x, y, z)$, find its original point $P_{t0}(x_0, y_0, z_0)$, such that

$$\begin{aligned} x &= x_0 + u(x_0, y_0, z_0) \\ y &= y_0 + v(x_0, y_0, z_0) \\ z &= z_0 + w(x_0, y_0, z_0) \end{aligned} \quad (6.14)$$

Based on this algorithm, a divergence free dataset consisting of 6 slices with a complete cycle covering 16 time frames was generated.

6.3.2 Image Acquisition for In Vivo Validation

In vivo validation was carried out on eleven normal volunteers and six symptomatic patients. The velocity mapping sequence described in Chapter 5 was used which consisted of a specially designed black-blood RF pulse being applied every other time frame followed by the imaging. It also incorporated a view-sharing technique to reduce the total scan time needed, hence allowing one reference image and three velocity encoded images to be acquired in a single breath-hold. The velocity encoding range in each direction was $\pm 20\text{cm/s}$. The spatial resolution was $1.6 \times 3.1 \times 8 \text{ mm}^3$ with a temporal resolution of 62ms. The in-plane velocity data was made more consistent by using the restoration scheme described in Figure 6.1. A full 3D dataset, *i.e.*, around 10 slices covering the whole of the LV, was acquired when time permitted. Otherwise, at least 4-5 adjacent mid-ventricular slices were acquired. The strain rate for all three dimensions, as well as the resulting strain rate magnitude, was calculated.

6.3.3 Normalisation

For statistical comparison, both spatial and temporal normalisation is required. Normalisation of the 11 normal datasets into a mean normal value entails anatomical and temporal alignment of all datasets. This is achieved by first choosing the mid-ventricular slice from each 3D dataset and manually selecting the RV insertion as the anatomical alignment landmark. A polar co-ordinate system is chosen with the origin at the centre of the rectangle that compactly covers the LV region. Each image is then rotated to ensure that the RV insertion is set at the 10 o'clock position, thus setting the anterior region to the top of the resulting image. The myocardial ring is then divided into a set of equally spaced radial lines crossing the myocardium once. The inner and outer boundaries on each radial line are detected automatically and 10 equally spaced control points are introduced, therefore allowing the data for all subjects to be represented by the same number of control points placed at the same anatomical locations. Temporal alignment is achieved by choosing the systolic and diastolic frames for each dataset and interpolating or deleting frames as necessary. Finally, the mean shape and strain rate field for the 11 normal datasets could be obtained and displayed for comparison to symptomatic patients. Figure 6.2 illustrates the overall procedures used.

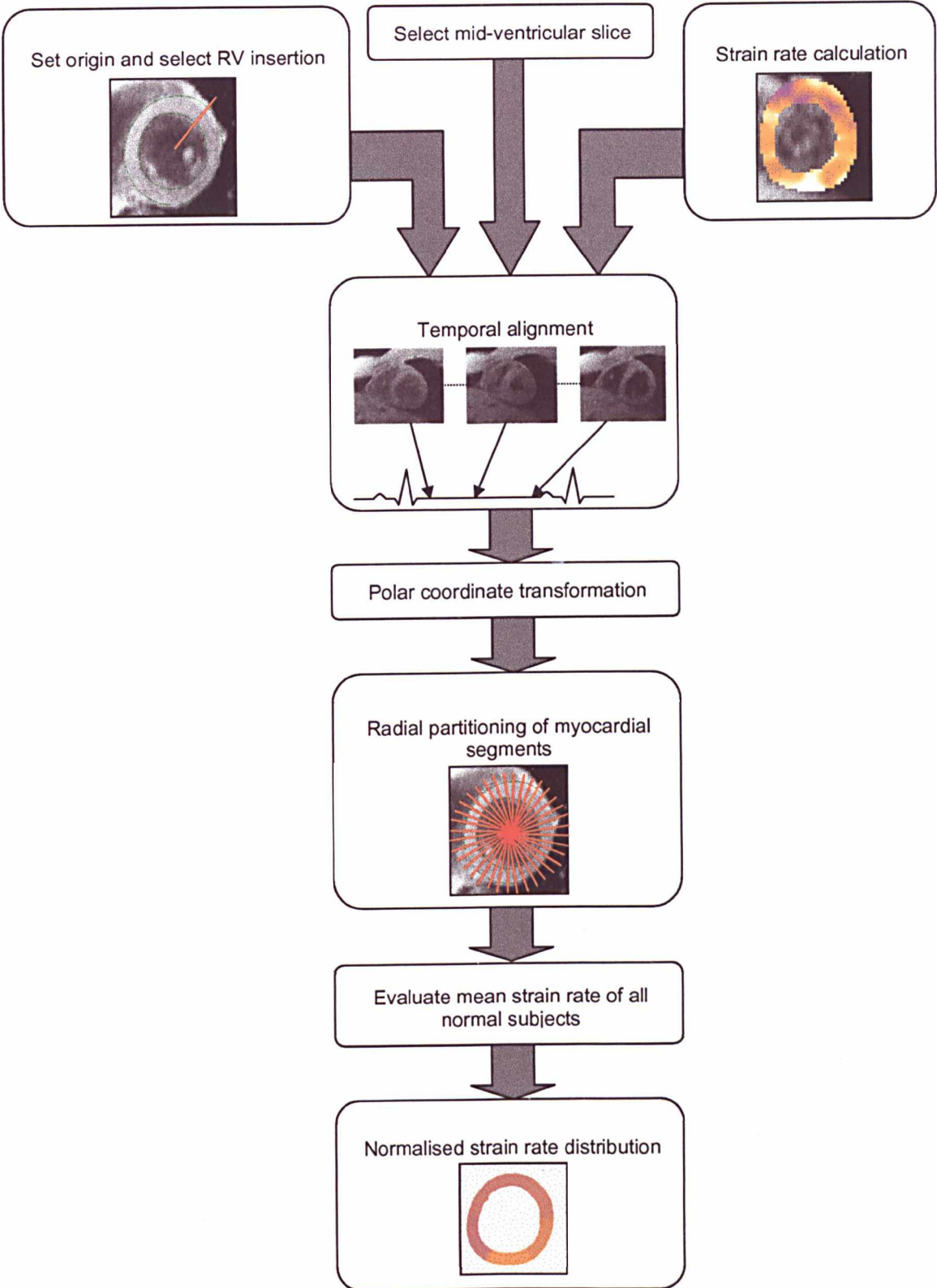


Figure 6.2 Flowchart showing the normalisation process used to find the mean strain rate for all normal subjects.

6.4 Results

6.4.1 Choice of Weighting Factor

The optimisation strategy of Equation 6.7 involves the selection of λ . The optimal weighting factor should be found in such a way that the weighting factor itself is treated as an independent variable. This is a typical Lagrange Multiplier problem that can be solved by the first-order technique described in Section 4.2.6. Since the divergence operator involves the derivatives of the velocity components, it has been found that the choice of step size has a significant impact on the convergence of the algorithm. This is highlighted in Figures 6.3 and 6.4, which show that, with step size exceeding $\delta=0.1/\lambda$, the iteration diverges rapidly. On the other hand, if the step size is too small, the iteration will converge too slowly making the process equivalent to the one with a fixed weighting factor. An optimum step size is located in the range of 0.02 to 0.05.

In this study, we have also evaluated the efficacy of the first-order technique and that with a fixed λ value. Figures 6.5 and 6.6 show that with λ fixed between 10 and 100, the algorithm can converge consistently, resulting in a small overall divergence residual of the entire volume.

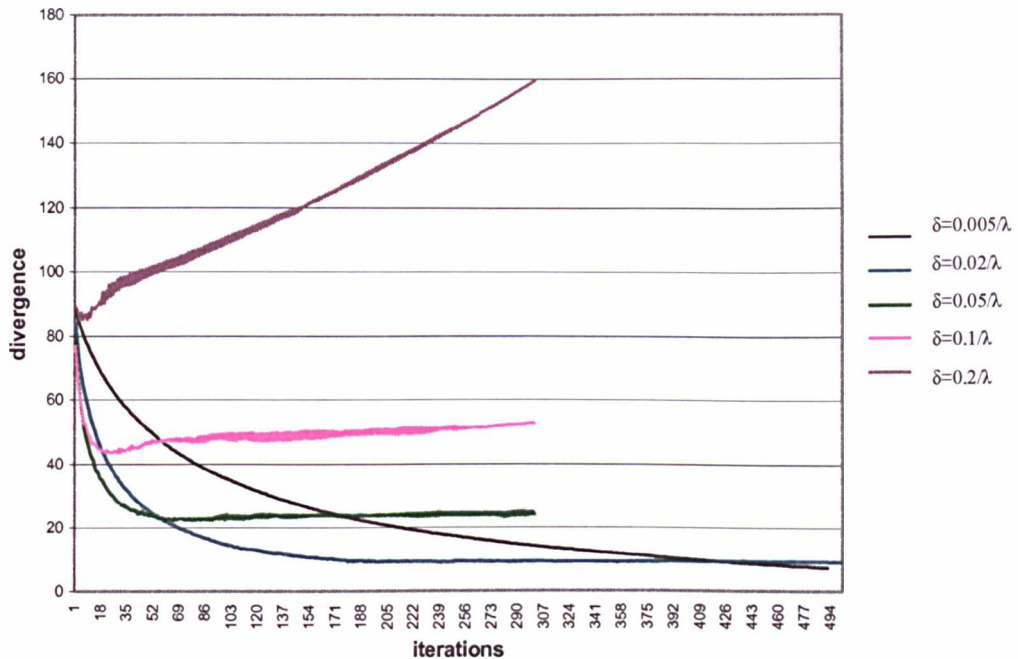


Figure 6.3 Plot of divergence against number iterations for the first-order technique for different step sizes with the starting λ set at 100.

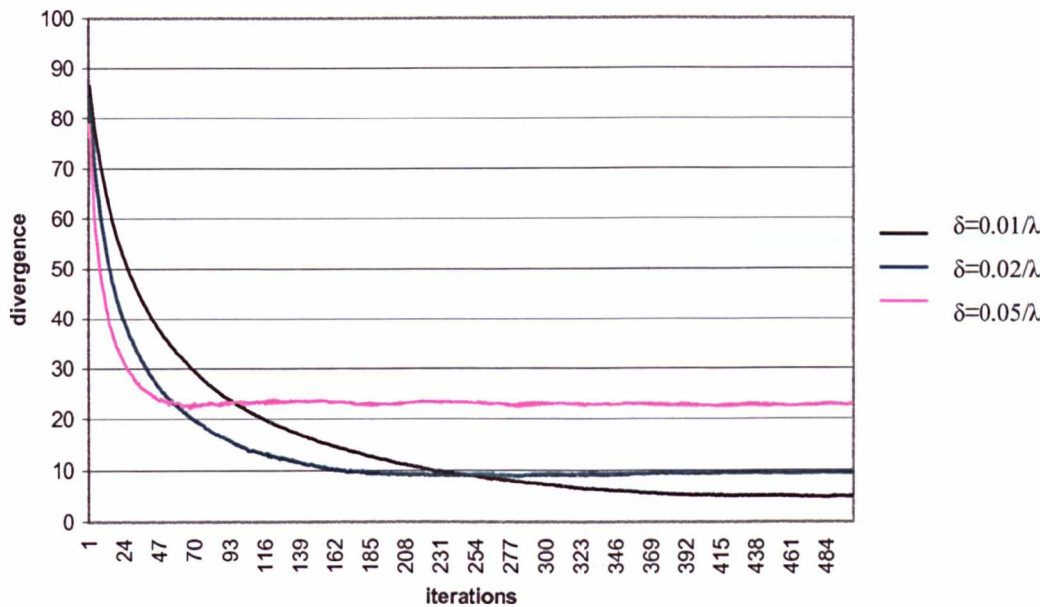


Figure 6.4 Plot of divergence against number of iterations for fixed $\lambda=100$ for different step sizes.

6.4.2 Simulation Data

To examine the robustness and accuracy of the proposed algorithm, the numerical simulation datasets outlined earlier were used. Velocity vector maps, strain rate and divergence were compared to those from simple smoothing and the total variation based restoration method. Figure 6.7 illustrates the vector maps, strain rates and divergence from the three methods with a simulation dataset with 50% additive noise. It can be seen that although the restored vector maps by different methods appear to be similar and noise free, the strain rate results show a marked difference. More importantly, the divergence free constraint is not met for simple smoothing or the vector restoration algorithm.

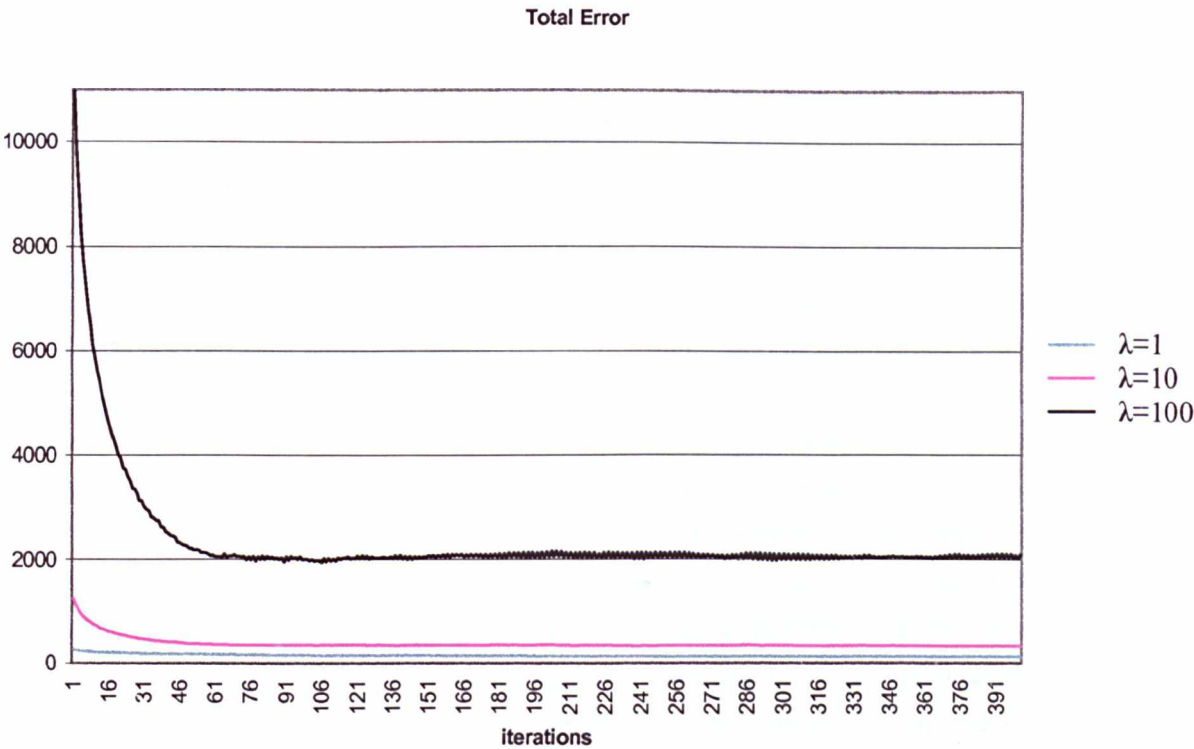


Figure 6.5 Plot of total cost against number of iterations for different values of λ .

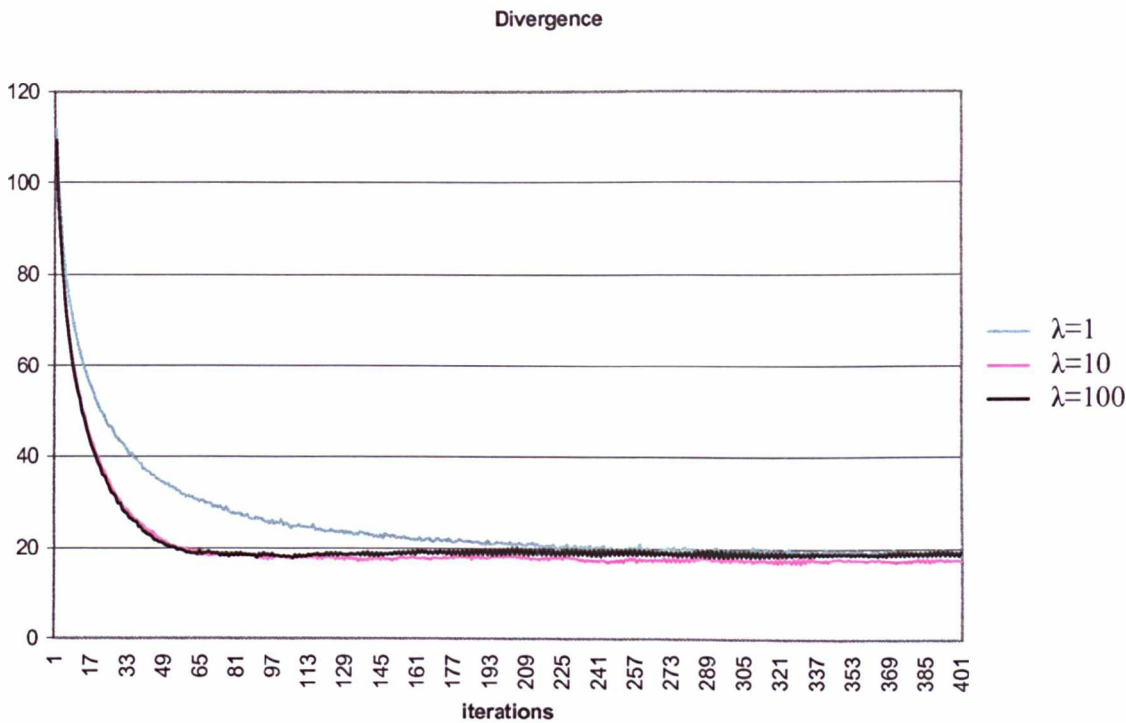


Figure 6.6 Plot of divergence for different values of λ .

Figure 6.5 shows that the $\lambda=1$ curve has a lower total cost. However, it should be noted that the result is not physically correct as can be seen from Figure 6.8(a). If optimisation is not used and only simple smoothing techniques are applied, the divergence is non-zero as demonstrated in Figure 6.7(i). It is evident the new method not only achieves the overall consistency of the velocity data but also guarantees the underlying physical meaning of the data. The result in Figure 6.7 also indicates that to enable the use of strain rate for comparing myocardial strain rate, the requirement on the quality of the velocity data is high. Figure 6.8 shows the behaviour of the strain rate magnitude and divergence at different values of λ after the same number of iterations. It is evident that a higher value of λ biases the optimisation towards a divergence free constraint, while a lower value biases it towards the error term. Thus, a lower value will eventually lead to the velocity field reverting back to the original noisy velocity field, as can be deduced from Equation (6.2).

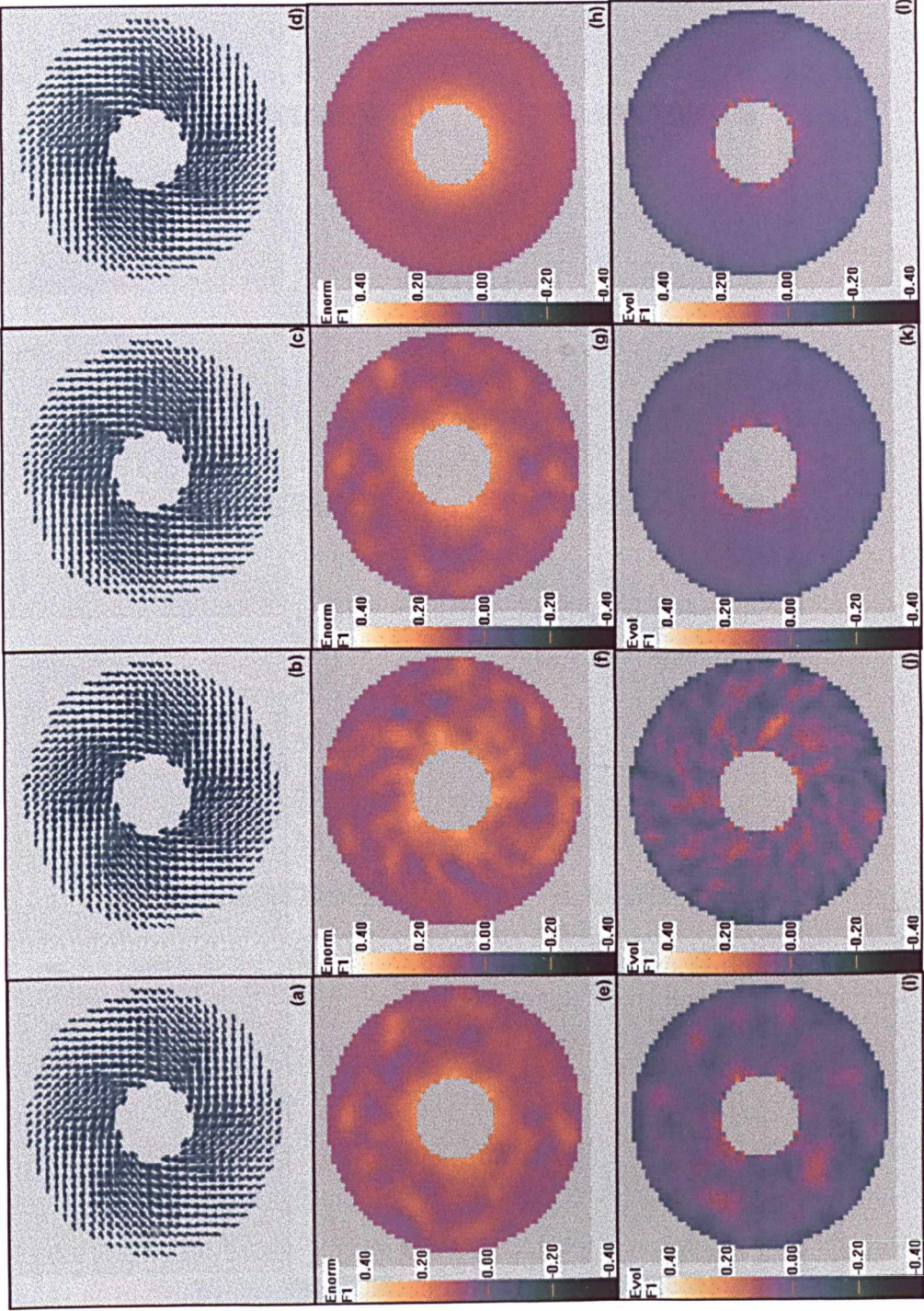


Figure 6.7 Comparison of restored velocity and derived strain rate for different techniques. First column shows the result from simple smoothing (a, e, i), second column using the vector restoration described in Section 4.2.6 (b, f, j), third column from the divergence free algorithm (c, g, k) and last column shows the original noise free dataset for comparison (d, h, l).

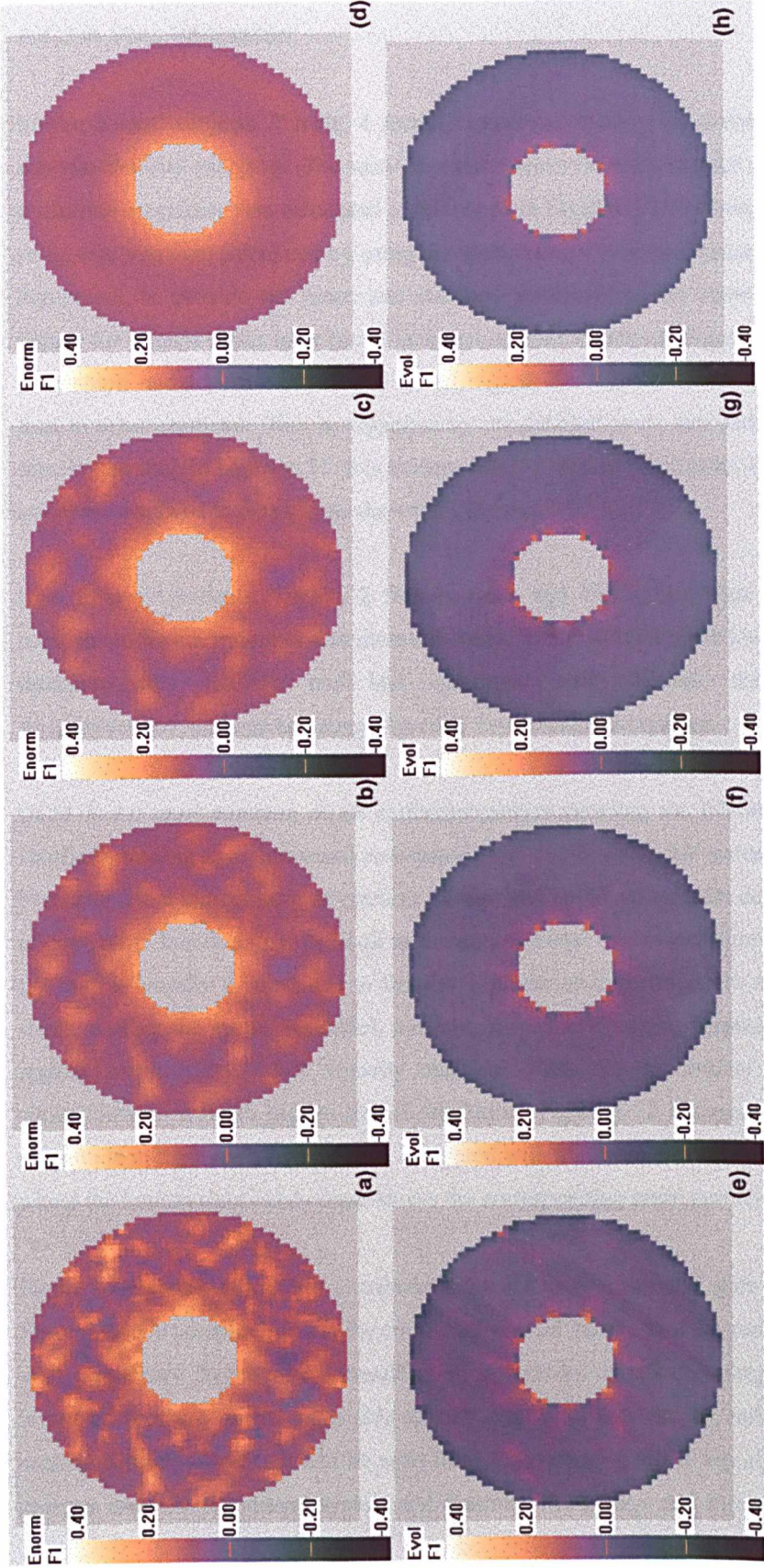


Figure 6.8 The strain rate magnitudes and divergences obtained for the simulation dataset using different values of Lamda. (a) $\lambda=1$, (b) $\lambda=10$, (c) $\lambda=100$ and (d) original noise free dataset for comparison.

6.4.3 In Vivo Validation

Eleven normal subjects, 7 male, 4 female, mean age 25 ± 5 , were scanned using MR phase contrast velocity mapping. The mid-ventricular slice for each subject was chosen and the strain rate magnitude was calculated as described in Section 6.2. Statistical distribution of the strain rate was then calculated by using the spatio-temporal normalisation method outlined in Figure 6.2, to provide the mean and standard deviations of the standardised distribution. Figure 6.9 depicts strain rates found in a typical normal subject. Figure 6.10 shows that the peak strain rate occurred in diastole for all regions but slightly earlier in the septal regions than in other segments. This is supported by the detailed strain rate distribution shown as a false colour map in Figure 6.11. It is evident that the highest strain rates (orange on the colour scale) are achieved in diastole, as shown in Figures 6.11(i-k).

Data from six patients, 4 male, 2 female, mean age 49 ± 13 , was also collected to enable comparison between normal and diseased states. Three patients were known to have dilated cardiomyopathy (DCM), one had ischaemic heart disease, one had undergone pericardiectomy, and one had a rare disorder, Eisenmenger's complex.

DCM is the most common of all cardiomyopathies entailing the dilatation of one or both ventricles leading to an increased end-systolic and end-diastolic LV volume. However, it has been found that indices such as ejection fraction and stroke volume are decreased, due to loss of contractile function. It is difficult to measure regional myocardial function in DCM as the LV wall is usually thinned due to the development of hypertrophy to reduce systolic wall stress, making the spatial resolution available from CMR tagging impractical for examining regional contractility. CMR velocity mapping offers the opportunity to assess regional contractility at a much higher spatial resolution. Figure 6.12 demonstrates the strain rate magnitude in the three DCM patients compared with the mean normal strain rate distribution, where the bottom right hand corner shows the corresponding mean normal strain rate frame.

Figure 6.13 shows strain rate distributions for the mid-ventricular slice in the patient with Eisenmenger's complex. This is the combination of an interventricular septal defect combined with pulmonary hypertension, resulting in a right-to-left shunt through the defect. The increased pressure on the right side usually results in a thickened and hypertrophied RV causing septal deviation. It can be seen from Figure 6.13 that the septal region experiences changes in strain rate during systole and diastole. The antero- and inferolateral regions also

have high strain rates associated with the motion needed to compensate for the lack of septal motion caused by equivalence of pressure in the two ventricles.

Figure 6.14 shows the segmental strain rate for a patient with ischaemic heart disease. Ischaemic heart disease is associated with a low oxygen state in part of the myocardium usually resulting from coronary artery disease. More details on the development of ischaemia can be found in Section 2.8. In this study, one patient had ischaemic heart disease caused by stenosis of the right coronary artery. It can be seen from Figure 6.14 that this led to a loss of function in the septal wall with enhanced contraction in the lateral wall.

For the six patients studied, one patient had a history of perimyocarditis leading to pericardial constriction, which in turn led to a pericardiectomy two years previous to the CMR scan. Pericardiectomy involves the removal of the pericardium and hence the motion of the heart is no longer constricted leading to abnormal deformation of the LV during cardiac cycle. This can be seen from the elongated shape adopted by the LV during diastole. The motion of the LV is also governed by how much and which regions of the pericardium have been removed during surgery. Figure 6.15 clearly illustrates how only the anterior regions seem to be developing strain, as compared to normals where higher strain rates are achieved in the inferior region.

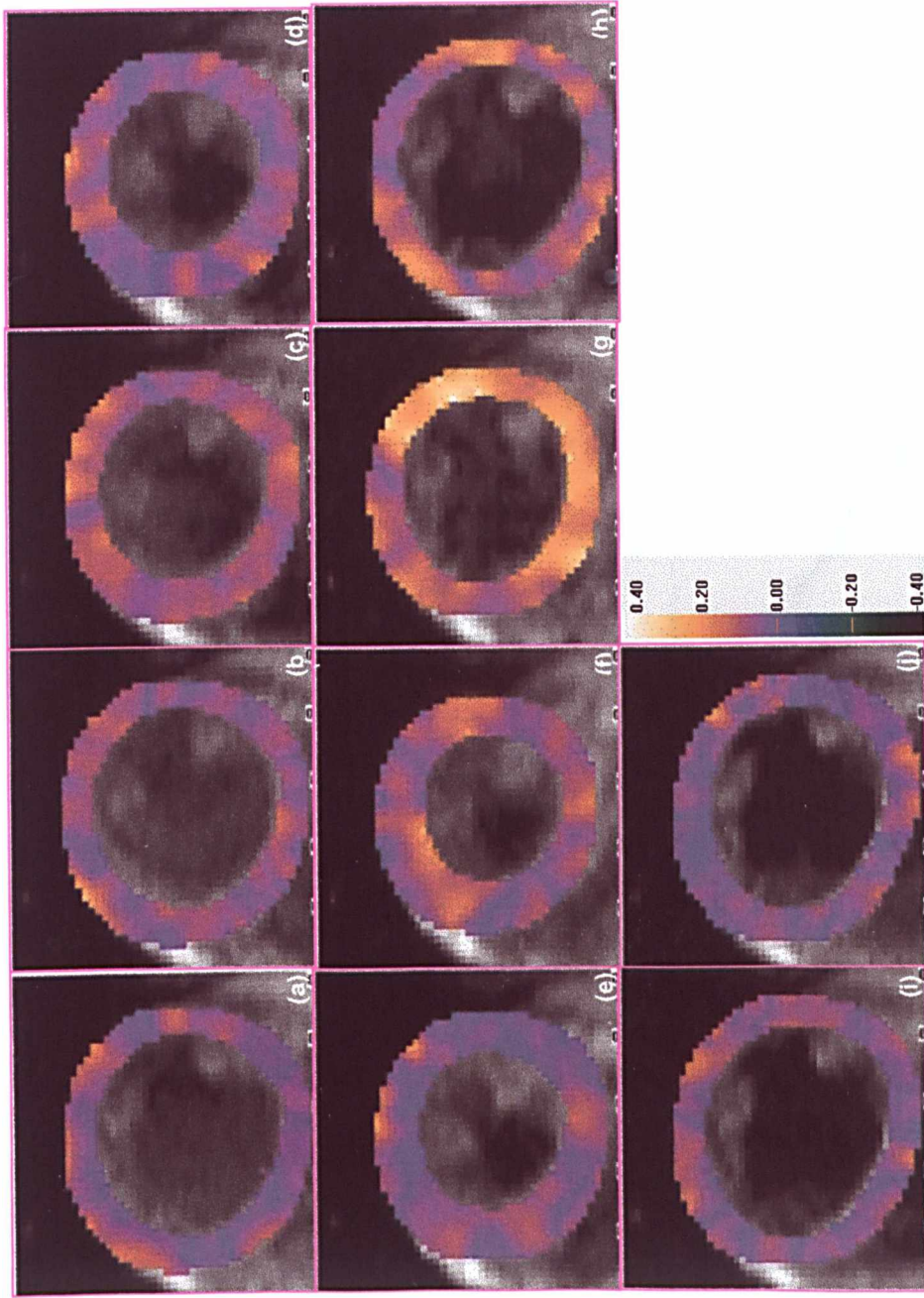


Figure 6.9 Strain rate distribution in a typical normal subject. Ten time frames showing the (c,d) systolic and (g) diastolic behaviour of the myocardium. The active recoil of the myocardium in early diastole is especially prominent.

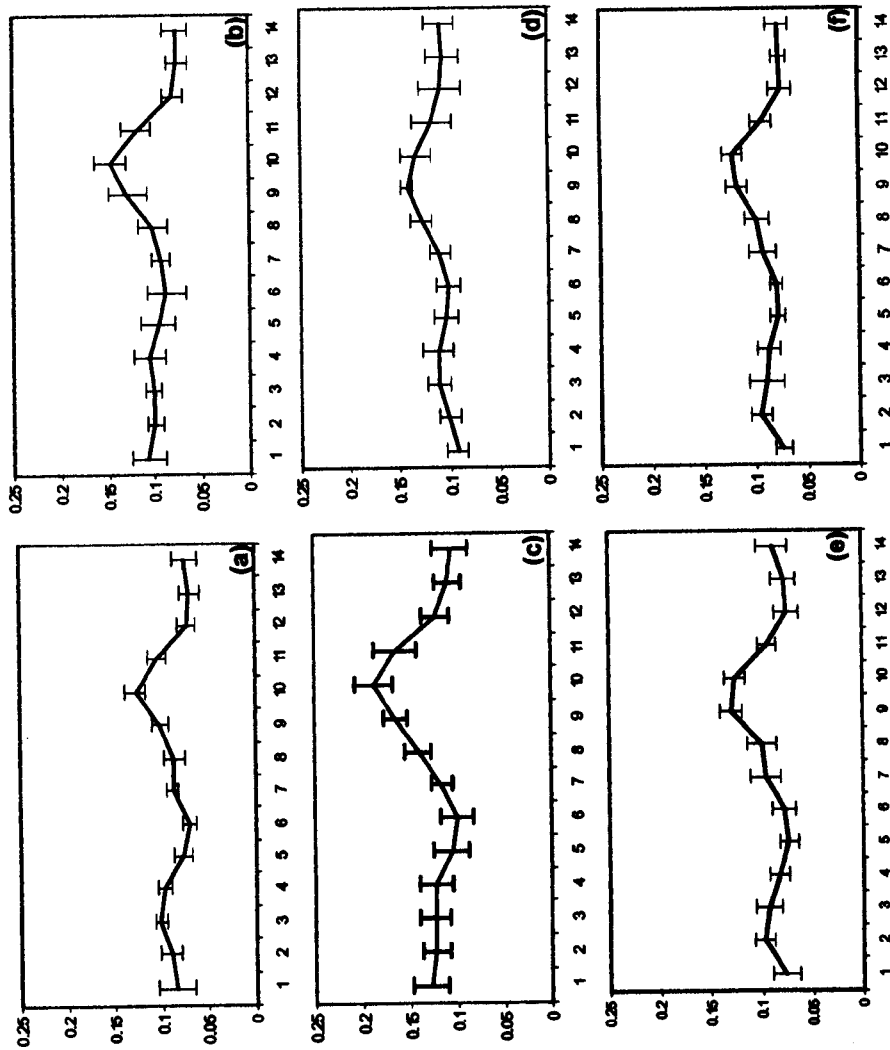


Figure 6.10 Mean normalised strain rate magnitude for 11 normal subjects in the (a) anterior, (b) anterolateral, (c) inferolateral, (d) inferior, (e) inferoseptal and (f) anterosseptal regions. The strain rate was normalised over time and space, *i.e.*, over the myocardial ring.

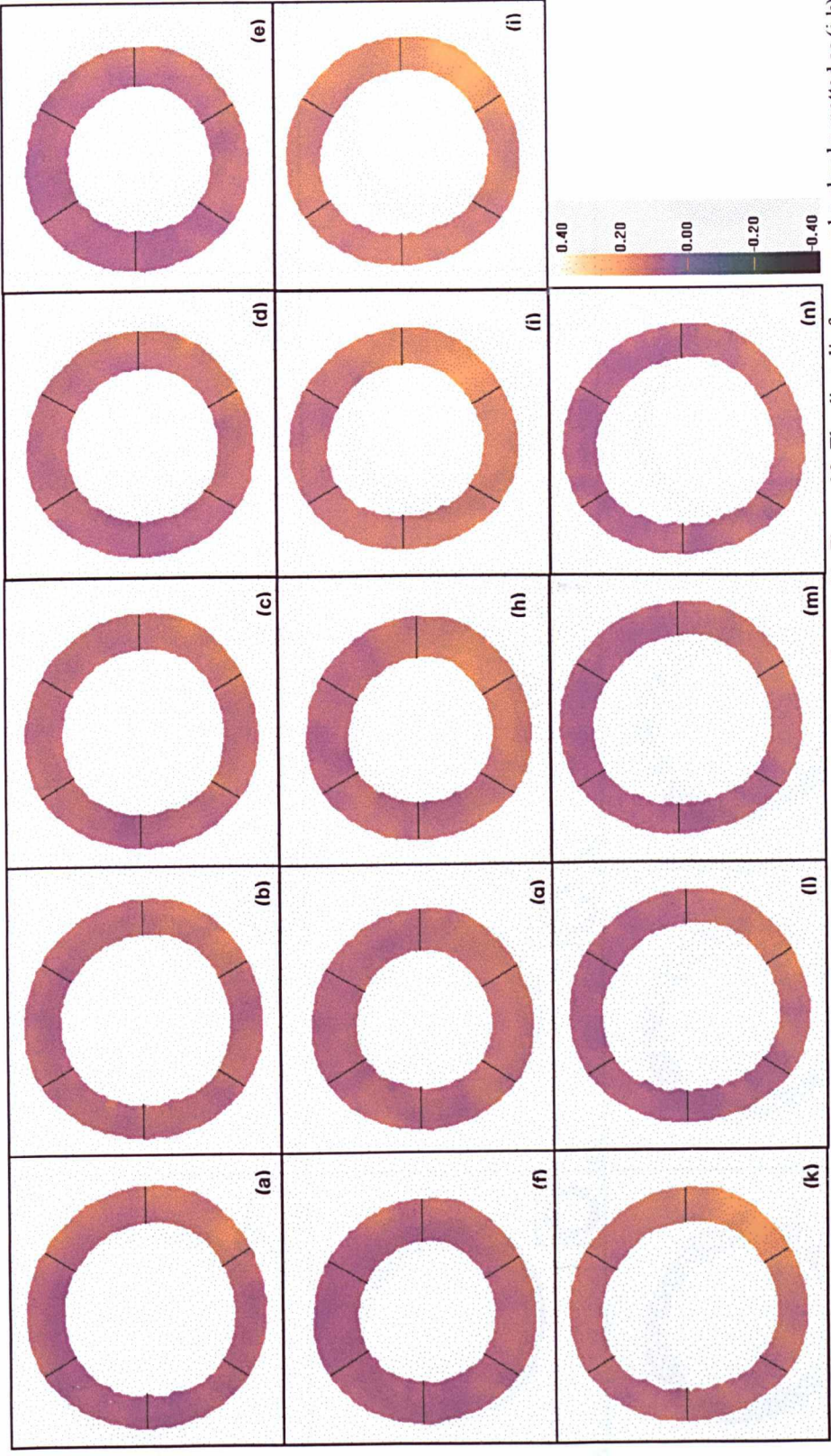


Figure 6.11 Standardised strain rate for 11 normal subjects, calculated using the scheme illustrated in Figure 6.2. The diastolic frames can be clearly spotted as (i-k).

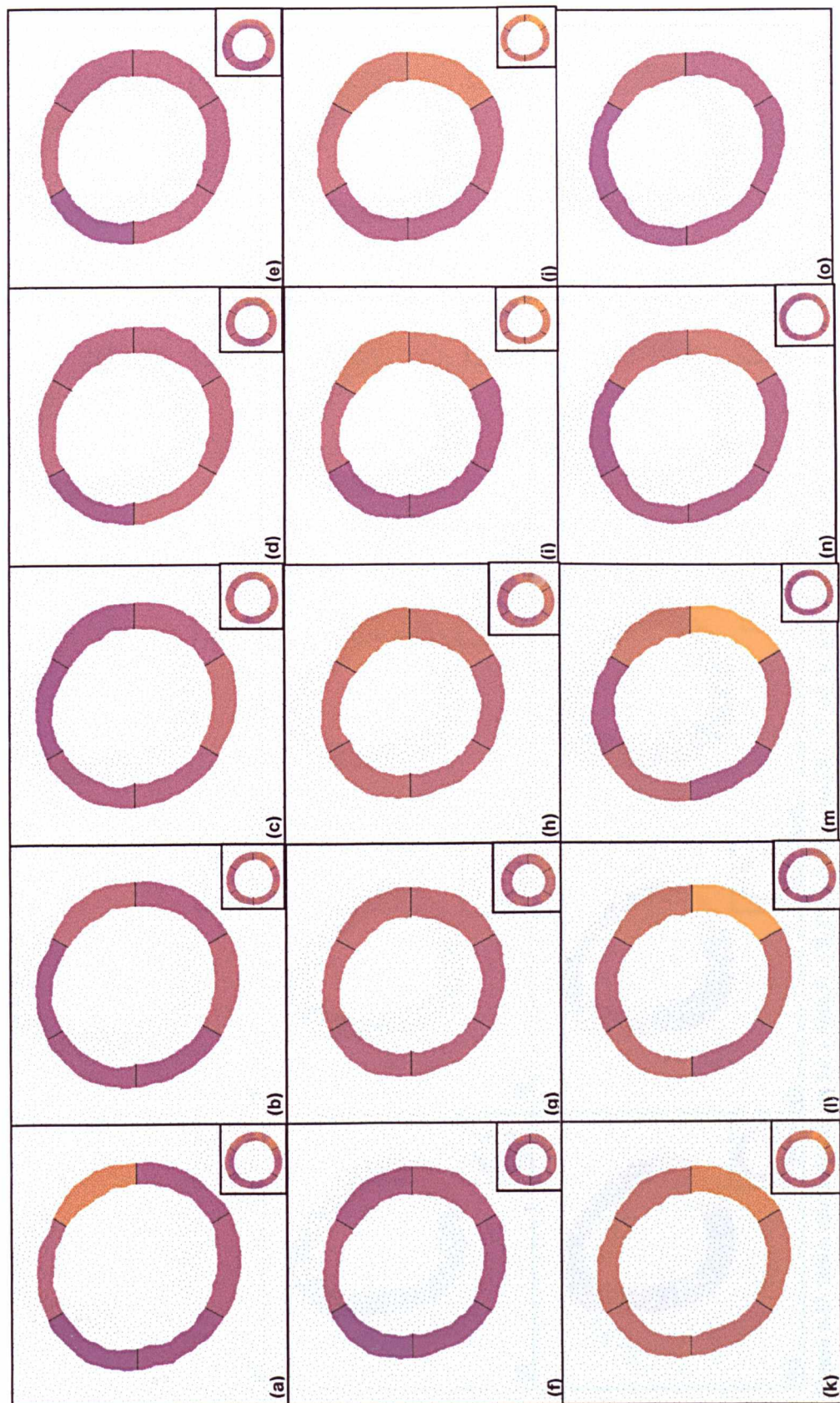


Figure 6.12 Strain rate maps for a patient with DCM. The overall strain rate is similar to that found in normal subjects. The corresponding normal strain rate is shown in the bottom right hand corner. The colour map is the same as Figure 6.11.

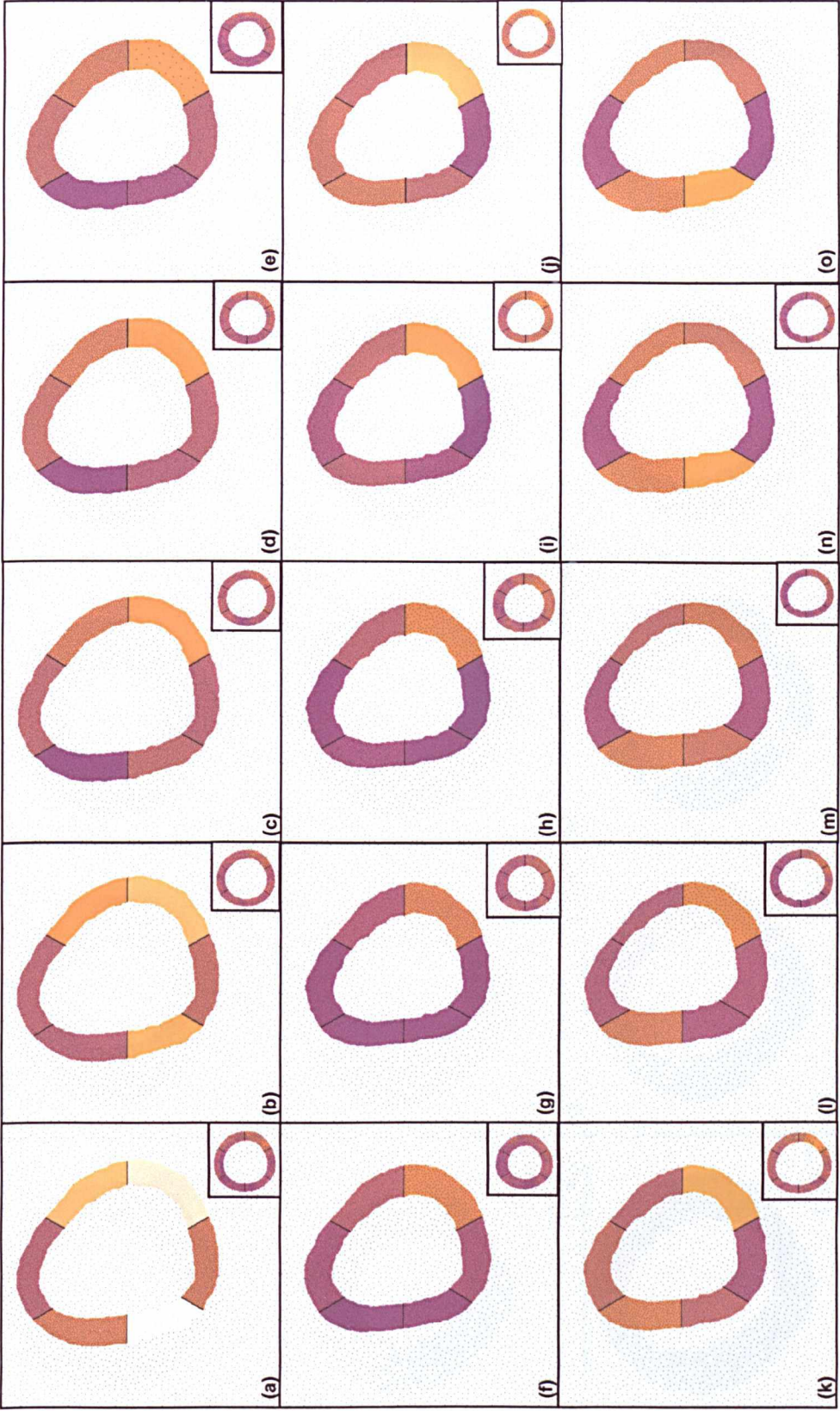


Figure 6.13 Strain rate distributions for a patient with Eisenmenger complex. It can be seen that there is septal deviation due to the pressure balance between the right and left sides, (a), (b), (m) and (n). There is also inferolateral motion to compensate for the septal deviation. The bottom right hand corner of each image shows the corresponding strain rate for the normal mean dataset. The colour map used is the same as that in Figure 6.11.

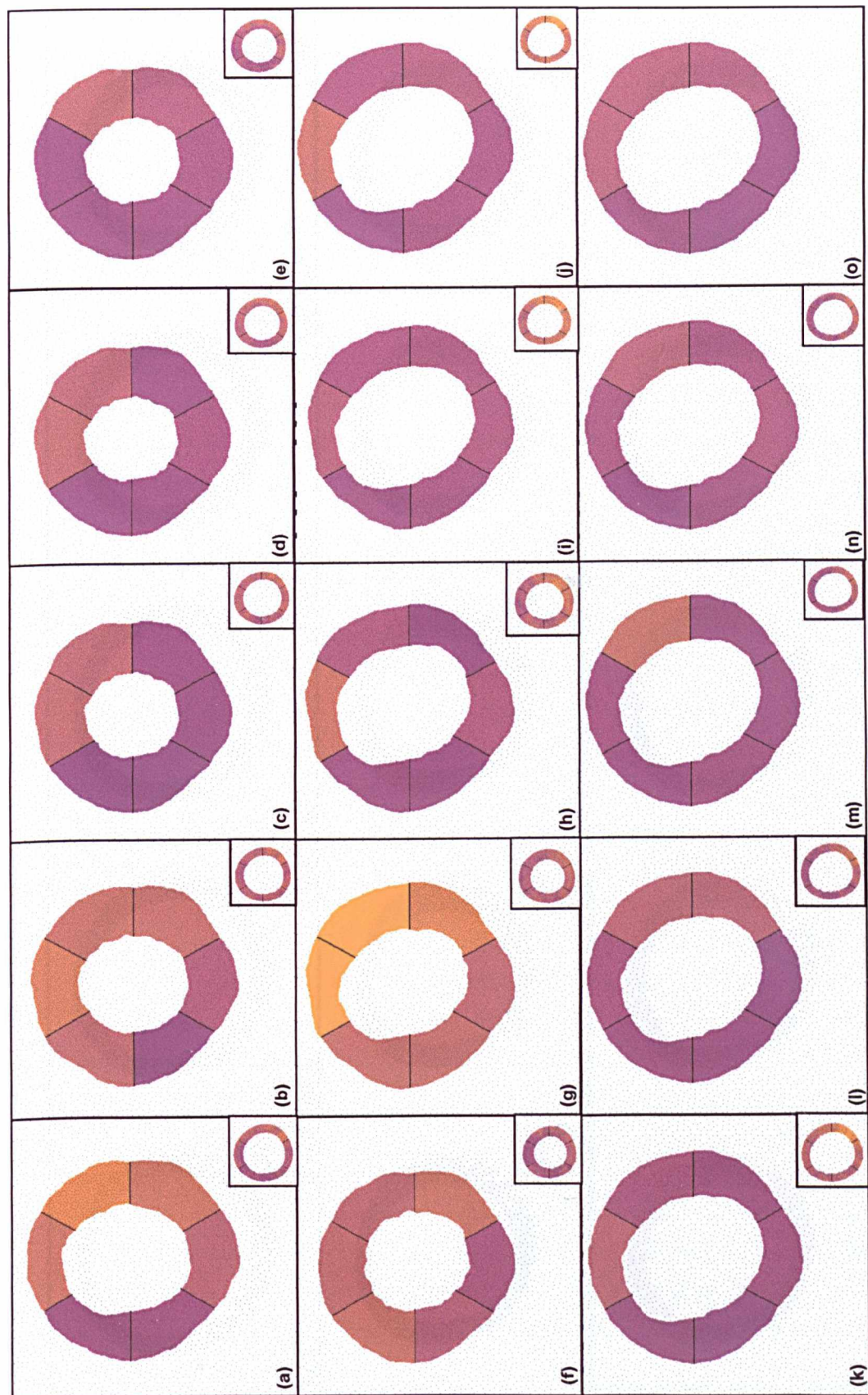


Figure 6.14 Strain rate distribution for a patient with ischaemic heart disease. The normal mean strain rate corresponding to the same frame is shown in the bottom right hand corner of each image. The colour map used is the same as Figure 6.11.

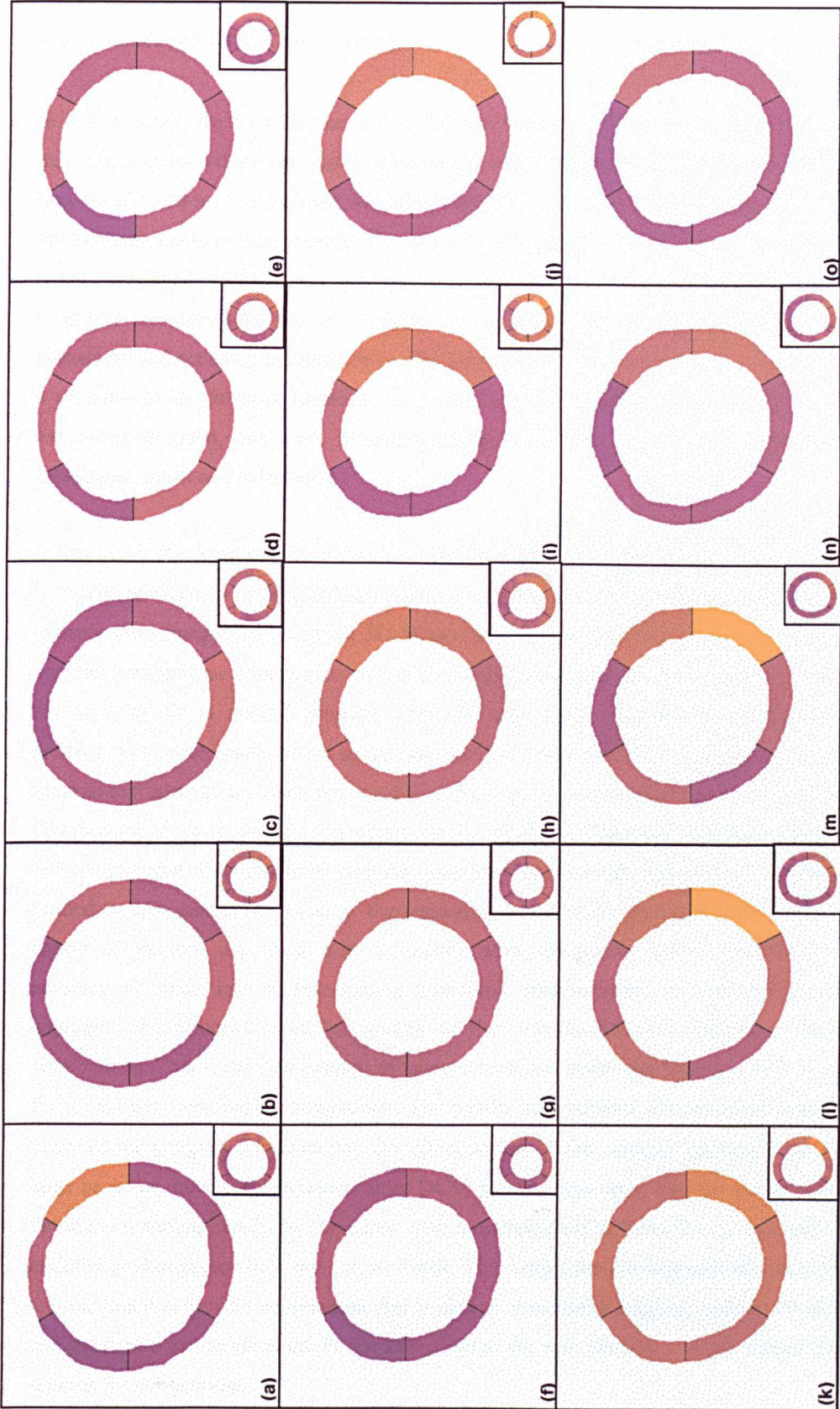


Figure 6.15 Strain rate maps for a patient having undergone a pericardiectomy. The overall strain rate is similar to that found in normal subjects. The normal mean strain rate corresponding to the same frame is shown in the bottom right hand corner of each image. The colour map is the same as Figure 6.11.

6.5 Discussion and Conclusion

In this chapter, we have demonstrated that the velocity data obtained from the velocity mapping sequence does not permit direct strain rate calculation as the in-plane VNR is too low. To circumvent this problem, we have implemented a novel velocity restoration iterative optimisation scheme incorporating the incompressibility constraint. This was tested against simple weighted average and the vector restoration scheme without apparent physical constraint developed by Ng and Yang¹³⁷. A synthetic dataset was used to evaluate the robustness and accuracy of the method. The zero divergence of the velocity field was used as a measure of its physical accuracy. In comparison to weighted averaging and the vector restoration scheme, the new incompressibility algorithm performed much better for subsequent strain rate calculation.

In this study, the proposed algorithm was evaluated with *in vivo* data to demonstrate its value in assessing changes in myocardial contractility in disease. Eleven normal subjects and six patients were imaged by using the 3D breath-hold velocity mapping sequence. To enable a detailed comparison, a normalised strain rate distribution was constructed which comprised the mean of all 11 normal subjects. This was used as the baseline for comparison with patients. The constructed normal strain rate distribution showed a trend of high strain rates in diastole that correspond to the active recoil of the myocardium to start rapid filling of the LV. Comparison of the strain rates in patients showed marked differences. Although initial results indicate regional strain rate to be a useful measure of contractility, further *in vivo* validation is needed to fully assess the value of the technique. It would be appropriate to study a single cohort of patients, *e.g.* those with ischaemic heart disease, to enable assessment of the accuracy of strain rate in determining functional abnormalities. In essence, this chapter highlights the importance of the quality of the velocity data for consistent strain rate distributions. This is the first attempt of using normalised strain rate from normals as an atlas for myocardial contractility comparison. The results from patients demonstrated the practical value of the imaging sequence and the effectiveness of the velocity restoration process. It must be noted, however, the results from DCM patients also show that the use of strain rate distribution should ideally be combined with morphological deformation of the heart as the underlying changes in strain rate can be subtle. This entails the development of a visualisation scheme that can provide information that is akin to myocardial tagging, such that both strain and strain rate can be assessed. In the next chapter, we will describe a novel Virtual Tagging scheme for this purpose.

7 The Virtual Tagging Framework

7.1 Introduction

Regional contractile abnormality is an accepted indicator of myocardial viability after heart attack⁴⁷. Recently, CMR has taken a key role in investigating regional contractile function as it provides a non-invasive and relatively easy way of assessing the intramural motion of the myocardium. Chapter 6 presents a novel technique for improving the consistency of velocity data using the mass conservation constraint. This allows the calculation and display of strain rate data, however myocardial deformation cannot be directly observed. Direct visualisation of myocardial deformation, as allowed by tagging, would be ideal for assessing regional transmural motion abnormalities *in vivo*.

This chapter presents the virtual tagging paradigm as applied to CMR myocardial velocity mapping. The importance of providing effective visualisation techniques for myocardial velocity mapping has been highlighted by previous research^{107-109,155}. Zhu and Pelc's approach relied on reconstructing the displacement from the harmonics of the periodic motion, the virtual tagging framework does not rely on any such temporal assumptions, rather it provides a spatially smoothed velocity field by using geometrical constraints, which can then be integrated to obtain displacement values. The introduction of the virtual tags facilitates the visual representation of the multi-dimensional velocity data sets, where the virtual tags resemble, in appearance and character, real MR tags. This enables easy visualisation and direct assessment of myocardial motion, which is an added advantage for its clinical use.

Furthermore, the use of virtual tags also permits the incorporation of geometrical constraints to derive physically accurate strain distributions as the proposed framework is considered in 4D (3D spatio-temporal) space with mass conservation. It is demonstrated that the use of geometrical constraints combined with global optimisation ensures that all tags deform in accordance with the constraint prescribed, therefore minimising the effects of noise and velocity integration errors. The virtual tagging framework has the added advantage that data from any modality could be used as input, for example velocities from HARP imaging or even tissue Doppler ultrasound could be used, enabling easy online visual assessment of strain.

7.2 Materials and Methods

7.2.1 *Generation of Virtual Tags*

The concept of virtual tagging is based on the superimposition of an artificial tag pattern onto the CMR velocity data and observing its subsequent deformation. At a given interval of the cardiac cycle, if the deformation of the virtual tags reflects the true motion of the myocardium, the associated displacement, and hence the velocity distribution, should be identical to the directly measured CMR velocity data in a least-mean-squares sense. Unlike conventional tagging where the tagged lines are usually perpendicular to each other due to practical constraints in CMR pulse sequence design, virtual tagging imposes no restriction on the shape of the tags to be used because they are numerically introduced. Therefore, the initial virtual tags can be generated in any desired fashion, either as polar or as Cartesian grids. They can be dense or sparse, with a uniformly spaced distribution or with spatially varying grid density. Figure 7.1 schematically illustrates several examples of different grid settings used for virtual tagging, where different grid density can also be adopted to delineate areas with potentially high deformation gradients. In this case, each intersection point, or vertex, of the grids acts as a control point that influences the surrounding sub-grids. Due to the flexibility of virtual tagging, the density of the grid-points can be chosen such that uniform material property and linear displacement gradient within each sub-grid can be guaranteed.

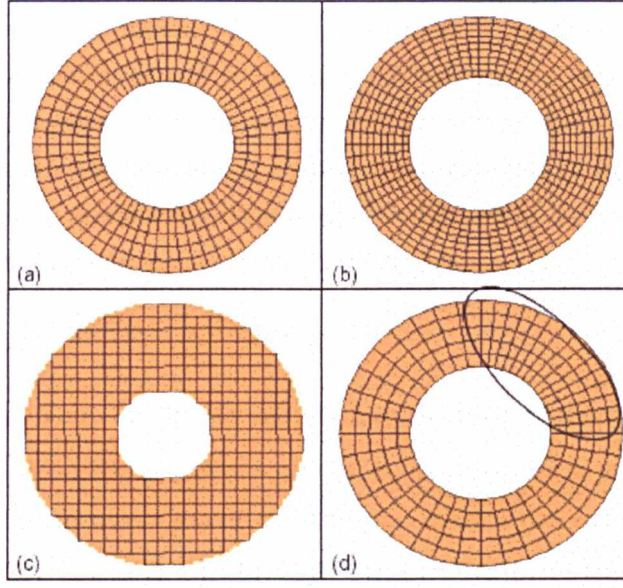


Figure 7.1 A schematic illustration of different configurations that can be used for virtual tagging, where (a-b) represent uniform polar grids with different densities, (c) Cartesian grid, and (d) polar grid with non-uniform grid density.

To evaluate whether the deformation of the virtual tags exactly follow the measured CMR velocity, a cost function which reflects the similarity of the two data sets needs to be defined. Denote \vec{d} as the derived velocity vector due to virtual tag deformation at a given time of the cardiac cycle and \vec{d}_R its counterpart by CMR measurements, the similarity measure between the two can be expressed as follows:

$$E = \int_{\Omega} \left| \vec{d} - \vec{d}_R \right|^2 dV \quad (7.1)$$

or in the 3D discrete form, it becomes

$$E = \sum_{x,y,z \in \Omega} \{ (\dot{u} - \dot{u}_R)^2 + (\dot{v} - \dot{v}_R)^2 + (\dot{w} - \dot{w}_R)^2 \} \quad (7.2)$$

In the above equations, the accented characters denote differentiation with respect to time, Ω is the region of interest, \dot{u}_R, \dot{v}_R and \dot{w}_R are the real CMR velocity components, and \dot{u}, \dot{v} and \dot{w} denote the derived velocity components from virtual tagging. The use of model induced deformation to fit with the measurement data follows the same strategy adopted by the field-fitting approaches in conventional tagging analysis^{77,79}.

The problem can now be formulated as finding the optimal values of \dot{u}, \dot{v} and \dot{w} such that E is minimised. Since we assume uniform material property and a locally linear deformation gradient, the velocity field within each sub-grid is uniquely characterised by the four

surrounding vertices. The intrinsic degrees of freedom of Equation (7.2) are therefore proportional to the number of grid points used. Numerically, we only need to iteratively change the spatial positions of these vertices until the optimal value of E is found. By adopting the tagging layout illustrated in Figure 7.1, the movement of any grid control point will affect the velocity distribution within its adjacent sub-regions, within which the velocity value at each voxel can be determined by B-spline interpolation, *i.e.*,

$$\vec{d}(x, y, z) = \sum_i \sum_j \sum_k B_i(x) B_j(y) B_k(z) \vec{d}_{i,j,k} \quad (7.3)$$

where B_i, B_j and B_k are the i th, j th and k th B-spline basis functions, and $\vec{d}_{i,j,k}$ is the deformation induced velocity at control point (i, j, k) , which is used as the weighting term in this interpolation. In this case, a second-order B-spline interpolation was used. Displacement can be derived from the velocity field by integrating with respect to time. It is assumed that the velocity between image frames is kept constant, which is reasonable when the temporal resolution of the imaging sequence is reasonably high. An ideal model would perform an interpolation over time as well as space, hence reducing errors caused by the constant velocity assumption between time frames.

7.2.2 Strain Calculation

Once the optimum virtual tag grid deformation is calculated, the strain distribution can be derived from the partial derivatives of the displacement field which are expressed in terms of the B-spline basis functions and the displacement components at control points, either in Cartesian or cylindrical coordinates. Since the deformation in soft tissues such as the myocardium can be large, *i.e.*, exceeding 10%, a general form of strain tensor, rather than the conventional linear expression, has to be used. In view of the method of data acquisition in CMR velocity mapping, the Lagrangian strain tensor is chosen in our study, *i.e.*,

$$\varepsilon_{ij} = \frac{1}{2}(u_{i|j} + u_{j|i} + u_{k|i} \cdot u_{k|j}) \quad i, j = 1, 2, 3 \quad (7.4)$$

In the above equations, the partial derivative $u_{i|j}$ is defined as

$$u_{i|j} = \frac{\partial u_i}{\partial x_j} \quad i, j = 1, 2, 3 \quad (7.5)$$

Where u_i is the displacement component along i th axis, ε_{ii} the normal strain which depicts the tissue expansion/contraction, whereas $\varepsilon_{ij} (i \neq j)$ is related to the shear strain γ_{ij}

and $\gamma_{ij} = 2\varepsilon_{ij}$. In tensor manipulations, a repetition of the suffix implies a summation operation, *i.e.*,

$$u_{k|i} \cdot u_{k|j} = \sum_k u_{k|i} \cdot u_{k|j} = \frac{\partial u_1}{\partial x_i} \cdot \frac{\partial u_1}{\partial x_j} + \frac{\partial u_2}{\partial x_i} \cdot \frac{\partial u_2}{\partial x_j} + \frac{\partial u_3}{\partial x_i} \cdot \frac{\partial u_3}{\partial x_j} \quad (7.6)$$

In practice, Cartesian strain components are used in general cases. Since the anatomical structure of the heart is closer to an ellipsoid, a cylindrical coordinate system is the preferred choice for data processing and visualisation. Thus, the in-plane strain components, ε_r (radial strain), ε_θ (circumferential strain) and $\gamma_{r\theta}$ (shear strain), and the through-plane strain components ε_z , γ_{rz} and $\gamma_{\theta z}$, can be used which are expressed in terms of the corresponding partial derivatives of radial displacement u_r , circumferential displacement u_θ , and through-plane displacement u_z , in a similar way to that of the Cartesian system. The in-plane polar strain components ε_r , ε_θ and $\gamma_{r\theta}$ are particularly useful for analysing myocardial contraction and relaxation. In addition, the use of the cylindrical coordinate system requires an explicit definition of the origin, which in our case is determined as the central axis of the myocardial mass. It is worth noting that it is also common to use the principal strain as a means of representing myocardial wall motion as explained in detail in Chapter 4.

7.2.3 Constraint of Mass Conservation

Regional contractile abnormality of the myocardium is best captured by using 3D cine coverage of the heart. Recent developments in rapid CMR velocity imaging sequence design, particularly by the use of locally focused imaging strategy^{130,156,157}, allow full 3D cine velocity imaging of the heart to be achieved in a reasonably short period of time. There are, however, a number of factors such as respiratory motion and inconsistencies between cardiac cycles that can influence the quality of the velocity data set.

To ensure the derived strain distribution represents physically meaningful results, the mass conservation constraint can be applied. If we ignore the variation of coronary flow at different phases of the cardiac cycle, the myocardium can be assumed to be an incompressible medium¹⁵⁸. This implies that the volume change ratio ξ , which is the determinant of the deformation gradient tensor calculated for the whole volume, should equal to unity.

$$\xi \equiv \left| \begin{array}{c} 1 + \frac{\partial u}{\partial x}, \frac{\partial u}{\partial y}, \frac{\partial u}{\partial z} \\ \frac{\partial v}{\partial x}, 1 + \frac{\partial v}{\partial y}, \frac{\partial v}{\partial z} \\ \frac{\partial w}{\partial x}, \frac{\partial w}{\partial y}, 1 + \frac{\partial w}{\partial z} \end{array} \right| = 1 \quad (7.7)$$

This constraint can be incorporated into the optimisation framework represented by Equation (7.2) by introducing a weighting factor λ such that

$$E = \sum_i \left| \Delta \bar{d}_i \right|^2 \Delta t^2 + \lambda \sum_i \left| \xi_i - 1 \right| S_i \quad (7.8)$$

where Δt is the time interval between successive frames, ξ_i, S_i and $\Delta \bar{d}_i$ are the associated relative volume change, the total surface area, and the variation between the virtual tagging induced and physically measured velocity distributions, of each volume element, respectively. The reason for introducing the surface area into the above mixed cost function is to ensure a correct normalisation factor between the two terms in Equation (7.8).

For 3D analysis, the three in-plane strain components ($\varepsilon_x, \varepsilon_y, \gamma_{xy}$) and three through-plane strain components ($\varepsilon_z, \gamma_{yz}, \gamma_{xz}$) can be calculated. In the cylindrical coordinate system, the corresponding strain components $\varepsilon_r, \varepsilon_\theta, \varepsilon_z, \gamma_{r\theta}, \gamma_{rz}$ and $\gamma_{\theta z}$ can be obtained by strain rotation. In addition to the in-plane strain components, the through-plane (z) shear strain $\gamma_{\theta z}$ represents the longitudinal shear, which is of particular clinical interest. This is because the shortening/lengthening of the ventricles is dictated by the torsion of the myocardium around its longitudinal axis. Due to the way that the muscle fibres are oriented, two contrary rotations occur during systole. When looking from the apex to base, a counter-clockwise rotation at the base and a clockwise rotation at the apex can be seen. These rotations imply a shortening of the ventricles as in a towel being wrung dry.

7.2.4 Optimisation

The problem formulated in Equation (7.7) involves multivariate optimisation with large degrees of freedom, typically in the range of 2,000-10,000 depending on the density of the grid and size of the object. To assess the numerical behaviour of the virtual tagging framework, the following optimisation strategies have been considered: (a) steepest descent, (b) Broyden-Fletcher-Goldfarb-Shanno (BFGS), (c) Powell, and (d) Marquatz-Levenberg methods¹⁵⁹. The steepest descent technique involves the calculation of the gradients of the

cost function at each control point at current $(\dot{u}, \dot{v}, \dot{w})$. The derived values are then normalised to the maximum gradients, which corresponds to the full step size. This forms an iteration process, which usually leads to a local minimum where the induced velocity distribution due to virtual tagging deformation is the closest to the MR measurement.

As an extension of the Newton's method, the BFGS algorithm is a variable metric optimisation method which uses gradient or partial derivatives of the cost function to accelerate the convergence of the iterative optimisation process¹⁵⁹. In practice, forward-difference is usually used to compute the gradients of the cost function when the explicit partial differentiation is difficult to derive, especially when the cost function is associated with some extra penalty functions, *e.g.* mass conservation. This algorithm is also commonly thought to work relatively fast, provided that calculating the partial derivatives is not too expensive.

For the Powell method, gradient information is also used in the iterative process. However, rather than being calculated explicitly, the gradient information is implemented by generating a set of conjugate vectors during the successive selection of the direction along which the local minima is reached¹⁵⁹. The Marquardt-Levenberg method, on the other hand, is one of the most widely used non-linear optimisation techniques. The algorithm uses a search direction that is a cross between the Gauss-Newton direction and the steepest descent. The solution to Equation (7.8) through multivariate optimisation generates a deformation field that is integrateable over time, allowing the deformation of the initial grid to be visualised.

7.3 Experiments

7.3.1 Numerical Validation

To evaluate the robustness of the proposed virtual tagging framework, a set of 3D simulation data was generated with the following velocity distribution:

$$\begin{aligned}\dot{u}_r &= d_r \cos(ax) \\ \dot{u}_\theta &= d_\theta \cos(ax) \\ \dot{u}_z &= d_z \cos(ax)\end{aligned}\tag{7.9}$$

where the in-plane kernel functions, d_r, d_θ , are designed as:

$$\begin{aligned}
d_r &= A[1 - (\frac{r}{b})^2] + B[(\frac{r}{a})^2 - 1] \\
d_\theta &= C[1 - (\frac{r}{b})^2] + D[(\frac{r}{a})^2 - 1]
\end{aligned} \tag{7.10}$$

The through plane kernel function, d_z , is deduced based on the mass conservation condition, and can be expressed as,

$$d_z = F(r, \theta)z \tag{7.11}$$

In Equation (7.10), A , B , C , and D are constants determined by the following boundary conditions:

$$\begin{aligned}
d_r|_{r=a} &= A(1 - \frac{a^2}{b^2}) \\
d_r|_{r=b} &= B(\frac{b^2}{a^2} - 1) \\
d_\theta|_{r=a} &= C(1 - \frac{a^2}{b^2}) \\
d_\theta|_{r=b} &= D(\frac{b^2}{a^2} - 1)
\end{aligned} \tag{7.12}$$

We choose $\omega = \pi/16$ to produce a cyclic deformation field with 16 time frames, and a and b are constants corresponding to the inner and outer radius of the cylinder. Hence, A and B are the maximum possible velocities of the inner and outer circle respectively. The generated velocity distribution models the contraction and relaxation of the myocardium by incorporating the bulk rotation, translation, wall thickening and twisting. To assess the robustness of the algorithm against measurement noise, different levels of additive Gaussian noise were introduced into the data set.

Since the in-plane velocity components in (7.10) are independent of z , the determinant of the deformation gradient tensor in equation (7.7) becomes:

$$(1 + \frac{\partial \dot{w}}{\partial z})(1 + \frac{\partial \dot{u}}{\partial x} + \frac{\partial \dot{v}}{\partial y} + \frac{\partial \dot{u}}{\partial x} \frac{\partial \dot{v}}{\partial y} - \frac{\partial \dot{u}}{\partial y} \frac{\partial \dot{v}}{\partial x}) = 1 \tag{7.13}$$

Therefore, the general solution is given by

$$\dot{w} = c(r, \theta) + F(r, \theta)z = c(x, y) + F(x, y)z \tag{7.14}$$

For simplicity, take $c(r, \theta) = 0$ which implies

$$F(x, y) = -\frac{\frac{\partial \dot{u}}{\partial x} + \frac{\partial \dot{v}}{\partial y} + \frac{\partial \dot{u}}{\partial x} \frac{\partial \dot{v}}{\partial y} - \frac{\partial \dot{u}}{\partial y} \frac{\partial \dot{v}}{\partial x}}{1 + \frac{\partial \dot{u}}{\partial x} + \frac{\partial \dot{v}}{\partial y} + \frac{\partial \dot{u}}{\partial x} \frac{\partial \dot{v}}{\partial y} - \frac{\partial \dot{u}}{\partial y} \frac{\partial \dot{v}}{\partial x}} \tag{7.15}$$

7.3.2 Phantom Validation and Experimental Set-up

To evaluate the accuracy of the proposed numerical framework with real MR data sets, a myocardial motion phantom was constructed. It consists of a cylindrical silicone gel (Sylgard 527, Dielectric Silicone Gel, Dow Corning, Michigan, USA), mixed as 2.25 parts catalyst to 1 part resin, baked at 110° for 1.5 hours to provide the right viscosity. This type of silicone gel phantom was first used by Young *et al* in their experiments to validate MR tagging¹⁶⁰. The motor was programmed to rotate the plate by 10° and then return to its original position. This caused the gel to compress in the z (through plane) direction and rotate in the x - y (image) plane causing shear in the through plane direction.

Figure (7.2) illustrates the overall design of the phantom when positioned inside a 1.5T Marconi EDGE whole-body scanner, where all MR data for this study was acquired. The system has a maximum slew rate of 72T/m/s and a peak gradient strength of 27mT/m. A Surrey Medical Imaging Systems (SMIS) console was used for driving the velocity mapping sequences, and acquiring and reconstructing the data.

A standard velocity mapping sequence, programmed on a SMIS console, was used to acquire a 3D data set of 6 transverse slices of the phantom. The data acquisition protocol was TE 14ms with a TR of 38ms. Sixteen phases with a temporal resolution of 38ms were acquired, with a velocity range of 30cm/s, slice thickness of 8mm and in-plane resolution of $1.37 \times 1.37 \text{ mm}^2$. The images were reconstructed on a SMIS console using in-house software. A 3D tagged data set was also acquired to examine the accuracy of the virtual tagging technique in following the deformation of the material over time. A standard SPAMM tagging sequence available on the Marconi EDGE system was used, again 6 slices, 8mm thick, and 16 phases were acquired with a temporal resolution of 35ms. In-plane resolution was $1.37 \times 1.37 \text{ mm}^2$ with a tag-spacing of 7mm.

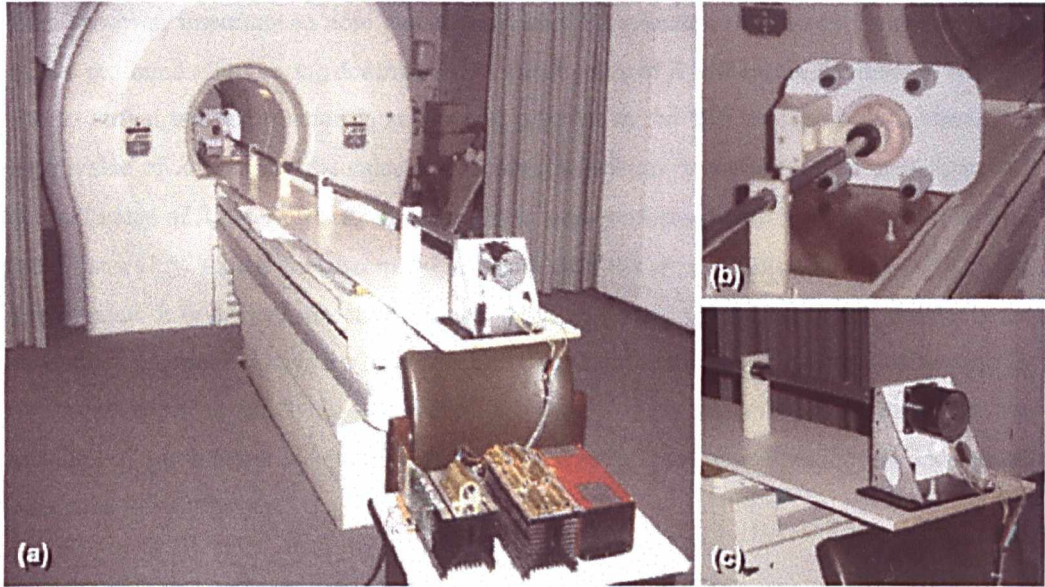


Figure 7.2 The design of the silicon gel phantom used for *in vitro* validation of the current study. (a) The overall system configuration, (b) the silicon gel assembly which allows both twisting and compression, and (c) the driving motor located away from the magnet.

7.4 Results

Figure (7.3) illustrates the virtual tagging algorithm as applied to the numerical simulated data with different levels of noise. Only five time frames, 0,2,7,12,14, are shown here, with the top row showing the noise free tag deformation results, calculated without the mass conservation constraint. The middle and bottom rows illustrate the corresponding results for the same data set with additive Gaussian noise, calculated with and without the incorporation of mass conservation constraint, respectively. The SNR of the data set was 16.32 dB, and the colour coding represents radial strain between the values of -0.6 and 0.6 . Figure (7.4) shows the same simulation results, but with colour coding representing the in-plane shear strain $\gamma_{r\theta}$ within the same range as that of Figure (7.3). For both figures, the weighting factor λ was fixed with a value of 0.6. It is evident from these figures that the incorporation of mass conservation is crucial to the accuracy of the virtual tagging result. The quality of the simulated velocity data with an SNR of 16.32 dB was much poorer than that of normal MR scanned data. Despite this, the proposed virtual tagging results held well in terms of following the twisting of the material. By incorporating the mass conservation constraint, the derived strain distributions were similar to those calculated from the theoretical noise free data.

It is, however, important to note that numerically, the selection of different values of λ can have a profound effect on tag deformation. A small value of λ will ensure the derived velocity due to virtual tag deformation is as close as possible to the MR measured data, whereas a large value of λ warrants the calculated strain distribution is isochoric. To investigate the optimal value of λ for this data set, calculations were performed with λ varying from 0.02 to 3.0. Figure (7.5) shows the corresponding result with the error function normalised with the initial value. It is evident that the optimum range of λ ranges from 0.5 to 1.0, but the exact value does not seem to have a major effect on the performance of the optimisation process as the curve becomes relatively flat within this region. This observation suggests that the selection of λ in practice is not sensitive to the final optimisation result, as long as it is located within the 0.5-1.0 range.

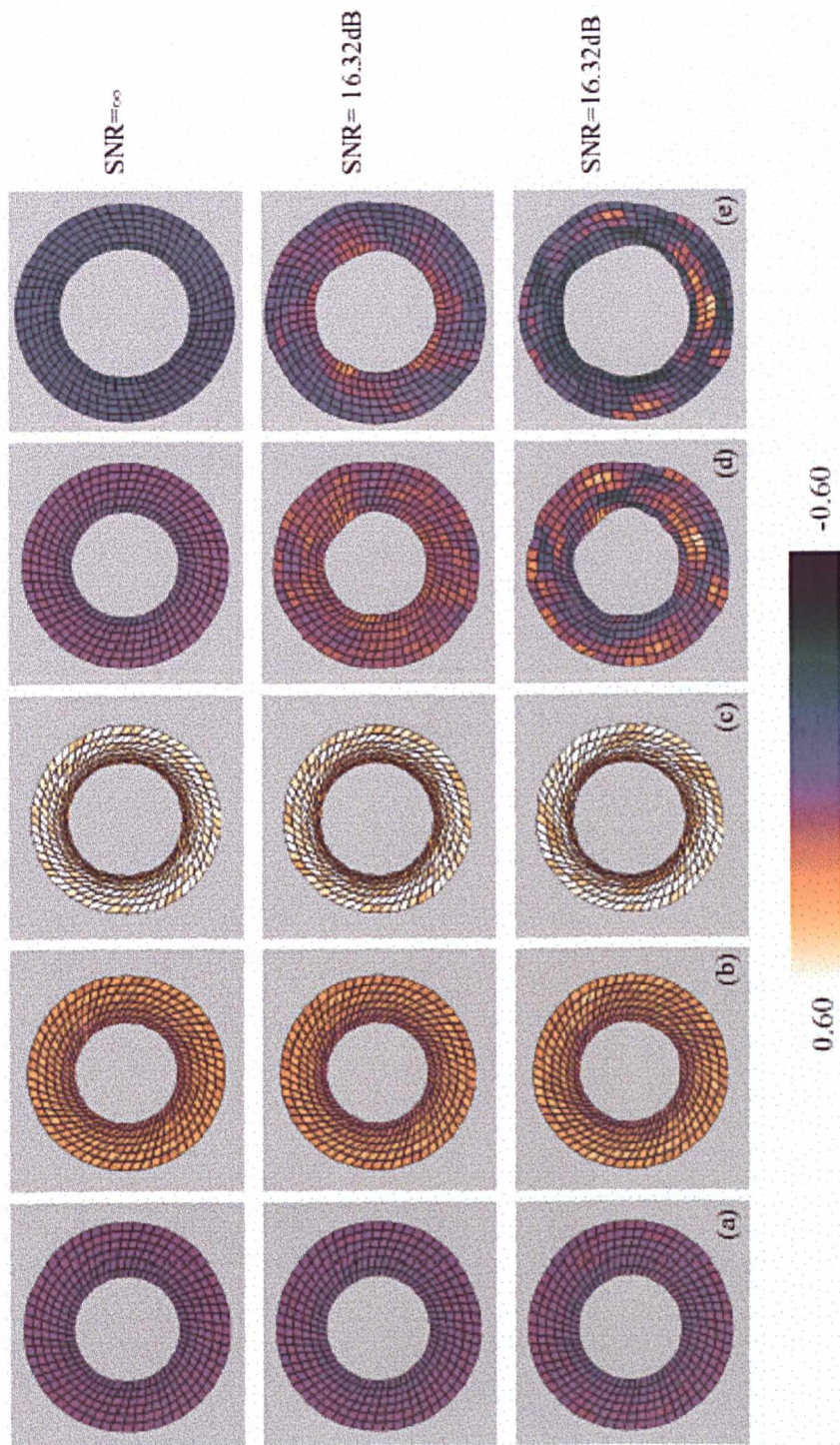


Figure 7.3 A numerically simulated data set based on Equations (7.9)-(7.11) for simulating the motion of the heart. Top row: virtual tag results at increasing time points of the motion cycle with a noise free data set. Mid and bottom rows: results for a data set with an SNR of 16.32 dB calculated with and without mass conservation, respectively. The colour coding represents the radial strain \mathcal{E}_r within the range of -0.6 and 0.6.

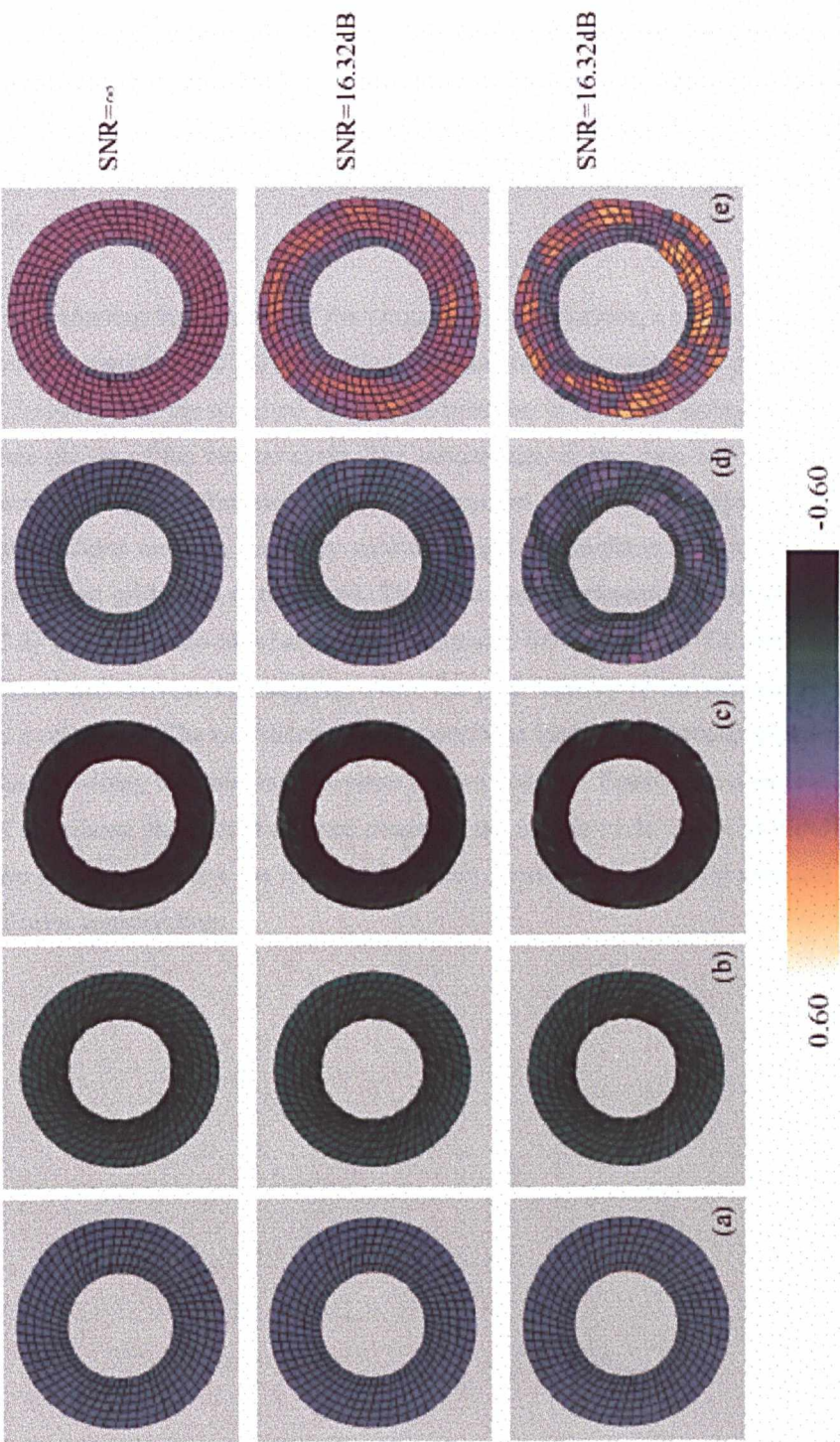


Figure 7.4 The same numerical results corresponding to Figure 7.3, but with colour coding representing the in-plane shear strain $\gamma_{r,\theta}$ in the range of -0.6 and 0.6 .

To compare the relative performance of the different optimisation techniques, the aforementioned techniques, namely steepest descent, BFGS, Powell, and Marquardt-Levenberg, were applied to the simulated data without noise, and data with SNRs of 28.07dB and 16.32dB, respectively. Figure (7.6) shows the relative performance, defined as the normalised error, of these four optimisation techniques with different values of λ . It appears that the four techniques had similar performances in terms of error minimisation, but in terms of computational time the BFGS approach out-performs all other techniques by a factor of 3-5.

For evaluating the accuracy of the virtual tagging technique, a comparison was made between velocity mapping and the conventional tagging technique using the motion phantom. Figures 7.7(a)-(c) show the acquired velocity distribution in the three orthogonal directions at three time phases of the motion cycle. The virtual tags, in this case laid out in a Cartesian form derived using the framework, are superimposed onto the SPAMM tagged data. The tag intersections are then manually delineated and the in-plane distance between the real and virtual tag grid-point is measured. The close match between the two is evident, and Figure (7.8) delineates the absolute mean differences for two of the six imaging slices between virtual and conventional tagging, where the peak velocity of the silicone gel is also provided as a reference. The two slices chosen were those closest to the rotating plate of the phantom, thus providing the maximum in-plane motion possible. Finally, the complete 3D deformation of the silicon phantom at selected phases of the motion cycle is provided in Figure (7.9). The two image rows show the longitudinal strain distribution calculated with and without the use of mass conservation.

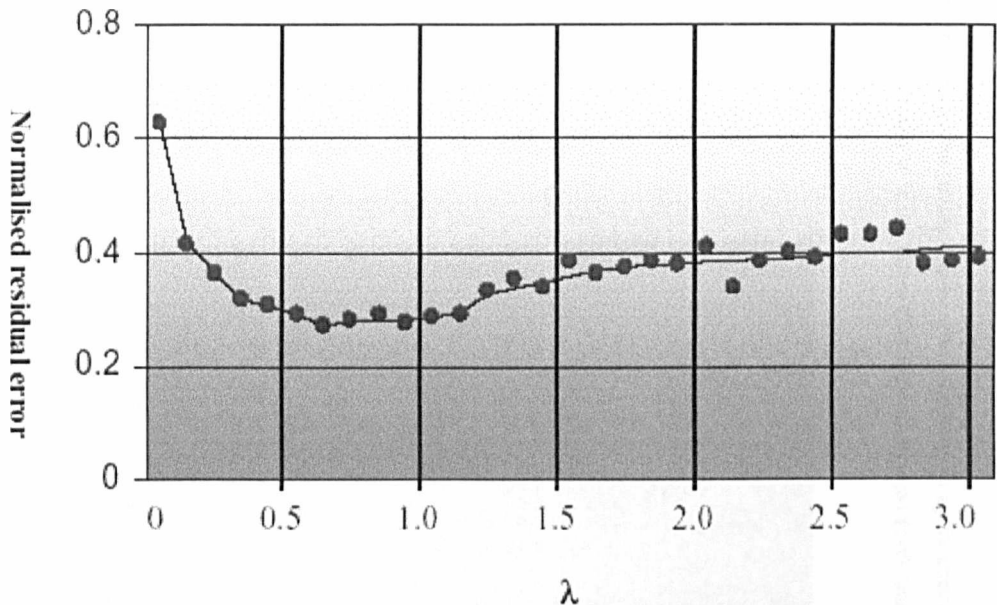


Figure 7.5 The influence of the values of the weighting factor λ on the accuracy of the virtual tagging result. All calculations were performed by using the numerically simulated data set used in Figures (7.3)–(7.4) with an SNR of 16.32 dB.

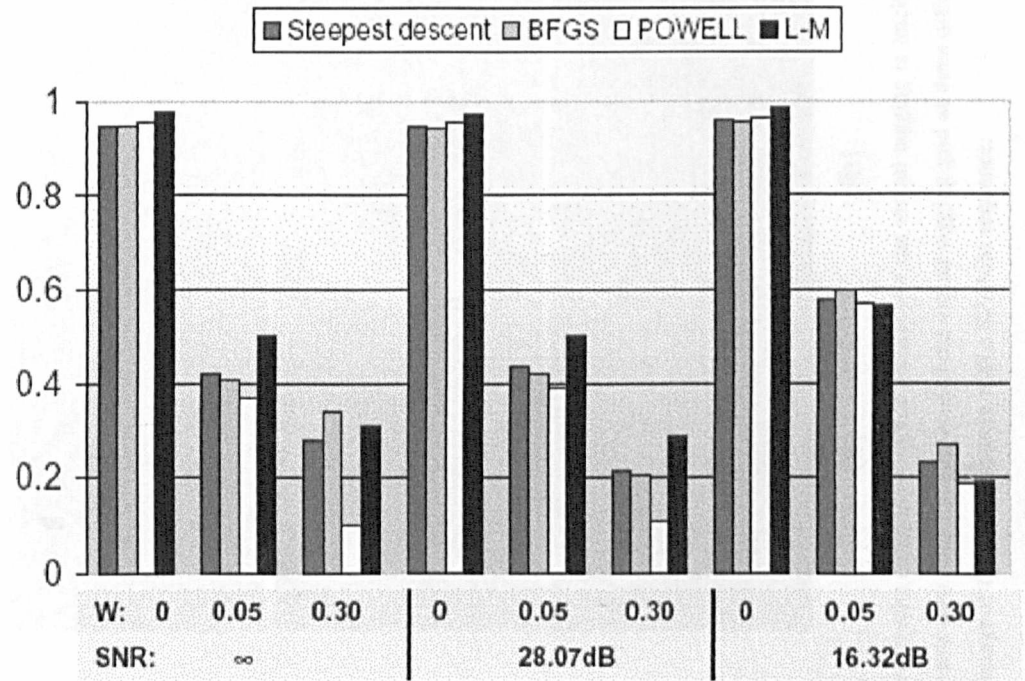


Figure 7.6 A comparison of the performance of different optimisation algorithms used and the effect of different weighting factors used for introducing the mass conservation constraint. Three simulation data sets, ranging from noise free, to an SNR of 28.07 dB and 16.32 dB, were used.

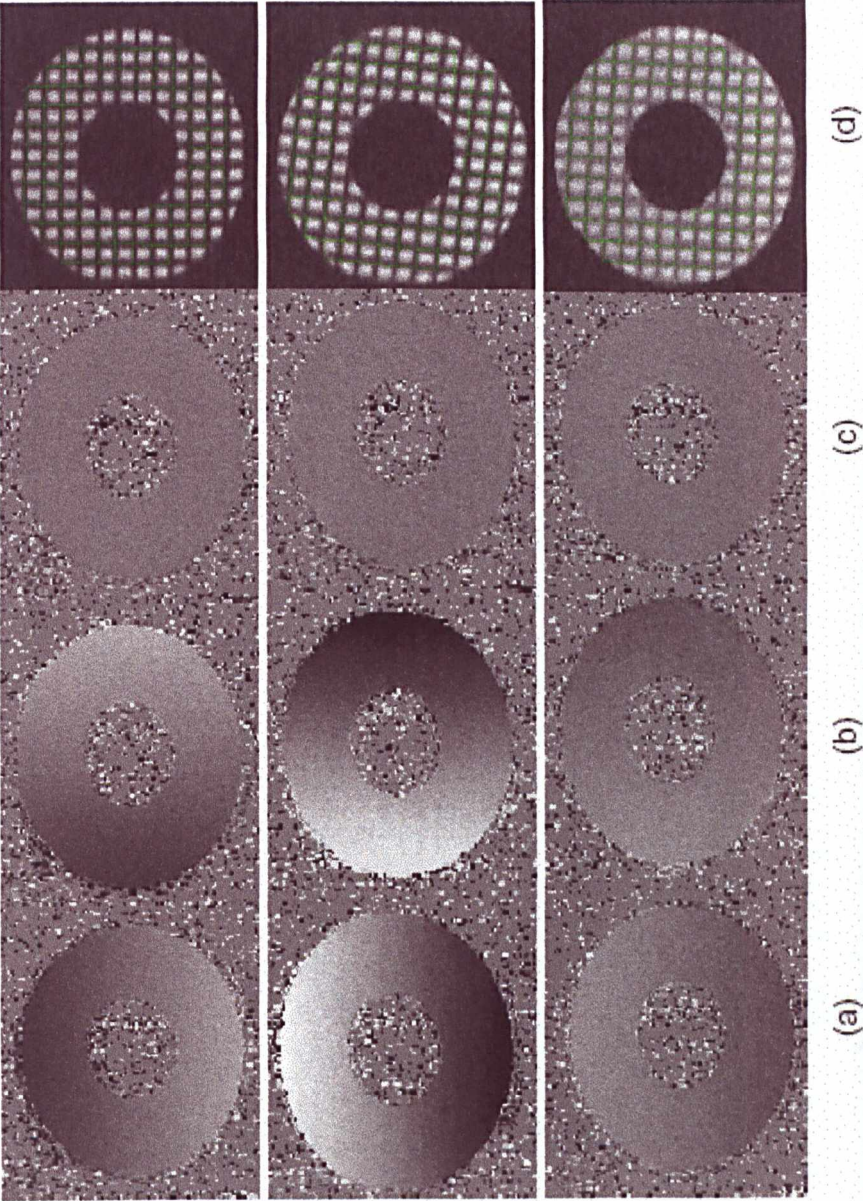


Figure 7.7 The *in vitro* results demonstrating the accuracy of the virtual tagging in tracking material over time, (a-c) velocity components along the x , y , and z axes where mid-grey value represents zero velocity, (d) the derived virtual tagging grid at three different times of the motion cycle (increasing down each column) superimposed on a conventional tagging image of the same phantom with a SPAMM sequence.

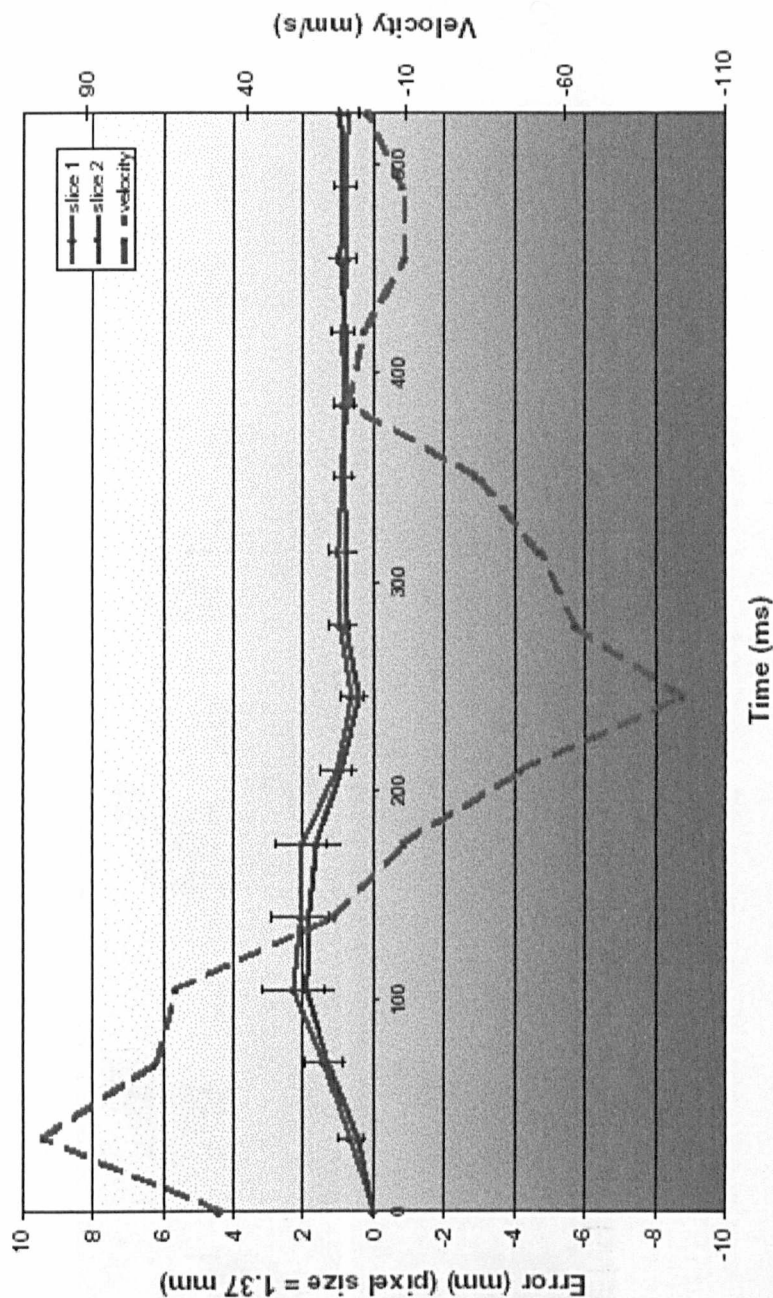


Figure 7.8 The manually measured absolute tracking error at two mid-slices of the phantom throughout the motion cycle, where the peak gel velocity is provided as a reference. It is evident that there is a slight increase in the tracking error during peak acceleration, which can be partially avoided by increasing the temporal resolution of the velocity sequence.

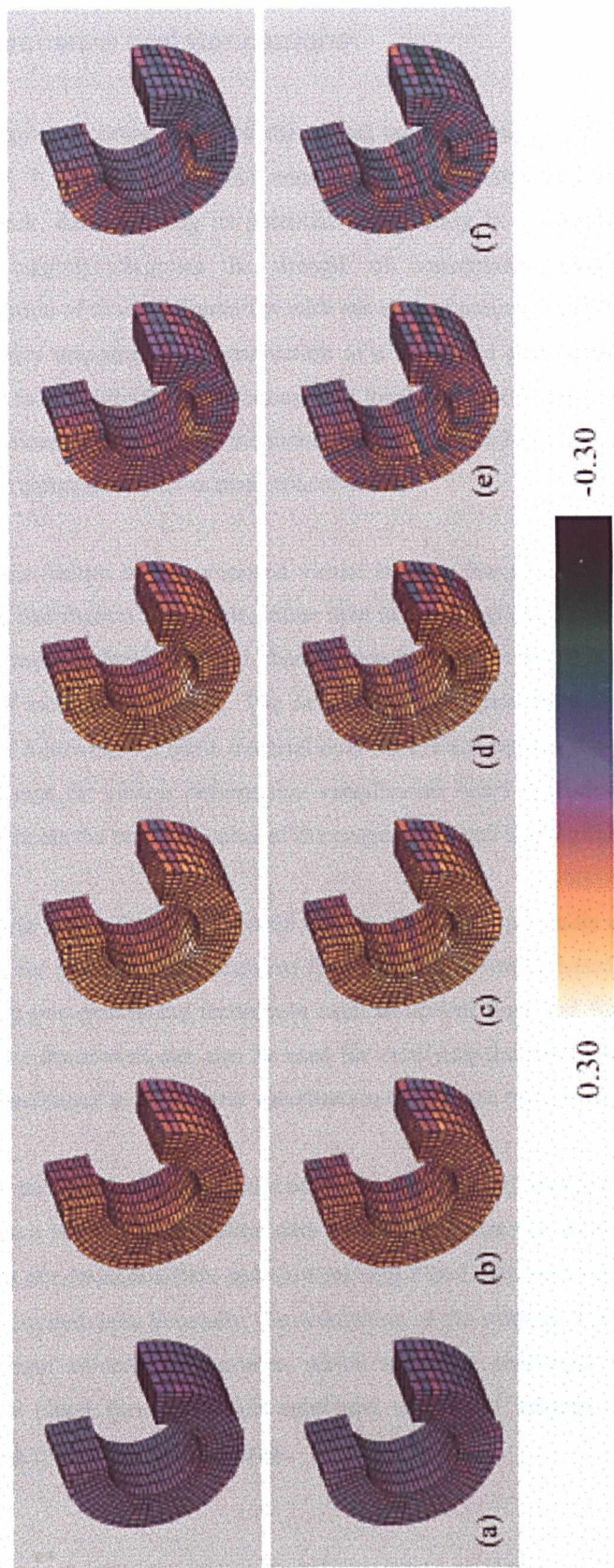


Figure 7.9 A 3D representation of the virtual tagging result for the phantom at six different time instances of the motion cycle, where the colour coding represents the longitudinal strain in the range of $-0.3 \sim 0.3$. The time increases across each row, with the phantom deforming and then returning to its original position. The top and bottom rows show, respectively, the results calculated with and without the mass conservation constraint.

7.5 Discussion and Conclusions

This chapter presents details of the virtual tagging approach for CMR myocardial velocity imaging. It also addresses the numerical considerations and phantom validation of this framework, demonstrating its potential applicability in a clinical environment. The use of virtual tagging integrates the strength of conventional tagging techniques for direct visualisation of tissue deformation with the ease of processing and accuracy of data provided by velocity mapping. The introduction of a structured grid superimposed onto the velocity data, in fact, implicitly incorporates both local and global geometrical constraints on object deformations. This improves the numerical accuracy and facilitates the incorporation of other physical constraints such as mass conservation.

The main feature of the proposed virtual tagging framework is that it relies on the entire velocity distribution as a whole, rather than isolated regions, to perform deformation tracking. Both numerical simulation and phantom results indicate that it is effective in addressing the effect of measurement noise. The existing data suggests the accuracy of the virtual tags in terms of following the same material over time. Furthermore, the temporal integration of the derived tags for clearer deformation visualisation bears little error accumulation effect. All these indicate the practical value of the proposed virtual tagging framework.

It is worth noting that the proposed framework is also applicable to myocardial displacement vectors, for instance, those acquired from DENSE or results based on normal tagging images by using post-processing techniques such as optical flow and free-form image registration. The same framework can also be used for rectifying the strain distribution derived from the HARP technique and for direct visualisation of intrinsic myocardial deformation.

Despite the fact that the potential of myocardial velocity imaging has long been recognised, there are a number of important data acquisition issues that need to be addressed. The flow artefacts due to inconsistent and slow moving blood represent a major problem to the quality of the acquired data. Secondly, the acquisition of the velocity data requires separate encoding of different velocity components, which results in prolonged imaging time. The use of effective blood flow saturation combined with rapid velocity acquisition will make this approach more attractive clinically.

The use of virtual tagging involves the manual delineation of region borders only in a single frame of the image sequence, and the algorithm will follow the subsequent motion of the material automatically. This greatly simplifies the processing task involved and the amount of user interaction is kept to be minimal. One of the caveats of applying the proposed framework is that we have assumed the velocity between adjacent image frames to be constant. Hence, it is important to keep the temporal resolution of the velocity imaging sequence to be reasonably short so that transient velocity changes are better accounted for. A detailed assessment of Figure (7.8) suggests that there is a slight increase in material tracking error during peak acceleration, which can be partially avoided by using reduced repeat time in velocity acquisition. Numerically, however, it is possible to incorporate the velocity changes between successive image frames to minimise this error, but this involves the solving of a coupled optimisation problem in the spatio-temporal domain. The incorporation of the Fourier tracking technique of Pelc *et al*¹⁰⁸ might simplify the problem.

In conclusion, we have investigated the potential numerical pitfalls of the virtual tagging framework for assessing myocardial contractility based on CMR velocity imaging. The proposed technique has the advantage of being flexible in the choice of tagging grids used both for direct visual assessment and strain calculation. The use of a structured tagging grid ensures that the entire velocity distribution is taken into consideration when deriving the deformation field, and is shown to be relatively robust against measurement errors. Both numerical simulation and phantom results suggest the importance of incorporating the mass conservation constraint for further improving the numerical stability of the proposed algorithm.

8 Conclusion

8.1 Importance of Measuring Myocardial Motion

Myocardial contractility has long been regarded to be an important measure of cardiac function. Thus far, reliable ways of measuring myocardial contractility have been limited. The earliest attempts, around the 1970s, employed implanted radio-opaque markers and ultrasonic crystals. They were then imaged by using standard X-ray imaging and ultrasound imaging respectively. With this method, the number of markers that can be introduced in practice was limited as they can only be placed on the epicardium. The placement of these markers required invasive surgery, which in itself could alter the contractility of the myocardium. Despite these limitations, these early studies proved that contractility could be an early marker of disease, and therefore a valuable research tool for understanding myocardial function.

Thus far, cardiac function and its link to anatomy and fibre architecture remains an active research topic. It has been shown that the myocyte array is disrupted in disease, and imaging techniques such as CMR with delayed Gd-DTPA contrast enhancement combined with contractility measurement are starting to unveil the relationship between scar tissue and myocardial function¹⁵¹. Clinical studies using CMR tagging and velocity mapping have already demonstrated the value of CMR in illustrating the direct link between diseases such as ischaemic heart disease and cardiomyopathies and intrinsic myocardial contractility. CMR diffusion tensor imaging augmented with strain rate from velocity mapping is also playing an important role in elucidating the relationship between fibre orientation and fibre shortening³¹.

8.2 Measuring Myocardial Motion

Over the years, a number of imaging modalities, *i.e.*, X-ray, ultrasound and MR, have been applied to the measurement of myocardial motion. Developments in MR imaging led to the use of CMR tagging and CMR velocity mapping for direct measurement of myocardial motion. Recently, tissue Doppler ultrasound has also emerged as valuable alternative, but it is limited by the acoustic windows available into the body, the SNR, and the fact that only the velocities of the tissue parallel to the ultrasound beam can be measured. Nonetheless, it is showing promise in assessing diseased myocardium by assessing velocity gradients across the myocardium. Although velocity gradients are a useful means of evaluating myocardial function, they can vary from subject to subject depending on individual anatomical geometry. Therefore, it is desirable to obtain strain rate data from tissue Doppler imaging as it is independent of geometry and bulk motion.

CMR, as a parallel technique, is more flexible and versatile in many ways. It allows access to any oblique imaging plane, thus allowing imaging of the heart using its intrinsic axes. Different functional and anatomical indices, such as ejection fraction, volume change, blood flow and perfusion, can be readily obtained. This makes CMR ideal for a 'one-stop' shop of cardiac imaging. A patient could be scanned in one hour with a complete study of ejection fraction, LV mass and volume, blood flow in the aorta and chambers, perfusion and contraction. The scanning workflow can be easily tailored to the disease with the imaging protocol designed to maximise the diagnostic capacity of the scan.

Thus far, the two traditional CMR techniques used for measuring motion are tagging and velocity mapping. CMR tagging uses the principle of magnetically tagging material and following its motion over time, whereas velocity mapping uses the intrinsic properties of the phase of the MR signal to encode its velocity. Both techniques were developed in the early 1980s and their respective strengths and potential pitfalls have been explored in detail in this thesis.

8.2.1 CMR Tagging

CMR tagging has been used to measure myocardial motion over the last 15 years with clinical studies showing the potential of its application in a range of diseases. However, its clinical

application is limited by a number of factors, probably the most important of which is the time needed for post-processing. At present, post-processing techniques are tedious requiring extensive user intervention, thus limiting the clinical use of tagging data. HARP imaging overcomes this limitation by using the phase of the tags to calculate their displacement rather than using the traditional tag-tracking algorithms. HARP imaging allows myocardial strain and velocity to be calculated within minutes after image acquisition.

In this thesis, we used a CSPAMM sequence to encode myocardial motion and in-house software was developed to calculate the strain tensor and velocity from HARP. This scheme allowed fast acquisition and processing of myocardial motion, which was further enhanced with navigator echoes for respiratory gating to improve the consistency and reproducibility of the data. The effect of respiration on strain distribution was demonstrated with a study involving normal volunteers. Changes in myocardial motion were observed during respiration. They were variable and unpredictable among subjects, highlighting the importance of effective respiration management if consistent contractility results are to be derived. This finding may have consequence on how future clinical image acquisition is carried out. A study involving patients with hypertrophic cardiomyopathy genotype as compared to normals was also carried out. This demonstrated the practical value of the method and the potential of using strain as an early marker.

As HARP imaging is based on CMR tagging, it inherits the main limitations associated with tag spacing, tag fading, limited temporal resolution and restriction on measuring only in-plane motion. Although the problems of tag spacing, tag fading and temporal resolution may be overcome by employing fast imaging techniques and innovative MR methods, 3D motion from HARP may only be obtained using a combination of short axis and long axis images, thus losing the advantage of fast processing as lengthy registration methods would be needed.

8.2.2 CMR Velocity Mapping

CMR velocity mapping, also known as phase contrast technique, uses the intrinsic properties of MR imaging to encode the velocity of the tissue as a phase difference using a bipolar gradient pulse. This allows measurement of velocity in all three directions with a much higher spatial resolution than tagging. However, it is riddled with other problems such as blood flow artefact, limitations on velocity sensitivity giving low velocity to noise ratio and low temporal resolution due to the long time needed to encode velocity with a sufficiently high range. If robust velocity data was available it would become easy to obtain strain rate and strain from such measurements. This would be desirable as strain and strain rate are independent of rigid

body motion and thus give a good marker of motion which can be even be used to compare hearts with different geometries.

The work in this thesis was focused on the use of a black blood pulse to limit the blood flow artefacts, and view-sharing to improve the temporal resolution¹⁵¹. Detailed analysis with *in vivo* data acquired with and without the blood saturation pulse was performed to evaluate the effectiveness of the blood saturation pulse. Our study has shown a significant difference between regional velocities measured with and without blood saturation. To ensure consistent myocardial velocity measurement, we have further improved the imaging sequence to incorporate prospective respiratory gating with navigator echoes. This allowed improved spatial and temporal resolution and a higher velocity sensitivity.

During the course of this study, it has been found that there is significant difference in the VNRs between in-plane and through-plane myocardial velocities. Direct calculation of strain rate from the measured myocardial velocity data has shown to be of little clinical value because of the significant artefact amplified by the derivation process. This is the main reason that limited the practical use of strain rate for clinical applications over the years. A novel iterative scheme was developed to improve the consistency of the velocity data. The scheme employed iterative optimisation to combine the incompressibility constraint with an error term that incorporates the different VNRs of the velocity components. The combination of the breath-hold velocity mapping sequence and the iterative optimisation scheme allowed successful clinical application of the technique for evaluating regional contractility in both normals and patients.

8.2.3 Virtual Tagging

One of the disadvantages associated with myocardial velocity data is that the original velocity images do not give any intuitive analysis capability. Thus a framework is needed where the velocity data can be easily visualised and processed. To this end, a novel virtual tagging framework has been developed. It allowed the velocity data to be easily visualised in the form of vector maps and the myocardial deformation to be visualised using virtual tags. This entails the superimposition of a grid onto the myocardium that deforms according to the velocities contained in each element. The virtual tagging framework provides an ideal way of visualising and processing 3D velocity data, allowing a range of displays including vector maps, strain and strain rate components. The proposed framework was validated by using both simulated and phantom data. Comparison between CMR tagged and virtual tagging was

carried out, confirming virtual tagging to be a robust and accurate way of analysing velocity data.

8.3 Future Work

The main contribution of this thesis is in the improvement of the effectiveness and quality of quantitative myocardial contractility analysis from both sequence design and medical image computing perspectives. HARP imaging was explored as a means of detecting gross changes in myocardial contractility and proved to be effective in measuring trends in 2D strain and velocity. To detect more subtle changes in contractility, a CMR velocity mapping sequence was developed which allowed encoding of velocity in all three directions. Combined with novel processing techniques, this allowed examination of regional changes in 3D contractility due to disease.

There are a number of improvements that can be made to further enhance the clinical applicability of the proposed technique. The first of these remains in the further improvement of data acquisition. At present, although the velocity mapping sequence performs well, the scan duration needs to be further reduced. Respiratory gating using navigator echoes can improve the consistency of the velocity data, however, the scan can take up to a minute per image. To cover the complete volume of the LV, an additional 10-15 minutes will be required in addition to the total scan time. Respiratory gating using navigator echoes can also introduce problems such as drift in breathing pattern during the scan. Future work should address the application of fast imaging techniques to myocardial velocity mapping. Spiral and EPI imaging have already been applied in coronary flow imaging, and combined with zonal selective imaging could improve the velocity sensitivity while reducing the breath-hold to a reasonable time^{130,157}. Alternatively, HARP imaging and CMR velocity mapping could be combined into a single sequence to allow delineation of 3D motion. The HARP technique could be used to calculate in-plane strain while velocity encoding in the through-plane direction could be used to quantify the third direction of motion. Kuijter *et al* accomplished similar results but the technique was limited by the lengthy processing needed for calculation and visualisation of strain data¹⁶¹. This could be overcome by using HARP processing rather than conventional tag tracking methods.

Another important area to be explored is the use of redundant information carried in different velocity components by the use of generalised series reconstruction of the velocity data. The use of generalised series for image reconstruction has been proven to be effective for dynamic

imaging and enables a times series of higher resolution images to be reconstructed from a single high resolution reference image and a set of low resolution dynamic images. For velocity mapping, as each of the velocity components depicts the same anatomical structure, a similar scheme can be explored to reduce the number of k -space encoding lines that need to be acquired. Our previous research has shown that this concept can be successfully adapted for rapid multi-spectral imaging both to enhance image quality and to facilitate regional segmentation.

Processing of myocardial motion data also needs to be further explored. Fast, robust and accurate techniques are needed to allow easy clinical implementation of regional contractility analysis. HARP imaging has tremendous potential to allow real-time indication of gross changes in regional myocardial strain⁸⁴. However, it has limited spatial resolution due to the paucity of tags across the myocardium. CMR velocity mapping, on the other hand, potentially allows accurate delineation of transmural strain rates. This is only limited by the spatial and velocity resolution achieved by current sequences but may be overcome by using the techniques mentioned earlier, leading to the ability to look at detailed changes in contractility allowing tracking of changes in contractility during a disease or recovery process. The virtual tagging framework brings velocity mapping a step closer to realisation in a clinical environment. It allows fast strain rate processing and deformation visualisation, and can potentially be applied to any imaging modality. Further work is needed on validating the technique *in vivo* on normal and patient data before its potential can be fully harnessed.

Research into clinical application of these techniques is also vital in evaluating their practical clinical value. It has already been shown that changes in regional myocardial contractility are a good indicator of disease. The multi-centre MESA study is currently evaluating HARP imaging on 6500 subjects to assess the usefulness of the method in clinical evaluation¹⁶². This work will be invaluable in not only assessing the applicability of HARP imaging but also in exploring the links between different diseases and myocardial contractility.

The assessment of intrinsic myocardial contractility is an essential research tool for exploring the normal function of the heart, and for further understanding of links between electrical activation, fibre architecture and contraction. A combination of suitable imaging protocol, CMR sequence design and reliable processing techniques is needed to enable measurement of myocardial motion *in vivo*. Further research is needed to explore which techniques are most suitable for specific cases, for instance in a case such as pulmonary hypertension where the patient has slow moving blood in the LV, CMR velocity mapping may not be suitable and HARP imaging would be more appropriate.

An important application of the techniques developed in this thesis is to compare myocardial function at rest and under pharmacological stress. This would allow assessment of hibernating and stunned myocardium, allowing the planning of an effective therapeutic strategy. Although HARP allows measurement of gross changes in contractility, velocity mapping potentially permits assessment of transmural function. Improvements in the spatial and temporal resolution of the velocity mapping sequence using fast imaging and volume selective techniques would allow subepicardial and subendocardial resolution of strain rate leading to more accurate diagnosis and detection of subtle changes in contractility. These are essential for providing accurate functional indices for recent advances in novel gene therapy for angiogenesis aimed at improving myocardial perfusion and contractility. It is hoped that this work will lay the basis for a clinically viable platform for functional correlation with other measures such as myocardial perfusion and diffusion, and to serve as an aid for further understanding of the links between intrinsic cardiac mechanics, localised genesis, and progression of cardiovascular disease.

APPENDIX I: MR Tagging

MR tagging is achieved by selective magnetic saturation of the tissue. The simplest kind of MR tagging is spatial modulation of magnetisation (SPAMM) tagging where two 90° RF pulses are used, separated by a gradient waveform as shown in Figure A.1^{49,65}. The direction of the gradient determines which plane the tags appear in, and the amplitude of the gradient dictates the spacing between the tags. The first RF pulse turns the longitudinal magnetisation into transverse magnetisation. The gradient pulse then causes a linear modulation of the phases of the spins in the transverse plane along the direction of the gradient. The second RF pulse mixes the modulated transverse magnetisation with the longitudinal magnetisation causing the total longitudinal magnetisation to be sinusoidally modulated, hence producing dark bands of magnetisation in the final image, as shown in Figure A.2.

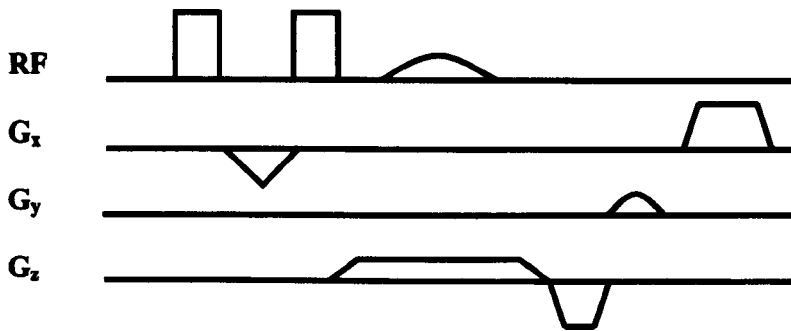


Figure A.1. A sequence diagram for a simple SPAMM sequence. Two $+90^\circ$, $+90^\circ$ RF pulses are separated by a gradient in the y-direction, which produces horizontal tags in the image. The tagging is followed by a standard FLASH imaging sequence.

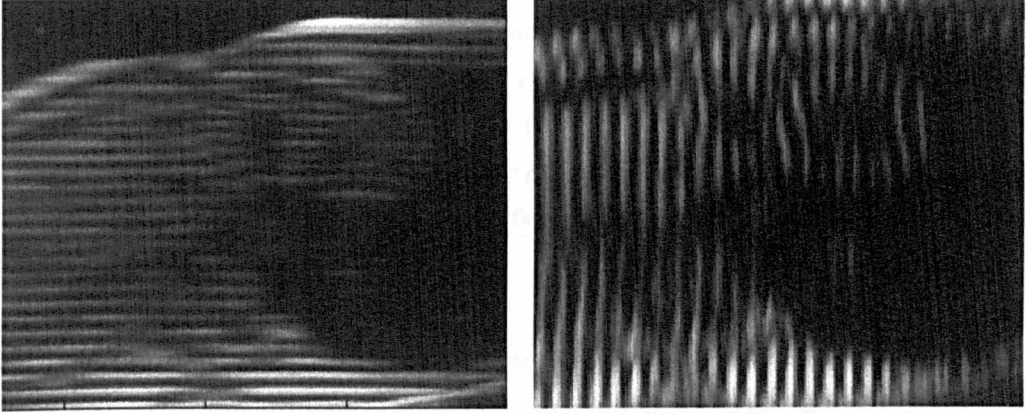


Figure A.2. MR tagged image of the heart, short axis view. Horizontal and vertical tags can be applied separately or a grid can be produced by applying both directions of tagging in one acquisition.

The tag pattern can be described mathematically as¹⁶³:

$$f(p) = \sum_{n=0}^{N-1} a_n \cos(ng^T p) \quad (\text{A1.1})$$

where N is the number of pulses used, a_n are the co-efficients determined by the flip angles of the RF pulses and g is the matrix of gradient pulses. This tag pattern multiplied by the underlying anatomical images provides the final tagged image:

$$I = I_0 \cdot f(p) \quad (\text{A1.2})$$

Usually, two SPAMM sequences are applied in quick succession to achieve a grid tagging pattern. This can be described as follows:

$$f(p) = \sum_{n=0}^{N-1} a_n \cos(ng_1^T p) \cdot \sum_{n=0}^{N-1} a_n \cos(ng_2^T p) \quad (\text{A1.3})$$

where g_1, g_2 are the two gradients directions.

Complementary SPAMM (CSPAMM)

Tag fading and contrast have been problematic issues for tag analysis ever since the development of tagging. Many sequences and image processing schemes have been devised to overcome this difficulty. Tag contrast can be improved by using more RF pulses and gradients to improve the “square” profile of the tags. As more RF pulses and gradients are added, there are more cosine terms in Equation (A1.1), causing the tags to have a sharper, rather than a simple cosine, profile. The sequences developed to do this include binomial SPAMM and DANTE type sequences.

To improve tag contrast and reduce fading during the later phases of the cardiac cycle, Fischer *et al*⁶⁸ noticed that the contrast can be greatly enhanced by subtracting two sets of tagged images with opposing tag phases. To measure the improvement in tag contrast we introduce the tagging contrast. This is defined as the ratio of the amplitude of the tag modulation and the maximum amplitude of the image at a specified location. This can be further explored by looking at the causes of tag fading.

We know that tag fading occurs due to two reasons: the longitudinal relaxation of the transverse component and the relaxation of the tagged signal into the transverse plane. We assume that n images, which lie on the (x, y) plane, are acquired with a SPAMM cine imaging sequence. M_0 is the spatially dependent magnetisation of the object before any MR experiment has been performed. M_{ss} is the magnetisation component before the tagging sequence is applied. The sequence of pulses consist of a tagging grid at t_0 , the first imaging RF pulse with flip angle α_1 at t_1 , the second RF pulse with flip angle α_2 at t_2 , and so on, and the n -th pulse with flip angle α_n at t_n .

The z-magnetisation M_z before the first RF imaging excitation pulse, at t_1 , can be expressed as the contribution of two components. The first component $Q_T(t_1)$ contains the tagging information and the second $Q_R(t_1)$ is the component of magnetisation that has relaxed since the application of the tagging pattern.

$$M_z(t_1) = \underbrace{M_{ss} \cdot f(p) \cdot e^{-\frac{t_1}{T_1}}}_{Q_T(t_1)} + \underbrace{M_0 \left(1 - e^{-\frac{t_1}{T_1}} \right)}_{Q_R(t_1)} \quad (\text{A1.4})$$

$f(p)$ is the tagging function from equation (A1.1) and T_1 is the relaxation time.

Subsequently, the longitudinal magnetisation M_z before the RF excitation pulse of the k -th heart phase image can be written as:

$$M_z(t_k) = \underbrace{M_{ss} \cdot f(p) \cdot e^{-\frac{t_k}{T_1}} \cdot \prod_{j=0}^{k-1} \cos \alpha_j}_{Q_T(t_k)} + \underbrace{\left(Q_R(t_{k-1}) \cos \alpha_{j-1} - M_0 \right) e^{-\frac{t_k - t_{k-1}}{T_1}} + M_0}_{Q_R(t_k)} \quad (\text{A1.5})$$

The transverse, x-y magnetisation, which contributes to the k -th image I_k is the sum of the tagging component $Q_T(t_k)$ and the relaxed component, $Q_R(t_k)$, rotated into the xy plane by the flip angle α_k :

$$I(t) = (Q_T(t_k) + Q_R(t_k)) \cdot \sin \alpha_k \quad (\text{A1.6})$$

The tagging contrast, considering the above definition and equation (A1.6), is given as:

$$\text{tagging contrast} = \frac{Q_T(t_k)}{Q_T(t_k) + Q_R(t_k)} \quad (\text{A1.7})$$

Therefore from equations (A1.7) and (A1.5) we can conclude that tag fading in later images of the cardiac cycle results from the decrease of the tagging component $Q_T(t_k)$ and the increase of $Q_R(t_k)$, which inherently does not contain tagging information. $Q_T(t_k)$ reduces due to relaxation, which is expressed by the exponential component of $Q_T(t_k)$ in equation (A1.5) and the RF excitation pulses of the imaging sequence, expressed as the product sequence of cosines of the respective flip angles. $Q_R(t_k)$ increases in later frames, especially when the relaxation time T_1 is small.

The basic idea of the tagging contrast enhancement proposed by Fischer *et al*⁶⁸ is based on eliminating the relaxed component $Q_R(t_k)$ by subtracting two images A and B with different tagging functions $f_A(p)$ and $f_B(p)$ respectively. The subtraction of both k -th images of the sequence leads to:

$$I_{\text{CSPAMM}}(t_k) = A(t_k) - B(t_k) \propto M_{SS} [f_A(p) - f_B(p)] \cdot e^{-\frac{t_k}{T_1}} \left(\prod_{j=0}^{k-1} \cos a_j \right) \sin a_k \quad (\text{A1.8})$$

Equation (A1.8) shows that not only has the relaxation component $Q_R(t_k)$ been eliminated but further more we can amplify the tagging-contrast by choosing tagging functions $f_A(p)$ and $f_B(p)$ that satisfy the equation (A1.9):

$$f_A(p) + f_B(p) = 0 \quad (\text{A1.9})$$

Experimentally, two tagging grids that satisfy equation (A1.9) can be induced by two sequences of 1-1 binomial SPAMM pulses. One of the four pulses has to be -90° and the rest 90° in order to obtain maximum tagging contrast.

APPENDIX II: MR Velocity Mapping (Phase Contrast Techniques)

Phase contrast velocity mapping was first developed by Bryant et al⁵¹ in the mid-1980s to measure blood flow and myocardial motion. MR velocity mapping relies on the fact that a uniform motion of tissue in the presence of a magnetic field gradient produces a change in the phase of the MR signal proportional to its velocity.

The principle behind phase contrast velocity mapping can be derived from basic MR principles. It uses the fact that a spin moving in a gradient field will experience a motion related phase shift. The phase acquired by a particle can be calculated from the zero and first moments of the gradients applied. For stationary spins the phase, $\phi(t)$, is given by the zero moment, Equation A2.1, and for spins moving at a constant velocity by the first moment, Equation A2.2.

$$\text{Zero gradient moment:} \quad \phi(t) = \gamma_0 \int G(t) dt \quad (\text{A2.1})$$

$$\text{First gradient moment:} \quad \phi(t) = \gamma_0 \int t G(t) dt \quad (\text{A2.2})$$

where γ is the gyromagnetic constant, $G(r) = (G_x, G_y, G_z)$ is the gradient magnetic field applied, r_0 is the spatial position of the spin, and v_0 is the spin's constant velocity¹⁶⁴. The phase shifts associated with higher orders of motion, such as acceleration, can also be calculated but will not be discussed here.

MR sequences can be specially designed to exploit this fact. This is done by using a "bipolar" gradient, *i.e.* a gradient pulse that has two symmetrical lobes. Although it may seem that this pulse achieves nothing, this is only true for stationary spins. Moving spins acquire a phase shift directly related to their velocity. This relationship between the gradient applied and the phase can now be used to measure the velocity of the moving spins. Thus, if a balanced bipolar gradient is applied before image acquisition, stationary tissues will not experience a phase change. However, spins moving at a constant velocity will experience a phase change, directly proportional to their velocity, Figure A2.1. By subtracting the phase images from a scan with and without the bipolar pulse, a direct measurement of the velocity can be obtained.

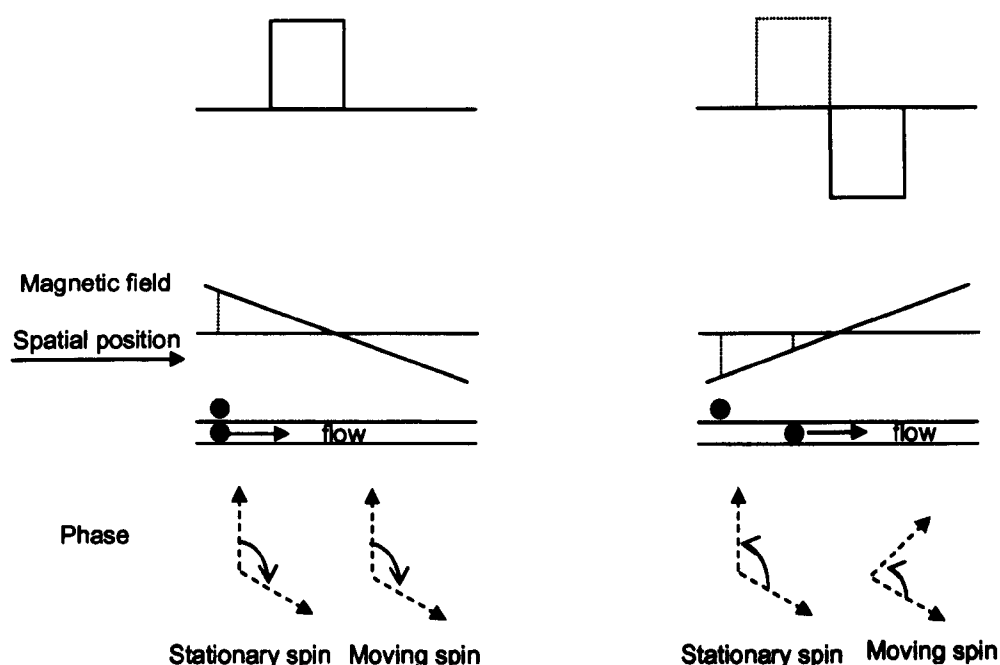


Figure A2.1 Effect of gradient field on the phase of a spin. The moving spin will acquire a phase shift directly proportional to its velocity during the second half of the bipolar gradient.

The velocity sensitivity of a bipolar gradient pulse can be easily derived using Equation A2.2.

$$\phi(t) = 2\gamma G \delta \Delta \quad (\text{A2.3})$$

γ , G , δ and Δ are constant for any particular MR sequence. Thus the phase is directly proportional to the velocity. The range of phase physically measured is set to 2π which allows the calculation of the velocity sensitivity (venc) of the gradient applied, or alternatively the gradient needed to achieve a particular venc. The velocities in the region of interest to be imaged should cause large phase shifts to be measured accurately. However, if they are too large, *i.e.*, greater than $\pm 180^\circ$, there will be velocity aliasing. To avoid this, the venc needed should be estimated before designing the MR sequence. For pulsatile flow, the sequence can be designed to have higher venc during the period with higher velocities and lower venc during the period with lower velocities to record them more accurately. For example, this would correspond to a higher venc during systole and lower venc during diastole in a cardiovascular application.

Practically, velocity mapping can be accomplished in two ways, either two opposing bipolar gradients are used or one reference scan without a bipolar gradient and a velocity encoded scan with a bipolar gradient can be used. In the first case, to accomplish three directions of

velocity encoding would require six separate acquisitions whereas in the second only four scans would be required as the same reference scan can be used for all three directions. The advantages in using two opposing bipolar gradients is that the velocity sensitivity range is doubled and eddy current effects are cancelled out during phase subtraction. If only one bipolar gradient is used the scan time is much shorter but eddy current effects are much more pronounced, especially at higher velocity sensitivities.

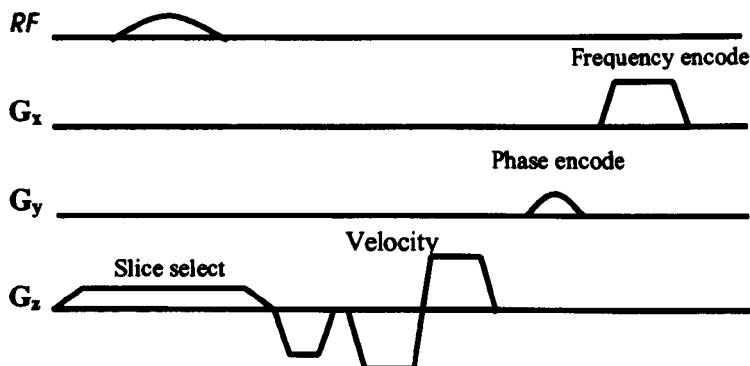


Figure A2.2 Schematic sequence diagram of through-plane velocity encoding sequence. The bipolar gradient pulse is played in the slice-select/through-plane direction. It can be played on the different axes to enable velocity mapping in different directions.

Myocardial velocity mapping has, in the past, had many problems associated with it. These include motion artefacts from respiration and blood flow and eddy current effects. Respiratory motion is overcome using breath-hold scans which implies that the sequence has to be sufficiently fast to be accomplished in a single breath-hold. This is not always possible for the different directions and sometimes the three velocity directions are acquired in three separate breath-holds, which can introduce registration errors in the dataset. Artefacts due to blood flow have been reduced using black-blood imaging schemes that introduce a pre-saturation pulse adjacent to the slice being imaged to significantly reduce the signal from the blood.

Whenever a linear gradient is switched on, concomitant non-linear magnetic fields result¹⁵³. These are a consequence of Maxwell's equations for the divergence and curl of a magnetic field, and can cause artefacts in the velocity image. This can be better understood by looking at Figure A2.3, where it can be seen that the non-zero gradient components in the x or y directions cause the length of the magnetic field vector to be greater than the sum of $B_0 + G \cdot r$ (where $G \cdot r = G_x x + G_y y + G_z z$) by an amount B_C .

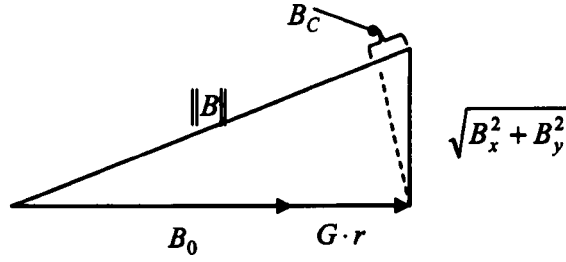


Figure A2.3 The concomitant gradient terms are due to the non-zero x and y components of the gradient field.

The concomitant gradient and resulting phase error can be accurately calculated from Maxwell's equations as follows:

$$B_C(x, y, z, t) = \frac{1}{2B_0} \left(G_x^2 z^2 + G_y^2 z^2 + G_z^2 \frac{x^2 + y^2}{4} - G_x G_z xz - G_y G_z yz \right) \quad (\text{A2.4})$$

which can be factored into the non-negative expression:

$$B_C(x, y, z, t) = \frac{1}{2B_0} \left\{ \left(G_x z - \frac{G_z x}{2} \right)^2 + \left(G_y z - \frac{G_z y}{2} \right)^2 \right\} \quad (\text{A2.5})$$

This concomitant field will cause a phase error to be accumulated during the time the gradients are switched on:

$$\phi_C = \gamma \int B_C(x, y, z) dt \quad (\text{A2.6})$$

$$\Delta\phi_C = \phi_{C, \text{venc1}}(x, y, z) - \phi_{C, \text{venc2}}(x, y, z)$$

where $\Delta\phi_C$ is the accumulated phase error in the subtracted phase contrast images from the two scans, *i.e.*, reference (venc1) and velocity encoded (venc2).

There are a few methods devised over the years to reduce these phase errors. The correction can be carried out in the final image or in the raw data. In the final image, a simple background correction can be done by fitting a polynomial to the final velocity images using the stationary material as points of zero velocity. The offset can then be calculated and subtracted from the image. This method is not always accurate as the offset can have quadratic terms and can be affected by the real velocity data, introducing further errors into the data.

A simpler way of dealing with this error can be devised if we examine Equation A2.6 closely. If two opposing bipolar gradients are used the phase due to the concomitant magnetic fields

during the encoding time will cancel out in the final phase subtraction. However, as mentioned earlier, this would make total scan time impractical for single breath-hold imaging.

The final way of eliminating the phase error is to calculate it directly from the pulse sequence and subtract it from the final image. The read-phase-slice gradient waveforms are transformed to x, y, z co-ordinate system using point-by-point multiplication by the orthogonal rotation matrix. The phase correction co-efficients are then calculated:

$$\begin{aligned}
 A &= \frac{\gamma}{2B_0} \int \left\{ \left(G_x^2(t) + G_y^2(t) \right)_{\text{venc1}} - \left(G_x^2(t) - G_y^2(t) \right)_{\text{venc2}} \right\} dt \\
 B &= \frac{\gamma}{8B_0} \int \left\{ G_z^2(t)_{\text{venc1}} - G_z^2(t)_{\text{venc2}} \right\} dt \\
 C &= -\frac{\gamma}{2B_0} \int \left\{ \left(G_x(t)G_z(t) \right)_{\text{venc1}} - \left(G_x(t)G_z(t) \right)_{\text{venc2}} \right\} dt \\
 D &= -\frac{\gamma}{2B_0} \int \left\{ \left(G_y(t)G_z(t) \right)_{\text{venc1}} - \left(G_y(t)G_z(t) \right)_{\text{venc2}} \right\} dt
 \end{aligned} \tag{A2.7}$$

These integrals are evaluated for all the gradients over the period between the two velocity encodes. Since the phase-encoding gradient changes throughout the scan, only one particular gradient value is chosen, usually the one corresponding to the centre of k -space. The calculated phase error can then be passed to the reconstruction program which can subtract it from the final image:

$$\Delta\phi_C = Az^2 + B(x^2 + y^2) + Cxz + Dyz \tag{A2.8}$$

Thus, the phase error for each pixel can be determined once its spatial co-ordinates, *i.e.*, x, y, z location in the magnet, are known. Hence, a pulse sequence-reconstruction correction can be used to eliminate the error due to the concomitant gradient terms.

APPENDIX III: Harmonic Phase (HARP) Imaging

Every MR image is actually a two-dimensional Fourier transform of the signal received from the scanner. MR tagging in the spatial (image) domain implies a sinusoidal modulation of the image in the simplest case, *i.e.*, SPAMM tagging. In the frequency domain, this gives a central DC peak surrounded by a two spectral peaks at the frequency of the tagging as illustrated in Figure A3.1. The position of this peak is directly dependent on the tag gradient used and is related to the desired tag spacing in the image domain.

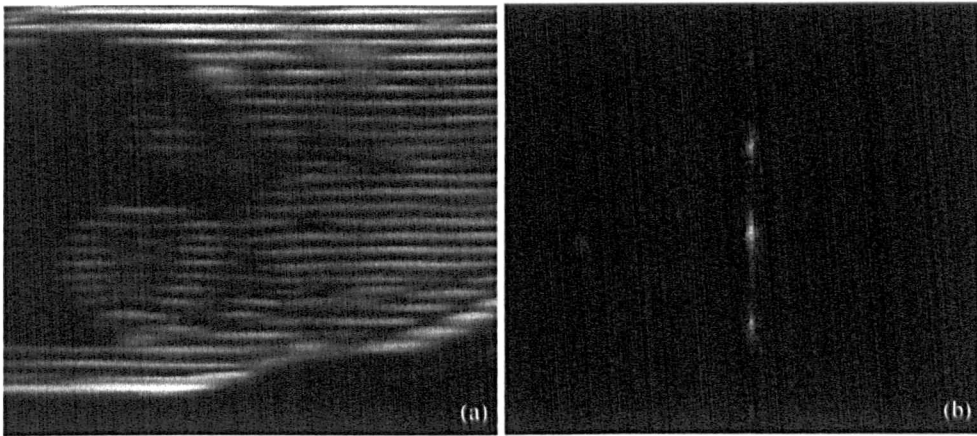


Figure A3.1. Short axis image of the heart with horizontal tagging and (b) its corresponding Fourier transform. As this is the second frame in the cardiac cycle, the spectral peaks are quite bright. Later on in the cardiac cycle as the tags fade the spectral peaks become dimmer and the central peak dominates the Fourier image.

The problem of tag tracking can now be considered from a signal processing perspective¹⁶⁵. It can be deduced that as the tags move closer or further apart due to cardiac motion the local tag frequency is going to change. This, in turn, will have an effect on the tag peak in the frequency domain. Osman *et al*^{82,83} found that cardiac deformation will produce a change in phase of the signal which can be tracked over time. This change in phase can be used to estimate the deformation, *i.e.*, instantaneous strain, and changes in deformation over time, velocity. This appendix outlines the method of HARP imaging for estimating cardiac strain and velocity using these phase changes.

MR Tagging: a Mathematical Description

If we look at image intensity $I(\bar{y}, t)$ at image position $\bar{y} = [y_1, y_2]^T$, which is a 2D co-ordinate vector. This image co-ordinate vector is related to its 3D position x by:

$$x(\bar{y}) = y_1 \bar{h}_1 + y_2 \bar{h}_2 + x_0 = \bar{H}\bar{y} + \bar{x}_0 \quad (\text{A3.1})$$

where \bar{h}_1 and \bar{h}_2 are 3D orthogonal unit vectors describing the image orientation and \bar{x}_0 is the image origin. And the tagged image can be described in the following way:

$$I(\bar{y}, t) = I_0(\bar{y}, t) \cdot f(\bar{y}, t) \quad (\text{A3.2})$$

where I_0 is the untagged image and $f(\bar{y}, t)$ is the deformed and faded tag pattern which can be modelled by:

$$f(\bar{y}, t) = \beta(t) f_0(p(\bar{y}, t)) + (1 - \beta(t)) \quad (\text{A3.3})$$

where $\beta(t)$ is the tag fading, a monotonically decreasing function, and $f_0(\bar{y}, t)$ is the tag pattern as explained in Appendix I, Equation (A1.2) and $p(\bar{y}, t)$ is the material point which is located at \bar{y} at time t ¹⁶³.

In the case of 1D SPAMM, the tag pattern is generated by applying an RF pulse of α degrees at end diastole, $t=0$, followed by a gradient of direction and strength \bar{w} , followed by another α -degree pulse, and completed by spoiling all lateral magnetisation. In this case the tag pattern can be defined as:

$$f(p; \bar{w}; \alpha; \theta) = \cos^2(\alpha) + \sin^2(\alpha) \cos(\bar{w}^T p + \theta) \quad (\text{A3.4})$$

where θ is a fixed shift for the SPAMM pattern. This equation can also be extracted from Equation (A1.2) in Appendix I.

The cosine function has two spectral peaks in the Fourier domain. Hence a 1D SPAMM pattern generated with N RF pulses has $(2N - 1)$ spectral peaks. A 2D SPAMM pattern is the product of two 1D SPAMM patterns and thus it has $(2N - 1)^2$ spectral peaks. Therefore any SPAMM tagged image in Fourier space can be written as⁸³:

$$I(p) \approx \sum_{k=1}^K I_0(p) \cdot d_k \cdot e^{j\bar{w}_k^T p} \quad (\text{A3.5})$$

where $K=2N - 1$ for 1D SPAMM and $K=(2N - 1)^2$ for 2D SPAMM, d_k can be easily determined from the flip angles α .

CSPAMM tagging is the subtraction of two SPAMM tagged images, one of which has tag lines inverted, i.e., the tagging is 90° out of phase in the image domain as explained in Appendix I^{68,132}. So combining Equation (A3.3) and Equation (A3.4) the tag pattern can be written as:

$$f(\bar{y}, t) = \frac{1}{2} \{ [2 - 2\beta(t) \sin^2(\alpha)] + 2\beta(t) \sin^2(\alpha) \cos(\bar{w}^T p + \theta) \} \quad (\text{A3.6})$$

which agrees with Kuijer *et al* if you set $s(t) = 2\beta(t)\sin^2(\alpha)$. The CSPAMM image can now be expressed as:

$$\begin{aligned} f_{CSPAMM}(\bar{y}, t) &= \frac{1}{2} \{ [2 - s(t)] + s(t) \cos(\bar{w}^T p + \theta) \} \\ &\quad - \frac{1}{2} \{ [2 - s(t)] - s(t) \cos(\bar{w}^T p + \theta) \} \\ &= s(t) \cos(\bar{w}^T p + \theta) \end{aligned} \quad (A3.7)$$

We can see that the DC term has now been eliminated leaving only the two spectral peaks. Figure A3.2 illustrates the effect of CPAMM subtraction on the images and their Fourier transforms.

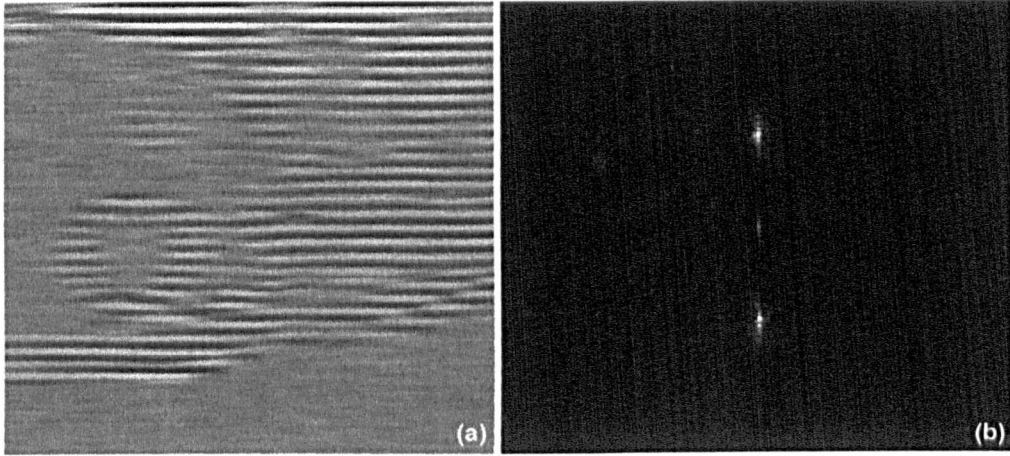


Figure A3.2. CPAMM magnitude image of the same short axis slice as in Figure A3.1 at the same point in the cardiac cycle. The corresponding Fourier transform shows how the DC peak has been suppressed and the spectral peaks are considerably enhanced.

Harmonic Images

As the tagged image consists of a DC component and the harmonic peaks, it can be expressed in the following way⁸³:

$$I(p, t) = \sum_{k=-L}^L I_k(p, t) \quad (A3.8)$$

The locations of the harmonic peaks in Fourier space are integer multiples of the fundamental tag frequency, which is determined by the tagging pulse sequence. This makes it easy to isolate one of these peaks automatically and then obtain its inverse Fourier transform to reconstruct the *harmonic image*. This harmonic image is a complex image, consisting of a

magnitude and phase image. This phase image is what is known as the *harmonic phase image* in HARP. Mathematically, the harmonic image is:

$$I_k(p, t) = D_k(p, t) e^{j(k \cdot w q(p, t) + \phi_k)} \quad (\text{A3.9})$$

where D_k is the magnitude image, which reflects both changes in geometry of the heart and the image intensity changes caused by tag fading. $q(p, t)$ is the *apparent reference map* and it characterises the heart motion and relates all points within an image to their reference positions. This is discussed further in the next section. Finally, $(k \cdot w)$ is the position of the k th harmonic image. Equation A3.9 establishes the mathematical relationship between the harmonic image and the reference map which is the basis for HARP imaging. Once the reference map has been found the deformation of the tagging pattern is described completely.

The goal is now to find the harmonic phase image:

$$\Phi_k(p, t) = k \cdot w \cdot q(p, t) + \phi_k \quad (\text{A3.10})$$

This is not an easy task as phase unwrapping is needed to determine Φ_k from I_k , which is a difficult and generally impractical procedure. However, the wrapped version of the harmonic phase image, a_k , can be calculated straightforwardly from the harmonic image:

$$a = W(\Phi) = \arctan\left(\frac{\text{imag}(I)}{\text{real}(I)}\right) \quad (\text{A3.11})$$

where W is the wrapping function given by:

$$W(\varphi) = \text{mod}(\varphi + \pi, 2\pi) - \pi \quad (\text{A3.12})$$

Determining Strain from HARP Images

This wrapped phase image can, however, be used to determine the deformation. Figure A3.3 illustrates how a change in phase due to tag deformation will result in changes in phase slope.

Mathematically, this can be explained by considering a point $P(\bar{y})$ in the image plane. Its phase is:

$$\phi_{10}(x, y) = k_{10} \cdot x; \quad \text{before deformation} \quad (\text{A3.13a})$$

$$\phi_{11}(x, y) = k_{10} \cdot x_0; \quad \text{after deformation} \quad (\text{A3.13b})$$

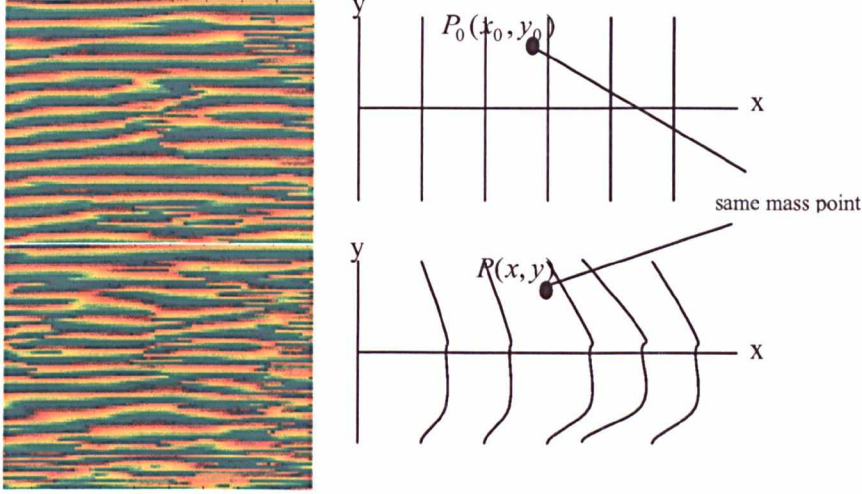


Figure A3.3. Change in phase as the tissue deforms. A particular mass point, $P(x,y)$, will carry its phase with it as it moves, changing the phase slope.

For a specific mass point, its locations before and after deformation bear the relationship:

$$x_0 + u(x_0, y_0) = x \quad (\text{A3.14})$$

Apply the gradient operator on Equation A3.13b:

$$\nabla \phi_{11} = k_{10} \cdot \nabla x_0 = k_{10} \begin{pmatrix} \frac{\partial x_0}{\partial x} \\ \frac{\partial x_0}{\partial y} \end{pmatrix} \quad (\text{A3.15})$$

Thus,

$$\begin{pmatrix} \frac{\partial x_0}{\partial x} \\ \frac{\partial x_0}{\partial y} \end{pmatrix} = \frac{1}{k_{10}} \nabla \phi_{11} \quad (\text{A3.16})$$

Similarly, for vertical modulation (horizontal tags),

$$\phi_{20}(x, y) = k_{20} \cdot y; \quad \text{before deformation} \quad (\text{A3.17a})$$

$$\phi_{21}(x, y) = k_{20} \cdot y_0; \quad \text{after deformation} \quad (\text{A3.17b})$$

For a specific mass point, its locations before and after deformation bear the relationship:

$$y_0 + v(x_0, y_0) = y \quad (\text{A3.18})$$

Apply gradient operator for (A3.17b):

$$\nabla \phi_{21} = k_{20} \cdot \nabla y_0 = k_{20} \begin{pmatrix} \frac{\partial y_0}{\partial x} \\ \frac{\partial y_0}{\partial y} \end{pmatrix} \quad (\text{A3.19})$$

Thus,

$$\begin{pmatrix} \frac{\partial y_0}{\partial x} \\ \frac{\partial y_0}{\partial y} \end{pmatrix} = \frac{1}{k_{20}} \nabla \phi_{21} \quad (\text{A3.20})$$

Combining (A3.16) and (A3.20), we get

$$\begin{bmatrix} \frac{\partial x_0}{\partial x}, \frac{\partial x_0}{\partial y} \\ \frac{\partial y_0}{\partial x}, \frac{\partial y_0}{\partial y} \end{bmatrix} = \begin{bmatrix} \frac{1}{k_{10}} \nabla \phi_{11}, \frac{1}{k_{20}} \nabla \phi_{21} \end{bmatrix}^T \quad (\text{A3.21})$$

To obtain the deformation tensor, we need to compute the derivatives of a new position with regard to its initial position, fixing at the same mass point. That is,

$$\begin{bmatrix} \frac{\partial x}{\partial x_0}, \frac{\partial x}{\partial y_0} \\ \frac{\partial y}{\partial x_0}, \frac{\partial y}{\partial y_0} \end{bmatrix} = \begin{bmatrix} \frac{\partial x_0}{\partial x}, \frac{\partial x_0}{\partial y} \\ \frac{\partial y_0}{\partial x}, \frac{\partial y_0}{\partial y} \end{bmatrix}^{-1} \quad (\text{A3.22})$$

We can now obtain the deformation tensor in terms of the phase slope by combining (A3.21) and (A3.22).

$$F = \begin{bmatrix} \frac{\partial x}{\partial x_0}, \frac{\partial x}{\partial y_0} \\ \frac{\partial y}{\partial x_0}, \frac{\partial y}{\partial y_0} \end{bmatrix} = \begin{bmatrix} \frac{1}{k_{10}} \nabla \phi_{11}, \frac{1}{k_{20}} \nabla \phi_{21} \end{bmatrix}^{-T} \quad (\text{A3.23})$$

For modulation with equal frequency in vertical and horizontal directions, $k_{10}=k_{20}=k_1$ giving

$$F = k_1 (\nabla^* a)^{-1}$$

where F is the deformation gradient tensor and $\nabla \Phi$ is related to the wrapped phase $\nabla^* a$ as follows:

$$\nabla \Phi = \nabla^* a = \begin{bmatrix} \nabla a_1 \\ \nabla a_2 \end{bmatrix} \quad (\text{A3.24})$$

$$\nabla^* a = \begin{cases} \nabla a & \|\nabla a\| \leq \|\nabla W(a + \pi)\| \\ \nabla W(a + \pi) & \text{otherwise} \end{cases} \quad (\text{A3.25})$$

To obtain the Eulerian strain the deformation tensor has to be decomposed into the rigid-body rotation, R , and the stretch tensor, U .

$$F = RU$$

$$F = \begin{bmatrix} a & b \\ c & d \end{bmatrix} = \underbrace{\begin{bmatrix} \cos(\theta) & \sin(\theta) \\ -\sin(\theta) & \cos(\theta) \end{bmatrix}}_R \cdot \underbrace{\begin{bmatrix} t_x & t_{xy} \\ t_{yx} & t_y \end{bmatrix}}_U \quad (\text{A3.26})$$

The strain tensor can now be calculated from the deformation tensor:

$$E = U - I = \begin{bmatrix} t_x - 1 & t_{xy} \\ t_{yx} & t_y - 1 \end{bmatrix} \quad (\text{A3.27})$$

The eigenvalues of the strain tensor indicate stretching, positive values, or shortening, negative values. Their corresponding eigenvectors indicate the direction the strain is acting in. The two eigenvectors are always orthogonal to each other. In the cardiac case, this usually implies radial thickening coupled with circumferential shortening or vice versa.

It is worth noting that what we are calculating is the 2D apparent motion of the heart. This motion is a projection of the 3D motion onto the 2D plane of the MR image. If we consider a material point, O , which is on the image plane at end-diastole when the tagging is applied, Figure A3.4. After time t it will have moved to point T , however, only its projection onto the image plane, A , is recorded. A tag line, in the same sense, is actually part of a tag plane orthogonal to the image plane. The tag plane distorts as the tissues move causing this line to distort into a curve. This curve intersects the image at a single point A . This point can be uniquely associated with the corresponding point at end-diastole representing an apparent motion within the image plane. Mathematically, apparent motion can be described using the apparent reference map that was described earlier⁸³:

$$q(p) = \bar{H}^T (p - x_0) \quad (\text{A3.28})$$

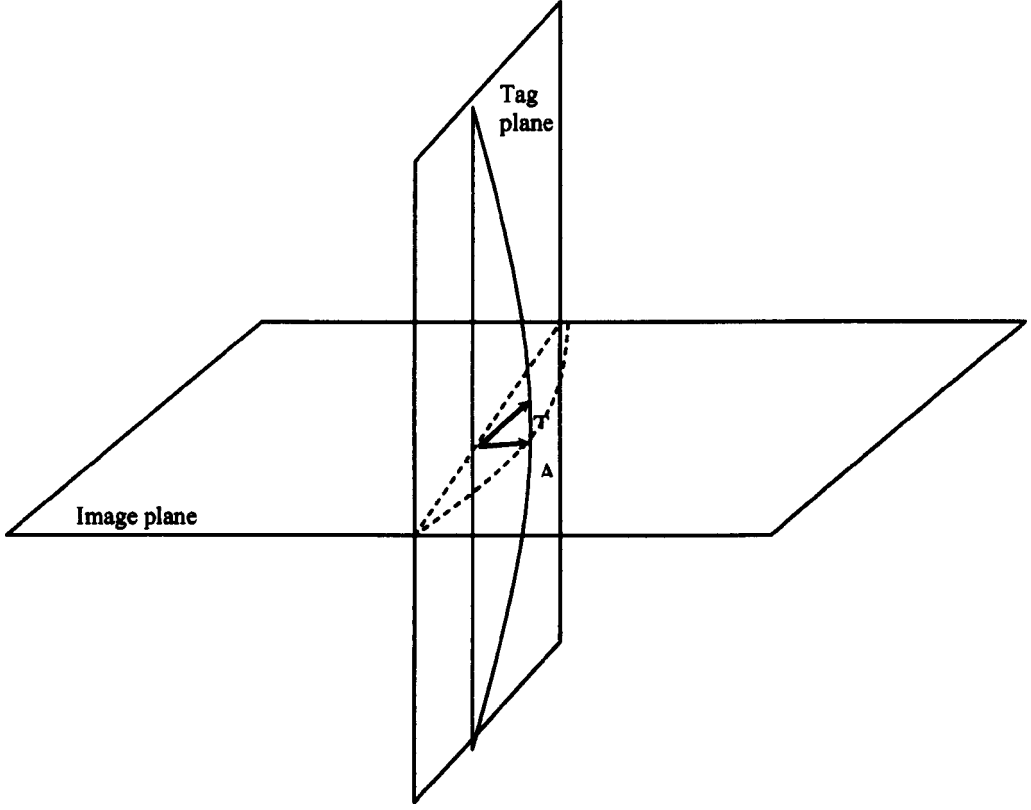


Figure A3.4. The tag plane intersects the image plane along the dotted line. As the tissue deforms, point O moves to point T. However, only the point where the tag plane intersects the image plane, A, is recorded.

Velocity from HARP Images

Velocity can be calculated from HARP images using the fact that as a material point moves, it carries its phase with it⁴. So for any material point, \bar{y} ,

$$\frac{d\Phi(\bar{y}, t)}{dt} = 0. \quad (\text{A3.29})$$

This can be rewritten using the chain rule:

$$\frac{\partial \Phi(\bar{y}, t)}{\partial \bar{y}} \frac{d\bar{y}}{dt} + \frac{\partial \Phi(\bar{y}, t)}{\partial t} \frac{\partial t}{\partial t} = 0 \quad (\text{A3.30})$$

$\underline{u(\bar{y}, t)}$

So the velocity can be written in terms of the harmonic phase:

$$u(y, t) = - \left[\frac{\partial \Phi(\bar{y}, t)}{\partial \bar{y}} \right]^{-1} \frac{\partial \Phi(\bar{y}, t)}{\partial t} \quad (\text{A3.31})$$

We do not have Φ_k , rather we have the wrapped version of the phase, a_k . In the case that the time difference between successive images is sufficiently small we can assume the phase difference to be in the range $[-\pi, \pi]$.

$$|\Phi(y, t_{n+1}) - \Phi(\bar{y}, t_n)| < \pi \quad (\text{A3.32})$$

Therefore, the partial time derivative of the phase is approximately equal to the wrapped difference of the wrapped phase. The wrapping function W maps the difference of the wrapped phases back onto the real phase difference $\Delta\Phi$.

So the velocity can now be turned into a discrete form, which can be solved from the information we have as follows:

$$\frac{\partial\Phi(y, t_n)}{\partial t} \approx \frac{1}{\Delta t} W[a(y, t_{n+1}) - a(y, t_n)] \quad (\text{A3.33})$$

$$u(y, t_n) = -\frac{1}{\Delta t} \nabla^* a^{-1}(y, t_n) W[a(y, t_{n+1}) - a(y, t_n)] \quad (\text{A3.34})$$

Strain and velocity can thus be calculated within seconds after image acquisition using HARP imaging.

Practical Implementation

The practical implementation of HARP in a clinical system is illustrated in Figure A3.5. This dataflow diagram shows how the form of data acquired, and how it is processed to produce strain or velocity maps. For this work, a package was written to allow automatic calculation of strain from CSPAMM magnitude and phase images. Screenshots of the package are shown in Figures A3.6 and A3.7. The software allowed the user to load and view the images, draw contours around the myocardium and calculate velocity or strain. The calculated velocity was displayed as shown in Figure A3.6, with the v_x and v_y displayed on top and the magnitude and direction displayed at the bottom. The strain eigenvalues were displayed with their corresponding eigenvectors, maximum principal strain in the top row and minimum principal strain in the bottom row as shown in Figure A3.7.

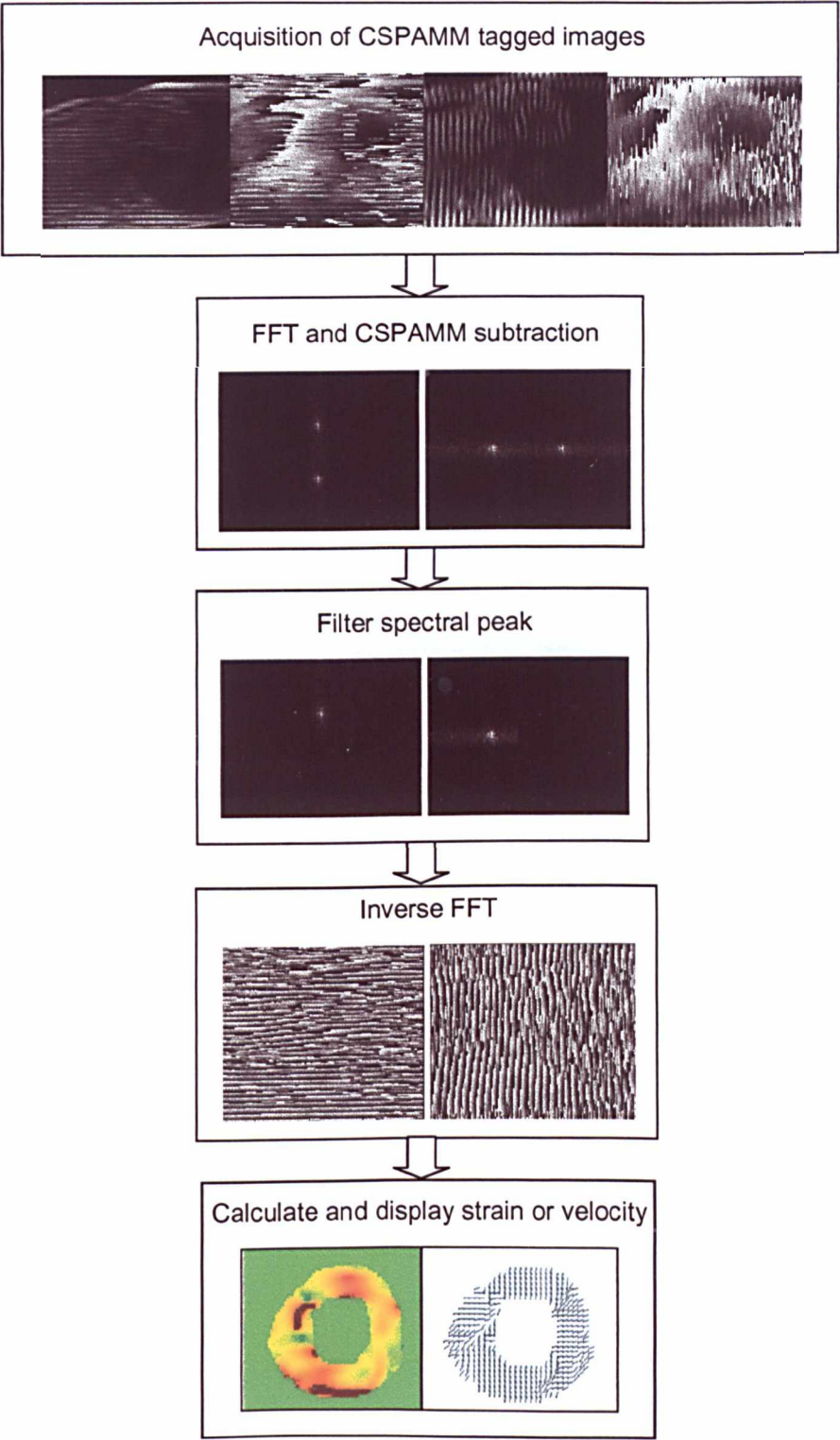


Figure A3.5. Data flow diagram for HARP processing. After acquisition, the magnitude and phase images are converted to real and imaginary and Fourier transformed. They are then subtracted to obtain the CSPAMM images in frequency space. These are then filtered and inverse Fourier transformed to obtain the HARP images which can then be used to calculate strain and/or velocity.

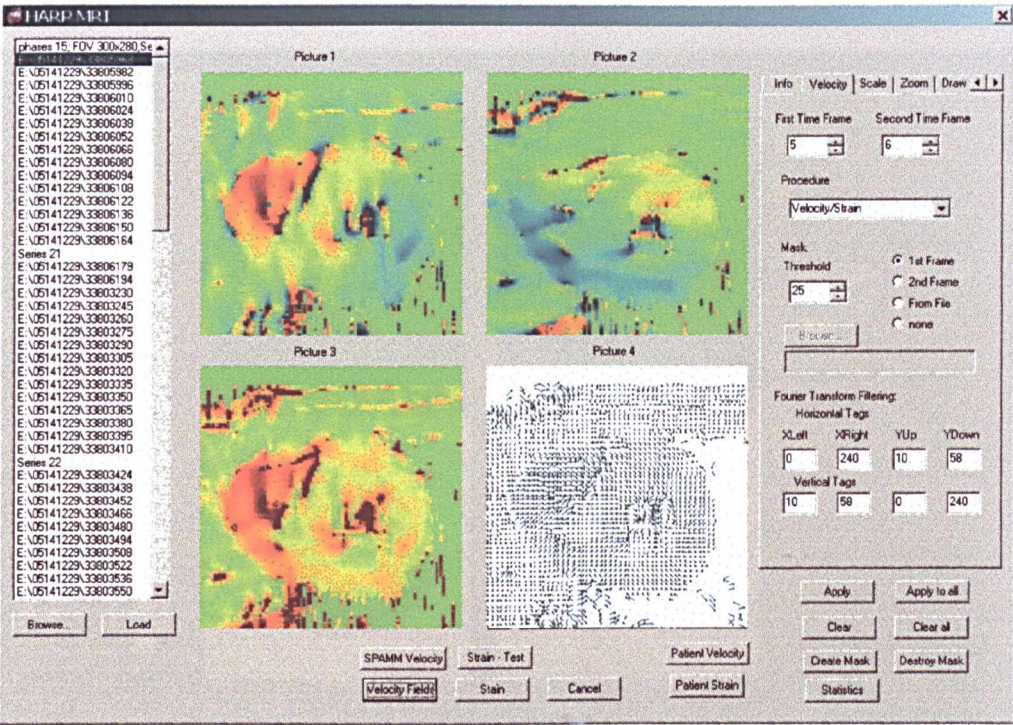


Figure A3.6. Velocity displayed in the HARP software. Pictures 1 and 2 are the velocities in the x and y directions respectively. Picture 3 is the magnitude of the velocity vector and Picture 4 is the direction. The software allows zooming in to the region of interest.

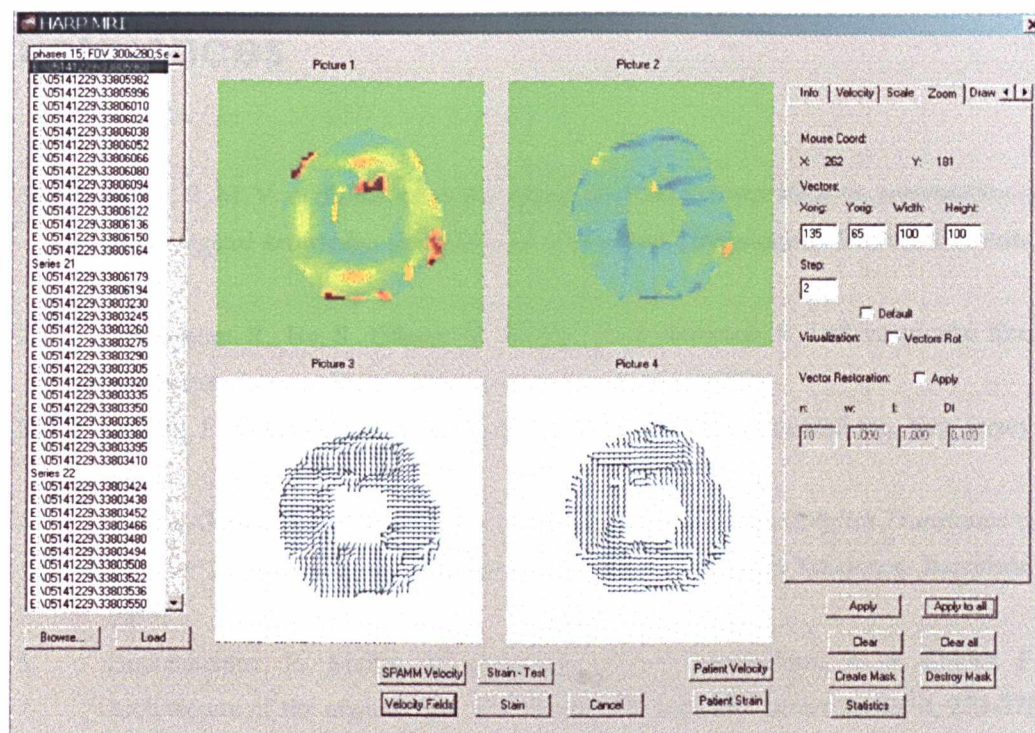


Figure A3.7. Strain displayed in the HARP software. Pictures 1 and 2 are the maximum and minimum principal strains respectively. Pictures 3 and 4 display their corresponding eigenvectors. The left ventricle has been selected after drawing contours around the myocardium and creating a mask which the software allows you to save for use later.

References

1. Berne, R. M. V. e. *Handbook of physiology: a critical, comprehensive presentation of physiological knowledge and concepts*. (American Physiological Society, Bethesda, 1979).
2. Greenbaum, R., Ho, S., Gibson, D., Becker, A. & Anderson, R. Left ventricular fiber architecture in man. *British Heart Journal* 3, 248-263 (1981).
3. Martini, F. *Fundamentals of Anatomy and Physiology* (Prentice Hall Inc, New Jersey, 1995).
4. Torrent-Guasp, F. et al. *Estructura Y Mecanica Del Corazon (English Translation of Chapter 2: Macroscopical Structure of the Heart)* (GRASS Ediciones, Barcelona, 1987).
5. Lunkenheimer, P., Muller, R., Konermann, C., Lunkenheimer, A. & Kohler, F. Architecture of the myocardium in computed tomography. *Invest Radiol* 4, 273-278 (1984).
6. McLean, M. & Prothero, J. Determination of relative fiber orientation in heart muscle: methodological problems. *Anat Rec* 4, 459-465 (1992).
7. Mall, F. On the muscular architecture of the ventricles of the human heart. *Am J Anat* 11, 211-266 (1911).
8. Benninghoff, A. Die Architektur des Herzmuskels. Eine vergleichend anatomische und vergleichend funktionelle Betrachtung. *Morph Jahrb* 67, 262-317 (1931).
9. Robb, J. & Robb, R. The normal heart - anatomy and physiology of the structural units. *Am Heart J* 23, 455-467 (1942).
10. Torrent-Guasp, F. in *El Fallo Mecànico del Corazon. Deciciones Toray* (ed. Perez, J.) 3-36 (Barcelona, 1975).
11. Lev, M. & Simkins, C. Architecture of the human ventricular myocardium. Technique for study using a modification of the Mall-MacCallum method. *Lab Invest* 5, 396-409 (1956).
12. Sanchez-Quintana, D., Anderson, R. & Ho, S. Ventricular myoarchitecture in tetralogy of Fallot. *Heart* 76, 280-286 (1996).
13. Torrent-Guasp, F., Whinmster, W. & Redman, K. A silicone rubber mould of the heart. *Techno Health Care* 5, 13-20 (1997).
14. Streeter Jr. , D. in *Handbook of Physiology. The cardiovascular system* (ed. Geiger, S.) 61-112 (Williams & Wilkins, Baltimore, 1979).

15. Lukenheimer, P. et al. The heart muscle's putative "secondary structure". Functional implications of a band like anisotropy. *Techno Health Care* 5, 52-64 (1997).
16. Krehl, L. Beiträge zur Kenntnis der Füllung und Entleerung des Herzens. *Abh Math-Phys Kl Saechs Akad Wiss* 17, 347-362 (1891).
17. Hort, W. Makroskopische und mikrometrische Untersuchungen am Myokard verschieden stark gefüllter linker Kammern. *Virchows Arch Pathol Anat* 333, 523-564 (1960).
18. Hort, W. Quantitative morphology and structural dynamics of the myocardium. *Achiev Exp Pathl* 5, 3-21 (1971).
19. Fox, C. & Hutchins, G. The architecture of the human ventricular myocardium. *Hopkins Med J* 130, 289-299 (1972).
20. Jouk, P.-S., Usson, Y., Michalowicz, G. & Grossi, L. Three-dimensional cartography of the pattern of the myofibers in the second trimester fetal human heart. *Anat Embryol* 202, 103-118 (2002).
21. Jouk, P.-S., Usson, Y., Michalowicz, G. & Parazza, F. Methods for the study of the three-dimensional orientation of myocardial cells by means of polarized light microscopy. *Microsc Res Tech* 30, 480-490 (1995).
22. Spotnitz, H. Macro Design, Structure, and Mechanics of the Left Ventricle. *Journal of Thoracic Cardiovascular Surgery* 5, 1053-1077 (2000).
23. Brauwald, E., Zipes, D. & Libby, P. *Heart disease: a textbook of cardiovascular medicine* (Saunders, Philadelphia, 2001).
24. Opie, L. *The heart: physiology, from cell to circulation* (Lippincott-Raven, Philadelphia, 1997).
25. Rosendorff, C. e. *Essential Cardiology: principles and practice* (Saunders, Philadelphia, 2001).
26. Torrent-Guasp, F. *The Normal Heart* (Unpublished).
27. LeGrice, I. et al. Laminar structure of the heart: ventricular myocyte arrangement and connective tissue architecture in the dog. *Am J Physiol* 2 Pt 2, H571-582 (1995).
28. Torrent Guasp, F. Macroscopic structure of the ventricular myocardium. *Revista Espanola de Cardiologia* 3, 265-287 (1980).
29. Torrent-Guasp, F. Structure and function of the heart. *Revista Espanola de Cardiologia* 2, 91-102 (1998).
30. Lunkenheimer, P. et al. The relationship between structure and function: why does reshaping the left ventricle surgically not always result in functional improvement? *Comput Biol Med* 33, 185-196 (2003).
31. Tseng, W., Reese, T., Weisskoff, R., Brady, T. & Wedeen, V. Myocardial fiber shortening in humans: initial results of MR imaging. *Radiology* 216, 128-139 (2000).

32. Tseng, W., Wedeen, V., Reese, T., Smith, R. & Halpern, E. Diffusion tensor MRI of myocardial fibers and sheets: Correspondence with visible cut-face texture. *J Magn Reson Imaging* 17, 31-42 (2003).
33. Dou, J., Tseng, W., Reese, T. & Wedeen, V. Combined diffusion and strain MRI reveals structure and function of human myocardial laminar sheets in vivo. *Magn Reson Med* 50, 107-113 (2003).
34. Lewis, T. *The Mechanism and Graphic Registration of the Heart Beat* (Shaw and Sons, London, 1920).
35. Wiggers, C. *Modern aspects of circulation in the heart and disease* (Lea and Febiger, Philadelphia, 1915).
36. Lorenz, C. & Bundy, J. Delineation of Normal Human Left Ventricular Twist Throughout Systole by Tagged Cine MRI. *Journal of Cardiovascular Magnetic Resonance* 2, 97-108 (2000).
37. Lunkenheimer, P. Comment on: The helix and the heart. *J Thorac Cardiovasc Surg*. 2002 Nov;124(5):863-83. *J Thorac Cardiovasc Surg* 126, 920-1; author reply 921-2 (2003).
38. Armour, J. & Randall, W. Functional anatomy of canine cardiac nerves. *Acta Anat* 91, 510-528 (1975).
39. Moore, C., Lugo-Olivieri, C., McVeigh, E. & Zerhouni, E. Three-dimensional systolic strain patterns in the normal human left ventricle: characterization with tagged MR imaging. *Radiology* 214, 453-466 (2000).
40. Rajappan, K., Bellenger, N., Anderson, L. & Pennell, D. The role of cardiovascular magnetic resonance in heart failure. *Eur J Heart Fail* 2, 241-252 (2000).
41. Mitchell, G., Lamas, G. & Pfeffer, M. Ventricular remodeling after myocardial infarction. *Adv Exp Med Biol* 346, 265-76 (1993).
42. Braunwald, E. & Pfeffer, M. Ventricular enlargement and remodeling following acute myocardial infarction: mechanisms and management. *Am J Cardiol* 68, 1D-6D (1991).
43. Hon, J. & Yacoub, M. Bridge to recovery with the use of left ventricular assist device and clenbuterol. *Ann Thorac Surg* 75, S36-41 (2003).
44. Yacoub, M. A novel strategy to maximize the efficacy of left ventricular assist devices as a bridge to recovery. *Eur Heart J* 22, 534-40 (2001).
45. Gerdes, A. & Capasso, J. Structural remodeling and mechanical dysfunction of cardiac myocytes in heart failure. *J Mol Cell Cardiol* 27, 849-56 (1995).
46. Gersh, B. & Rahimtoola, S. *Acute Myocardial Infarction* (Chapman & Hall, New York, 1997).

47. Mohiaddin, R. & Longmore, D. Functional Aspects of cardiovascular nuclear magnetic resonance imaging: techniques and application. *Circulation* **88**, 264-281 (1993).
48. Mosher, T. & Smith, M. A DANTE Tagging Sequence for the evaluation of Transitional Sample Motion. *Magnetic Resonance in Medicine* **15**, 334-339 (1990).
49. Axel, L. & Dougherty, L. MR Imaging of Motion with Spatial Modulation of Magnetisation. *Radiology* **171**, 841-845 (1989).
50. van Dijk, P. Direct cardiac NCMR imaging of heart wall and blood flow velocity. *Journal of Computer Assisted Tomography* **8**, 429-436 (1984).
51. Bryant, D., Payne, J., Firmin, D. & Longmore, D. Measurement of flow with NMR imaging using a gradient pulse and phase difference technique. *Journal of Computer Assisted Tomography* **8**, 588-593 (1984).
52. Edelman, R. et al. In vivo measurement of water diffusion in the human heart. *Magnetic Resonance in Medicine* **32**, 423-428 (1994).
53. Young, A., Imai, H., Chang, C. & Axel, L. Two-dimensional Left Ventricular Deformation During Systole Using Magnetic Resonance Imaging With Spatial Modulation of Magnetization. *Circulation* **89**, 740-752 (1994).
54. Meier, G., Ziskin, M., Santamore, W. & Bove, A. Contractile function in canine left ventricle. *Am J Physiol* **239**, H794-804 (1980).
55. Meier, G., Bove, A., Santamore, W. & Lynch, P. Kinematics of the Beating Heart. *IEEE Trans Biomed Eng* **27**, 319-329 (1980).
56. Young, A., Kramer, C., Ferrari, V., Axel, L. & Reichek, N. Three-dimensional Left Ventricular Deformation in Hypertrophic Cardiomyopathy. *Circulation* **90**, 854-887 (1994).
57. Karwatowski, S. et al. Regional myocardial velocity imaged by magnetic resonance in patients with ischaemic heart disease. *Brit Heart Jour* **72**, 332-338 (1994).
58. Karwatowski, S. et al. Assessment of regional left ventricular long-axis motion with MR velocity mapping in healthy subjects. *J Mag Res Imag* **4**, 151-155 (1994).
59. Markl, M. et al. Cardiac phase contrast gradient echo MRI: measurement of myocardial wall motion in healthy volunteers and patients. *Intl Jour Cardiac Imag* **15**, 441-452 (1999).
60. Beache, G. et al. Intramural mechanics in hypertrophic cardiomyopathy: functional mapping with strain-rate CMR imaging. *Radiology* **197**, 117-124 (1995).
61. Nastar, C. & Ayache, N. Frequency-Based Nonrigid Motion Analysis: Application to four dimensional medical images. *IEEE Transactions on Pattern Analysis and Machine Intelligence* **18**, 1067-1079 (1996).

62. Declerck, J., Feldmar, J. & Ayache, N. Definition of a four-dimensional continuous planispheric transformation for the tracking and analysis of left-ventricular motion. *Medical Image Analysis* 2, 197-213 (1998).
63. Park, J., Metaxas, D. & Axel, L. Analysis of left ventricular wall motion based on volumetric deformable models and MRI-SPAMM. *Medical Image Analysis* 1, 53-71 (1996).
64. Park, J., Metaxas, D. & Axel, L. Deformable models with parameter functions for cardiac motion analysis from tagged MRI data. *IEEE Transactions on Medical Imaging* 15, 278-289 (1996).
65. Zerhouni, E., Parish, D., Rogers, W., Yang, A. & Shapiro, E. Human heart: tagging with CMR imaging—a method for non-invasive assessment of myocardial motion. *Radiology* 169, 59-63 (1988).
66. Axel, L. & Dougherty, L. Heart Wall Motion: Improved method of Spatial Modulation of Magnetisation for CMR Imaging. *Radiology* 172, 349-350 (1989).
67. Huang, J., Abendschein, D., Davila-Roman, V. & Amini, A. Spatio-temporal tracking of myocardial deformations with a 4-D B-spline model from tagged MRI. *IEEE Transactions on Medical Imaging* 18, 957-972 (1999).
68. Fischer, S., McKinnon, G., Maier, S. & Boesiger, P. Improved myocardial tagging contrast. *Magnetic Resonance in Medicine* 30, 191-200 (1993).
69. Fischer, S. et al. in *4th Scientific Meeting International Society of Magnetic Resonance* 297 (New York, 1996).
70. Tsekos, N. et al. Myocardial Tagging with B1 Insensitive Adiabatic DANTE Inversion Sequences. *Magnetic Resonance in Medicine* 35, 395-401 (1995).
71. Ryf, S., Spiegel, M., Gerber, M. & Boesiger, P. Myocardial Tagging With 3D-CSPAMM. *Journal of Magnetic Resonance Imaging* 16, 320-325 (2002).
72. Herzka, D., Guttman, M. & McVeigh, E. Myocardial Tagging With SSFP. *Mag Res Med* 49, 329-340 (2003).
73. Zwanenburg, J., Kuijter, J., Marcus, J. & Heethaar, R. Steady-State Free Precession With Myocardial Tagging: CSPAMM in a single breathhold. *Mag Res Med* 49, 722-730 (2003).
74. Zwanenburg, J., Gotte, M., Marcus, J., Cock, C. d. & Rossum, A. v. in *European Cardiovascular Magnetic Resonance* (2003).
75. Young, A. Model tags: direct three-dimensional tracking of heart wall motion from tagged magnetic resonance images. *Medical Image Analysis* 1, 361-372 (1999).
76. Kerwin, W. & Prince, J. Generating 3D cardiac material markers using tagged MRI. *Lecture Notes in Computer Science* 1230, 313-326 (1997).

77. O'Dell, W., Moore, C., Hunter, W., Zerhouni, E. & McVeigh, E. Three-dimensional Myocardial Deformations: Calculation with Displacement Field Fitting to Tagged CMR Images. *Radiology* **195**, 829-835 (1995).
78. Moulton, M. et al. Spline surface interpolation for calculating 3-D ventricular strains from CMRI tissue tagging. *Am J Physiol* **270**, H281-297 (1996).
79. Denney, T. & McVeigh, E. Model Free Reconstruction of Three-Dimensional Myocardial Strain from Planar Tagged CMR Images. *Journal of Magnetic Resonance Imaging* **7**, 799-810 (1997).
80. Dougherty, L., Asmuth, J., Blom, A., Axel, L. & Kumar, R. Validation of an Optical Flow Method for Tag Displacement Estimation. *IEEE Trans Med Imaging* **18**, 359-363 (1999).
81. Koerkamp, M., Snoep, G., Muijtjens, A. & Kemerink, G. Improving Contrast and Tracking of Tags in Cardiac Magnetic Resonance Images. *Mag Res Med* **41**, 973-982 (1999).
82. Osman, N., Kerwin, W., McVeigh, E. & Prince, J. Cardiac Motion Tracking Using CINE Harmonic Phase (HARP) Magnetic Resonance Imaging. *Mag Res Med* **42**, 1048-1060 (1999).
83. Osman, N., McVeigh, E. & Prince, J. Imaging Heart Motion Using Harmonic Phase MRI. *IEEE Trans Med Imaging* **19**, 186-202 (2000).
84. Sampath, S., Derbyshire, J., Atalar, E., Osman, N. & Prince, J. Real-time imaging of two-dimensional cardiac strain using a harmonic phase magnetic resonance imaging (HARP-MRI) pulse sequence. *Mag Res Med* **50**, 154-163 (2003).
85. Kraitchman, D. et al. Quantitative ischemia detection during cardiac magnetic resonance stress testing by use of FastHARP. *Circulation* **107**, 2025-2030 (2003).
86. Amini, A., Chen, Y., Curwen, R., Mani, V. & Sun, J. Coupled B-snake grids and constrained thin-plate splines for analysis of 2D tissue deformations from tagged MRI. *IEEE Trans Med Imaging* **17**, 344-356 (1998).
87. Chandrashekara, R., Mohiaddin, R. & Rueckert, D. in *SPIE International Symposium on Medical Imaging 2002: Image Processing* (ed. Fitzpatrick, J.) (SPIE, San Diego, Calif., USA, 2002).
88. Chandrashekara, R., Mohiaddin, R. & Rueckert, D. in *International Society for Magnetic Resonance in Medicine 11th Annual Scientific Meeting* (ISMRM, Toronto, Canada, 2003).
89. Chandrashekara, R., Mohiaddin, R. & Rueckert, D. in *Workshop on Interactive Medical Image Visualization and Analysis* (ed. Gerritsen, F.) (Utrecht, The Netherlands, 2001).

90. Clark, N. et al. Circumferential myocardial shortening in the normal left ventricle: Assessment by magnetic resonance imaging myocardial tagging. *Circulation* **84**, 67-74 (1991).
91. Rogers, W. J. et al. Quantification of and Correction for left ventricular systolic long axis shortening by magnetic resonance tissue tagging and slice isolation. *Circulation* **84**, 721-731 (1991).
92. Dong, S. et al. Left Ventricular wall thickness and regional systolic function in patients with hypertrophic cardiomyopathy. *Circulation* **90**, 1200-1209 (1994).
93. Dong, S. et al. Regional left ventricular systolic function in relation to cavity geometry in patients with chronic right ventricular pressure overload. *Circulation* **91**, 2359-2370 (1995).
94. Fogel, M., Weinberg, P., Fellows, K. & Hoffman, E. A study in ventricular-ventricular interaction: Single right ventricles compared with systemic right ventricles in a dual-chamber circulation. *Circulation* **92**, 219-230 (1995).
95. MacGowan, G. et al. Non-invasive measurement of shortening in the fibre and cross-fibre directions in the normal human left ventricle and in idiopathic dilated cardiomyopathy. *Circulation* **96**, 535-541 (1997).
96. Geskin, G. et al. Quantitative assessment of myocardial viability after infarction by dobutamine magnetic resonance tagging. *Circulation* **98**, 217-223 (1998).
97. Stuber, M. et al. Alterations in the local myocardial motion pattern in patients suffering from pressure overload due to aortic stenosis. *Circulation* **100**, 361-368 (1999).
98. Prinzen, F., Hunter, W., Wyman, B. & McVeigh, E. Mapping of regional myocardial strain and work during ventricular pacing: experimental study using magnetic resonance imaging tagging. *Journal of the American College of Cardiology* **33**, 1735-1742 (1999).
99. Wyman, B., Hunter, W., Prinzen, F. & McVeigh, E. Mapping propagation of mechanical activation in the paced heart with CMRI tagging. *Am J Physiol* **276**, H881-891 (1999).
100. Marcus, J. et al. Myocardial function in infarcted and remote regions early after infarction in man: assessment by magnetic resonance tagging and strain analysis. *Mag Res Med* **38**, 803-810 (1997).
101. Yang, G.-Z. Exploring in vivo blood flow dynamics. *IEEE Eng in Med and Bio* **17**, 64-73 (1998).
102. Nayler, G., Firmin, D. & Longmore, D. Blood flow imaging by cine magnetic resonance. *Journal of Computer Assisted Tomography* **10**, 715-722 (1986).

103. Wedeen, V. Magnetic Resonance Imaging of myocardial kinematics, technique to detect, localize, and quantify the strain rates of the active human myocardium. *Mag Res Med* 27, 52-67 (1992).
104. Yang, G., Burger, P., Kilner, P., Karwatowski, S. & Firmin, D. Dynamic range extension of cine velocity measurements using motion-registered spatiotemporal phase unwrapping. *J Mag Res Imag* 6, 495-502 (1996).
105. Drangova, M., Zhu, Y. & Pelc, N. Effect of artifacts due to flowing blood on the reproducibility of phase-contrast measurements of myocardial motion. *J Mag Res Imag* 7, 664-668 (1997).
106. Hennig, J. et al. Analysis of myocardial motion based on velocity measurements with a black blood prepared segmented gradient-echo sequence: Methodology and applications to normal volunteers and patients. *J Mag Res Imag* 8, 868-877 (1998).
107. Zhu, Y., Drangova, M. & Pelc, N. Estimation of deformation gradient from cine-PC velocity data. *IEEE Trans Med Imag* 16, 840-851 (1997).
108. Zhu, Y., Drangova, M. & Pelc, N. Fourier tracking of myocardial motion using cine-PC data. *Mag Res Med* 35, 471-480 (1996).
109. Zhu, Y. & Pelc, N. Three-dimensional motion tracking with volumetric phase contrast CMR velocity imaging. *J Mag Res Imag* 9, 111-118 (1999).
110. Arai, A., Gaither, C. r., Epstein, F., Balaban, R. & Wolff, S. Myocardial velocity gradient imaging by phase contrast CMRI with application to regional function in myocardial ischaemia. *Mag Res Med* 42, 98-109 (1999).
111. Robson, M. & Constable, R. Three-dimensional strain-rate imaging. *Mag Res Med* 36, 537-546 (1996).
112. Meyer, F., Constable, R., Sinusas, A. & Duncan, J. Tracking myocardial deformation using phase contrast MR velocity fields: a stochastic approach. *IEEE Trans Med Imag* 15, 453-465 (1996).
113. Van der Geest, R., Kayser, H., Wall, E. V. d., Roost, A. d. & Reiber, J. in *Society for Cardiovascular Magnetic Resonance* 65 (Atlanta, USA, 1998).
114. Van der Geest, R. et al. in *Annual Scientific Meeting International Society Magnetic Resonance Medicine* (1999).
115. Le Bihan, D. et al. MR imaging of intravoxel incoherent motions: application to diffusion and perfusion in neurologic disorders. *Radiology* 161, 401-407 (1986).
116. Reese, T. et al. Imaging myocardial fibre architecture in vivo with magnetic resonance. *Magn Reson Med* 34, 786-791 (1995).
117. Hsu, E., Muzikant, A., Matulevicius, S., Penland, R. & Henriquez, C. Magnetic resonance myocardial fibre-orientation mapping with direct histological correlation. *Amer Jour Physiology* 274, H2308-2318 (1998).

118. Scollan, D., Holmes, A., Winslow, R. & Forder, J. Histological validation of myocardial microstructure obtained from diffusion tensor magnetic resonance imaging. *Amer Jour Physiology* **275** (1998).
119. Trouard, T., Theilmann, R., Altbach, M. & Gmitro, A. High-resolution diffusion imaging with DIFRAD-FSE CMRI. *Magn Reson Med* **42**, 11-18 (1999).
120. Tseng, W., Reese, T., Weisskoff, R. & Wedeen, V. Cardiac diffusion tensor CMRI in vivo without strain correction. *Magn Reson Med* **42**, 393-403 (1999).
121. Firmin, D., Gatehouse, P., Yang, G., Jhooti, P. & Keegan, J. in *5th Annual Scientific Meeting ISMRM* 188 (1997).
122. Firmin, D. & Keegan, J. Navigator echoes in cardiac magnetic resonance. *J Cardiovasc Magn Reson* **3**, 183-193 (2001).
123. Ehman, R. & Felmlee, J. Adaptive technique for high-definition MR imaging of moving structures. *Radiology* **173**, 255-263 (1989).
124. Wang, Y., Grimm, R., Felmlee, J., Riederer, S. & Ehman, R. Algorithms for extracting motion information from navigator echoes. *Mag Res Med* **36**, 117-123 (1996).
125. Sachs, T. et al. Real-time motion detection in spiral MRI using navigators. *Mag Res Med* **32**, 639-645 (1994).
126. Oshinski, J. et al. Two-dimensional coronary MR angiography without breath holding. *Radiology* **201**, 737-743 (1996).
127. Sachs, T. et al. The diminishing variance algorithm for real-time reduction of motion artifacts in MRI. *Mag Res Med* **34**, 412-422 (1995).
128. Jhooti, P. et al. Hybrid ordered phase encoding (HOPE): an improved approach for respiratory artifact reduction. *J Mag Res Imag* **8**, 968-980 (1998).
129. Bunce, N. et al. Evaluation of free-breathing three-dimensional magnetic resonance coronary angiography with hybrid ordered phase encoding (HOPE) for the detection of proximal coronary artery stenosis. *J Mag Res Imag* **14**, 677-684 (2001).
130. Yang, G., Burger, P., Gatehouse, P. & Firmin, D. Locally focused 3D coronary imaging using volume selective RF excitation. *Mag Res Med* **41**, 171-178 (1999).
131. Sinkus, R. & Bornert, P. Motion pattern adapted real-time respiratory gating. *Mag Res Med* **9**, 395-401 (1999).
132. Kuijer, J., Jansen, E., Marcus, J., Rossum, A. v. & Heethaar, R. Improved harmonic phase myocardial strain maps. *Mag Res Med* **46**, 993-999 (2001).
133. Chan, T. & Shen, J. Variational Restoration of Non-Flat Image Features: Models and Algorithms. *SIAM Journal on Applied Mathematics* (2000).
134. Rudin, L., Osher, S. & Fatemi, E. Nonlinear total variation based noise removal algorithms. *Physica D* **60**, 259-268 (1992).

135. Blomgren, P. & Chan, T. Color TV: Total Variation Methods for Restoration of Vector-Valued Images. *IEEE Trans Image Processing* 7 (1998).
136. Coulon, O., Alexander, D. & Arridge, S. in *Medical Image Understanding and Analysis* (Birmingham, UK, 2001).
137. Ng, Y. & Yang, G.-Z. in *11th International Conference in Central Europe on Computer Graphics, Visualisation and Computer Vision (WSCG)* (2003).
138. Taylor, A., Jhooti, P., Firmin, D. & Pennell, D. Automated monitoring of diaphragm end-expiratory position for real-time navigator echo MR coronary angiography. *J Mag Res Imag* 9, 395-401 (1999).
139. Ehlert, F. Comparison of dilated cardiomyopathy and coronary artery disease in patients with life-threatening ventricular arrhythmias: Differences in presentation and outcome in the AVID registry. *Am Heart J* 142, 816-822 (2001).
140. Grothues, F. et al. Comparison of interstudy reproducibility of cardiovascular magnetic resonance with two-dimensional echocardiography in normal subjects and in patients with heart failure or left ventricular hypertrophy. *Am J Cardiol* 90, 29-34 (2002).
141. Maron, B. Hypertrophic cardiomyopathy: a systematic review. *JAMA* 287, 1308-1320 (2002).
142. Cerqueira, M. et al. Standardized myocardial segmentation and nomenclature for tomographic imaging of the heart: a statement for healthcare professionals from the Cardiac Imaging Committee of the Council on Clinical Cardiology of the American Heart Association. *Circulation* 105, 539-542 (2002).
143. Pislaru, C., Abraham, T. & Belohlavek, M. Strain and strain rate echocardiography. *Curr Opin Cardiol* 17, 443-454 (2002).
144. Edvardsen, T. et al. Quantitative assessment of intrinsic regional myocardial deformation by Doppler strain rate echocardiography in humans: validation against three-dimensional tagged magnetic resonance imaging. *Circulation* 106, 50-56 (2002).
145. Garot, J. et al. Fast determination of regional myocardial strain fields from tagged cardiac images using harmonic phase MRI. *Circulation* 101, 981-988 (2000).
146. Jhooti, P. et al. 3D coronary artery imaging with phase reordering for improved scan efficiency. *Mag Res Med* 41, 555-562 (1999).
147. Jhooti, P. et al. Phase ordering with automatic window selection (PAWS): a novel motion-resistant technique for 3D coronary imaging. *Mag Res Med* 43, 470-480 (2000).
148. Perman, W., Moran, P., Moran, R. & Bernstein, M. Artifacts from pulsatile flow in MR imaging. *Journal of Computer Assisted Tomography* 10, 473-483 (1986).

149. Wolf, R. et al. Blood flow imaging through detection of temporal variations in magnetization. *Radiology* **185**, 559-567 (1992).
150. Felmlee, J. & Ehman, R. Spatial presaturation: a method for suppressing flow artifacts and improving depiction of vascular anatomy in MR imaging. *Radiology* **164**, 559-564 (1987).
151. Jung, B., Jahnke, C., Föll, D. & Hennig, J. in *Annual Scientific Meeting ISMRM* 1614 (ISMRM, Toronto, Canada, 2003).
152. Conturo, T. & Smith, G. Signal-to-noise in phase angle reconstruction: dynamic range extension using phase reference offsets. *Mag Res Med* **15**, 420-437 (1990).
153. Bernstein, M. et al. Concomitant gradient terms in phase contrast MR: analysis and correction. *Mag Res Med* **39**, 300-308 (1998).
154. Firmin, D., Naylor, G., Kilner, P. & Longmore, D. The application of phase shifts in NMR for flow measurement. *Mag Res Med* **14**, 230-241 (1990).
155. Zhu, Y. & Pelc, N. A spatiotemporal model of cyclic kinematics and its application to analysing nonrigid motion with MR velocity images. *IEEE Trans Med Imag* **18**, 557-569 (1999).
156. Firmin, D. in *Cardiovascular Magnetic Resonance* (eds. Pennell, D. & Manning, W.) (Churchill Livingstone, Philadelphia, Pennsylvania, USA, 2002).
157. Yang, G., Gatehouse, P., Keegan, J., Mohiaddin, R. & Firmin, D. Three-dimensional coronary MR angiography using zonal echo-planar imaging. *J Mag Res Imag* **39**, 833-842 (1998).
158. Peshock, R. in *Cardiovascular Magnetic Resonance* (eds. Pennell, D. & Manning, W.) (Churchill Livingstone, Philadelphia, Pennsylvania, USA, 2002).
159. Press, W., Teukolsky, S., Vetterling, W. & Flannery, B. *Numerical Recipes in C, the art of scientific computing* (Cambridge University Press, Cambridge, 1999).
160. Young, A., Axel, L., Dougherty, L., Bogen, D. & Parenteau, C. Validation of tagging with MR imaging to estimate material deformation. *Radiology* **188**, 101-108 (1993).
161. Kuijter, J., Marcus, J., Gotte, M., Rossum, A. v. & Heethaar, R. Simultaneous MRI tagging and through-plane velocity quantification: a three-dimensional myocardial motion tracking algorithm. *J Magn Reson Imag* **9**, 409-419 (1999).
162. NHLBI, N. R. in <http://www.nhlbi.nih.gov/new/index.htm> (2000).
163. Kerwin, W., Osman, N. & Prince, J. in *Handbook of Medical Image Processing* (ed. Bankman, I.) (Academic Press, 2000).
164. Haacke, M., Brown, R., Thompson, M. & Venkatesan, R. *Magnetic Resonance Imaging: Physical Principles and Sequence Design* (John Wiley & Sons Inc, 1999).
165. Bayram, E., Hamilton, C. & Hundley, W. in *23rd Annual Conference IEEE Engineering in Medicine and Biology Society* (IEEE, Istanbul, Turkey, 2001).